UNIVERSIDAD DE OVIEDO

Departamento de Física

Selected Topics on Molecular Electronics, Magnetism and Surface Science

Víctor Manuel García Suárez

UNIVERSIDAD DE OVIEDO

Departamento de Física

Doctoral Thesis for the Degree of
Doctor of Philosophy

Selected Topics on Molecular Electronics, Magnetism and Surface Science

Author: Víctor Manuel García Suárez
Thesis Advisor: Jaime Ferrer Rodríguez

Oviedo, September 8, 2005

Agradecimientos

Las colaboraciones con otros equipos científicos y el intercambio de ideas con otras personas fueron partes fundamentales en el desarrollo de esta tesis, sin las cuales tal vez nunca hubiese visto la luz. Es por ello que me gustaría empezar dándoles las gracias a todos ellos, que a continuación paso a listar en orden cronológico.

Quería sobre todo agradecer a mi director de tesis Jaime Ferrer su apoyo y dedicación durante todo este tiempo. Él me enseño la mayor parte de los conocimientos relacionados con la tesis y me ayudó a superar muchos problemas. Su entusiasmo y motivación también consiguieron hacerme disfrutar a la vez que aprendía.

Mis primeros pasos en las simulaciones ab initio y la introducción al código SIESTA se los debo a Jose Miguel Alonso Pruneda. También quiero agradecerle su inestimable ayuda con la espiral.

José Soler me enseño los secretos de SIESTA y me ayudó también a implementar la espiral y los magnones. Gracias a él la versión de la espiral se incluyó oficialmente en SIESTA. Por eso quería agradecerle su sincero apoyo y dedicación. También sus estudiantes Eduardo Anglada y Óscar Paz me hicieron pasar buenos ratos durante mi estancia en Madrid. Además Jose me puso en contacto con Pablo García, con el que tuve interesantes discusiones sobre los magnones, y con Rodolfo Miranda, que me dió acceso a sus datos experimentales para hacer las simulaciones sobre las superficies de cobre y rutenio.

Gracias a la colaboración con Colin Lambert y a las charlas con sus estudiante Chris Newman y su postdoctorando Steve Bailey pude avanzar sustancialmente en mis cálculos de transporte. Quería sobre todo agradecer a Colin el permitirme continuar con mi trabajo como investigador en la Universidad de Lancaster.

El desarrollo de SMEAGOL fue posible gracias a la colaboración con Stefano Sanvito

y su estudiante Alexandre Reily Rocha, con los que obtuvimos además algunos de los resultados con mayor impacto de la tesis. Alex y yo programamos las subrutinas de las funciones de Green de no equilibrio e implementamos la conexión con SIESTA.

También hubiese sido difícil pasar estos años sin la compañia en el despacho de Pablo Victorero, Ana Domínguez, Lucas Fernández, Jose Ignacio Martín y María Vélez. La labor de Lucas como administrador de los ordenadores fue imprescindible para resolver multitud de problemas informáticos.

Quería extender también mi agradecimiento a mis amigos y a todas las personas que he conocido y me han ayudado durante estos años y pedirles disculpas por no nombrarlos explícitamente. Sin ellos no estaría donde estoy.

Finalmente quería agradecer a mi familia y a mis seres queridos su constante apoyo y comprensión. A ellos va dedicada esta tesis.

ÍNDICE

INDEX

LIST OF FIGURES

LIST OF TABLES

Resumen en Español

Introducción: Cálculos de Primeros Principios

Desde el descubrimiento de la ecuación de Schrödinger muchos esfuerzos se han hecho por aproximarla. Los dos desarrollos teóricos más populares en la actualidad son la configuración de interacción [6] y la teoría del funcional de la densidad [1, 2]. El primero permite ser mejorado sistemáticamente pero tiene el problema de que al aumentar la precisión o el número de átomos el tiempo y la memoria de cálculo crecen muy rápidamente. En cambio, la teoría del funcional de la densidad a pesar de no poder ser mejorada de forma sistemática permite llevar a cabo simulaciones con muchos átomos y da resultados bastante precisos en la mayoría de los casos.

El problema de la estructura electrónica de la materia

La materia está formada básicamente por núcleos, que en un sólido o molécula vibran alrededor de sus posiciones de equilibrio, y electrones, que se mueven alrededor de los núcleos y a través del material. La distribución de probabilidad de los electrones se obtiene al resolver la ecuación de Schrödinger:

$$\hat{\mathcal{H}}\Psi(\vec{R}_1, ..., \vec{R}_{N_N}, \vec{r}_1, ..., \vec{r}_{N_e}) = E\Psi(\vec{R}_1, ..., \vec{R}_{N_N}, \vec{r}_1, ..., \vec{r}_{N_e}) \tag{0.1}$$

donde $\hat{\mathcal{H}}$ es el Hamiltoniano, Ψ es la función de onda y N_N y N_e representan el número de átomos y electrones, respectivamente. En el caso simplificado de un sistema sin polarización de espín, el Hamiltoniano tiene la siguiente forma:

$$\hat{\mathcal{H}} = -\sum_A \frac{\nabla_A^2}{2M_A} - \sum_i \frac{\nabla_i^2}{2} - \sum_{A,i} \frac{Z_A}{R_{Ai}} + \sum_{A>B} \frac{Z_A Z_B}{R_{AB}} + \sum_{i>j} \frac{1}{r_{ij}} + \sum_A V^{\text{ext}}(\vec{R}_A) + \\ + \sum_i V^{\text{ext}}(\vec{r}_i) = \hat{T}^N + \hat{T}^e + V^{Ne}(\{\vec{R}\},\{\vec{r}\}) + V^{NN}(\{\vec{R}\}) + V^{ee}(\{\vec{r}\}) + \\ + V^{\text{ext}}(\{\vec{R}\},\{\vec{r}\}) \tag{0.2}$$

Los respectivos términos representan la energía cinética nuclear, la energía cinética electrónica, la interacción entre núcleos y electrones, la interacción entre núcleos, la interacción entre electrones y los potenciales externos, que actúan individualmente sobre cada partícula.

En principio la mayoría de las propiedades físicas de la materia pueden ser obtenidas resolviendo la ecuación de Schrödinger. Sin embargo, debido al gran número de grados de libertad, que se manifiestan a la hora de calcular y almacenar la función de onda [4], este problema se antoja imposible para la mayoría de los casos, por lo que se deben buscar aproximaciones.

La primera simplificación, debida a Born y Oppenheimer, se basa en el hecho de que los electrones son mucho más ligeros que los núcleos y por tanto desde un punto de vista clásico se pueden considerar también mucho más rápidos. Esto significa que las coordenadas de los dos tipos de partículas se pueden desacoplar y sólo es necesario resolver los grados de libertad electrónicos para cada configuración de los núcleos, con lo que el sistema se simplifica considerablemente. A pesar de todo, el problema electrónico todavía es muy complicado de resolver.

El principal inconveniente a la hora de tratar la parte electrónica es el término de interacción electrón-electrón que hace que la función de onda no se pueda separar en funciones de onda de una sola partícula. Aún así, una aproximación muy popular, la aproximación Hartree-Fock (HF) [5], se basa precisamente en descomponer la función de onda de esa forma, es decir, en expresarla como un sólo determinante de Slater. Como consecuencia los elecrones se quedan completamente descorrelacionados y muchas propiedades físicas predichas por HF difieren completamente de las medidas en los experimentos. A pesar de todo, este método se puede mejorar sistematicamente añadiendo determinantes formados con estados excitados para ir completando el espacio de Hilbert, lo que se conoce como configuración de interacción [6]. Sin embargo, el esfuerzo computacional aumenta dramáticamente con el número de átomos y de determinantes.

La Teoría del funcional de la densidad

Una alternativa a los anteriores métodos es la teoría del funcional de la densidad (DFT), donde la variable básica es la densidad electrónica. DFT está basada en los teoremas de

Hohenberg-Kohn [1]:

- Primer teorema de Hohenberg-Kohn: Hay una correspondencia exacta entre la densidad y el potencial externo, es decir, la densidad determina unívocamente el potencial, salvo una constante.
- Segundo teorema de Hohenberg-Kohn: La densidad que minimiza la energía es la densidad del estado fundamental (principio variacional).

Estos teoremas implican que cualquier observable es función de la densidad. Consequentemente, el estado fundamental se puede obtener de manera autoconsistente utilizando la densidad como variable.

Por otro lado, debido al hecho de que distintas funciones de onda pueden dar la misma densidad, es posible elegir como referencia de nuestro sistema una función de onda formada por un sólo determinante de Slater. Esto significa que el sistema original de muchas partículas interactuando entre ellas se puede mapear a un sistema de partículas no interactuantes en un potencial efectivo. Dentro de este esquema, conocido como esquema de Kohn-Sham [2], la ecuación de Schrödinger tiene la siguiente forma:

$$\left(-\frac{1}{2}\nabla^2 + V^{\mathrm{H}}[n] + V^{xc}[n] + V^{\mathrm{ext}}[n]\right)\varphi_i = \varepsilon_i\varphi_i \tag{0.3}$$

donde el potencial de interacción electrón-electrón ha sido separado en el término Hartree, debido a la energía clásica asociada con la distribución de carga, y un término de canje y corelación que incluye a modo de potencial efectivo los términos de interacción entre partículas.

En principio, si todos los términos anteriores se conociesen de forma exacta cualquier sistema compuesto por muchas partículas se podría resolver de forma muy sencilla y sin errores. Sin embargo el canje y la correlación no se conocen exactamente y tienen que ser aproximados. La aproximación más sencilla es la aproximación de la densidad local (LDA), que calcula en cada punto el canje y la correlación utilizando la fórmula local de un gas de electrones uniforme [10, 11]. Este funcional da buenos resultados en muchos casos debido a que el promedio del hueco de canje y correlación, que es lo que importa a la hora de calcular la energía, es muy parecido al promedio del hueco verdadero y además dicho hueco corresponde a un sistema físico, lo que hace que verifique la regla de la suma y la parte de canje sea siempre negativa [8, 9].

Sin embargo, la LDA falla estrepitosamente cuando la densidad tiene variaciones pronunciadas, como por ejemplo en los metales de transición. En ese caso se utiliza la aproximación de gradientes generalizados (GGA), que incluye también el gradiente de la densidad dentro del funcional [13].

El método SIESTA

SIESTA (iniciativa española para simulaciones electrónicas con miles de átomos) es un código basado en DFT que permite simular sistemas relativamente grandes de forma aproximada o sistemas pequeños con mucha precisión [21]. Sus principales características se basan en el uso de pseudopotenciales y combinaciones lineales de orbitales atómicos.

Los pseudopotenciales se utilizan para no tener que incluir en los cálculos los electrones más interiores de los átomos, que habitualmente no participan en el enlace atómico, y para evitar las oscilaciones pronunciadas de las funciones de onda cerca del núcleo [22]. Para que las propiedades físicas sean las mismas que las propiedades físicas del sistema electrónico original los pseudopotenciales deben tener las siguientes características:

- Los autovalores y la dependencia energética de los orbitales calculados con el pseudopotencial (pseudoorbitales) deben ser los mismos que los obtenidos con todos los electrones.
- La parte radial de los pseudoorbitales debe ser suave y no tener nodos dentro de la región interior. Esto implica que para cada canal de momento angular l debe generarse un tipo distinto de pseudopotencial $V_l(r)$.
- La carga dentro del radio de corte (donde se redefinen los potenciales y las funciones de onda) calculada con las pseudofunciones de onda debe ser igual a la carga calculada con los orbitales originales dentro del mismo radio [24].
- Para radios mayores que los radios de corte los pseudoorbitales deben coincidir con los orbitales originales, calculados con todos los electrones. Como consecuencia el pseudopotencial más allá del radio de corte más grande debe ser igual al potencial nuclear original.

Los pseudopotenciales también pueden tener correciones relativistas [26, 27, 28], en el caso de elementos muy pesados, y correcciones de core no lineales para algunos de los electrones interiores [29] cuando las funciones de onda de valencia y las de dichos electrones solapan.

Otra característica de SIESTA es el uso de combinaciones lineales de orbitales atómicos, $\phi(\vec{r}-\vec{R})$ ($\vec{R}$ es el vector entre celdas unidad), que se extienden hasta un cierto radio atómico [30]. Esta aproximación, que es básica para que el programa escale linealemente con el número de átomos, tiene la ventaja de que la descripción del sistema obtenida con bases relativamente sencillas es bastante mejor que la descripción obtenida empleando, por ejemplo, pocas ondas planas, y la convergencia en energía de los cálculos es más rápida [31].

La función de onda en SIESTA en el caso general de un sistema periódico y no colinear tiene por tanto la siguiente forma:

$$\hat{\Psi}_{n\vec{k}}(\vec{r}) = \frac{1}{\sqrt{N_u}} \sum_{\vec{R},\mu} e^{i\vec{k}\cdot\vec{R}_\mu} \hat{c}_{n\vec{k}\mu} \phi_{\vec{R}_\mu}(\vec{r} - \vec{R}_\mu) \tag{0.4}$$

donde $\hat{\Psi}$ y $\hat{c}$ son espinores, μ es un índice de orbital que va a la celda unidad, n es el índice de la banda, $\vec{k}$ representa el punto k, relacionado con el teorema de Bloch, y N_u es el número de celdas unidad del sistema total. Partiendo de esta expresión la ecuación de Schrödinger puede escribirse en función de los elementos de matriz del Hamiltoniano y de la los solapes de la siguiente forma:

$$\sum_{\nu,\sigma'} \left(\mathcal{H}^{\sigma\sigma'}_{\mu\nu} - \varepsilon_{n\vec{k}} S_{\mu\nu} \delta^{\sigma\sigma'} \right) c^{\sigma'}_{n\vec{k}\nu} = 0 \tag{0.5}$$

donde σ, σ' representan las componentes de espín.

Una vez resuelta la ecuación de Schrödinger se calcula la densidad:

$$n^{\sigma\sigma'}(\vec{r}) = \sum_{\mu,\vec{R},\nu} \rho^{\sigma\sigma'}_{\mu\vec{R}_\nu} \phi_\mu(\vec{r} - \vec{d}_\mu) \phi_{\vec{R}_\nu}(\vec{r} - \vec{R}_\nu) \tag{0.6}$$

donde

$$\rho^{\sigma\sigma'}_{\mu\vec{R}_\nu} = \frac{1}{N_k} \sum_{n,\vec{k}} f_{n\vec{k}} e^{i\vec{k}\cdot(\vec{d}_\mu - \vec{R}_\nu)} c^{\sigma}_{n\vec{k}\mu} c^{\sigma'*}_{n\vec{k}\nu} \tag{0.7}$$

representa la matriz densidad. A partir de aquí se calcula la energía y vuelve a obtenerse el Hamiltoniano que se utiliza de nuevo para resolver la ecuación de Schrödinger, etc. El proceso acaba cuando las diferencia entre los elementos de las matrices densidad de un paso y el anterior son menores que una cierta tolerancia.

Un ejemplo paradigmático: impurezas de cobalto en matrices de SnO_2

Experimentalmente se observa que el SnO_2 con impurezas de Co, $Sn_{1-x}Co_xO_{2-\delta}$, es ferromagnético y tiene un momento magnético por átomo de cobalto de 7.5 ± 0.5 μ_B [38].

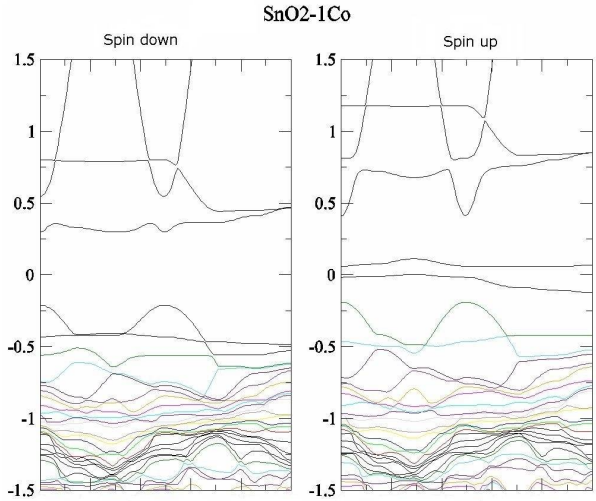

Fig. 0.1: Estructura de bandas de una matriz de SnO_2 de 48 átomos con un Sn substituído por un Co. Para espines mayoritarios (izquierda) aparece una banda al nivel de Fermi que está ausente en el caso de espines minoritarios (derecha).

Este valor tan alto del momento magntético implica que, o bien hay contribuciones importantes del momento magnético orbital, por ejemplo en los átomos de la superficie, o bien algún momento magnético aparece en los átomos alrededor del cobalto.

Para responder a estas preguntas llevé a cabo varias simulaciones de matrices de SnO_2 con bases doble-ζ polarizadas y el funcional LDA. En primer lugar utilicé 48 átomos y un Sn substituído por un Co. El sistema resultante se magnetiza y desarrolla un momento magnético de 1 μ_B alrededor del cobalto, que comparten este átomo y los oxígenos circundantes dando lugar a un estado localizado similar a un polarón. El sistema se convierte además en 'medio metálico' [39], con una banda al nivel de Fermi poco dispersiva para espines minoritarios, como se puede ver en la figura (0.1). Por otro lado, empleando matrices de 72 átomos con dos Co comprobé que el sistema es paramagnético, ya que los 'polarones' no interaccionan entre ellos y la diferencia de energía entre el caso ferromagnético y el antiferromagnético es despreciable.

En resumidas cuentas, los cálculos no concuerdan con los experimentos. Sin embargo, la razón de las discrepancias es conocida y se debe a que en los óxidos metálicos los electrones están fuertemente correlacionados [36] y la LDA produce resultados inexactos debido en parte a la autointeracción, que no está corregida [11]. Esto se puede solucionar en parte con el funcional LDA+U [40], que incluye un término Hubbard de repulsión entre nubes electrónicas del mismo espín.

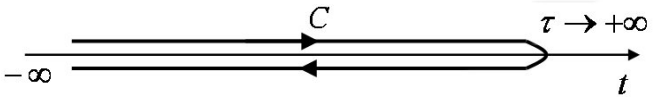

Fig. 0.2: Contorno de Keldysh.

Electrónica Molecular y Nanométrica

Recientemente se ha demostrado la posibilidad de alcanzar el último límite en la industria electrónica, es decir, el tamaño atómico. Mediante el microscopio de efecto túnel y las uniones de rotura mecánica controlable se han podido fabricar contactos de un sólo átomo e ir incluso más allá y producir cadenas atómicas [41, 42]. Por otra parte, empleando moléculas [43, 44] y nanotubos de carbono [45, 46, 47, 48, 49, 50, 51] se están dando los primeros pasos hacia la construcción de ordenadores de tamaño microscópico y capacidades de procesamiento y memoria sin precedentes.

Para estudiar estos sistemas tan pequeños es necesario emplear teorías de transporte cuántico que tengan en cuenta la estructura electrónica y los contactos. Uno de los formalismos más populares para estudiar sistemas fuera del equlibrio es el formalismo de Keldysh [55], que ha sido implementado en el código SMEAGOL (electrónica de espín y molecular en un formalismo de orbitales atómicos) [57] y ha permitido simular las propiedades de transporte de constricciones atómicas, moléculas y nanotubos.

Teoría de transporte

El formalismo de Keldysh [55] se basa en el hecho de que en situaciones fuera del equilibrio no es posible conocer el estado del sistema en tiempos posteriores a la aplicación de la perturbación ($+\infty$) y por tanto es necesario emplear un contorno de integración que vuelva atrás en el tiempo, como el de la figura (0.2). Utilizando esta técnica es posible obtener la siguiente ecuación de Dyson para las funciones de Green retardada (G^{R}), avanzada (G^{A}), $\hat{G}^{<}$ y $\hat{G}^{>}$:

$$\hat{G}^{\mathrm{R/A}} = \hat{g}_0^{\mathrm{R/A}} + \hat{g}_0^{\mathrm{R/A}}\hat{\Sigma}^{\mathrm{R/A}}\hat{G}^{\mathrm{R/A}} \tag{0.8}$$

$$\hat{G}^{</>} = (\hat{1} + \hat{G}^{\mathrm{R}}\hat{\Sigma}^{\mathrm{R}})\hat{g}^{</>}(\hat{1} + \hat{\Sigma}^{\mathrm{A}}\hat{G}^{\mathrm{A}}) - \hat{G}^{\mathrm{R}}\hat{\Sigma}^{</>}\hat{G}^{\mathrm{A}} \tag{0.9}$$

En el límite de equilibrio, $\hat{G}^{<}(E) = i\hat{A}(E)f(E)$ y $\hat{G}^{>}(E) = i\hat{A}(E)[f(E) - 1]$, donde $f(E) = f(E - \varepsilon_{\mathrm{F}})$ es la función de distribución de Fermi y $\hat{A}(E) = i[\hat{G}^{\mathrm{R}}(E) - \hat{G}^{\mathrm{A}}(E)]$ se conoce como función espectral.

Con estos ingredientes es muy sencillo obtener las propiedades electónicas y de transporte. Pero primero hay que dividir el sistema en tres partes [71, 72, 73]: el electrodo izquierdo, la región de dispersión y el electrodo derecho. La función de Green retardada, que en equilibrio es suficiente para obtener la función $G^<$ y por tanto la matriz densidad, tiene la siguiente forma:

$$\hat{G}^{\mathrm{R}}_{\mathrm{MM},\mu\nu}(Z) = [Z\hat{S}_{\mathrm{MM}} - \hat{\mathcal{H}}_{\mathrm{MM}} - \hat{\Sigma}^{\mathrm{R}}_{\mathrm{L}}(Z) - \hat{\Sigma}^{\mathrm{R}}_{\mathrm{R}}(Z)]^{-1}_{\mu\nu} \tag{0.10}$$

donde $Z = E + i\delta$ para cantidades retardadas (mientras que $Z^* = E - i\delta$ es para cantidades avanzadas) y $\hat{\Sigma}_{\mathrm{L(R)}} = \hat{V}_{\mathrm{ML(R)}}\hat{g}_{\mathrm{LL(RR)}}\hat{V}_{\mathrm{L(R)M}}$ son la autoenergías, que incluyen el acoplo a los electrodos $\hat{V}_{\mathrm{L(R)M}}$ y la función de Green de superficie $\hat{g}_{\mathrm{LL(RR)}}$. La matriz densidad viene dada por la siguiente expresión:

$$\hat{\rho}_{\mathrm{MM},\mu\nu} = -\frac{1}{\pi}\int_{C+L} \mathrm{Im}[\hat{G}^{\mathrm{R}}_{\mathrm{MM},\mu\nu}(Z)]f(Z-\varepsilon_F)\mathrm{d}Z - 2\pi i k_{\mathrm{B}}T\sum_{n=1}^{N_p}\hat{G}^{\mathrm{R}}_{\mathrm{MM},\mu\nu}(Z_n) \tag{0.11}$$

La integración se lleva a cabo en el plano complejo para disminuir el número de puntos y por tanto el tamaño del cálculo. Nótese que también hay que incluir los puntos singulares de la función de Fermi.

Fuera del equilibrio hay que calcular explícitamente la función $\hat{G}^<$, que es distinta de la obtenida en equilibrio, como paso previo para determinar la matriz densidad:

$$\begin{aligned}\hat{G}^<_{\mathrm{MM}}(Z) &= \hat{G}^<_{\mathrm{MM,eq,L}}(Z) + i\hat{G}^{\mathrm{R}}_{\mathrm{MM}}(Z)\hat{\Gamma}_{\mathrm{R}}(Z-eV_{\mathrm{R}})\hat{G}^{\mathrm{A}}_{\mathrm{MM}}(Z)[f(Z-\mu_{\mathrm{R}}) - f(Z-\mu_{\mathrm{L}})] = \\ &= \hat{G}^<_{\mathrm{MM,eq,L}}(Z) + \delta\hat{G}^<_{\mathrm{MM}}(Z)\end{aligned} \tag{0.12}$$

donde $\mu_{\mathrm{L(R)}} = \varepsilon_{\mathrm{F}} + eV_{\mathrm{L(R)}}$, $\hat{G}^<_{\mathrm{MM,eq,L}} = i\hat{G}^{\mathrm{R}}_{\mathrm{MM}}(\hat{\Gamma}_{\mathrm{L}} + \hat{\Gamma}_{\mathrm{R}})\hat{G}^{\mathrm{A}}_{\mathrm{MM}}f_{\mathrm{L}}$ (con $f_{\mathrm{L}} = f(Z-\mu_{\mathrm{L}})$) y $\hat{\Gamma} = i(\hat{\Sigma}^{\mathrm{R}} - \hat{\Sigma}^{\mathrm{A}})$. El último término de la ecuación (0.12) no es analítico en el plano complejo y debe integrarse en el eje real a lo largo de $\varepsilon_{\mathrm{L}} - \varepsilon_{\mathrm{R}} = e\Delta V + 2k_{\mathrm{B}}T$, donde $e\Delta V = e(V_L - V_R) = \mu_{\mathrm{L}} - \mu_{\mathrm{R}}$.

Por último, la corriente viene dada por la siguiente expresión [79], que también hay que integrar en el eje real porque la función no es analítica:

$$I(V) = \frac{e}{h}\int_{\varepsilon_{\mathrm{R}}}^{\varepsilon_{\mathrm{L}}} \mathrm{Tr}[\hat{G}^{\mathrm{A}}_{\mathrm{MM}}\hat{\Gamma}_{\mathrm{R}}\hat{G}^{\mathrm{R}}_{\mathrm{MM}}\hat{\Gamma}_{\mathrm{L}}](E,V)[f(E-\mu_{\mathrm{L}}(V)) - f(E-\mu_{\mathrm{R}}(V))]\mathrm{d}E \tag{0.13}$$

o, lo que es lo mismo

$$I(V) = \frac{e}{h}\int_{\varepsilon_{\mathrm{R}}}^{\varepsilon_{\mathrm{L}}} \mathrm{Tr}[\hat{t}^{\dagger}\hat{t}](E,V)[f(E-\mu_{\mathrm{L}}(V)) - f(E-\mu_{\mathrm{R}}(V))]\mathrm{d}E = \tag{0.14}$$

$$= \frac{e}{h}\int_{\varepsilon_{\mathrm{R}}}^{\varepsilon_{\mathrm{L}}} T(E,V)[f(E-\mu_{\mathrm{L}}(V)) - f(E-\mu_{\mathrm{R}}(V))]\mathrm{d}E \tag{0.15}$$

donde $\hat{t}(E,V) = [\hat{\Gamma}_{\mathrm{R}}(E,V)]^{1/2}\hat{G}_{\mathrm{MM}}(E,V)[\hat{\Gamma}_{\mathrm{L}}(E,V)]^{1/2}$ es la matriz de transmisión [80] y $T(E,V)$ es la transmisión total. La conductancia en el régimen lineal, $G = I/V$, viene dada por [56]

$$G(V) = \frac{G_0}{2V}\int_{\varepsilon_{\mathrm{R}}}^{\varepsilon_{\mathrm{L}}} T(E,V)[f(E-\mu_{\mathrm{L}}(V)) - f(E-\mu_{\mathrm{R}}(V))]\mathrm{d}E \tag{0.16}$$

donde $G_0 = 2e^2/h$ es el quanto de conductancia y el 2 en el denominador aparece debido a que en la suma de la traza utilizada para obtener $T(E,V)$ también se tienen en cuenta las componentes de espín. En los casos de voltajes pequeños (régimen lineal) la conductancia se reduce a $G = (G_0/2)T(E_{\mathrm{F}},0)$.

El código SMEAGOL

SMEAGOL [57] utiliza los elementos del Hamiltoniano y la matriz de solape proporcionados por SIESTA para determinar la matriz densidad de la región de dispersión dentro y fuera del equilibrio. Al final de la autoconsistencia y, opcionalmente, de la dinámica molecular, también calcula la transmisión y la corriente.

Cada simulación hecha con SMEAGOL está compuesta en realidad por dos o tres cálculos independientes: los dos cálculos de la estructura electrónica de los electrodos (en caso de que sean diferentes) y el cálculo de transporte, propiamente dicho. En los dos primeros casos hay que determinar los elementos de volumen del Hamiltoniano, $\hat{\mathcal{H}}_0$ y $\hat{\mathcal{H}}_1$, y de la matriz de solape, $\hat{S}_0$ y $\hat{S}_1$. Para ello es necesario aplicar condiciones periódicas e incluir puntos k a lo largo de la dirección z, que se toma como la dirección a lo largo de la cual fluye la corriente. Estos elementos se utilizan posteriormente para determinar las funciones de Green de volumen y las autoenergías.

En el cálculo de transporte se substituye la diagonalización de SIESTA por las subrutinas que calculan la función de Green y se determina la matriz densidad integrando dicha función a lo largo de un contorno semicircular en el plano complejo. Esto es necesario hacerlo en vez de la diagonalización por dos razones: la primera es que SIESTA no puede simular sistemas en los que aparecen electrodos semiinfinitos, que en SMEAGOL se tienen en cuenta a través de las autoenergías. La segunda razón es que SIESTA tampoco puede calcular matrices densidad fuera del equilibrio, debido al hecho de que los electrodos tienen

funciones de distribución de Fermi distintas (calculadas a distintos voltajes) y por tanto la función de distribución en la región de dispersión no es igual a la de Fermi. También es necesario aplicar un desplazamiento rígido al potencial Hartree en los extremos de la celda unidad, para hacerlo casar con las autoenergías, y una rampa conectando ambos extremos.

Finalmente, la principal ventaja que tiene SMEAGOL sobre otros códigos es el cálculo de la función de Green de superficie, ya que utiliza un método semianatlítico [75] que es mucho más eficiente y estable que los métodos recursivos (ver por ejemplo [76]). Este método permite incluir puntos k perpendiculares y magnetismo sin problemas de convergencia. En el caso del magnetismo SMEAGOL ha sido un código realmente pionero, con el que se han llevado a cabo cálculos de magnetorresistencia en moléculas orgánicas situadas entre electrodos magnéticos y nanocontactos de níquel.

Magnetorresistencia en moléculas orgánicas entre electrodos magnéticos

Desde las primeras medidas de la conductancia en moléculas orgánicas entre electrodos de oro [43], este tipo de sistemas han sido extensivamente estudiados (ver por ejemplo [81]). Los casos más interesantes son sin embargo aquellos en los que los electrodos son magnéticos, ya que pueden dar lugar a efectos magnetorresistivos. Como ejemplos se pueden citar el uso de nanotubos de carbono como válvulas de espín [83], la transferencia e inyección de espines en moléculas orgánicas [84, 85, 86] y las uniones túnel orgánicas [87]. Todos estos sistemas permiten mantener la coherencia de espín a lo largo de grandes distancias gracias a que sus interacciones hiperfina y de espín órbita muy débiles.

Uno de los primeros cálculos que se realizaron dentro de la colaboración de SMEAGOL fue llevado a cabo por Alexandre Reily Rocha, que simuló dos tipos de moléculas, octano-ditiolato y 1,4-triceno-ditiolato, entre electrodos de Níquel fcc con 4 y 5 átomos por sección. Para ello utilizó el funcional LDA y bases simple-ζ para los s del H, C y S, doble-ζ polarizadas para el C y el p del S y doble-ζ para todos los orbitales del Ni. En el octano observó que la conductancia decrece exponencialmente cuando se emplean moléculas similares de mayor longitud, lo que demuestra que el transporte está en el régimen túnel. La magnetorresistencia, definida como $\Delta G = (G_P - G_{AP})/G_{AP}$, resultó ser del 40% al nivel de Fermi. En el triceno, sin embargo, tanto la conductancia como la magnetorresistencia ($\sim 100\%$ al nivel de Fermi) fueron bastante mayores, lo cual permite concluir que el transporte está en este caso en el régimen metálico. Estos resultados demuestran que los efectos magnetorresistivos dependen del tipo de molécula y abren la puerta al campo de la espintrónica molecular.

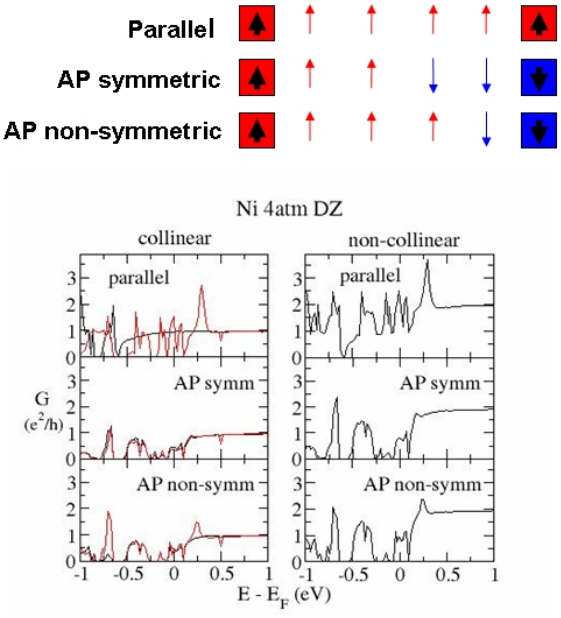

Fig. 0.3: Posibles paredes de dominio en la cadena de cuatro átomos y conductancias de los casos paralelo, antiparalelo simétrico y antiparalelo no simétrico (de arriba a abajo) calculados con espines colineales (izquierda) o no colineales (derecha). Como puede verse, las conductancias no colineales son iguales a la suma de las conductancias colineales.

Nanoncontactos de níquel

La mayoría de los sistemas magnetorresistivos tienen una región de dispersión no magnética y electrodos de un material magnético distinto, como en el ejemplo anterior. Sin embargo, efectos magnetorresistivos también han sido medidos en nanocontactos de níquel [88, 89, 90, 91, 92, 93, 94, 95, 96, 97], donde tanto los electrodos como la región de dispersión son magnéticos y del mismo material. A pesar de ello, el problema que tiene este sistema es que la reproducibilidad de los resultados es muy pequeña, debido al hecho de que los cambios en la corriente son muy sensibles a la estructura del contacto.

Para demostrar toda la capacidad de SMEAGOL en cálculos de transporte con polarización de espín y magnetismo no colineal llevé a cabo una serie de cálculos de varios nanocontactos de níquel (cadenas de uno a cuatro átomos[1] entre electrodos fcc crecidos a lo largo de la dirección (001) con secciones alternadas de 4 y 5 átomos, simulados con una base de orbitales doble-ζ y el funcional LDA) en la configuración 'especial' en la que los átomos están situados a las distancias de volumen. Los resultados indican que la pared

[1] Los casos de 3 y 4 átomos hay que considerarlos como casos extremos porque el níquel no tiene tendencia a formar cadenas atómicas muy largas [64].

de dominio es abrupta, ya que los momentos magnéticos permanecen colineales. Además la magnetización aumenta en los átomos centrales de la cadena como consecuencia de la reducción del campo cristalino, lo cual favorece además que se forme la pared cerca de los contactos. Los coeficientes de transmisión predichos para el caso de 4 átomos pueden observarse en la figura (0.3). La magnetorresistencia en este sistema es del 68%, cuando el contacto es simétrico, y del 60%, cuando es no simétrico. Para cadenas atómicas más pequeñas la magnetorresistencia disminuye e incluso se hace negativa en cadenas de uno y dos átomos. Estos resultados demuestran la posibilidad de simular con SMEAGOL sistemas con configuraciones magnéticas muy variadas.

Conductancia a través de un sólo canal en moléculas H_2 entre electrodos de platino o paladio

Desde el esperimento de Smit y colaboradores [44], en el que se demostró que una molécula de hidrógeno entre electrodos de platino tiene una conductancia de casi 1.0 G_0 (fácilmente distinguible por la presencia de un pico muy agudo en los histogramas de conducción), ha habido una serie de cálculos ab initio sobre la transmisión de dicha molécula en los que ésta podía estar en las configuraciones paralela o perpendicular al flujo de corriente [59, 60, 61, 62]. Sin embargo, a pesar de la simplicidad del sistema todavía no se ha conseguido aclarar del todo cuál de esas dos configuraciones es más estable y por qué.

Por otro lado, experimentos con electrodos de paladio [58] muestran un pico alrededor de 0.6 G_0, el cual puede moverse ligeramente cuando se aumenta la presión de hidrógeno y la temperatura en la cámara de vacío. Además, en este último caso también aparece otro pico cercano al quanto de conductancia. La razón de tal comportamiento ha sido atribuida a la disolución de hidrógeno en los electrodos. Aún así la pregunta más evidente es por qué en ausencia de tal disolución la conductancia es 0.6 y no 1.0 G_0.

Para tratar de entender tales sistemas y aclarar la controversia llevé a cabo una serie de simulaciones con SIESTA y SMEAGOL de electrodos de platino fcc crecidos a lo largo de la dirección (001), con capas formadas por dos planos alternados de 3×3 átomos cada uno y un máximo de 3 capas (6 planos) para cada electrodo. Empleé bases doble-ζ y doble-ζ polarizada para el H y el Pt/Pd, respectivamente, y el funcional LDA. También incluí condiciones de contorno periódicas y puntos k a lo largo de la direcciones perpendiculares (xy). Como contactos utilicé dos "pirámides" formadas cada una por cuatro átomos unidos a la capa 3×3 más externa, siguiendo la dirección fcc (001), y otro átomo en contacto con la molécula.

La configuración más estable la determiné relajando la parte central del sistema, es decir, las dos pirámides y la molécula, y manteniendo fijos los planos 3×3 siguientes. La configuración perpendicular resultó ser más estable que la paralela para distancias cortas. Pero si se permite una configuración "zigzag", en la que los átomos de los electrodos no

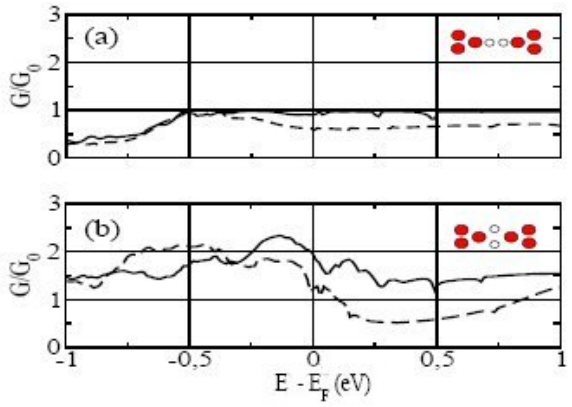

Fig. 0.4: Coeficientes de transmisión en (a) la configuración paralela y (b) la configuración perpendicular. Las líneas continuas y a trazos indican platino y paladio, respectivamente.

están frente a frente, y se pone la molécula en la superficie, contactando directamente los átomos de platino, la energía es menor. Sin embargo, si también se permite que las configuraciones paralela y perpendicular (con la molécula en medio) adquieran alineamientos zigzag, las energías no mejoran.

Los resultados de transporte, mostrados en la figura (0.4) para el platino, dan una conductancia de 0.9 G_0 en la configuración paralela y de 2.0 G_0 en la perpendicular. En el primer caso, si se proyecta la densidad de estados en la molécula central y en los átomos de contancto se observa que el estado antienlazante hibridiza completamente con los orbitales s y d_{z^2}, mientras que el enlazante queda fuera de las bandas d y aparece como un estado localizado. En la configuración perpendicular, sin embargo, ambos estados hibridizan y aparecen también solapes directos entre los átomos de platino. De aquí se deduce que en la configuración paralela sólamente hay un canal, mientras que en la perpendicular puede haber dos o más.

La razón de que en los histogramas no se vea un pico a 2.0 G_0 se debe a que para distancias pequeñas la configuración perpendicular compite con la zigzag, que produce conductancias que varían entre valores muy grandes y 1.5 G_0. Para distancias grandes, sin embargo, la configuración zigzag rompe y la paralela se convierte en la más estable. Esto se traduce en los histogramas de conducción en un pico claro alrededor de 1.0 G_0.

La discusión anterior también se puede aplicar al caso del paladio. Sin embargo, los valores de la conductancia son bastante menores, como puede verse en la figura (0.4). El origen de esta discrepancia está en el mayor desalineamiento del nivel antienlazante de la molécula y los niveles s-d de los átomos de contacto del paladio. De hecho esto es lo que se observa con un modelo muy sencillo formado por la molécula y electrodos

unidimensionales: la transmisión se redondea y disminuye cuando los valores de la energía de de la molécula y los electrodos empiezan a diferir.

En resumen, las discrepancias entre los distintos cálculos sobre las configuraciones paralela y perpendicular se puede resolver fácilmente teniendo en cuenta otras fases, como la zigzag, que para algunas distancias son más estables. Por otro lado, las diferencias entre el platino y el paladio se explican también fácilmente a partir del desalineamiento de los niveles de la molécula y los átomos de contacto. De esta forma se han conseguido entender los principales ingredientes que influyen en el transporte a través de moléculas de hidrógeno.

Oscilaciones de la conductancia en cadenas zigzag de platino

La existencia de cadenas de oro con un sólo átomo por sección y una conductancia de 1.0 G_0 fue demostrada con el microscopio de efecto túnel y las uniones de rotura mecánica controlable [41, 42]. Desde entonces varios experimentos [104, 63] y predicciones teóricas [64] han probado que cadenas relativamente largas sólo se pueden formar con oro, platino e iridio. En el caso del platino todavía no se conocen con exactitud las propiedades estructurales, aunque se saben las distancias de equilibrio (1.9-2.3 Å), obtenidas a partir de los histogramas de longitud. Por otro lado, los promedios de las curvas de conductancia muestran una pendiente negativa y oscilaciones con el número de átomos en la cadena que han sido atribuidas a un efecto de paridad universal [63, 105, 106].

Para entender y dilucidar las propiedades estructurales de estos sistemas realicé con SIESTA y SMEAGOL varias simulaciones de cadenas de platino infinitas y cadenas de platino entre electrodos fcc crecidos a lo largo de la dirección (001), formados por planos de 3×3 átomos y puntos k en las direcciones transversales. Para ello utilicé una base doble-ζ polarizada y el funcional LDA. Con cadenas infinitas zigzag empleé dos átomos por celda unidad y en el caso de cadenas entre electrodos de volumen determiné las posiciones de equilibrio relajando la parte central, formada por los cuatro átomos del contacto y la cadena, y permitiendo además que todos los átomos de movieran a lo largo de las direcciones perpendiculares.

En el caso de cadenas infinitas la configuración más estable corresponde a cadenas zigzag, como puede verse en la figura (0.5). Sorprendentemente, el número de canales al nivel de Fermi, dados por las bandas s y d, decrece de un valor de 5, para cadenas zigzag muy comprimidas, hasta 2, en la configuración de equilibrio, para volver después a aumentar. En el mínimo zigzag los enlaces forman ángulos de 24.8 ° con el eje del transporte (z) y tienen una distancia de 2.37 Å, correspondiente a 2.15 Å a lo largo de z. Cuando se aumenta la distancia los ángulos decrecen hasta que en el mínimo lineal, $d_z = 2.38$ Å, ambas configuraciones son casi indistinguibles.

En casos más realista de cadenas entre electrodos de volumen muchos canales pierden

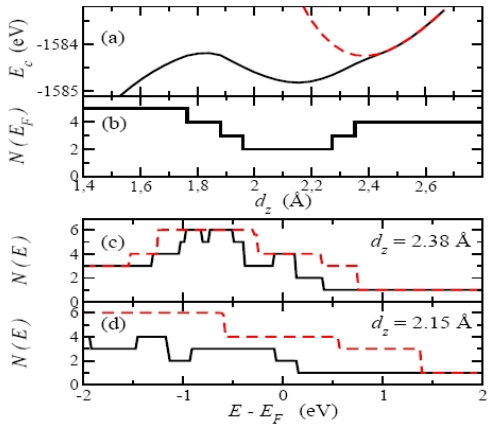

Fig. 0.5: (a) Energía de cohesión E_c y (b) número de canales a la energía de Fermi $N(E_{\mathrm{F}})$ en cadenas infinitas de platino como función de la distancia d_z. Número de canales $N(E)$ como función de la energía E calculados en (c) $d_z = 2.38$ y (d) $d_z = 2.15$ Å. Las líneas sólidas y quebradas corresponden a cadenas zigzag y lineales, respectivamente.

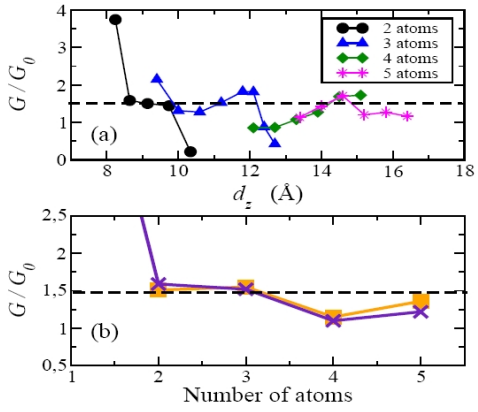

Fig. 0.6: (a) Evolución de la conductancia en cadenas de 2, 3, 4 y 5 átomos (círculos, triángulos, diamantes y estrellas, respectivamente) entre electrodos fcc en función de d_z. (b) Conductancia frente al número de átomos en la cadena, medida en las posiciones de equilibrio (cruces) o promediada en un intervalo de 2 Å alrededor de las posiciones de equilibrio (cuadrados).

conductancia y otros son suprimidos debido a los contactos. Lo primero que llama la atención es que el caso de un sólo átomo es muy distinto de todos los demás, tanto por su separación de la cadena de dos átomos, 2.8 Å, como por el gran valor de la conductancia, 5.9 G_0. De aquí se puede concluir que el primer pico observado en los histogramas de distancias no corresponde a una cadena de un sólo átomo, sino a una cadena de dos átomos. Efectivamente, las demás cadenas, de 2 a 5 átomos, están separadas 1.9-2.1 Å y los valores de la conductancia cerca del equilibrio se mantienen entre 2.0 y 1.0 G_0, oscilando y decreciendo progresivamente, como se ve en la figura (0.6) (a). Por otra parte, el caso de dos átomos muestra un comportamiento distinto dependiendo de si los átomos se sitúan enfrentados o si se relajan también en las direcciones perpendiculares. En este primer caso la conductancia tiene valores alrededor de 2.0 G_0 cerca de la posición de equilibrio, que es lo que se mide cuando los electrodos retornan después de la rotura [105], mientras que en el segundo caso la conductancia se mantiene alrededor de 1.5 G_0. De aquí se deduce que la configuración más probable en situaciones de retorno es lineal.

El comportamiento no monótono de la conductancia con la distancia se puede explicar teniendo en cuenta varios factores. Por un lado está el efecto de estirar la cadena, que, para un número de átomos fijo, hace que la conductancia aumente al pasar de la configuración zigzag a la configuración lineal. Por otro lado también aparece un efecto de paridad [106] que produce pequeñas oscilaciones, como se ve en la figura (0.6) (b). También se observa que las conductancias medidas en las posiciones de equilibrio y promediadas alrededor de dichas posiciones, para simular el promedio experimental, son casi indistinguibles.

La disminución de la conductancia a medida que aumenta el número de átomos puede asociarse con el ángulo que forman los átomos en el medio de la cadena. En cadenas pequeñas los ángulos son menores que los ángulos que aparecen en cadenas más largas (4 y 5 átomos), ya que a medida que aumenta el número de átomos se tiende en el medio de la cadena a la configuración de una cadena infinita, cuyos ángulos son menores.

En conclusión, utilizando cálculos de primeros principios se han podido determinar las características estructurales y electrónicas de cadenas de platino. Además también se han podido comprender diversas propiedades como la variación no monótona de la conductancia y la pendiente negativa y entender mejor los contactos de uno y dos átomos.

Nanohilos eléctricos

Desde que se demostró la posibilidad de llenar nanotubos con distintos compuestos [67] se han producido nanohilos con diversas propiedades eléctricas y de transporte [45, 46, 47, 48, 49, 50, 51, 108]. En uno de estos experimentos se consiguieron encapsular metalocenos dentro de nanotubos de una sola pared [108], un proceso que depende fuertemente del diámetro del nanotubo y que, debido a transferencias de carga, altera dramáticamente las propiedades físicas y químicas del nanotubo y del metaloceno.

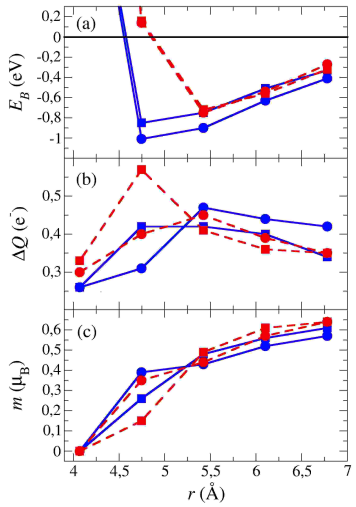

Fig. 0.7: (a) Energía de enlace E_B, (b) carga transferida al nanotubo y (c) momento magnético total, para $CoCp_2@N(n,n)$, donde n varía de 6 a 10. Las líneas sólidas y las quebradas corresponden a las configuraciones paralela y perpendicular, respectivamente. Los círculos representan el caso $N = 3$ y los cuadrados $N = 4$.

Como primer paso para estudiar estos sistemas simulé metalocenos aislados, también conocidos como bis-ciclopentadienil TM ($TMCp_2$), formados por un metal de transición (TM) y dos anillos aromáticos de cinco carbonos y cinco hidrógenos cada uno. Para ello utilicé bases doble-ζ para el hidrógeno y el carbono y una base doble-ζ polarizada para el metal de transición, además del funcional GGA para aproximar el canje y la correlación.

Lo primero que llama la atención es que, debido al campo cristalino creado por los anillos aromáticos y la interacción de canje, los electrones del metal de transición se desaparean y la molécula adquiere un momento magnético neto. Dicho momento crece en unidades enteras de 1 μ_B alrededor del ferroceno, es decir, VCp_2, $CrCp_2$, $MnCp_2$, $FeCp_2$, $CoCp_2$ y $NiCp_2$ tienen momentos magnéticos de 3, 2, 1, 0, 1 y 2 μ_B, respectivamente.

También simulé cadenas de metalocenos a lo largo del eje C_5 de la molécula. Sin embargo, a pesar de que son más estables que la molécula aislada, la diferencia energética es tan pequeña (< 0.02 eV) que en la práctica estas estructuras no se forman.

Las diferentes comportamientos de los metalocenos se pueden aprovechar para diseñar nanohilos con distintas características introduciéndolos dentro de nanotubos. Las propiedades de cobaltocenos dentro de nanotubos conductores (n,n), que fueron los primeros sistemas de este tipo que estudié, se muestran en la figura (0.7). Como puede verse, la configuración en la que el eje C_5 del cobaltoceno es paralelo al eje del nanotubo es casi siempre más estable que la configuración perpendicular. Por otro lado, el caso $N = 3$, donde los cobaltocenos interaccionan entre sí, resulta ser más favorable que el

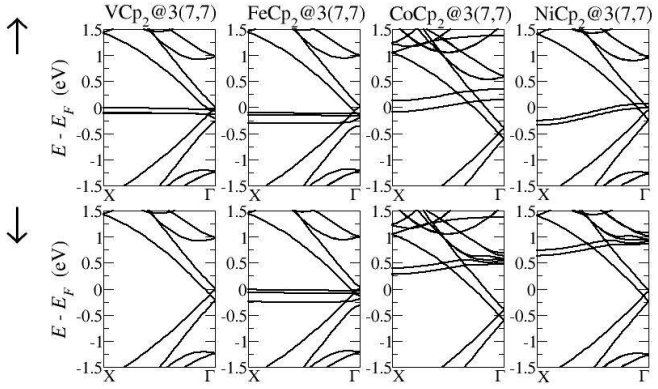

Fig. 0.8: Estructura de bandas de $TMCp_2$@3(7,7) paralelos, donde TM = V, Fe, Co y Ni. Los casos perpendiculares son parecidos pero las bandas son totalmente planas debido a la falta de interacción entre los metalocenos.

$N = 4$, que corresponde a metalocenos aislados, debido a la energía de formación de la cadenas. El sistema más estable es el $CoCp_2$@3(7,7). También se comprueba que hay una transferencia de carga del metaloceno al nanotubo y el momento magnético es menor que el del cobaltoceno aislado, aunque éste aumenta al crecer el radio del nanotubo.

En la figura (0.8) se muestra la estructura de bandas de algunos de estos sistemas. Como puede verse, los nanohilos tienen propiedades de transporte muy distintas dependiendo del tipo de metaloceno. Con el ferroceno los niveles son iguales para los dos espines. En cambio, en el vanadoceno, cobaltoceno y niqueloceno las bandas al nivel de Fermi son distintas para espín hacia arriba o espín hacia abajo, aunque en el caso del vanadoceno son bastante planas. Si a continuación se calcula con SMEAGOL la conductancia de una cadena perfecta de $CoCp_2$@3(7,7) y varios casos en los que se invierte la magnetización de uno, dos o tres cobaltocenos seguidos, se obtienen valores de magnetorresistencia ($\delta G = (G_u - G_d)/G_d$) entre el 22 y el 25%, como puede verse en la figura (0.9).

En vista de los anteriores resultados parece lógico suponer que utilizando nanotubos aislantes se podría aumentar considerablemente la magnetorresistencia, puesto que sólo quedarían las bandas del metaloceno al nivel de Fermi y la polarización de espín sería perfecta. Sin embargo, cuando se simulan tales configuraciones se observa que las bandas del nanotubo bajan al nivel de Fermi, como consecuencia de la transferencia de carga, y el resultado es bastante parecido al caso del nanotubo conductor.

En conclusión, encapsulando metalocenos dentro de nanotuboes de carbono es posible diseñar nanohilos con propiedades de transporte específicas. Los resultados indican que el $CoCp_2$@3(7,7) es estable y puede producir una magnetorresistencia del 25%. Este

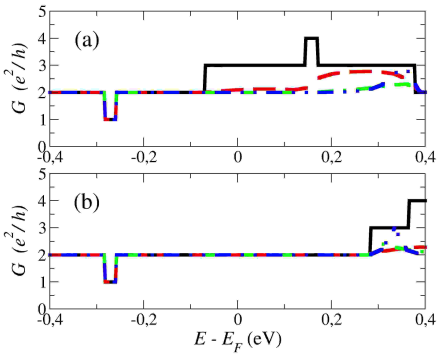

Fig. 0.9: Conductancia de la cadena perfecta de $CoCp_2$@3(7,7) (línea negra sólida) y varias configuraciones en las que se invierte la magnetización de uno (línea roja a trazos), dos (línea verde a trazos y puntos) o tres (línea azul a trazos y dobles puntos) cobaltocenos para electrones con (a) espín hacia arriba y (b) espín hacia abajo.

porcentaje no se puede mejorar utilizando nanotubos aislantes debido a la transferencia de carga.

Magnetismo No Colineal y Espirales de Espín

La mayoría de los sistemas físicos tienen configuraciones magnéticas colineales, en las que los momentos magnéticos son todos paralelos a un eje de cuantización (ferromagnetos) o alternados paralelos/antiparalelos (antiferromagnetos). El Hamiltoniano y la matriz densidad que describen tales sistemas se pueden descomponer por tanto en dos partes, $\uparrow$ y $\downarrow$, con diferentes potenciales de canje y correlación [110]. En otros sistemas en cambio la configuración magnética es no colineal [111, 112, 113, 114] y cada término del Hamiltoniano y la matriz densidad se transforma en una matriz 2×2.

Estructuras de espines espirales

En sistemas periódicos no colineales se puede utilizar el terorema de Bloch generalizado [109] para disminuir el tamaño efectivo del cálculo. El truco consiste en introducir matrices de rotación dependientes de un vector de onda $\vec{q}$, tales que

$$\{\vec{R}|\vec{q}\cdot\vec{R}\}\hat{\Psi}_{\vec{k}}(\vec{r}) = \Psi_{\vec{k}}(\vec{r}+\vec{R})\hat{U}_{z,\vec{q}}(\vec{R})\hat{\chi} = e^{i\vec{k}\cdot\vec{R}}\hat{\Psi}_{\vec{k}}(\vec{r}) \tag{0.17}$$

donde el operador $\{\vec{R}|\vec{q}\cdot\vec{R}\}$ traslada y gira el espinor. De esta manera un sistema periódico

con magnetización que varía también de forma periódica, se puede describir utilizando sólamente una celda unidad. Esto además permite simular configuraciones en las que el cambio en la magnetización no está conmensurado con la red cristalina, algo que de otra manera sería imposible de llevar a cabo.

Dentro de este esquema la función de onda en SIESTA (ecuación (0.4)) adquiere la siguiente forma:

$$\hat{\Psi}_{n\vec{k}\vec{q}}(\vec{r}) = \frac{1}{\sqrt{N_u}} \sum_{\vec{R},\mu} e^{i\vec{k}\cdot\vec{R}_\mu} \hat{U}^{\dagger}_{z,\vec{q}}(\vec{R}_\mu) \hat{c}_{n\vec{k}\mu} \phi_{\vec{R}_\mu}(\vec{r} - \vec{R}_\mu) \tag{0.18}$$

donde la matriz $\hat{U}_{z,\vec{q}}(\vec{r})$ rota un ángulo azimutal el espinor. Para que esta rotación tenga efecto es necesario girar inicialmente el espinor un ángulo polar de 90 grados.

Potencial de canje y correlación

En los sistemas no colineales también hay que tener cuidado al calcular el potencial de canje y correlación puesto que los funcionales actuales sólo están bien definidos para sistemas paramagnéticos o colineales. A pesar de todo se puede emplear un procedimiento relativamente sencillo: rotar en cada punto la matriz densidad hasta tenerla en un sistema de referencia colineal, utilizar los elementos colineales para obtener el potencial de canje y correlación y aplicar por último la rotación inversa a dicho potencial. Esto no genera problemas con la LDA porque el funcional es local y no afecta al vector del momento magnético. Sin embargo, con la GGA se debe de tener más cuidado porque el funcional también depende del gradiente de la densidad y las rotaciónes que diagonalizan estos términos no son en general iguales a la rotación que diagonaliza la densidad. A pesar de todo el problema se puede resolver empleando cualesquiera de estas dos aproximaciones: (i) se rota la densidad y se calcula el gradiente de los elementos colineales para obtener el potencial,

$$\hat{n}(\vec{r}) \rightarrow \hat{n}^d(\vec{r}), \nabla\hat{n}^d(\vec{r}) \rightarrow \hat{V}^{xc\,d}[\hat{n}^d(\vec{r}), \nabla\hat{n}^d(\vec{r})] \tag{0.19}$$

o (ii) se calcula el gradiente no colineal, se rota y se elimininan los términos de fuera de la diagonal [125]:

$$\begin{aligned} \hat{n}(\vec{r}), \nabla\hat{n}(\vec{r}) &\rightarrow \hat{n}^d(\vec{r}), \begin{pmatrix} [\nabla n(\vec{r})]^{\uparrow'} & \vec{\delta} \\ \vec{\delta}' & [\nabla n(\vec{r})]^{\downarrow'} \end{pmatrix} \rightarrow \\ &\rightarrow \hat{n}^d(\vec{r}), \begin{pmatrix} [\nabla n(\vec{r})]^{\uparrow'} & \vec{0} \\ \vec{0} & [\nabla n(\vec{r})]^{\downarrow'} \end{pmatrix} \rightarrow \hat{V}^{xc\,d}[\hat{n}^d(\vec{r}), \nabla\hat{n}^{d'}(\vec{r})] \end{aligned} \tag{0.20}$$

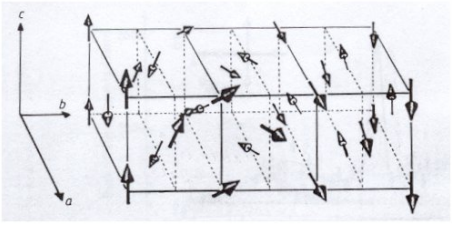

Fig. 0.10: Configuración espiral de la fase γ del hierro.

Aunque estas dos aproximaciones parecen bastante diferentes los resultados obtenidos con ambas son casi indistinguibles, lo que significa que las rotaciones de la densidad y su gradiente son muy similares. Esto sugiere que los cambios intraatómicos en la dirección de la magnetización son muy pequeños [126].

Propiedades magnéticas y estructurales del hierro

La fase más común del hierro es la fase bcc ferromagnética. Sin embargo a gran presión ($\approx$ 13 GPa) hay una transición a una fase hcp (hierro-ϵ) que no tiene ordenamiento magnético y puede ser superconductora. A altas temperaturas también hay otra transición, esta vez hacia una fase fcc (hierro-γ), que también puede ser estabilizada a bajas temperaturas en la forma de aleaciónl [130], capas delgadas [132, 133] o micropartículas en matrices de metales nobles [119, 134].

La fase γ tiene un ordenamiento magnético espiral, como el mostrado en la figura (0.10), caracterizado por un vector $\vec{q}_{\text{exp}} = (2\pi/a)(0.12, 0, 1)$. Dicho ordenamiento ha sido tratado de reproducir por muchos autores utilizando cálculos ab initio [136, 137, 138, 139, 140, 141, 125, 126] pero ninguno lo ha conseguido, a pesar de los muchos métodos y aproximaciones utilizados. Para tratar de resolver este problema o encontrar una solución mejor llevé a cabo una serie de simulaciones de primeros principios de las fases del hierro, haciendo especial énfasis en la fase γ.

Lo primero que hice fue converger los diversos parámetros que entran en los cálculos. Para ello estudié la variación de la energía en función del pseudopotencial, del número de puntos k, del parámetro de corte de la malla en espacio real, de la temperatura, de los radios de los orbitales y del número de orbitales de la base. En general los resultados no dependen mucho del pseudopotencial. En cambio hay que meter bastantes puntos k (4.000) y puntos de la malla real (hasta 50.000, que corresponde a un parámetro de corte de 700 Ry) y una temperatura no superior a 300 Ry para que la energía converja con una precisión de 0.01 eV. También es necesario emplear una base muy bien convergida, formada por orbitales con radios largos minimizados variacionalmente y con al menos triple-ζ y polarización (orbitales p). Si se usan bases más pobres, como la doble-ζ polarizada, se

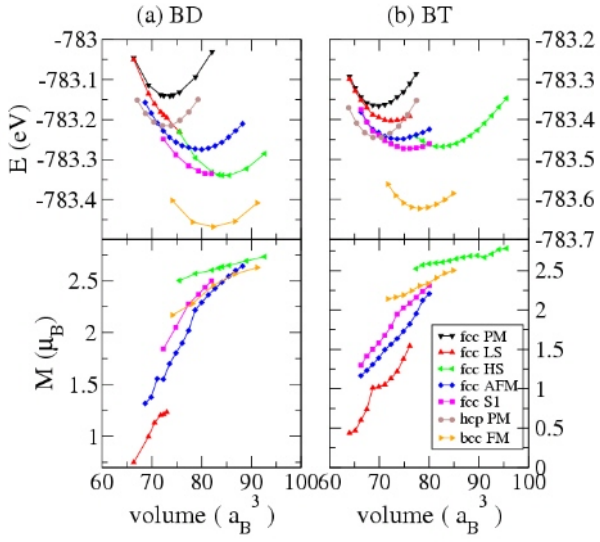

Fig. 0.11: Enería libre y momento magnético como función del volumen atómico ($V_{\mathrm{bcc}} = a^3/2$, $V_{\mathrm{fcc}} = a^3/4$) de las fases del hierro, obtenidos con GGA y bases con doble (a) y triple (b) ζ. PM = paramagnético, LS = espín bajo ferromagnético, HS = espín alto ferromagnético, AF = antiferromagnético, SS = espiral de espín, FM = ferromagnético.

obtiene con la LDA un ordenamiento de las fases incorrecto: la bcc resulta ser más estable que la fcc, lo que está de acuerdo con los experimentos, curiosamente, pero es contrario a lo predicho por otros cálculos [145].

Con LDA y triple-ζ los resultados son sin embargo bastante buenos y casan bastante bien con cálculos de ondas planas que incluyen todos los electrones [145]. Por ejemplo, para la fase bcc se obtiene una constante de red de 2.76 Å, un momento magnético de $2.08\mu_{\mathrm{B}}$ y un módulo de volumen de 2.68 Mbar. La constante de red de la fcc paramagnética también es muy similar al cálculo de ondas planas, 3.38 Å, aunque la diferencia energética con la bcc resulta estar un poco subestimada (55 meV frente a 70-80 meV) [145]. A pesar de todo, es bien conocido que los resultados con la LDA no están de acuerdo con los experimentos, por lo que debe utilizarse la GGA para mejorarlos. Con esta última se obtiene 2.85 Å, $2.31\mu_{\mathrm{B}}$ y 1.83 Mbar para la fase bcc, que comparan también muy bien con resultados teóricos previos [146, 125] y por supuesto con los valores experimentales, 2.87 Å, 2.22 μ_{B} y 1.68 Mbar. Las curvas de cohesión obtenidas con la GGA pueden verse en la figura (0.11), donde también se hace una comparación entre las bases doble y triple ζ.

También se simularon clústeres de hierro con un número de átomos entre 2 y 5 em-

Tab. 0.1: Longitud de enlace a (Å), enería de enlace por átomo E_b (eV/atom) y momento magnético total M (μ_B) para clústeres de hierro de dos a cinco átomos, calculados con una base triple-ζ y la GGA no colineal.

	a (Å)	B (eV/Å)	M (μ_B)
Fe_2	2.02	1.51	6.00
Fe_3 $D_{\infty h}$	2.28	1.72	5.62
Fe_3 C_{3v}	2.27	1.88	10.00
Fe_4 C_{4v}	2.30	2.21	14.00
Fe_4 T_d	1,2↔3,4 2.27	2.31	14.00
	1↔2, 3↔4 2.65		
Fe_5 D_{3h}	1↔2,3 2↔3 2.43	2.58	17.07
	1,2,3↔4,5 2.37		

pleando la aproximación GGA no colineal. Los resultados, mostrados en la tabla (0.1) comparan muy bien con resultados teóricos previos [113, 147, 142, 148, 115] e incluso mejoran el caso del Fe_2 cuando se comparan con los valores experimentales [149].

El último cálculo hecho con el hierro correspondió a las configuraciones espirales. Con la LDA se predicen dos configuraciones estables: para constantes de red cercanas a la experimental el vector de onda que da menor enería es $\vec{q}_1 = (2\pi/a)(0, 0, 6)$, mientras que cuando la constante de red baja de $a \approx 3.50$ Å es más estable la configuración con $\vec{q}_2 = (2\pi/a)(0.2, 0, 1)$, que es similar al experimental. Por tanto, la configuración magnética en el equilibrio es correcta, pero la constante de red es demasiado pequeña. En cambio con la GGA la constante de red en el equilibrio es muy parecida a la experimental, 3.56 Å, pero la configuración más estable resulta ser la correspondiente a $\vec{q}_1$, como se puede ver en la figura (0.12). En este caso se encuentra sin embargo que la curva espiral interpola entre la fase antiferromagnética y la fase ferromagnética de espín alto y tiene un mínimo claro (ver figura (0.11)), mejorando también este aspecto otros resultados teóricos [125].

En resumen, los resultados obtenidos concuerdan bastante bien con simulaciones de otros autores e incluso las mejoran. El mayor problema aparece al intentar reproducir el orden magnético correcto de la fase γ, que con GGA, a pesar de obtener una constante de red de equilibrio muy cercana a la experimental y mejor que otros autores, se desarrolla para volúmenes atómicos bastante más pequeños. Las discrepancias pueden ser debidas a algún fallo inherente a la aproximación GGA en sistemas colineales. Para mejorar los resultados sería por tanto necesario un nuevo funcional que incluyese explícitamente los elementos de la matriz densidad de fuera de la diagonal.

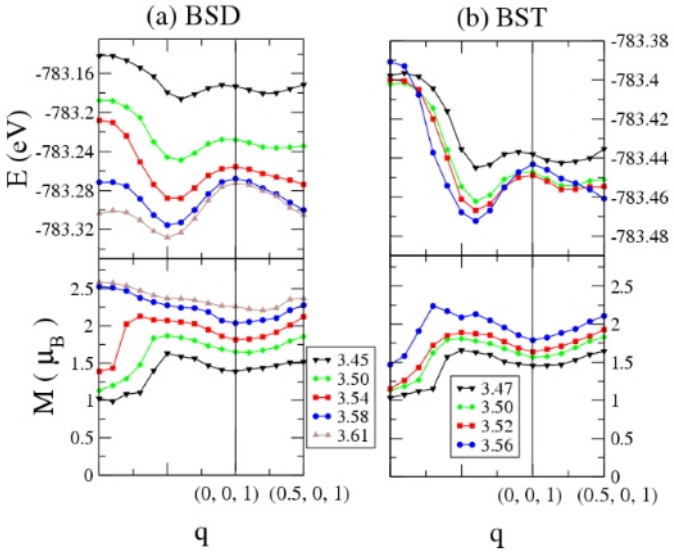

Fig. 0.12: Enería libre (arriba) y momento magnético (abajo) de las fases espirales del hierro obtenidos con GGA y bases con (a) doble y (b) triple ζ, para constantes de red entre 3.45 y 3.61 Å.

Cálculos Ab Initio de Espectros de Ondas de Espín

Las fluctuaciones de espín, que rotan o reorientan localmente los momentos magnéticos, son la base de muchos fenómenos magnéticos. Por ejemplo, pueden explicar la ley de Curie-Weiss y las diferentes temperaturas de Curie [120] y participan en procesos como el transporte eléctrico o de calor, el calor específico y la superconductividad. Información sobre tales fluctuaciones se puede obtener a partir de la susceptibilidad, $\hat{\chi}$, definida como

$$\delta\vec{M}(\vec{r},t) = \int \mathrm{d}\vec{r}' \int_{-\infty}^{t} \mathrm{d}t' \hat{\chi}(\vec{r},\vec{r}';t,t')\vec{H}(\vec{r}',t') \tag{0.21}$$

o, en espacio recíproco,

$$M_\nu(\vec{k},\Omega) = \sum_{\vec{q}} \int \mathrm{d}\omega \hat{\chi}(\vec{k},\vec{q};\Omega,\omega)\vec{H}(\vec{q},\omega) \tag{0.22}$$

donde $\vec{M}$ es la magnetización y $\vec{H}$ es el campo manético. La parte imaginaria de la susceptibilidad es, de acuerdo con el teorema de fluctuación disipación, directamente proporcional a la transformada de Fourier de la función de correlación [151]. Por ello que los cálculos teóricos de la susceptibilidad magnética permiten conocer de forma precisa

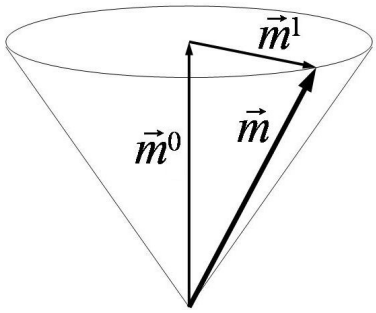

Fig. 0.13: Cambio inducido en el vector de espín (la magnetización tiene el signo contrario) por el campo magnético. Esta perturbació se propaga por la red a lo largo de una dirección determinada para dar lugar a un magnón.

el comportamiento magnético de muchos materiales y se pueden tomar como un primer paso para entender otras propiedades.

Ondas de espín (magnones)

Las ondas de espín, también conocidas como magnones, son respuestas dinámicas cuyo espectro se puede obtener a partir de cálculos ab initio de la susceptibilidad. Para generar este tipo de ondas es necesario aplicar un campo magnético transversal y oscilatorio a un sistema ferromagnético[2] [155, 156, 157, 158]. Dicho campo induce un cambio en la magnetización, $\vec{m} = \vec{m}^0 + \vec{m}^1$, donde $\vec{m}^1$ va en la dirección perpendicular al eje de cuantización (véase la figura (0.13)). Si el cambio inducido es lo suficientemente pequeño se puede aplicar teoría de perturbaciones dependiente del tiempo y obtener, tras un poco de álgebra, la siguiente ecuación integral:

$$\begin{aligned}
\tilde{\chi}_{++}(\vec{G},\vec{q},-\omega) = & \sum_{n,n',\vec{k}} \frac{f^{\uparrow}_{n\vec{k}} - f^{\downarrow}_{n'\vec{k}+\vec{q}}}{\omega + \varepsilon^{\downarrow}_{n'\vec{k}+\vec{q}} - \varepsilon^{\uparrow}_{n\vec{k}} - i\delta} \times \\
& \times \int e^{-i(\vec{G}+\vec{q})\cdot\vec{r}} \sum_{\mu,\vec{R},\nu} e^{i\vec{q}\cdot d_\mu} e^{-i\vec{k}\cdot(\vec{d}_\mu - \vec{R}_\nu)} c^{\downarrow\,*}_{n'\vec{k}+\vec{q}\mu} c^{\uparrow}_{n\vec{k}\nu} \times \\
& \times \phi_\mu(\vec{r} - \vec{d}_\mu)\phi_{\vec{R}_\nu}(\vec{r} - \vec{R}_\nu)\mathrm{d}\vec{r} \times \\
& \times \int \left(-\frac{V^{xc\,\uparrow}(\vec{r}\,') - V^{xc\,\downarrow}(\vec{r}\,')}{m_0(\vec{r}\,')} \sum_{\vec{G}'} \tilde{\chi}_{++}(\vec{G}',\vec{q},-\omega) e^{i(\vec{G}'+\vec{q})\cdot\vec{r}\,'} + e^{i\vec{q}\cdot\vec{r}\,'} \right) \times
\end{aligned}$$

[2] Los magnones también se pueden generar en otras configuraciones magnéticas y con otro tipo de campos, pero sólo consideraré el caso ferromagnético transversal, que es el más común y sencillo de estudiar.

$$\times\ e^{i\vec{q}\cdot\vec{r}\,'} \sum_{\mu',\vec{R}',\nu'} e^{-i\vec{q}\cdot\vec{d}_{\mu'}} e^{i\vec{k}(\vec{d}_{\mu'}-\vec{R}'_{\nu'})} c^{\downarrow}_{n'\vec{k}+\vec{q}\mu'} c^{\uparrow\,*}_{n\vec{k}\nu'} \times$$
$$\times\ \phi_{\mu'}(\vec{r}\,' - \vec{d}_{\mu'})\phi_{\vec{R}'_{\nu'}}(\vec{r}\,' - \vec{R}'_{\nu'})\mathrm{d}\vec{r}\,' \tag{0.23}$$

donde f son los factores de Fermi, ε los autovalores del Hamiltoniano y $\vec{G}$ son los vectores de red del espacio recíproco. Juntando los términos, la ecuación final se puede escribir como sigue:

$$\tilde{\chi}_{++}(\vec{G},\vec{q},-\omega) = \tilde{\chi}^0_{++}(\vec{G},\vec{q},-\omega) + \sum_{\vec{G}} \Pi(\vec{G},\vec{G}',\vec{q},-\omega)\tilde{\chi}_{++}(\vec{G}',\vec{q},-\omega) \tag{0.24}$$

cuya solución es

$$\tilde{\chi}_{++}(\vec{G},\vec{q},-\omega) = \sum_{\vec{G}'} \left[\hat{I} - \Pi\right]^{-1} (\vec{G},\vec{G}',\vec{q},-\omega)\tilde{\chi}^0_{++}(\vec{G}',\vec{q},-\omega) \tag{0.25}$$

Aunque finalmente se obtiene el resultado para cualquier vector de onda $\vec{G}$, sólo se necesita el término $\vec{G} = \vec{0}$, que da la susceptibilidad integrada en la celda unidad.

A partir de las anteriores ecuaciones también se puede tomar el límite en el que $n^{0\uparrow} - n^{0\downarrow}$ tiende a cero, utilizando la regla de L'Hopital, y obtener una expresión para sistemas paramagnéticos. Utilizando el funcional LDA,

$$\lim_{m\to 0} \frac{V^{xc\uparrow}[n,m] - V^{xc\downarrow}[n,m]}{m} = \frac{\delta\left(V^{xc\uparrow}[n,m] - V^{xc\downarrow}[n,m]\right)}{\delta m} =$$
$$= \frac{1}{2}\sum_{\sigma=\uparrow,\downarrow} \mathrm{sgn}(\sigma)\left(\frac{\delta V^{xc\uparrow}[n^\uparrow,n^\downarrow]}{\delta n^\sigma} - \frac{\delta V^{xc\downarrow}[n^\uparrow,n^\downarrow]}{\delta n^\sigma}\right) \tag{0.26}$$

donde $\mathrm{sgn}(\uparrow) = 1$ y $\mathrm{sgn}(\downarrow) = -1$. Con la GGA la derivación es un poco más complicada porque hay que tener en cuenta los gradientes:

$$\lim_{m\to 0} \frac{V^{xc\uparrow}[n,m,\nabla n,\nabla m] - V^{xc\downarrow}[n,m,\nabla n,\nabla m]}{m} =$$
$$= \frac{1}{2}\sum_{\sigma=\uparrow,\downarrow} \mathrm{sgn}(\sigma)\left\{\frac{\delta V^{xc\uparrow}[n^\uparrow,n^\downarrow,\nabla n^\uparrow,\nabla n^\downarrow]}{\delta n^\sigma} - \frac{\delta V^{xc\downarrow}[n^\uparrow,n^\downarrow,\nabla n^\uparrow,\nabla n^\downarrow]}{\delta n^\sigma} + \right.$$
$$\left. + \sum_{i=1}^{3}\left(\frac{\delta V^{xc\uparrow}[n^\uparrow,n^\downarrow,\nabla n^\uparrow,\nabla n^\downarrow]}{\delta(\nabla n^\sigma)_i} - \frac{\delta V^{xc\downarrow}[n^\uparrow,n^\downarrow,\nabla n^\uparrow,\nabla n^\downarrow]}{\delta(\nabla n^\sigma)_i}\right)\frac{\delta(\nabla n^\sigma)_i}{\delta n^\sigma}\right\} \tag{0.27}$$

La susceptibilidad paramagnética calculada a frecuencia cero da información sobre las estructuras espirales que puede tener el sistema. Esto procura un método alternativo al teorema de Bloch generalizado [109], explicado en el capítulo anterior.

Aproximaciones

Los principales problemas del código de magnones vienen del hecho de que, debido a la presencia de muchos ciclos numéricos, el tiempo y la memoria de cómputo aumentan espectacularmente con el tamaño del cálculo. Para simplificar las simulaciones es necesario por tanto introducir diversas aproximaciones.

Como primera aproximación utilicé un método análogo a la teoría de perturbaciones, donde supuse que en cada fila (o columna) de la matriz $\Pi(\vec{G},\vec{G'})$ los términos más importantes eran $\Pi(\vec{G},\vec{0})$ (el que tiene una fase nula) y $\Pi(\vec{G},\vec{G})$. Aunque esta aproximación es muy eficiente desde el punto numérico los resultados que se obtienen son bastante imprecisos y no verifican el teorema de Goldstone.

Otra simplificación se basó en el aproximante de Padé [168], que consiste en calcular las funciones en el eje imaginario de energías y hacer una continuación analítica hacia el eje real utilizando el método recíproco de Thiele [168]. De esta forma se puede reducir el número efectivo de puntos de energía que entran en el cálculo.

Finalmente, como en las matrices y en los ciclos numéricos hay muchos elementos despreciables es conveniente identificarlos y eliminarlos, definiendo nuevas matrices más pequeñas. En primer lugar, sólamente las bandas cuya diferencia está dentro de la ventana de ω que se va a calcular y cuya diferencia en los pesos no es muy pequeña, dan una contribución importante. Por tanto sólo es necesario usar determinadas combinaciones de bandas alrededor del nivel de Fermi. Por otro lado, también hay elementos de las matrices Hamiltonianas y de solapes (que en este caso están también multiplicados por una fase dependiente de los vectores $\vec{G}$) que son bastante pequeños y que si se eliminan no estropean el resultado. Lo mismo se puede aplicar a los elementos de la matriz $\hat{\Pi}$, que disminuyen a medida que los módulos $|\vec{G}|$ o $|\vec{G'}|$ aumentan.

Utilizando las aproximaciones anteriores e introduciendo cortes numéricos de forma inteligente es posible reducir considerablemente el tiempo y la memoria de ejecución sin dañar la precisión del cálculo.

Espectros de ondas de espín del hierro y el níquel

Para estudiar el funcionamiento del código utilicé la fase bcc del hierro y la fase fcc del níquel. En el primer caso la relación de dispersión es parabólica a lo largo de la dirección

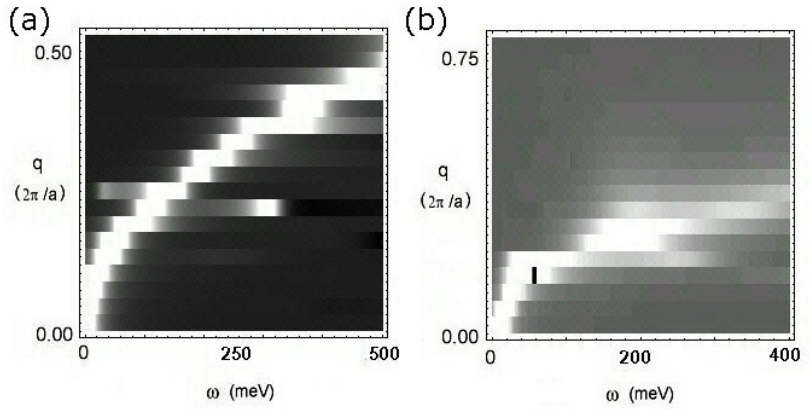

Fig. 0.14: (a) Relación de dispersión del hierro bcc ferromagnético obtenida con una base doble-ζ y la LDA a la constante de red teórica (2.78 Å). (b) Relación de dispersión del níquel fcc ferromagnético obtenida con una base doble-ζ y la LDA a la constante de red teórica (3.40 Å). En ambos casos se emplearon 39304 puntos k, 1331 puntos G, 25 puntos de Padé y cortes numéricos del orden de 10^{-5}. La escala va desde el negro ($\chi = 0$) hasta el blanco (valores de χ) más altos.

(001) del vector $\vec{q}$ (en unidades de $2\pi/a$) [155, 157, 169, 170, 152, 171, 153, 154, 172]. En el níquel la relación de dispersión también empieza siendo parabólica [156, 159, 170] pero se desdobla después en una rama acústica y otra óptica, que no son bien descritas por la LDA debido a la sobreestimación del desdoble de canje en las bandas [173, 169, 174, 175, 152, 154, 172].

El primer paso consistió en optimizar el código utilizando las aproximaciones y cortes del apartado anterior. Para ello empleé el teorema de Goldstone, que dice que en $\vec{q} = \vec{0}$ y $\omega = 0$ debe existir un magnón, es decir, la parte imaginaria de la susceptibilidad debe tener un polo en el origen. Por tanto elegí el número mínimo de vectores $\vec{G}$ y puntos de Padé y los cortes en los distintos ciclos numéricos lo más grandes posible que reprodujesen dicho pico. El número de puntos k no afecta mucho en este caso pero es muy importante para $\vec{q} \neq \vec{0}$: si hay pocos puntos k las curvas aparecen cortadas y con mucho ruido.

Los resultados finales, obtenidos con LDA y bases doble-ζ, a las constantes de red teóricas (2.78 Å para el hierro y 3.40 Å para el níquel) se muestran en las figura (0.14). Comparando el hierro con los resultados teóricos y experimentales se observa que la curva se va hacia frecuencias bastante mayores, lo cual puede deberse al hecho de que la base de orbitales empleada era muy pobre (para simular correctamente este elemento se necesita al menos triple-ζ polarizada, como se vio en el anterior apartado). El níquel no verifica los experimentos pero casa mejor con los resultados teóricos (aunque es difícil hacer una comparación exacta debido a que se emplearon pocos puntos en la simulación para ahorrar tiempo y memoria). En resumidas cuentas, a pesar de algunos problemas de precisión se

puede decir que el código funciona, lo cual abre la puerta a nuevos cálculos de magnones y configuraciones magnéticas en diversos materiales.

Modificación de Estados de Superficie Aplicando Tensión

Cada superficie tiene propiedades físicas y químicas específicas que dependen del tipo de material y de la dirección de crecimiento. Entre dichas propiedades, la reactividad y el comportamiento catalítico juegan un papel fundamental y grandes esfuerzos se han realizado para caracterizarlas, entenderlas y modificarlas a voluntad [177]. Sin embargo, sólo en tiempos relativamente recientes, gracias al desarrollo de nuevas técnicas experimentales y métodos teóricos, ha sido posible alcanzar el ansiado objetivo de fabricar superficies con las características deseadas. Este avance tendrá profundas consecuencias en los procesos relacionados con la adsorción y modificación de moléculas y en general en todo lo que tenga que ver con los procesos catalíticos y reactivos.

Estados de superficie y reactividad

Los estados electrónicos de una superficie se pueden clasificar en dos tipos: *resonancias de superficie*, que son estados de volumen con mucho peso en la superficie y que por tanto decaen suavemente hacia el interior de sólido, y *estados de superficie* propiamente dichos, que están confinados en la superficie y decaen exponencialmente tanto hacia el vacío como hacia el interior del sólido. Los primeros tienen energías que aparecen en zonas donde hay bandas de volumen mientras que los segundos se encuentran en las zonas prohibidas.

Para caracterizar los estados de superficie se puede utilizar espectroscopía inversa de fotoemisión resuelta en momentos [186, 184], que consiste en bombardear la muestra con electrones que forman un ángulo θ con la superficie y medir la intensidad de fotones emitida. La técnica más popular sin embargo es el microscopio de efecto túnel [190] que permite determinar la densidad de estados directamente sobre la superficie a través de la conductancia diferencial [192]. Con ambas técnicas es posible caracterizar de forma muy precisa los estados de superficie y estudiar cómo varían en función de diversos cambios electrónicos y estructurales, como por ejemplo modificaciones en la función de trabajo [196, 197], cambios en la anchura de las terrazas [198] y aplicación de tensión [199, 196].

Los estados de superficie también pueden tener gran influencia en la reactividad, puesto que un estado poblado aumenta la respulsión electrónica entre la superficie y las moléculas que llegan, mientras que si el estado está vacío la repulsión es mucho menor y las moléculas pueden ser adsorbidas con más facilidad. Los procesos de fisisorción y quimisorción se pueden explicar fácilmente observando la curva de la figura (0.15). Primero la molécula es atraía por un potencial dipolar y llevada al mínimo de fisisorción. Si se la acerca más empieza a sentir la repulsión electrónica de los estados sp, hasta que los electrones

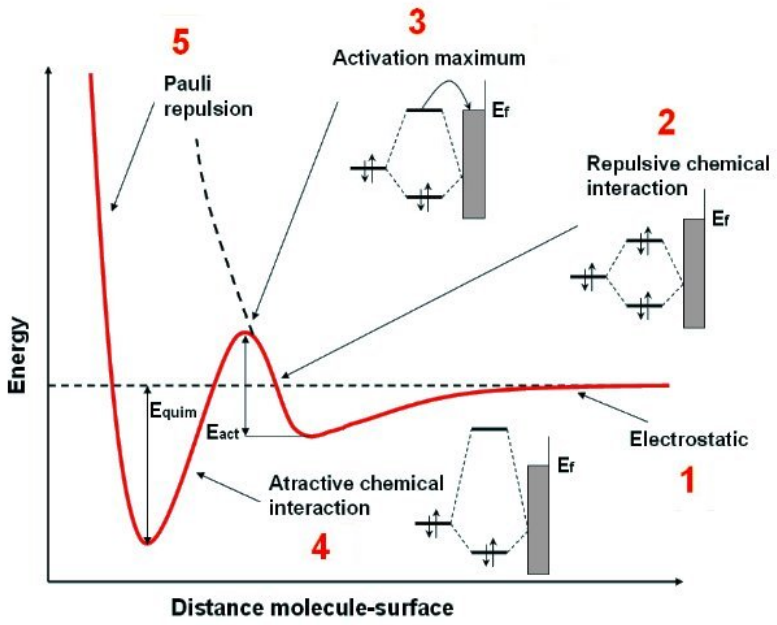

Fig. 0.15: Curva de energía que describe el proceso de adsorción de un átomo o molécula simple que se aproxima a la superficie. Lo primero que ve la molécula es el potencial electrostático atractivo (1) que la lleva al mínimo de fisisorción. Si la distancia se reduce más, la interacción con los orbitales sp se convierte en repulsiva (2) hasta que el estado atienlazante cruza el nivel de Fermi y sus electrones pasan a la superficie (3). El proceso se convierte de nuevo en energéticamente favorable (4) hasta que, debido a la repulsión de Pauli, la molécula es repelida de la superficie (5), quedándose finalmente en el mínimo de quimisorción.

de los orbitales antienlazantes pasan a la superficie y el proceso se convierte de nuevo en favorable. Este proceso define la barrera de fisisorción, que tiene gran influencia en la reactividad. Finalmente, la molécula se queda en el mínimo de quimisorción, ya que la repulsión de Pauli evita que se acerque más. La barrera de fisisorción es producida por tanto por los estados sp, que conforman los estados de superficie, mientras que los orbitales d intervienen en el mínimo de quimisorción.

Los estados d y sp se pueden modificar estirando o comprimiendo la superficie. Por ejemplo, creciendo un material encima de otro que tenga una constante de red distinta [206, 196, 207, 208]. La expansión aumenta la reactividad, algo que tradicionalmente ha sido atribuído al cambio en los estados d [209]. Sin embargo, la importancia de los estados sp ha sido subestimada hasta el momento.

El sistema Cu/Ru(0001)

El interés en este sistema viene motivado por el hecho de que la superficie Ru(0001) funciona como catalizador para convertir hidrocarbonos. Esta propiedad puede ser considerablemente aumentada (alrededor de un 40%) añadiendo una capa de cobre sobre la superficie [210], lo cual tiene profundas consecuencias en las reacciones químicas en las que intervienen estas moléculas.

La estructura de estas capas ha sido extensivamente estudiada utilizando difracción de electrones y rayos X [211, 212, 207, 208]. Se sabe que la primera capa de cobre crece de forma pseudomórfica sobre el substrato [206], mientras que las demás tienden hacia la la configuración normal del Cu(111) relajándose según unas direcciones determinadas (a lo largo de los vectores de red de la superficie para la segunda capa, mientras que para las siguientes la estructura va haciéndose más complicada).

El experimento en el que se basaron los cálculos fue llevado a cabo por el grupo de Rodolfo Miranda. En él se estudió la densidad de estados sobre las superficies Cu(111), Ru(0001) y Cu/Ru(0001) mediante el microscopio de efecto túnel. Un ejemplo de imagen tomada con este microscopio se muestra en la figura (0.16). De acuerdo con el experimento el estado de superficie del rutenio se encuentra vacío (por encima del nivel de Fermi) mientras que el del cobre aparece lleno. Sin embargo, cuando se añade una capa de cobre al rutenio dicho estado se va hacia arriba y se despuebla. Finalmente, cuando se ponen más capas cambia de tendencia y se mueve hacia abajo. Este movimiento del estado de superficie está correlacionado con la reactividad, ya que a absorción de moléculas, que es máxima con una sóla capa de cobre, disminuye al aumentar el espesor.

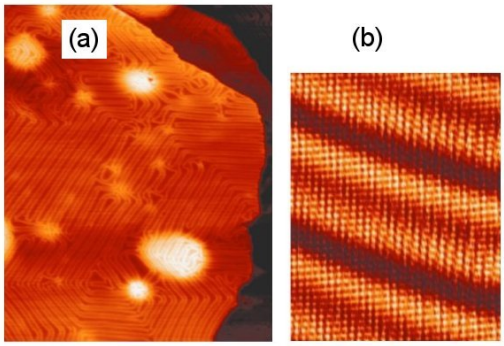

Fig. 0.16: (a) Imagen 160 nm × 127 nm tomada con el microscopio de efecto túnel en 2 monocapas de Cu crecidas sobre Ru(0001). Las partes brillantes corresponden a burbujas de argón que hay bajo la superficie. (b) Imagen de 10 nm × 8 nm de 2 monocapas de Cu sobre Ru(0001) que muestra los detalles de la reconstrucción.

Estudio ab initio del sistema Cu/Ru(0001)

Para estudiar la física relacionada con los estados de superficie y entender la contribución de la tensión, proximidad al substrato y otros factores, llevé a cabo una serie de simulaciones con SIESTA de superficies Cu(111), Ru(0001) y Cu/Ru(0001) de una a cuatro monocapas. Para ello se elegí el funcional LDA, que da buenos resultados en sistemas no magnéticos, y bases doble-ζ polarizadas para el rutenio y el cobre. En este último fue necesario además incluir triple-ζ en los orbitales d para reproducir de forma precisa los comportamientos observados experimentalmente. Por otro lado, los radios de corte los elegí de forma que optimizasen los parámetros estrucutrales, que son muy importantes en estas simulaciones.

Primero hay que determinar el número mínimo de capas que debe tener el bloque 'bidimensional' que simula la superficie. Para ello comparé la densidad de estados de los átomos en el centro del bloque con la densidad de estados del sistema de volumen, las cuales no deberían diferir mucho cuando el número de capas es suficientemente grande. El resultado fue que al menos 15 capas de cobre y 13 de rutenio son necesarias para que tanto los estados en el centro del bloque como los de la superficie estén bien convergidos. Esto es manifiestamente mejor que otros cálculos teóricos en los que el número de capas era bastante más pequeño [202, 203, 213]. Por otro lado, es necesario mencionar que el sistema no lo relajé en la dirección z porque las distancias experimentales en los átomos cercanos a la superficie son bastante similares a las distancias de volumen [207, 208].

El estado de superficie lo determiné observando dónde tiene picos la densidad de estados de carácter sp proyectada en los átomos de la superficie. Como la mayor contribución a la corriente túnel viene dada por los electrones con el momento lo más perpendicular posible a la superficie, integré la densidad de estados sólamente en el centro de la zona de

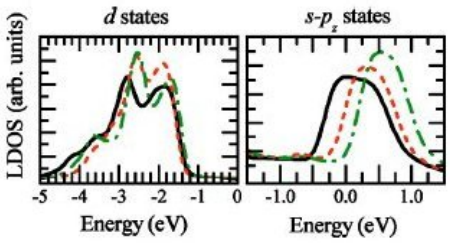

Fig. 0.17: Densidad de estados de los átomos superficiales proyectada en los estados d (izquierda) o s + p_z (derecha). La línea continua corresponde a las distancias de volumen del cobre (a_{xy} = 2.55 Å y a_z = 2.08 Å), la línea quebrada a una red uniformemente expandida hasta las distancias del rutenio de volumen (a_{xy} = 2.70 Å y a_z = 2.20 Å) y la línea de puntos y trazos a la red expandida con la última capa contraída a 1.94 Å.

Brillouin (1/4 del total). Por otra parte, discriminando en orbitales se ve que la mayor contribución viene de los estados s y p_z, que son los que más salen hacia afuera.

El estado de superficie puede ser afectado por varios factores, como la tensión, la proximidad al substrato o la dirección de crecimiento. Para separar algunas de estas contribuciones consideré primero superficies de cobre fcc (111) o cobre hcp (0001) bajo diferentes tensiones. En el primer caso, calculado a las distancias de volumen a_{xy} = 2.55 Å y a_z = 2.08 Å, se observa el típico estado del cobre que empieza un poco por debajo de la energía de Fermi. Cuando el sistema se expande hasta las distancias del rutenio de volumen a_{xy} = 2.55 Å y a_z = 2.08 Å el estado se mueve hacia arriba, al igual que el centroide (centro de masas) de la banda d. Lo mismo ocurre al comprimir la última capa (a 1.94 Å), aunque en este caso el centroide sigue la tendencia opuesta. Este comportamiento se puede observar en la figura (0.17). Los resultados obtenidos para el Cu hcp (0001) son muy similares.

Cuando se añade una monocapa de cobre sobre Ru(0001) el pico del cobre se mueve 250 meV hacia el nivel de Fermi, apareciendo incluso más arriba que el pico del rutenio puro, y se despuebla. Esto concuerda bien con experimentos que muestran que tanto los estados $2p_{3/2}$ [216] como los d [215] se mueven 0.3 eV hacia arriba. Sin embargo los cálculos indican que el centroide de las bandas d (que en este caso muestran un único pico) sólamente se mueve 110 meV, lo cual viene a sugerir que esta cantidad no es un buen parámetro para caracterizar las propiedades superficiales. Al añadir más capas es necesario comprimir las distancias laterales. Para simplificar no tuve en cuenta las reconstrucciones, que requerirían simulaciones hercúleas, y las sustituí por la red fcc habitual a la constante de red experimental. Como puede verse en la figura (0.18) tanto las bandas d (y su centroide) como los estados s + p_z se mueven hacia abajo con el número de capas. Sin embargo, si se hace lo mismo manteniendo las distancias de la primera capa

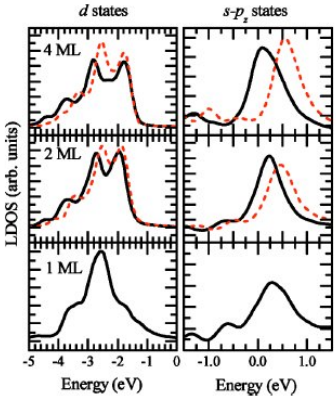

Fig. 0.18: Evolución de la densidad de estados superficial proyectada en los estados d (izquierda) y en los estados s + p_z (derecha) en función del número de capas. La línea continua indica los resultados calculados a las distancias laterales experimentales (2.70, 2.61 y 2.55 Å para 1, 2 y 4 monocapas, respectivamente) mientras que la línea quebrada muestra los mismos casos sin comprimir (2.70 Å).

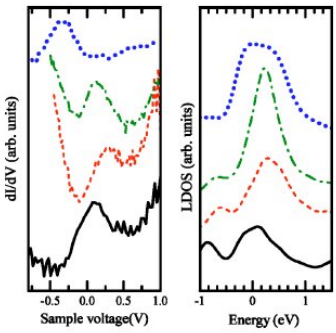

Fig. 0.19: La parte izquierda muestra resultados de conductancia frente al voltaje aplicado para Ru(0001) puro (línea continua) y, de abajo hacia arriba, la misma superficie cubierta con 1, y 2 monocapas de cobre y Cu(111) puro. La parte izquierda muestra los cálculos ab initio correspondientes.

la tendencia resulta ser la opuesta. Esto indica que la influencia del substrato produce un efecto contrario al generado por la expansión. No obstante, el efecto total baja la energía del estado.

Finalmente, la comparación de los resultados teóricos con los expermientales puede observarse en la figura (0.19). El acuerdo entre ambos casos es excelente y demuestra la viabilidad de los cálculos ab initio para simular estados de superficie. Estos resultados pueden también relacionarse con la reactividad puesto que en los mismos experimentos se comprobó que esta propiedad aumenta considerablemente con una monocapa de cobre sobre rutenio y disminuye a medida que se añaden más capas.

Preface

This thesis is a theoretical work on the solid state using computational physics. The basic tool underlying most of the calculations is Density Functional Theory, which describes the system in terms of the electronic density and maps the interacting system onto an equivalent non-interacting set of particles in an effective potential. These simplifications allow us to perform accurate and fast simulations of the ground state physical properties of crystalline solids and isolated systems with a relatively large number of atoms. Such simulations are known as ab initio or first principles simulations because no free parameters enter into them, everything is derived from the postulates of quantum mechanics. However, in practice some parts of the simulation have to be approximated and other parts have to be simplified in order to speed it up and make it computable. This is one of the reasons computational physics is not simply reduced to 'enter some parameters in the computer and wait for the result' since prior to the main study one has to carefully determine the most efficient set of 'simplifications'. Additionally, one has to understand very well the different concepts underlying the basic theory and approximations and know a series of numerical algorithms and computer programs to be able to modify and improve the numerical code. Furthermore, the results have to be carefully analyzed and interpreted and, most importantly, they have to be compared with the experiments and one has to explain why they do or do not match. As I will show, these conditions were completely followed in all the calculations.

The first chapter, an introduction to the ab initio simulations, explains the main theoretical tools used by the physical and chemical communities to approximate the Schrödinger equation, namely Density Functional Theory and Configuration Interaction, and shows their advantages and disadvantages. The main focus is on density functional theory, its basic theorems and approximations. The final part of the chapter introduces a very efficient implementation of this theory, the SIESTA code.

The second chapter presents the basic formalism to calculate quantum transport properties of systems with small numbers of atoms and describes its implementation in the SMEAGOL code, which is used to study the electronic and transport characteristics of three different systems: (a) H_2 molecules sandwiched between platinum or palladium electrodes, (b) monoatomic platinum chains, and (c) metallocenes inside carbon nanotubes.

The third chapter shows how the generalized Bloch's theorem and the non-collinear Generalized Gradient Approximation can be included in SIESTA. These approaches are used to fully characterize the structural and magnetic properties of iron. The final part of the chapter focuses on the γ phase and discusses how the theoretical results and the experiments compare.

The fourth chapter is devoted to magnetic waves, also known as magnons. It introduces the basic theories and approximations employed to calculate the magnetic susceptibility and shows how the code can be optimized to reduce the computer execution time and memory. At the end of the chapter the magnon dispersion relation in iron and nickel is calculated.

Finally, the fifth chapter studies how the surface states of copper evolve as a function of the applied strain when layers of this material are deposited on top of ruthenium. The results are successfully compared with the experiments and linked to the changes in the surface reactivity.

1

Introduction: First Principles Calculations

Since the discovery of the Schrödinger equation great effort and resources have been devoted to solve or approximate it. It was evident from the beginning that only very small systems, such as single atoms or diatomic molecules, admitted exact or very precise solutions. To deal with larger numbers of particles many theoretical schemes use the Hartree-Fock approximation, which expresses the wave function as a single Slater determinant, constructed with single-electron states that are varied to minimize the energy. However, this method has the serious drawback that the electronic correlations are discarded. More sophisticated approaches can be developed including additional Slater determinants built with excited states, as a first step to cover the full Hilbert space of the many-electron wave functions. However, this approximation, which is the basis of the configuration interaction method (CI), has the disadvantage that the computer execution time and memory grow dramatically with the number of functions and, consequently, only simulations of simple systems can be performed.

The term which forbids to express the wave function as a product of single-electron orbitals is the two-body electron-electron interaction. Condensed matter physics would be then much simpler to study if this term did not exist. From this idea, and taking as a base the Hohenber-Kohn theorems [1], Kohn and Sham [2] proposed an alternative approach to the multi-configuration method, based on mapping the original interacting many-body system onto a one-electron system in an effective potential, with the condition that the electronic densities of both systems have to be the same. This was the foundation of density functional theory (DFT).

DFT is more powerful than other methods in the sense that it allows to simulate

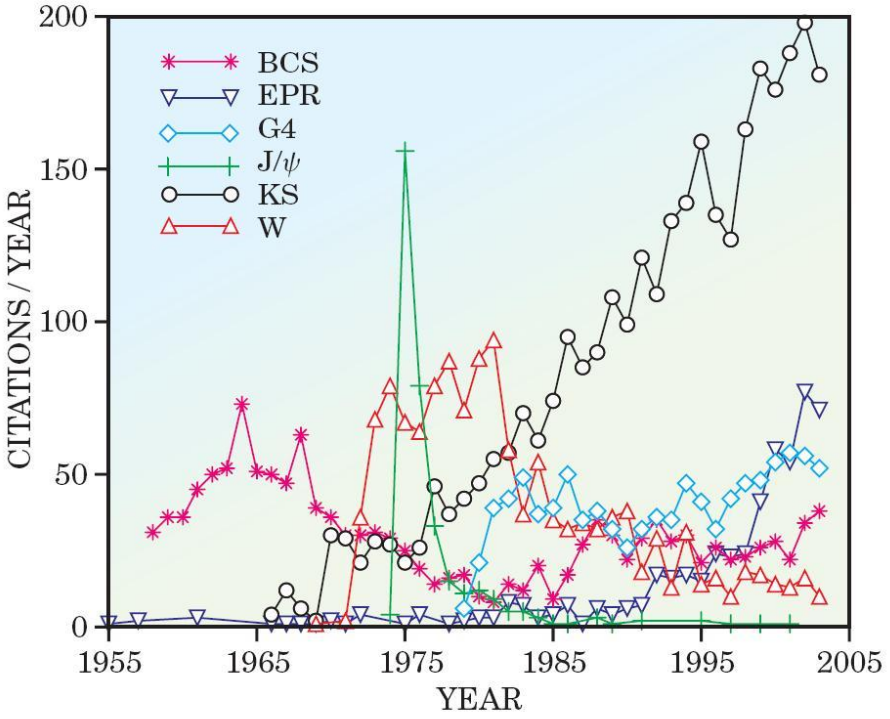

Fig. 1.1: Six classic, highly cited papers. BCS = J. Bardeen, L. Cooper, and R. Schrieffer (*Theory of Superconductivity*, Physical Review **108**, 1175 (1957)), EPR = A. Einstein, B. Podolsky, and N. Rosen (*Can Quantum-Mechanical Description of Physical Reality Be Considered Complete?*, Physical Review **47**, 777 (1935)), G4 = 'gang of four' = E. Abrahams, P. W. Anderson, D. Licciardello, and T. V. Ramakrishnan (*Scaling Theory of Localization: Absence of Quantum Difussion in Two Dimensions*, Physical Review Letters **42**, 673 (1979)), J/ψ = J. J. Aubert *et al.* (*Experimental Observation of a Heavy Particle J*, Physical Review Letters **33**, 1404 (1974)), KS = W. Kohn and L. J. Sham (*Self Consistent Equations Including Exchange and Correlation Effects*, Physical Review **140**, A1133 (1965)), W = S. Weinberg (*A Model of Leptons*, Physical Review Letters **19**, 1264 (1967)) . Figure from [3].

larger numbers of atoms with lower execution and memory resources, but it has the important drawback that the exchange and correlation potentials have to be approximated and, contrary to CI, there is no possible way of systematically improve the calculations. However, in many cases this theory works rather well and can predict the ground state properties with a reasonable degree of accuracy. This is the reason why most of the current ab initio codes are based on DFT and this theoretical scheme is more popular every day [3]. Indeed, the seminal paper of Kohn and Sham [2] is the only 'classical' paper whose number of cites grows every year, as can be seen in figure (1.1). In is possible to conclude then that computational methods based on approximations like DFT will become increasingly important and will shape the future of physics.

1.1 The problem of the Electronic Structure of Matter

Ordinary matter is made of nuclei, which in a solid or molecule vibrate around fixed positions, and electrons, which orbit each nucleus or travel through the material. Both kinds of particles are described by means of quantum mechanics, i. e. in terms of operators acting on a wave function whose square gives the probability distribution. In case of non-relativistic and stationary systems, the probability distribution is calculated using the time-independent Schrödinger equation:

$$\hat{\mathcal{H}}\Psi(\vec{R}_1,...,\vec{R}_{N_N},\vec{r}_1,...,\vec{r}_{N_e}) = E\Psi(\vec{R}_1,...,\vec{R}_{N_N},\vec{r}_1,...,\vec{r}_{N_e}) \tag{1.1}$$

where Ψ is the wave function, $\hat{\mathcal{H}}$ is the Hamiltonian, N_N (N_e) is the number of nuclei (electrons) and $\{\vec{R}_i\}_{i=1,...,N_N}$ ($\{r_i\}_{i=1,...,N_e}$) are the nuclear (electronic) coordinates. For the sake of simplicity I have supposed that the system is not spin polarized so that the wave function does not depend on the spin degrees of freedom. Generalizations to spin polarized and non-collinear spin configurations will be made later. The Hamiltonian has the following form:

$$\begin{aligned}\hat{\mathcal{H}} = &-\sum_A \frac{\nabla_A^2}{2M_A} - \sum_i \frac{\nabla_i^2}{2} - \sum_{A,i} \frac{Z_A}{R_{Ai}} + \sum_{A>B} \frac{Z_A Z_B}{R_{AB}} + \sum_{i>j} \frac{1}{r_{ij}} + \sum_A V^{\text{ext}}(\vec{R}_A) + \\ &+ \sum_i V^{\text{ext}}(\vec{r}_i) = \hat{T}^N + \hat{T}^e + V^{Ne}(\{\vec{R}\},\{\vec{r}\}) + V^{NN}(\{\vec{R}\}) + V^{ee}(\{\vec{r}\}) + \\ &+ V^{\text{ext}}(\{\vec{R}\},\{\vec{r}\})\end{aligned} \tag{1.2}$$

where i,j,r and A,B,R represent electrons and nuclei, respectively, $R_{Ai} = \left|\vec{R}_A - \vec{r}_i\right|$, $R_{AB} = \left|\vec{R}_A - \vec{R}_B\right|$, $r_{ij} = |\vec{r}_i - \vec{r}_j|$, and atomic units are used ($\hbar = 1$, $m_e = 1$, $e = 1$,

$4\pi\epsilon_0 = 1$). The first two terms are the kinetic energy of nuclei and electrons, next three terms give the electrostatic repulsion or attraction between these particles and the last terms are the external potentials, which act on each particle individually.

In principle the problem of the physical structure of matter can be solved by finding the solutions of the Schrödinger equation. Once the eigenfunctions and eigenvalues have been determined, most of the physical properties (crystallographic structure, specific heat, transport characteristics, etc.), are be easily calculated. However, the solution of this equation is almost impossible when the number of particles is relatively large. The difficulties are mainly due to two important problems related with the wave function [4]:

- The number of parameters needed to approximate the wave function grows exponentially with the number of particles: $P = p^{3N}$, where N is the number of particles and p is the number of parameters along each direction.
- The number of grid points necessary to store the wave functions also grows exponentially: $G = g^{3N}$, where g is the number of points along each direction.

These problems start being important when the number of particles is approximately larger than 6, which corresponds for example to a light atom or a simple molecule. It is then necessary to look for alternative ways and approximations to solve this equation.

1.1.1 The Born-Oppenheimer approximation

Since nuclei are much more massive than electrons they can be considered to be fixed, i. e. electrons immediately adjust to the change in atomic positions and remain in the ground state for every nuclear configuration. With this assumption it is possible to decouple the electronic and nuclear degrees of freedom:

$$\Psi(\{\vec{R}\},\{\vec{r}\}) = \Psi^e(\{\vec{R}\},\{\vec{r}\})\Psi^N(\{\vec{R}\}) \tag{1.3}$$

The problem is then reduced to solving two separate Scrhödinger equations:

$$\hat{\mathcal{H}}^e(\{\vec{R}\},\{\vec{r}\})\Psi^e(\{\vec{R}\},\{\vec{r}\}) = E^e(\{\vec{R}\})\Psi^e(\{\vec{R}\},\{\vec{r}\}) \tag{1.4}$$

and

$$\left[\hat{T}^N + V^{NN}(\{\vec{R}\}) + V^{\text{ext}}(\{\vec{R}\}) + E^e(\{\vec{R}\})\right]\Psi^N(\{\vec{R}\}) = E\Psi^N(\{\vec{R}\}) \tag{1.5}$$

where $E^e(\{\vec{R}\})$ is the ground state energy of the electronic cloud for a given nuclear configuration and $\hat{\mathcal{H}}^e(\{\vec{R}\},\{\vec{r}\}) = \hat{T}^e + V^{Ne}(\{\vec{R}\},\{\vec{r}\}) + V^{ee}(\{\vec{r}\})$.

The electronic configuration for each nuclear arrangement is found by solving the first Schrödinger equation, where the $\vec{R}$ coordinates enter as parameters. Once the electronic potential is obtained, the second equation gives the motion of the nuclei, which is usually computed by calculating the atomic forces on each atom and relaxing the atomic coordinates using a classical equation of motion.

1.1.2 Hartree-Fock and configuration interaction

Once the atomic coordinates have been put aside, the easier problem of the electronic configuration is a bit more tractable. However, even this simplified case is very difficult to solve because the number of electrons can still be very large and, consequently, the problems related to the wave function arise again.

The first step towards possible simplifications is to realize that every wave function can be expanded using an infinite sum of Slater Determinants:

$$\Psi(\{\vec{r}\}) = \sum_{i_1,..,i_n} C_{i_1,...,i_n} \sum_p (-1)^p \varphi_{i_1}(\vec{r}_{p_1}) \times ... \times \varphi_{i_n}(\vec{r}_{p_n}) \tag{1.6}$$

where $\varphi_i(\vec{r})$ are one-electron wave functions. The simplest approach, which is the Hartree-Fock method [5], uses only one slater determinant to construct the wave function. This method, which is the basis of many quantum mechanical codes and more refined approximations, is, however, very crude since it removes all the electronic correlations (excluding exchange). As a consequence, the probability of finding an electron in a certain region of space becomes independent of the other electrons.

The natural way of improving Hartree-Fock is including other slater determinants constructed with excited one-electron states. This systematic addition of correlation effects is the basis of 'configuration interaction' (CI) [6], a method very popular among the chemical community and used in many ab initio codes. It has the obvious advantage that the accuracy of the calculations can be systematically improved adding more and more determinants. However, the great drawback is that computer memory and processor time increase dramatically with the number of states and electrons, so that only very small systems can be simulated.

1.2 Density Functional Theory

An alternative but very powerful approach is Density Functional Theory (DFT) [1, 2] where the basic variable is the electronic density:

$$n(\vec{r}) = N_e \int |\Psi(\vec{r}, \vec{r}_2, ..., \vec{r}_{N_e})|^2 \, \mathrm{d}\vec{r}_2 ... \mathrm{d}\vec{r}_{N_e} \tag{1.7}$$

This quantity, which is a function of one single spatial-spin variable, is much easier to handle and store than the wave function and can simplify the problem considerably.

1.2.1 Hohenberg-Kohn theorems

DFT is based on two theorems [1]:

- 1st Hohenberg-Kohn Theorem: there is an exact correspondence between the density and the external potential of a physical system, i. e. the density uniquely determines the external potential up to a constant.
- 2nd Hohenberg-Kohn Theorem: the density that minimizes the energy is the exact ground state density (variational principle).

According to the first theorem, the density determines the Hamiltonian, that in turn determines the wave function. Therefore, any quantity is a functional of the density:

$$n \rightarrow V^{\mathrm{ext}}[n] \rightarrow \hat{\mathcal{H}} \rightarrow \Psi = \Psi[n] \rightarrow \langle \Psi | \Theta | \Psi \rangle = \langle \Theta \rangle [n] \tag{1.8}$$

The second theorem implies that the density can be used to minimize the energy functional:

$$E = \min_{\Psi} \left\langle \Psi \left| \hat{\mathcal{H}} \right| \Psi \right\rangle = \min_{n} \left\{ F[n(\vec{r})] + \int n(\vec{r}) V^{\mathrm{ext}}(\vec{r}) \mathrm{d}\vec{r} \right\} \tag{1.9}$$

where

$$F[n] = \min_{\Psi \rightarrow n} \left\langle \Psi \left| \hat{T} + V^{ee} \right| \Psi \right\rangle \tag{1.10}$$

is a universal functional of the electronic density.

1.2.2 Kohn-Sham scheme

The energy functional can be decomposed into the following terms:

$$\begin{aligned} E[n] &= T[n] + E^{ee}[n] + E^{\text{ext}}[n] = T[n] + E^{\text{H}}[n] + E^{xc}[n] + E^{\text{ext}}[n] = \\ &= \left\langle \Psi \left| -\frac{1}{2}\nabla^2 \right| \Psi \right\rangle + \frac{1}{2}\int \frac{n(\vec{r})n(\vec{r}\,')}{|\vec{r}-\vec{r}\,'|}\mathrm{d}\vec{r}\mathrm{d}\vec{r}\,' + \int n(\vec{r})\epsilon^{xc}(\vec{r})\mathrm{d}\vec{r} + \\ &+ \int n(\vec{r})V^{\text{ext}}(\vec{r})\mathrm{d}\vec{r} \end{aligned} \tag{1.11}$$

The electron-electron interaction energy has been separated into the Hartree term, corresponding to the classical electrostatic energy of a system of charged particles, and the exchange-interaction term, which includes the remaining quantum effects and can be written as the integral of the charge density multiplied by the exchange-correlation (XC) energy density, ϵ^{xc}.

The ground state of the electronic system can be found by minimizing the energy functional with respect the density or the wave function and taking into account the constraint of the number of particles:

$$\frac{\delta}{\delta n}\left(E[n] - \mu\int n(\vec{r})\mathrm{d}\vec{r}\right) = 0 \quad or \quad \frac{\delta}{\delta\Psi^*}\left(E[\Psi^*,\Psi] - \mu\langle\Psi|\Psi\rangle\right) = 0 \tag{1.12}$$

where μ is the chemical potential. This minimization defines precisely the Scrödinger equation, where the Hamiltonian is given by the functional derivative of the energy with respect to the density.

At this point it is worth to realize the following: since the same density can be given by intrinsically different wave functions, it is possible to choose the wave function of a non-interacting system, given by single Slater determinant

$$\Psi(\vec{r}_1,...,\vec{r}_{N_e}) = \sum_p (-1)^p \varphi_1(\vec{r}_{p_1}) \times ... \times \varphi_{N_e}(\vec{r}_{p_{N_e}}) \tag{1.13}$$

in such a way that its density, which is calculated as a sum over single electron densities

$$n(\vec{r}) = \sum_i \left|\varphi_i(\vec{r})^2\right| \tag{1.14}$$

is the same as the density of the interacting system. This means that the many-body interacting system is mapped onto a non-interacting system (Kohn-Sham system) in an

effective one-body potential, which is much easier to study and solve. The original formulation is then substituted by the Kohn-Sham equations [2]:

$$\frac{\delta}{\delta\varphi_i}\left(E[\Psi^*,\Psi]-\varepsilon_i\left\langle\Psi|\Psi\right\rangle\right)=0 \tag{1.15}$$

$$\left(-\frac{1}{2}\nabla^2+V^{\mathrm{H}}[n]+V^{xc}[n]+V^{\mathrm{ext}}[n]\right)\varphi_i=\varepsilon_i\varphi_i \tag{1.16}$$

The problem is then reduced to solving a simple one-particle Scrödinger equation. Once the energy functional dependence on the density is known, it is possible, as stated above, to calculate the Hamiltonian as its functional derivative, obtain the new wave function and compute once more the density, repeating the same process again. This results in a self-consistent field (SCF) procedure:

$$n_{\mathrm{initial}}\rightarrow\hat{\mathcal{H}}\rightarrow\Psi\rightarrow n'\rightarrow\hat{\mathcal{H}}'\rightarrow ... \tag{1.17}$$

which is iterated until there is no difference between the input and the output density matrices, i. e. until the ground state is reached.

1.2.3 Kinetic energy

Hitherto, no approximations were made to obtain the basic equations of DFT and everything could be considered exact, within the limits of quantum mechanics. Consequently, if the correct dependence of the energy functional on the density is known, the physical properties obtained using the Kohn-Sham system coincide exactly with the physical properties given by solving the many-body Schrödinger equation. However, the density dependence is not known in general and some of the Hamiltonian terms have to be approximated. The first problem comes from the kinetic energy since, due electronic correlations the expectation value of the kinetic operator calculated with the many-body wave function is not the same as the expectation value obtained with the one-electron wave function. The many-body contributions can be separated using the functional dependence of an interacting system with coupling constant λ [7]:

$$G_\lambda\left[n\right]=\left\langle\Psi|\hat{T}+\lambda V^{ee}|\Psi\right\rangle-\lambda E^{\mathrm{H}}\left[n\right] \tag{1.18}$$

The full interacting system is found for $\lambda=1$ whereas $\lambda=0$ corresponds to the non-interacting Kohn-Sham system:

$$G_0\left[n\right] = \sum_i \left\langle \varphi_i | \hat{T} | \varphi_i \right\rangle = T^s[n] \tag{1.19}$$

where T^s is the kinetic energy evaluated with the non interacting Kohn-Sham wave function. The many-body contributions to the kinetic energy and the exchange and correlation, which are the parts of the electron-electron interaction non included in the Hartree term, are then given by:

$$\begin{aligned} E^{xc}\left[n\right] &= G_1\left[n\right] - G_0\left[n\right] = \int_0^1 \frac{\delta G_\lambda\left[n\right]}{\delta\lambda}\mathrm{d}\lambda = \\ &= \int_0^1 \left\langle \Psi_\lambda | V^{ee} | \Psi_\lambda \right\rangle \mathrm{d}\lambda - E^{\mathrm{H}}\left[n\right] = \\ &= \frac{1}{2}\int \frac{n(\vec{r})\bar{n}^{xc}(\vec{r},\vec{r}\,')}{|\vec{r}-\vec{r}\,'|}\mathrm{d}\vec{r}\mathrm{d}\vec{r}\,' \end{aligned} \tag{1.20}$$

where

$$\bar{n}^{xc}(\vec{r},\vec{r}\,') = \int_0^1 n_\lambda^{xc}(\vec{r},\vec{r}\,')\mathrm{d}\lambda \tag{1.21}$$

is the average of the exchange-correlation hole over the coupling constant λ [8].

1.2.4 Exchange and correlation

All many-body effects are then included in the exchange and correlation term, which has to be properly calculated to obtain a good description of the system and find a reliable energy functional. As shown above it can be written in a way very similar to the Hartree term, something which comes directly from the definition of the electron-electron interaction energy [7, 8]:

$$E^{ee} = \frac{N_e(N_e-1)}{2}\int \frac{\left|\Psi(\vec{r},\vec{r}\,',\vec{r}_3,...,\vec{r}_{N_e})\right|^2}{|\vec{r}-\vec{r}\,'|}\mathrm{d}\vec{r}\mathrm{d}\vec{r}\,'\mathrm{d}\vec{r}_3...\mathrm{d}\vec{r}_{N_e} = \frac{1}{2}\int \frac{P(\vec{r},\vec{r}\,')}{|\vec{r}-\vec{r}\,'|}\mathrm{d}\vec{r}\mathrm{d}\vec{r}\,' \tag{1.22}$$

where $P(\vec{r},\vec{r}\,')$ is the pair density, which tells the probability of finding one electron at $\vec{r}$ and other electron at $\vec{r}\,'$ simultaneously [9]. If the electrons were independent particles, this probability would be simply the product of probabilities $(n(\vec{r})n(\vec{r}\,'))$, but due to electronic correlations the independence is lost and the correct expression turns out to be

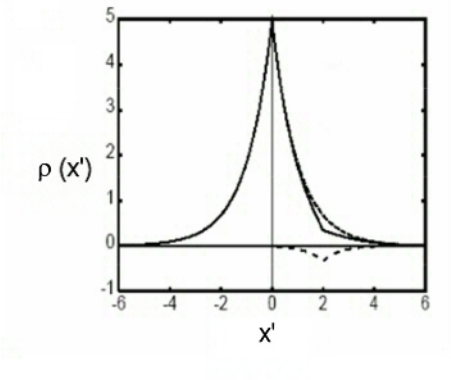

Fig. 1.2: Electronic density $n(x')$ (dashed line), conditional probability $n(2, x')$ (continuous line) and their difference, the exchange-correlation hole $n^{xc}(2, x')$ (long dashed line) as a function of the distance x (in arbitrary units) for a one-dimensional electronic system (1-d H atom). Figure from [9].

$$P(\vec{r}, \vec{r}') = n(\vec{r}) n_2(\vec{r}, \vec{r}') = n(\vec{r}) \left[n(\vec{r}') + n^{xc}(\vec{r}, \vec{r}') \right] \tag{1.23}$$

where $n_2(\vec{r}, \vec{r}')$ is the conditional probability of finding an electron at $\vec{r}'$ provided that another electron has already been found at $\vec{r}$, and it is equal to the 'independent' probability minus the exchange-correlation hole $n^{xc}(\vec{r}, \vec{r}')$. An example of this hole is shown in figure (1.2).

The most important property verified by every exchange-correlation hole is the sum rule [7]:

$$\int n^{xc}(\vec{r}, \vec{r}') \mathrm{d}\vec{r}' = -1 \tag{1.24}$$

which comes from the fact that the conditional probability integrates to $N_e - 1$. This fixes important constraints on the hole.

The exchange-correlation dependence can also be split into the exchange hole and the correlation hole. The former integrates to -1 and is always negative, which means that the exchange interaction always avoid electrons to be in the same quantum state, whereas the later can have positive and negative contributions and integrates to zero [9].

The problem of solving the electronic structure of a physical system reduces then to the problem of finding the exact shape of its hole. However, excluding some cases (like the uniform electron gas), its exact dependence is not known and many approximations

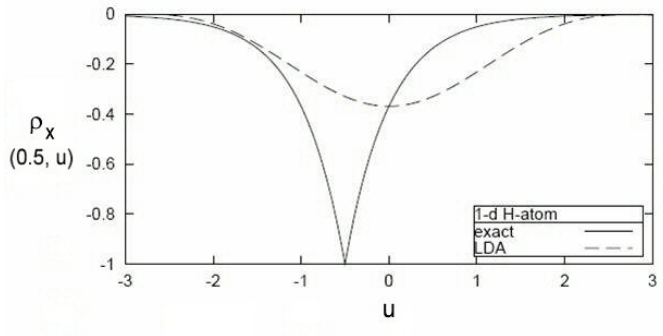

Fig. 1.3: Exact exchange hole and the corresponding LDA exchange hole for a one-dimensional electronic system (1-d H atom), where the electron is located at $x = 0.5$. Figure from [9].

have to be used.

1.2.5 The Local Density Approximation

The simplest approximation to the exchange-correlation hole is based on the uniform electron gas, where the hole depends only on the local density at each point $\vec{r}$:

$$E^{xc}[n] = \frac{1}{2}\int n(\vec{r})\epsilon^{xc}\left[n(\vec{r})\right]\mathrm{d}\vec{r} \tag{1.25}$$

ε_{xc} is the exchange-correlation energy per electron in a uniform electron gas. This is the basis of the Local Density Approximation (LDA) or Local Spin Density Approximation (LSD) for spin-polarized systems, which was already proposed in the original paper of Kohn and Sham [2] and, even though its apparent simplicity, has been one of the most successful approaches [10, 11].

A comparison between an exact hole and the LDA hole can be seen in figure (1.3), which shows the clear disagreement between them. But, despite this large dissimilitude, the LDA works reasonably well in many cases (for example, many lattice constants and structural distances are predicted with an accuracy smaller that 10%). Why? There are basically two reasons [8, 9]:

1. Only the system average and the spherical average of the hole influences the energy:

$$E^{xc}[n] = \frac{N_e}{2}\int_0^\infty 4\pi r''\left\langle \bar{n}^{xc}(r'')\right\rangle \mathrm{d}r'' \tag{1.26}$$

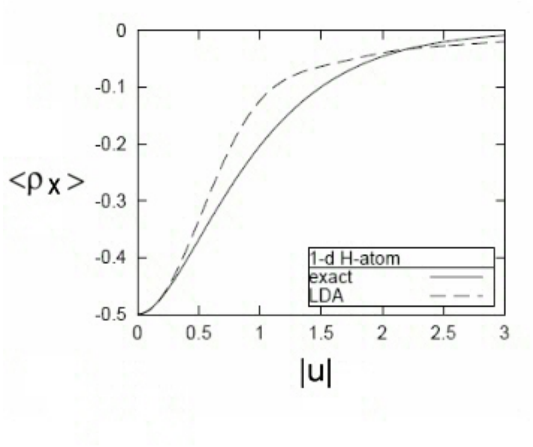

Fig. 1.4: Average of the exact exchange hole and the LDA hole for the same one-dimensional electronic system shown in figure (1.3). Figure from [9].

where

$$\langle \bar{n}^{xc}(\vec{r}'')\rangle = \frac{1}{N_e}\int \mathrm{d}\vec{r} n(\vec{r}) \int \frac{\mathrm{d}\Omega_{r''}}{4\pi} \bar{n}^{xc}(\vec{r}, \vec{r}+\vec{r}'') \tag{1.27}$$

2. The LDA hole corresponds to a physical system, which means that it verifies the sum rule, i. e. it is normalized and, in the case of the exchange hole, always negative.

These conditions produce a partial cancellation of the errors of the approximation and the resulting averaged hole is remarkably similar to the true hole, as can be seen in figure (1.4). These are then the reasons why exchange and correlation energy can be evaluated with reasonable accuracy in many systems.

1.2.6 The Generalized Gradient Approximation and other functionals

The LDA fails when the density varies sharply, as for example in transition metal compounds (see chapter 3). When this happens it is necessary to use better approximations which take into account these variations, expanding in series the functional dependence and including the gradient of the density [12]:

$$E^{xc}[n] = \frac{1}{2}\int n(\vec{r})\epsilon^{xc}\left[n, \nabla n\right](\vec{r})\mathrm{d}\vec{r} \tag{1.28}$$

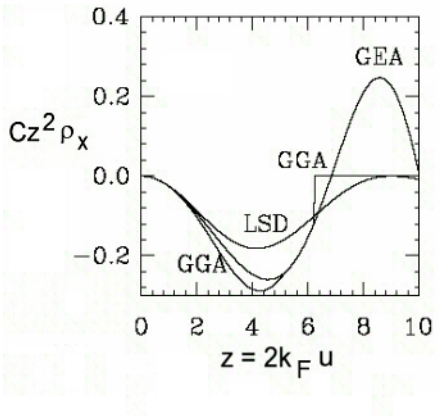

Fig. 1.5: LSD, GEA and GGA exchange holes for a one-dimensional electronic system (1-d H atom). C is a normalization constant. Figure from [9].

But in many cases Gradient Expansion Approximations (GEA) produce unphysical results (positive exchange holes) [9] due to the fact that they do not correspond to physical systems (like the LDA). In order to correct these positive contributions the Generalized Gradient Approximation (GGA) [13] truncates the hole and forces it to integrate to -1, as shown in figure (1.5).

In general, LDA works better for systems where the density varies smoothly, like for example alkaline metals, light elements, noble metals, etc. GGA improves remarkably the results in case of transition metals, being the iron the most clear example, as shown in Chapter 3. Current strategies to improve the accuracy of GGA and LDA [14] are based on hybrid functionals [15] and the 'Jacob's ladder' [16]. The former mix exact exchange [15, 17] with the GGA, fitting certain properties of molecules. However, the 'Jacob's ladder' strategy relies on adding more functionality to already developed functionals. The first rung is the LDA which employs only the electron density. Next rung is the GGA which also includes the gradient of the density. Third and fourth rungs would add the kinetic energy density (meta-GGA [18, 19]) and the exact exchange (hyper-GGA). Finally, the last rung would include a improved correlation functional with part of it evaluated exactly. In case it would be possible to reach the top of the Jacob's ladder the accuracy and universality of DFT would be dramatically improved and the result would be the 'divine functional'.

1.3 The SIESTA Method

SIESTA (Spanish Initiative for Electronic Simulations with Thousands of Atoms) is a DFT code specially suitable to simulate entirely from first principles systems which are

very big (of the order of one thousand atoms or even more) as well as simpler systems with a very high degree of precision [20, 21]. This is accomplished by using norm-conserving pseudopotentials and linear combinations of atomic orbitals (LCAO), which allow the simulations to scale linearly with the number of atoms (order-N). These and other characteristics make this code one of the most popular among the ab initio community. Its main features and the basic theory of some of its functionalities are explained in this section.

1.3.1 Norm-conserving pseudopotentials

The electrons in a solid or molecule can be classified in two types: core electrons, which belong to the inner atomic shells and are localized very close to the nucleus, and valence electrons, which belong to the external shells and are responsible of the electronic bonds and most of the physical and chemical properties. In a majority of systems the core electrons are spatially and energetically separated from the valence electrons and do not overlap with the electronic clouds of other atoms, so that their only influence is an indirect modification of the valence wave functions of the same atom[1]. The core electrons can be then effectively decoupled from the rest of the system and substituted by an effective potential, the pseudopotential, which reproduces the same valence states and, therefore, the same physical properties.

The valence wave functions generated with the pseudopotential, $\phi_{nlm}(\vec{r}) = R_{nl}(r)Y_{lm}(\hat{\vec{r}})$, have to verify certain characteristics. For norm-conserving pseudopotential (NCPS) these are the following:

- The radial part of the pseudovalence orbitals has to be smooth and nodeless inside the core region (see figure (1.6))[2]. The wave functions are then parametrized close to the nucleus (for example with the Troullier-Martins parametrization [22]). As a consequence different pseudopotentials $V_{nl}^{\mathrm{ps}}(r)$ have to be generated for each set of quantum numbers (n, l) of the valence orbitals.
- Norm conservation of each wave function inside a cutoff radius r_l^c [24]:

$$\int_0^{r_l^c} \left|R_{nl}^{\mathrm{ps}}(r)\right|^2 r^2 \mathrm{d}r = \int_0^{r_l^c} \left|R_{nl}^{\mathrm{ae}}(r)\right|^2 r^2 \mathrm{d}r \tag{1.29}$$

[1] In some elements there are states which are half between the core and the valence, i. e. bound states which interact with the electronic clouds of other atoms (for example the 3d orbitals in iron). These are known as semicore states and can no be included in the pseudopotential.

[2] Due to orthonormalization conditions the atomic orbitals oscillate sharply near the nucleus. To reproduce such oscillations in the simulation of a solid or molecule it would be necessary a very fine real space mesh, which in turn would increase dramatically the amount of memory and CPU time needed to perform the calculation.

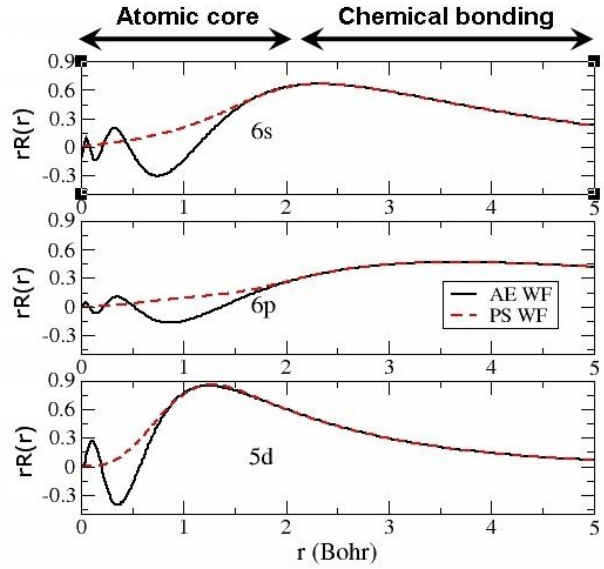

Fig. 1.6: All-electron and pseudovalence orbitals for a gold atom. Note that all the nodes of the true orbitals are included in the core region. The pseudovalence orbitals do not have nodes.

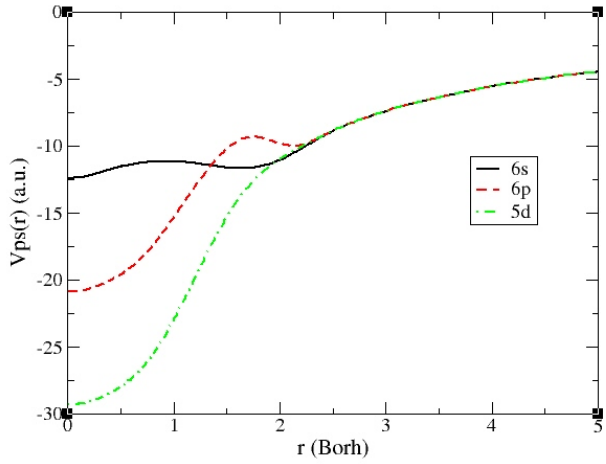

Fig. 1.7: Pseudopotentials generated for each angular momentum of the valence band in the gold atom.

where ae means 'all-electrons' and the cutoff radius depends on the angular momentum. This condition, which is related to the transferability of the pseudopotential[3] ensures charge conservation.

- The pseudovalence orbitals have to coincide with the all-electron orbitals beyond the cutoff radius:

$$R_{nl}^{\mathrm{ps}}(r > r_l^c) = R_{nl}^{\mathrm{ae}}(r > r_l^c) \tag{1.30}$$

  This implies that the pseudopotential is equal to the bare nuclear potential $-Z/r$ in that region. The radius, which can vary between 0.5 Å (light elements) and 2.0 Å or even more (heavy elements), defines a central region which should be big enough to include most of the core charge density and allow a smooth definition of the wave functions. In general, as the radius increases the smoothness improves but the transferability worsens.

- The eigenvalues and the energy dependence in different environments of the pseudoorbitals and the all-electron orbitals have to be the same for a reasonable range of energies. This ensures the transferability of the pseudopotential.

From the pseudoorbital, the screened pseudopotential for a given set of quantum numbers is calculated by inverting the radial Schrödinger equation:

$$V_{nl,\mathrm{s}}^{\mathrm{ps}}(r) = \varepsilon_{nl} - \frac{l(l+1)}{2r^2} + \frac{1}{2rR_{nl}^{\mathrm{ps}}(r)}\frac{\mathrm{d}^2}{\mathrm{d}r^2}[rR_{nl}^{ps}(r)] \tag{1.31}$$

Finally, the ionic pseudopotential, which is used on each atom of the solid or molecule, is obtained by removing the screening of the valence electrons calculated with the pseudoorbitals:

$$V_{nl}(r) = V_{nl,\mathrm{s}}(r) - V^{\mathrm{H}}[n^{\mathrm{ps}}(r)] - V^{xc}[n^{\mathrm{ps}}(r), ...] \tag{1.32}$$

In most of the elements all valence shells have different quantum numbers l but can have the same or different quantum number n. For that reason the dependence on the principal quantum number is not explicitly written and the pseudopotential is labelled with l. The total operator is then expressed in the angular momentum basis as follows:

[3] There is another kind of pseudopotentials, called 'ultrasoft' [25], which do not use the norm-conservation condition and allow the wave functions to be smoother inside the core region. However, these pseudopotentials only make a significant improvement in plane wave calculations, where smoothness is very important.

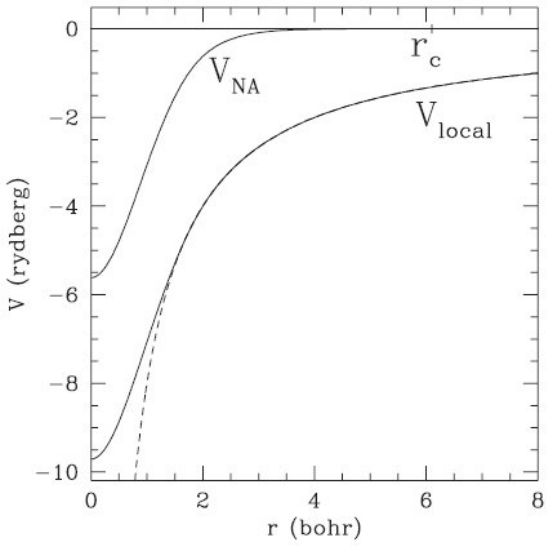

Fig. 1.8: Local pseudopotential for silicon and the corresponding 'neutral atom' potential. The dashed line corresponds to the bare nuclear potential $-Z/r$. Figure from [21].

$$\hat{V}(r) = \sum_{l=0}^{l_{\max}} \sum_{m=-l}^{l} \sum_{p=1}^{P_l} |\, Y_{lmp}\rangle \; V_{lp}(r) \, \langle Y_{lmp}\,| \tag{1.33}$$

When semicore states are included there can be some P_l shells with the same l. In that case it is necessary to use P_l different pseudopotentials for each of those angular momenta.

From the semilocal expression it is possible to split a local part, which is common to all components,

$$\hat{V}(r) = V^{\mathrm{loc}}(r) + \sum_{l=0}^{l_{\max}} \sum_{m=-l}^{l} \sum_{p=1}^{P_l} |\, Y_{lmp}\rangle \; \delta V_{lp}(r) \, \langle Y_{lmp}\,| \tag{1.34}$$

This spherically symmetric local part can be in principle arbitrary inside the region defined by the largest radius, but it is chosen as the potential given by a certain positive charge, which is optimized for smoothness. Outside that region it is equal to the bare nuclear potential $-Z/r$. Since this term is long ranged, a large number of grid points have to be used to represent it. However, for every system it is possible to define a screening valence charge, the 'atomic' charge, i. e. $n(\vec{r}) = \delta n(\vec{r}) + \sum_I n_I^{\mathrm{atom}}(|\vec{r} - \vec{R}_I|)$, so that the Hartree potential produced by it cancels the long range dependency and the local part is then only defined in a tiny region, as can be seen in figure (1.8).

The semilocal part, which vanishes beyond the core region, can also be optimized by transforming it into a fully non-local expression, as proposed by Kleinman and Bylander [23],

$$\hat{V}^{\mathrm{KB}} = \sum_{l=0}^{l_{\max}} \sum_{m=-l}^{l} \sum_{p=1}^{P_l} \frac{|\,\delta V_{lp}\phi_{lmp}\rangle\,\langle\phi_{lmp}\delta V_{lp}\,|}{\langle\,\phi_{lmp}\,|\,\delta V_{lp}\,|\,\phi_{lmp}\rangle} = \sum_{l=0}^{l_{\max}} \sum_{m=-l}^{l} \sum_{p=1}^{P_l} \left|\chi^{\mathrm{KB}}_{lmp}\right\rangle \left\langle \chi^{\mathrm{KB}}_{lmp}\right| \tag{1.35}$$

If in the previous semilocal expression the number of matrix elements per (l, m, p) component was $M(M+1)/2$ (M is the number of basis functions), now it reduces to only M, since each matrix element can be factorized in two individual terms and it is only necessary to calculate the product of each basis function with one of them.

The pseudopotentials can also have relativistic corrections (scalar corrections and spin orbit coupling) [26, 27, 28], which have to be added in heavy elements due to the high velocities of the electrons close to the nucleus. Also, in case of atoms with strong overlaps between the core and the valence (for example the transition metals) it is necessary to include non-linear core corrections [29], since the contributions of the core and valence exchange-correlation potentials can not be separated where the charge densities of both regions have a significant weight. Furthermore, in magnetic systems the exchange-correlation potential depends on the spin polarization $\xi(r) = (n^{\uparrow}(r) - n^{\downarrow}(r))/n(r)$, where $n(r)$ is the sum of the valence and the core charges. The ionic pseudopotential is therefore obtained by removing the exchange-correlation potential calculated with the usual valence charge density plus the core electronic charge density found beyond a certain cutoff radius, where the core and valence charges start having the same order of magnitude (this region is known as the pseudocore). That charge is included in the molecule or solid simulation as a fixed contribution which is added to the density to calculate the self-consistent V^{xc}.

1.3.2 Basis set

In order to obtain a linear dependence of the computer memory and CPU time as a function of the number of atoms[4] the Hamiltonian matrix has to be very sparse, i.e. it must have many zeros, so that it can be easily divided into smaller parts. Such sparsity can be achieved with basis sets made of localized atomic orbitals which extend only up to a certain cutoff radii [30]. This definition of the Hilbert space, which is the base of the LCAO programs, has the additional advantage that the properties of the system obtained using a poor basis set are much closer to the converged properties than those calculated with few PW, i. e. the states constructed with few atomic orbitals resemble converged states. Furthermore, the calculations converge relatively fast with the number of atomic orbitals [31], although this convergence is not systematic.

[4] Other approaches, like plane waves (PW), scale as N^3.

The minimal LCAO basis set (called single-ζ, single-zeta or SZ), uses only one orbital per quantum channel, i.e., one orbital for a given set of n, l and m quantum numbers in the valence shells (1 for s states, 3 for p, 5 for d, etc.). These orbitals, known as pseudo atomic orbitals (PAO), are eigenfunctions of the atomic pseudo-Hamiltonian in a spherical box [30, 33]. The potential is defined as the sum of the screened l-dependent pseuoatomic potential and a certain confinement potential which makes the wave function approach zero smoothly at the cutoff radius r_l^c [32],

$$\left[-\frac{1}{2r}\frac{\mathrm{d}^2}{\mathrm{d}r^2}r + \frac{l(l+1)}{2r^2} + V_l(r) + V_l^c(r - r_c^l)\right] R_l(r) = (\varepsilon + \delta\varepsilon_l)R_l(r) \tag{1.36}$$

The determination of the radii (or, alternatively, the energy shift $\delta\varepsilon_l$) is variational, which means that the energy of the system has to be minimized for each of them.

The size of the Hilbert space can be increased by adding more ζ to each atomic shell. The number of ζ on different shells does not have to be the same, but it should not be very different in order to have well balanced basis sets. The second and subsequent ζ, $R_l^{i\zeta}(r)$, are calculated using the 'split-valence' method [34, 35]: they have the same norm as the previous ζ between their corresponding cutoff radii r_l^i and r_l^{i-1} ($r_l^i < r_l^{i-1}$) and a polynomial form inside r_l^i:

$$R_l^{i\zeta}(r) = \begin{cases} r^l(a_l - b_l r^2) & r < r_l^i \\ R_l^{(i-1)\zeta}(r) & r_l^i \leq r < r_l^{i-1} \end{cases} \tag{1.37}$$

where a_l and b_l are chosen so that the wave function and its derivative are continuous at r_l^i. Finally, instead of $R_l^{i\zeta}$ SIESTA uses $R_l^{(i-1)\zeta} - R_l^{i\zeta}$, which produces the same description of the Hilbert space but gives functions which are more localized.

To give more freedom to the electrons and take into account the deformation induced by the chemical bonding, SIESTA can also include orbitals of different angular momenta which are unoccupied in the isolated atom (for example, in the case of Au the isolated atom has electrons in the valence orbitals $6s$ and $5d$, but not in the $6p$, which can also be included in the solid or molecule calculations) and orbitals with higher angular momenta which are built polarizing the existing orbitals with an electric field:

$$\left[-\frac{1}{2}\frac{\mathrm{d}^2}{\mathrm{d}r^2}r + \frac{(l+1)(l+2)}{2r^2} + V_l(r) - E_l\right] \mathcal{R}_{l+1}(r) = -rR_l(r) \tag{1.38}$$

where $R_l(r)$ is the radial part of the orbital that is going to be polarized, $\phi_{lm}(\vec{r}) = R_l(r)Y_{lm}(\hat{\vec{r}})$. The new polarized orbitals are then $\varphi_{(l+1)m}(\vec{r}) = C\mathcal{R}_{l+1}(r)Y_{(l+1)m}(\hat{\vec{r}})$, with C a normalization constant.

1.3.3 Wave function

As stated above, the wave function in SIESTA is obtained as a linear combination of atomic orbitals centered on the atomic positions. In the general case of a periodic and non-collinear system it has the following form:

$$\hat{\Psi}_{n\vec{k}}(\vec{r}) = \frac{1}{\sqrt{N_u}} \sum_{\vec{R},\mu} e^{-i\vec{k}\cdot\vec{R}_\mu} \hat{c}_{n\vec{k}\mu} \phi_{\vec{R}_\mu}(\vec{r} - \vec{R}_\mu) \tag{1.39}$$

n is the band index, $\vec{k}$ is the k point, N_u is the number of unit cells in the system, $\vec{R}_\mu = \vec{R} - \vec{d}_\mu$ ($\vec{d}_\mu$ is the position of orbital $\mu = (I, n, l, m)$ localized on atom I within the unit cell and $\vec{R}$ is the vector between unit cells) and $\hat{\Psi}$ and $\hat{c}$ are spinors:

$$\hat{\Psi} = \begin{pmatrix} \Psi^\uparrow \\ \Psi^\downarrow \end{pmatrix} = \sum_{\sigma=\uparrow,\downarrow} \Psi^\sigma \hat{\chi}^\sigma \tag{1.40}$$

$$\hat{c} = \begin{pmatrix} c^\uparrow \\ c^\downarrow \end{pmatrix} = \sum_{\sigma=\uparrow,\downarrow} c^\sigma \hat{\chi}^\sigma \tag{1.41}$$

where

$$\hat{\chi}_\uparrow = \begin{pmatrix} 1 \\ 0 \end{pmatrix} \quad \hat{\chi}_\downarrow = \begin{pmatrix} 0 \\ 1 \end{pmatrix} \tag{1.42}$$

are the basis vectors of the spin space.

1.3.4 Hamiltonian

The Hamiltonian can be written in the following way, according to the Kohn-Sham formulation [2]:

$$\hat{\mathcal{H}} = \hat{T} + \sum_I V_I^{\mathrm{loc}}(|\vec{r} - \vec{R}_I|) + \sum_I \hat{V}_I^{\mathrm{KB}} + V^{\mathrm{H}}(\vec{r}) + \hat{V}^{xc}(\vec{r}) + V^{\mathrm{ext}}(\vec{r}) \tag{1.43}$$

where $\hat{T} = -\frac{1}{2}\nabla^2$ is the kinetic energy operator, V_I^{loc} and $\hat{V}_I^{\mathrm{KB}}$ are the local and nonlocal parts of the pseudopotential of atom I, and V^{H} and $\hat{V}^{xc}$ (the only terms that depend on the self-consistent density), are the Hartree and exchange-correlation potentials, respectively. In spin polarized systems the exchange-correlation potential is different for spin up and

spin down densities, while in the general situation of non-collinear spin systems it is a 2×2 matrix:

$$\hat{V}^{xc} = \begin{pmatrix} V^{xc\uparrow\uparrow} & V^{xc\uparrow\downarrow} \\ V^{xc\downarrow\uparrow} & V^{xc\downarrow\downarrow} \end{pmatrix} \tag{1.44}$$

The local part of the pseudopotential, which is long-ranged, can be then conveniently screened by using the potential V_I^{atom} produced by populating the valence orbitals with an appropiate charge n_I^{atom}, in such a way that the neutral-atom potential

$$V_I^{\text{na}}(|\vec{r} - \vec{R}_I|) = V_I^{\text{loc}}(|\vec{r} - \vec{R}_I|) + e^2 \int \frac{n_I^{\text{atom}}(|\vec{r} - \vec{R}_I|)}{|\vec{r} - \vec{r}\,'|} \mathrm{d}\vec{r}\,' \tag{1.45}$$

is short ranged, i. e. it is zero beyond the maximum cutoff radius of the pseudopotential, $r_I^c = \max_l(r_{lI}^c)$ [21]. That contribution has to be subtracted from the Hartree potential, defining $\delta n(\vec{r}) = n(\vec{r}) - \sum_I n_I^{\text{atom}}(|\vec{r} - \vec{R}_I|)$, so that the Hamiltonian can be finally rewritten as

$$\hat{\mathcal{H}} = \hat{T} + \sum_I V_I^{\text{na}}(|\vec{r} - \vec{R}_I|) + \sum_I \hat{V}_I^{\text{KB}} + \delta V^{\text{H}}(\vec{r}) + \hat{V}^{xc}(\vec{r}) + V^{\text{ext}}(\vec{r}) \tag{1.46}$$

The first two terms are calculated only once using two center integrals. The neutral atom potential is also calculated once but it has to be defined on a real space grid. Finally, the last two terms depend on the self-consistent electronic density and have to be calculated for every SCF step on the real space grid.

1.3.5 Schrödinger equation

The Schrödinger equation is expressed as follows:

$$\left\langle \hat{\Psi}_{n\vec{k}} \left| \hat{\mathcal{H}} \right| \hat{\Psi}_{n\vec{k}} \right\rangle = \varepsilon_{n\vec{k}} \left\langle \hat{\Psi}_{n\vec{k}} \left| \hat{\Psi}_{n\vec{k}} \right. \right\rangle \tag{1.47}$$

where

$$\hat{\mathcal{H}} = \begin{pmatrix} \mathcal{H}^{\uparrow\uparrow} & \mathcal{H}^{\uparrow\downarrow} \\ \mathcal{H}^{\downarrow\uparrow} & \mathcal{H}^{\downarrow\downarrow} \end{pmatrix} \tag{1.48}$$

is the Hamiltonian matrix in the general case of a non-collinear system. The first part of the equation has this form:

$$\begin{aligned}\left\langle \hat{\Psi}_{n\vec{k}} \left| \hat{\mathcal{H}} \right| \hat{\Psi}_{n\vec{k}} \right\rangle &= \sum_{\mu,\vec{R},\nu} e^{-i\vec{k}\cdot(\vec{d}_\mu - \vec{R}_\nu)} \hat{c}^{\dagger}_{n\vec{k}\mu} \hat{\mathcal{H}}_{\mu\vec{R}_\nu} \hat{c}_{n\vec{k}\nu} = \\ &= \sum_{\mu,\nu} \sum_{\sigma,\sigma'} c^{\sigma\,*}_{n\vec{k}\mu} \left\{ \sum_{\vec{R}} e^{-i\vec{k}\cdot(\vec{d}_\mu - \vec{R}_\nu)} \mathcal{H}^{\sigma\sigma'}_{\mu\vec{R}_\nu} \right\} c^{\sigma'}_{n\vec{k}\nu} = \\ &= \sum_{\mu,\nu} \sum_{\sigma,\sigma'} c^{\sigma\,*}_{n\vec{k}\mu} \mathcal{H}^{\sigma\sigma'}_{\mu\nu} c^{\sigma'}_{n\vec{k}\nu} \end{aligned} \tag{1.49}$$

where

$$\mathcal{H}^{\sigma\sigma'}_{\mu\vec{R}_\nu} = \left\langle \phi_\mu \right| \hat{T} + V^{\mathrm{na}} + \hat{V}^{\mathrm{KB}} + \delta V^{\mathrm{H}} + V^{xc\,\sigma\sigma'} + V^{\mathrm{ext}} \left| \phi_{\vec{R}_\nu} \right\rangle \tag{1.50}$$

are the matrix elements in the supercell[5], whereas the term between braces, $\mathcal{H}^{\sigma\sigma'}_{\mu\nu}$, is expressed in terms of the orbitals of the unit cell.

The overlap matrix is defined in a similar manner:

$$\begin{aligned}\left\langle \hat{\Psi}_{n\vec{k}} \left| \hat{\Psi}_{n\vec{k}} \right\rangle &= \sum_{\mu,\vec{R},\nu} e^{-i\vec{k}\cdot(\vec{d}_\mu - \vec{R}_\nu)} \hat{c}^{\dagger}_{n\vec{k}\mu} \hat{S}_{\mu\vec{R}_\nu} \hat{c}_{n\vec{k}\nu} = \\ &= \sum_{\mu,\nu} \sum_{\sigma,\sigma'} c^{\sigma\,*}_{n\vec{k}\mu} \left\{ \sum_{\vec{R}} e^{-i\vec{k}\cdot(\vec{d}_\mu - \vec{R}_\nu)} S^{\sigma\sigma'}_{\mu\vec{R}_\nu} \right\} c^{\sigma'}_{n\vec{k}\nu} = \\ &= \sum_{\mu,\nu} \sum_{\sigma,\sigma'} c^{\sigma\,*}_{n\vec{k}\mu} S^{\sigma\sigma'}_{\mu\nu} c^{\sigma'}_{n\vec{k}\nu} \end{aligned} \tag{1.51}$$

with

$$S^{\sigma\sigma'}_{\mu\vec{R}_\nu} = \left\langle \phi_\mu \right| \delta^{\sigma\sigma'} \left| \phi_{\vec{R}_\nu} \right\rangle = S_{\mu\vec{R}_\nu} \delta^{\sigma\sigma'} \tag{1.52}$$

The final matrix equation is then

$$\sum_{\nu,\sigma'} \left(\mathcal{H}^{\sigma\sigma'}_{\mu\nu} - \varepsilon_{n\vec{k}} S_{\mu\nu} \delta^{\sigma\sigma'} \right) c^{\sigma'}_{n\vec{k}\nu} = 0 \tag{1.53}$$

where all matrices are expressed in terms of the basis orbitals of the unit cell.

[5] In periodic systems with k points it is necessary to define a supercell to calculate the matrix elements between atoms in the unit cell, μ, and atoms in the neighbor cells, ν, which are afterwards multiplied by the phase $e^{-i\vec{k}(\vec{d}_\mu - \vec{R}_\nu)}$.

1.3.6 Density matrix and magnetization

The density is calculated as the sum of the product of the eigenvectors multiplied by the occupation:

$$n^{\sigma\sigma'}(\vec{r}) = \frac{1}{N_k}\sum_{n,\vec{k}} f_{n\vec{k}}\Psi^{\sigma}_{n\vec{k}}(\vec{r})\Psi^{\sigma',*}_{n\vec{k}}(\vec{r}) = \\ = \frac{1}{N_k}\sum_{n,\vec{k}} f_{n\vec{k}}\sum_{\mu,\vec{R},\nu} e^{i\vec{k}\cdot(\vec{d}_\mu-\vec{R}_\nu)}c^{\sigma}_{n\vec{k}\mu}c^{\sigma',*}_{n\vec{k}\nu}\phi_\mu(\vec{r}-\vec{d}_\mu)\phi_{\vec{R}_\nu}(\vec{r}-\vec{R}_\nu) \tag{1.54}$$

where $f_{n\vec{k}} \equiv f(\varepsilon_{n\vec{k}} - \varepsilon_{\mathrm{F}})$ is the Fermi distribution function, which gives the occupation of each state (ε_{F} is the Fermi energy), and N_k is the number of k points. This equation can be expressed in the following way:

$$n^{\sigma\sigma'}(\vec{r}) = \sum_{\mu,\vec{R},\nu} \rho^{\sigma\sigma'}_{\mu\vec{R}_\nu}\phi_\mu(\vec{r}-\vec{d}_\mu)\phi_{\vec{R}_\nu}(\vec{r}-\vec{R}_\nu) \tag{1.55}$$

where

$$\rho^{\sigma\sigma'}_{\mu\vec{R}_\nu} = \frac{1}{N_k}\sum_{n,\vec{k}} f_{n\vec{k}}e^{i\vec{k}\cdot(\vec{d}_\mu-\vec{R}_\nu)}c^{\sigma}_{n\vec{k}\mu}c^{\sigma',*}_{n\vec{k}\nu} \tag{1.56}$$

is the density matrix.

At every point $\vec{r}$ the non-collinear density can be expressed as follows:

$$\hat{n}(\vec{r}) = \frac{1}{2}\left[n(\vec{r})\hat{I} + \vec{m}(\vec{r})\cdot\hat{\vec{\tau}}\right] \tag{1.57}$$

The total density and the spin vector at $\vec{r}$ are given by

$$n(\vec{r}) = \mathrm{Tr}\{\hat{I}\hat{n}(\vec{r})\} = n^{\uparrow\uparrow}(\vec{r}) + n^{\downarrow\downarrow}(\vec{r}), \tag{1.58}$$

$$\vec{m}(\vec{r}) = m(\vec{r})\vec{u}_m(\vec{r}) = \mathrm{Tr}\{\hat{\vec{\tau}}\hat{n}(\vec{r})\} \tag{1.59}$$

where $\hat{I}$, and $\hat{\vec{\tau}}$ are the identity and the Pauli matrices respectively. Introducing now the polar, θ, and the azimutal, φ, angles of the spin vector (see figure (3.2)) the density can also be written in this way:

$$\hat{n}(\vec{r}) = \begin{pmatrix} n(\vec{r}) + \frac{1}{2}m(\vec{r})\cos\theta(\vec{r}) & \frac{1}{2}m(\vec{r})\sin\theta(\vec{r})e^{-i\varphi(\vec{r})} \\ \frac{1}{2}m(\vec{r})\sin\theta(\vec{r})e^{i\varphi(\vec{r})} & n(\vec{r}) - \frac{1}{2}m(\vec{r})\cos\theta(\vec{r}) \end{pmatrix} \tag{1.60}$$

The magnetization is proportional to the spin vector and is given by

$$\vec{M}(\vec{r}) = -g\mu_{\mathrm{B}}\mathrm{Tr}\{\hat{\vec{S}}\hat{n}\} \simeq -\mathrm{Tr}\{\hat{\vec{\tau}}\hat{n}(\vec{r})\} = -\vec{m}(\vec{r}) \tag{1.61}$$

where g the electron form factor, μ_{B} is the Bohr magneton (which in atomic units is equal to one) and $\hat{\vec{S}} = \frac{1}{2}\hat{\vec{\tau}}$ is the spin operator.

1.3.7 Energy

The energy obtained as the expectation value of the Hamiltonian is the band-structure (BS) energy [21]:

$$E^{\mathrm{BS}} = \sum_{n\vec{k}} f_{n\vec{k}} \left\langle \hat{\Psi}_{n\vec{k}} \right| \hat{\mathcal{H}} \left| \hat{\Psi}_{n\vec{k}} \right\rangle = \sum_{\sigma,\sigma'} \sum_{\mu,\vec{R},\nu} \rho^{\sigma\sigma'}_{\mu\vec{R}_\nu} \mathcal{H}^{\sigma'\sigma}_{\vec{R}_\nu\mu} = \mathrm{Tr}(\hat{n}\hat{\mathcal{H}}) \tag{1.62}$$

But, in order to obtain the total or Kohn-Sham energy of the system it is necessary to subtract the double counting terms, since the potential elements

$$V^{\mathrm{H}}(\vec{r}) = \frac{\delta E^{\mathrm{H}}[\hat{n}]}{\delta n(\vec{r})} = \int \frac{n(\vec{r}\,')}{|\vec{r} - \vec{r}\,'|}\mathrm{d}\vec{r}\,' \tag{1.63}$$

and

$$V^{xc\,\sigma}(\vec{r}) = \frac{\delta E^{xc}[\hat{n}]}{\delta n^{\sigma}(\vec{r})} = (\delta_{\uparrow,\sigma} + \delta_{\downarrow,\sigma})\epsilon(\vec{r}) + \int n(\vec{r}\,')\frac{\delta\epsilon(\vec{r}\,')}{\delta n^{\sigma}(\vec{r})}\mathrm{d}\vec{r}\,' \tag{1.64}$$

where $\sigma = \{\uparrow\uparrow, \uparrow\downarrow, \downarrow\uparrow, \downarrow\downarrow\}$ and in general $\epsilon(\vec{r}) = \epsilon(n_{\uparrow\uparrow}(\vec{r}), n_{\uparrow\downarrow}(\vec{r}), n_{\downarrow\uparrow}(\vec{r}), n_{\downarrow\downarrow}(\vec{r}))$, are not the same as those employed in the determination of the energy. In addition, the nuclear-nuclear interaction energy has also to be included. The Kohn-Sham energy acquires then the following form:

$$E^{\mathrm{KS}} = E^{\mathrm{BS}} - \frac{1}{2}\int n(\vec{r})V^{\mathrm{H}}(\vec{r})\mathrm{d}^3\vec{r} + \int \left[n(\vec{r})\epsilon^{xc}(\vec{r}) - \mathrm{Tr}\left\{\hat{n}(\vec{r})\hat{V}^{xc}(\vec{r})\right\}\right]\mathrm{d}^3\vec{r} + \sum_{I<J}\frac{Z_I Z_J}{R_{IJ}} \tag{1.65}$$

where $R_{IJ} = |\vec{d}_I - \vec{R} - \vec{d}_J|$. To avoid the long range interactions of the last term it can be screened in a similar way to the screening of $V^{\rm loc}$, employing $V_I^{\rm na} = V_I^{\rm loc} + V_I^{\rm atom}$ and the corresponding densities, $n_I^{\rm na} = n_I^{\rm loc} + n_I^{\rm atom}$. Finally the energy reads:

$$\begin{aligned} E^{\rm KS} = & \sum_{\sigma,\sigma'} \sum_{\mu,\vec{R},\nu} \rho^{\sigma\sigma'}_{\mu\vec{R}_\nu} (T_{\vec{R}_\nu\mu} + V^{\rm KB}_{\vec{R}_\nu\mu}) \delta^{\sigma\sigma'} + \sum_{I<J} E^{\rm na}_{IJ}(R_{IJ}) + \sum_{I<J} \delta E^{\rm loc}_{IJ}(R_{IJ}) + \\ & + \sum_I E_I^{\rm atom} + \sum_I \int \delta n(\vec{r}) V_I^{\rm na}(|\vec{r} - \vec{R}_I|) {\rm d}^3\vec{r} + \frac{1}{2} \int \delta n(\vec{r}) \delta V^{\rm H}(\vec{r}) {\rm d}^3\vec{r} + \\ & + \int n(\vec{r}) \epsilon^{xc}(\vec{r}) {\rm d}^3\vec{r} + \int n(\vec{r}) V^{\rm ext}(\vec{r}) {\rm d}^3\vec{r} \end{aligned} \tag{1.66}$$

where

$$E^{\rm na}_{IJ}(R_{IJ}) = \int V_I^{\rm na}(|\vec{r} - \vec{R}_I|) n_J^{\rm na}(|\vec{r} - \vec{R}_J|) {\rm d}^3\vec{r}, \tag{1.67}$$

$$\delta E^{\rm loc}_{IJ}(R_{IJ}) = \frac{Z_I Z_J}{R} - E^{\rm loc}_{IJ}(R_{IJ}), \tag{1.68}$$

$$E^{\rm loc}_{IJ}(R) = \int V_I^{\rm loc}(|\vec{r} - \vec{R}_I|) n_J^{\rm loc}(|\vec{r} - \vec{R}_J|) {\rm d}^3\vec{r}, \tag{1.69}$$

and

$$E_I^{\rm atom} = \int_0^\infty \left(V_I^{\rm loc}(|\vec{r} - \vec{R}_I|) + \frac{1}{2} V_I^{\rm atom}(|\vec{r} - \vec{R}_I|) \right) n_I^{\rm atom}(|\vec{r} - \vec{R}_I|) 4\pi r^2 {\rm d}r, \tag{1.70}$$

The SCF procedure finishes when the differences between the input and output density matrices are small enough, i. e. when the electronic ground state is reached. Then it is possible to obtain the main physical properties (energy, electronic density, spin polarization, etc.) or calculate the forces on some atoms and relax them to a new configuration.

1.4 A Paradigmatic Example: Cobalt Impurities in SnO_2 Matrices

Magnetic oxides are an interesting class of materials. From the point of view of magnetism they can be ferromagnetic, ferrimagnetic, antiferromagnetic, non-collinear, etc. Taking into account transport properties, on the other hand, they can be insulating, conducting or even superconducting (for a review see [36]). The behavior of the metallic host atoms,

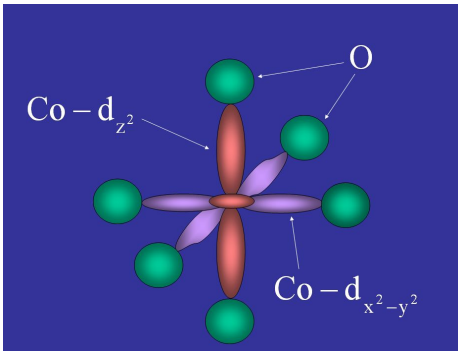

Fig. 1.9: Typical octahedric configuration in a magnetic oxide. In this case a Co atom surrounded by the oxygens.

which gives rise to the most interesting physical properties, can be easily explained using only Hund's rules and the Pauli exclusion principle. For example, consider the following Co^{3+} atom (d^6) surrounded by six oxygens in a octahedric configuration, as shown in figure (1.9). Due to the electrostatic repulsion and the hybridization with the oxygens, the energy of the d levels which go along the cartesian directions, namely the d_{z^2} and the $d_{x^2-y^2}$, goes up, while the remaining orbitals feel smaller interactions and are less affected. The net result is an effective splitting in two levels: 2 e_g and 3 t_{2g} (see figure (1.10). The energy difference, Δ, is the crystal field splitting

The electronic and magnetic configurations depend on the relative strength of the crystal field. If the difference between the e_g and the t_{2g} levels is small enough, some electrons can 'jump' to the e_g states, following Hund's rules. The total spin is then maximized (high-spin configuration). However, if Δ is large, the electrons remain in the t_{2g} states with opposite spin, giving rise to the low-spin configuration. This simple model explains why in many materials the magnetization increases when a pressure is applied and can also account for some intriguing phenomena like the invar effect [135].

Some other magnetic and transport properties of magnetic oxides are fairly well described by the Hubbard Hamiltonian:

$$\hat{\mathcal{H}} = \sum_{i,j,\sigma} t_{ij} \hat{c}^{\dagger}_{i\sigma} \hat{c}_{j\sigma} + \frac{U}{2} \sum_{i,\sigma} \hat{n}_{i\sigma} \hat{n}_{i,-\sigma} \tag{1.71}$$

Depending on the ratio between the hopping parameter t and the intraatomic repulsion U it its possible to have insulator or metallic behavior. On one hand, for $U \ll t$ electrons can easily move between atoms and the system is metallic. On the other hand, for $U \gg t$ electrons can not hop to other atoms and the system behaves like an insulator, with an energy gap $E_g \sim U - 4t$. This regime gives rise to what are known as strongly correlated systems [36], whose magnetic configurations can be easily predicted with the Anderson-

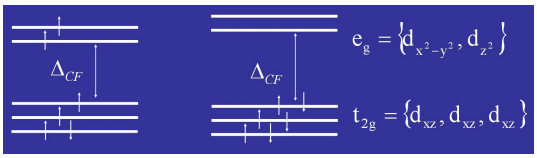

Fig. 1.10: High spin (left) and low spin (right) configurations of the Co^{3+} ion shown in figure (1.9).

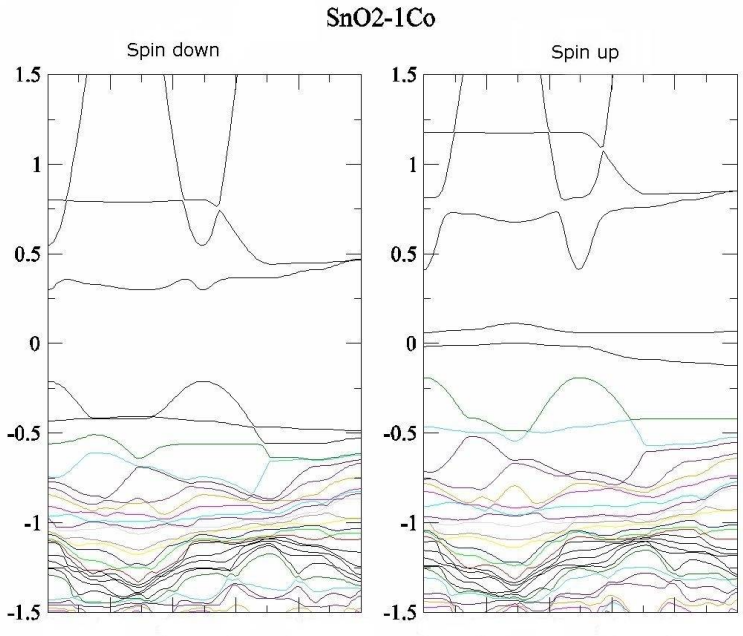

Fig. 1.11: Majority (left) and minority (right) band structure for a matrix of SnO_2 with 48 atoms and a Co substituting one Sn. Energies in the vertical axis are given in eV and the zero corresponds to the Fermi energy.

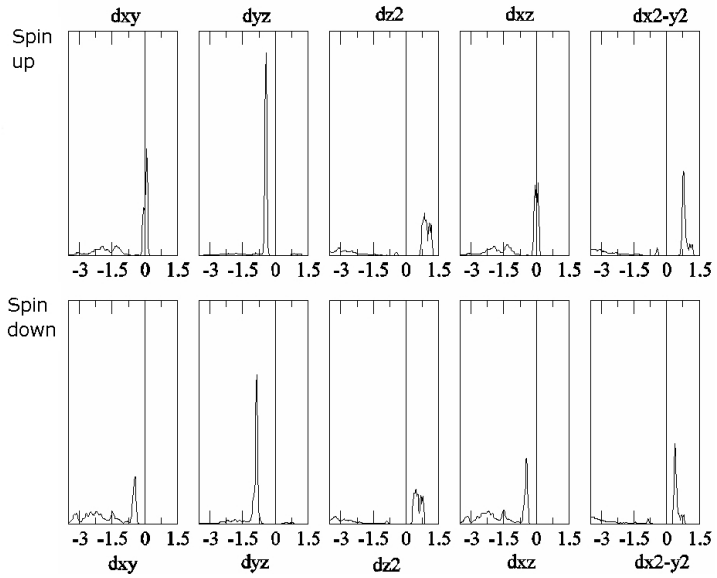

Fig. 1.12: Projected density of states on the Co d orbitals for minority (above) and majority (below) electrons. The energies on the horizontal axis are given in eV and the zero corresponds to the Fermi energy.

Goodenough-Kanamori rules [37].

An interesting example of magnetic oxide is the diluted magnetic semiconductor $Sn_{1-x}Co_xO_{2-\delta}$, made by doping SnO_2 (rutile) with small concentrations of Co. This material was found to be ferromagnetic, with a Curie temperature of 650 K and a giant magnetic moment of $7.5 \pm 0.5\ \mu_B$/Co for low dopant concentration [38]. Such a magnetic moment suggests that either the orbital magnetic moment is not quenched or some moment appears in the atoms around the Co.

To calculate the ground state properties of this material I performed a series of ab initio simulations of SnO_2 matrices with Co impurities, using the LDA approximation and double-ζ polarized basis sets for O, Sn and Co. Firstly I used a unit cell with 48 atoms, constructed with 8 basic unit cells (each unit cell has 2 Sn and 4 O), where one Sn was substituted by a Co ($x = 1/15 \simeq 0.07$). In such a configuration the Co atom is coordinated by 6 oxygens situated in the vortexes of a deformed octahedron, i. e. two of the oxygens are symmetrically displaced along the perpendicular direction of one of the C_4 axes.

The band structure, plotted if figure (1.11), shows a clear half metallic behavior [39]. The minority bands that cross the Fermi level come from the Co since they are absent in pure SnO_2. To find out their character I plot in figure (1.12) and (1.13) the projected density of states (PDOS) on the Co d and some of the surrounding O p, respectively. The

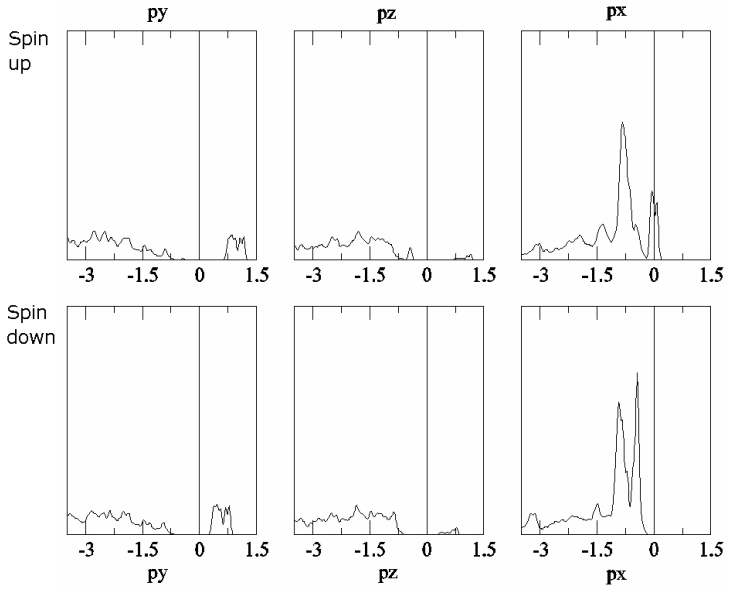

Fig. 1.13: Projected density of states on the p orbitals of one of the O surrounding the Co, for minority (above) and majority (below) electrons. The energies on the horizontal axis are given in eV and the zero corresponds to the Fermi energy.

minority orbitals that have the largest weight at the Fermi energy are the d_{xy} and the d_{xz}. These are the closest orbitals to the O atoms (the other t_{2g} orbital, the d_{yz}, has an smaller interaction due to the deformation of the octahedron). An example of the spatial distribution of some of them is shown in figure (1.14), where I plot the partial charge density, defined as the difference between the total charge density and the neutral atom charge.

The system is then magnetic, with a total magnetic moment of 1 μ_B. From the PDOS of the oxygen p states it is also clear that the closest orbitals to the Co-d_{xy} and Co-d_{xz} suffer also exchange-splitting and acquire a net magnetic moment. The Mulliken populations analysis reveals that the cobalt has only 0.77 μ_B, while the surrounding O get 0.23 μ_B. Such a distribution of the magnetization charge, which resembles a magnetic polaron, can be observed in figure (1.15). These magnetic states do not interact between them, since the bands at E_F are almost flat. Indeed, by calculating the energy difference between the ferromagnetic and the antiferromagnetic configurations in a system with a unit cell of 72 atoms and two cobalts ($x = 2/22 = 0.09$) as far away as possible from each other, I find that the system is paramagnetic (the energy difference of the whole unit cell is very small, of the order of various meV). This clearly does not agree with experiments.

These results imply that, either the experiments were not accurate enough (for example, high magnetic moments can appear on the surface atoms, where the orbital magnetic

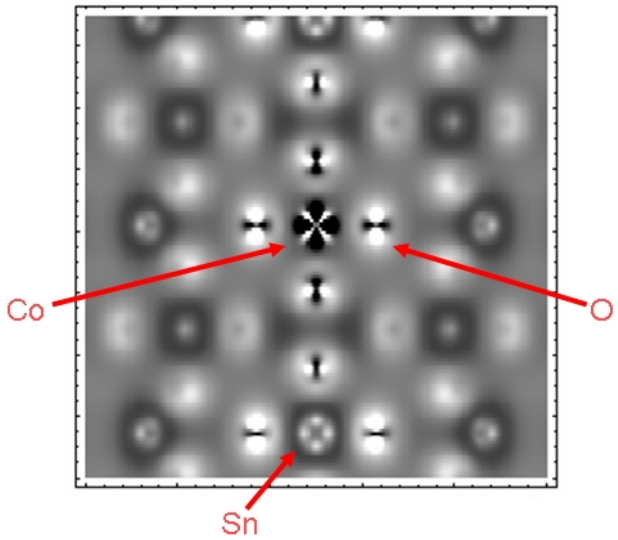

Fig. 1.14: Partial charge density (defined as the difference between the total charge and the neutral atom charge densities) along a certain plane for $Sn_{0.93}Co_{0.07}O_2$. The highest values are plotted as white and the lowest as black.

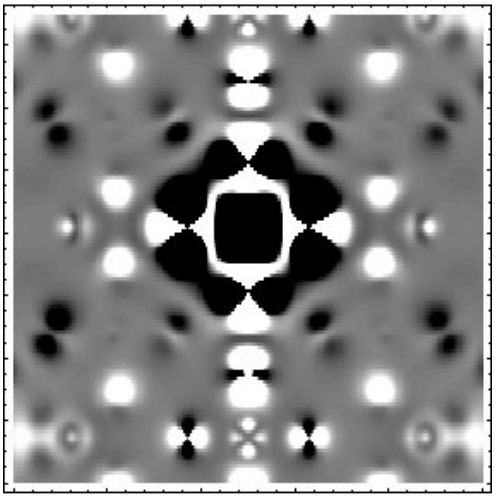

Fig. 1.15: The same as figure (1.14) for the magnetization charge density. Note the polaron around the Co atom.

moments are not quenched) or the calculations had something wrong. In this last case, the most obvious source of errors comes from the strong electronic correlations that feel the electrons confined in the atoms surrounded by the oxygens, which are not properly taken into account by the LDA functional. Part of such correlations can be described by including the intraatomic repulsion between charge densities of different spins, i. e. adding a Hubbard-like term to the DFT Hamiltonian (LDA+U [40]). Other errors can also come from the electronic self interaction (SIC) [11], which is not corrected in the DFT Hamiltonian and is important in systems with localized states.

In summary, I have shown that using a DFT code, like SIESTA, it is possible to obtain systematically a lot of information on the ground state properties of a given material. In this particular case, however, the results do not agree with the experiments, due probably to failures of the exchange-correlation functional. Possible improvements include more sophisticated approximations and corrections, like the LDA+U and SIC.

2

Molecular and Nanoscale Electronics

I describe in this chapter the main physical concepts and methods behind the determination of the transport properties of nanoconstrictions and systems with small numbers of atoms. I explain the main characteristics of the SMEAGOL code (Spin and Molecular Electronics in an Atomically-Generated Orbital Landscape) [57] and I show results for the following systems: i) an H_2 molecule sandwiched between platinum or palladium electrodes, ii) platinum chains, and iii) metallocene chains encapsulated in carbon nanotubes.

2.1 Introduction

During the last years a series of experiments and theoretical predictions have demonstrated the possibility of reaching the ultimate limit in the electronics industry, namely the atomic scale. Experiments performed with scanning tunnelling microscope (STM) and mechanically controllable break junctions (MCBJ) measured the conductivity of contacts and chains of atomic size [41, 42], whose mechanical and electrical properties differ strongly from the bulk properties. Other experiments involving molecules [43, 44] and carbon nanotubes [45, 46, 47, 48, 49, 50, 51] proved the possibility of using very small molecular systems as new electronic components. These steps pave the way to the construction of tiny computers with incredibly high processing speed and storage capacity.

In atomic-size devices the conductance does not depend on the scattering at defects and impurities but only on the electronic structure and geometry of the constriction. The transport is then ballistic and the coherence of the electrons is conserved over long dis-

tances in absence of inelastic scattering. The constriction produces the highest resistance and therefore determines the transport characteristics of the whole system. The conductance is quantized [52] in a certain number of channels, but the contacts to the leads can kill many of them and/or decrease their transmission. To study such small systems it is necessary then a quantum transport theory which takes into account the precise electronic structure of the scattering region and the contacts.

Since the derivation by Landauer of the conductance formula for non interacting electrons in a disordered medium [53] and its generalization to leads with many channels [54], the Büttiker-Landauer approach has been widely used to compute steady-state currents in systems with small numbers of atoms. An alternative approach is the non-equilibrium Green's function formalism, which is based on the Keldysh approach [55]. Such a method has been implemented in SIESTA (TranSIESTA) [56]: the transport code reads the DFT Hamiltonian and computes the non-equilibrium density and the current using non-equilibrium Green's Functions. The implementation of the SMEAGOL code (Spin and Molecular Electronics in an Atomically-Generated Orbital Landscape) [57] is very similar but differs from TranSIESTA in the possibility of using spin-polarized or non-collinear spin options, k points along the perpendicular directions and the calculation of the surface Green's function (GF).

SMEAGOL has been successfully applied to the theoretical study and characterization of atomic-size constrictions and molecules sandwiched between metallic leads or placed inside carbon nanotubes. Some of these calculations were motivated by experiments performed using STM's and MCBJ's, where conductances close to the quantum of conductance, $G_0 = 2e^2/h$, were measured. Two of the most spectacular experiments, carried out by Smit *et al.* [44] and Csonka *et al.* [58], studied the conductance through the smallest molecular bridge, namely an H_2 molecule, sandwiched between platinum or palladium electrodes, respectively. Although the existence of only one channel and the presence of a single molecule between the contacts has been clearly established by fluctuation and phonon measurements, there is still a strong debate about the exact orientation of the molecule (parallel or perpendicular to the current flow) [59, 60, 61, 62]. Moreover, the clear differences between the conductance of the molecule between platinum ($\sim 1.0\ G_0$) and palladium ($\sim 0.6\ G_0$) electrodes have not been explained yet.

Platinum leads were also used to grow monoatomic chains [104, 63]. These interesting systems, which comprise the smallest possible wires, can also be produced with gold and iridium [104, 64, 63] and are characterized by the presence of conductance oscillations which have been attributed to a universal parity or even-odd effect. In the case of gold [41, 42] there is only one channel at the Fermi energy (the s channel) and the conductance oscillates around G_0. However, platinum and iridium, which have also the d bands at E_F, are characterized by bigger values of G and the presence of a negative slope superimposed to the oscillations [63], whose origin has not been clearly established. Additionally, it is not clear whether these chains form linear or zigzag arrangements [65, 66] and how is their precise evolution when the electrodes are pulled apart.

Another kind of systems that can be used to fabricate nanodevices is based on carbon nanotubes (CNTs), whose stability and mechanical resistance make them promising candidates to act as nanowires. In addition, the demonstration of the possibility of filling CNTs with different compounds [67] has opened a new and growing field of research, where nanowire devices with new electronic properties can be produced using simple chemical methods. Examples include the encapsulation of transition metal nanowires [45], fullerenes that modify the local electronic structure of the nanotube [46], metallofullerenes that modulate the bandgap of semiconductor nanotubes and divide them into multiple quantum dots [47], organic molecules that allow to produce n- and p-doped nanotubes [48, 49], and iron nanoparticles that facilitate the inclusion of magnetic properties [50, 51]. Following these experiments it was also demonstrated the diameter-selective encapsulation of cobaltocenes inside CNTs [108]. This experiment motivated the simulation of chains of metallocenes inside metallic or insulating nanotubes, in search of possible magnetoresistive effects.

2.1.1 Non-Equilibrium Green's functions

As a first step I introduce the basic theory underlying the quantum transport formalism. I start then by describing the basic notation of many-body theory and the non-equilibrium concept.

One of the central issues in many-body theory is the evaluation of expectation values:

$$\mathcal{I}(t,t',...) = \left\langle \hat{\Psi}_H \left| \hat{T}[\hat{A}_H(t)\hat{B}_H(t')...] \right| \hat{\Psi}_H \right\rangle \tag{2.1}$$

where the wave function $\hat{\Psi}$ and the operators $\hat{A}$, $\hat{B}$, etc. are expressed in the Heisemberg representation and $\hat{T}$ is the time-order operator. If the system, described by the Hamiltonian $\hat{\mathcal{H}} = \hat{\mathcal{H}}_0 + \hat{V}(t)$ (a non-interacting part $\hat{\mathcal{H}}_0$ plus a time-dependent interaction $\hat{V}(t)$), is in equilibrium, the above expectation value can be written in the interaction representation as follows:

$$\mathcal{I}(t,t',...) = \frac{\left\langle \hat{\psi}_{0,I} \left| \hat{T}[\hat{A}_I(t)\hat{B}_I(t')...\hat{S}(\infty,-\infty)] \right| \hat{\psi}_{0,I} \right\rangle}{\left\langle \hat{\psi}_{0,I} \left| \hat{S}(\infty,-\infty) \right| \hat{\psi}_{0,I} \right\rangle} \tag{2.2}$$

$\hat{\psi}_0$ is the ground state of the non-interacting system, which exist in the remote past before the interaction is turned on adiabatically, $\hat{S}(t,t') = \hat{T}\left[\exp - i\int_{t'}^{t} \hat{V}_{\hat{\mathcal{H}}_0}(t_1)\mathrm{d}t_1\right]$ is the S matrix, with $\hat{V}_{\hat{\mathcal{H}}_0}(t) = \exp(i\hat{\mathcal{H}}_0 t)\hat{V}(t)\exp(-i\hat{\mathcal{H}}_0 t)$, and $\langle ... \rangle$ represents an expectation value or a thermal average. The assumption of equilibrium implies that the system in the remote future, when the interaction is turned off adiabatically, recovers the same non-interacting state multiplied by a phase, $e^{i\varphi}\hat{\psi}_0$.

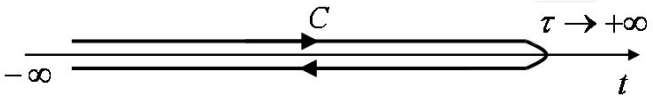

Fig. 2.1: Keldysh contour.

In a non-equilibrium situation, however, the number of particles changes and hence the final state can differ from the original one, i. e. the evolution of the system is irreversible. To avoid the uncertainty associated with the remote future, Schwinger [68] and Keldysh [55] proposed to evaluate the S matrix in the contour shown in figure (2.1), where all the times on the positive branch, which are time-ordered, are previous to the times on the negative branch, which are anti-time-ordered [69]. The initial and final state are then the same, $\hat{\psi}_0$, and

$$\mathcal{I}(t,t',...) = \left\langle \hat{\psi}_{0,I} \left| \hat{T}_C[\hat{A}_I(t)\hat{B}_I(t')...\hat{S}_C(\infty,-\infty) \right| \hat{\psi}_{0,I} \right\rangle \tag{2.3}$$

where $\hat{T}_C$ orders the times along the C contour.

Green's functions in equilibrium

Focusing now on the GF, whose causal version in the Heisemberg representation is defined as [70]

$$G(\lambda;t,t') = -i \left\langle \hat{\Psi}_H \left| \hat{T}[\hat{C}_{H,\lambda}(t)\hat{C}^{\dagger}_{H,\lambda}(t')] \right| \hat{\Psi}_H \right\rangle \tag{2.4}$$

where $\hat{C}_\lambda(C^{\dagger}_\lambda)$ is the destruction (creation) operator and λ represents some set of quantum numbers associated with each particular system (I will drop it for simplicity). In the interaction representation one finds in equilibrium

$$G(t,t') = \frac{-i \left\langle \hat{\psi}_{0,I} \left| \hat{T}[\hat{C}_I(t)\hat{C}^{\dagger}_I(t')\hat{S}(\infty,-\infty)] \right| \hat{\psi}_{0,I} \right\rangle}{\left\langle \hat{\psi}_{0,I} \left| \hat{S}(\infty,-\infty) \right| \hat{\psi}_{0,I} \right\rangle} \tag{2.5}$$

Next step is to expand the S matrix using Wick's theorem and express the GF as a sum of products of single particle GFs. If one moves also to the absolute and relative time reference frames, i. e. $G(t,t') \to G(T,\tau)$, where $T = (t+t')/2$ and $\tau = t-t'$, and assumes that the system has reached an stationary state, i. e. G does not depend on T but only on τ, applying a Fourier transform with respect to τ,

$$G(E) = \frac{1}{\sqrt{2\pi}} \int G(\tau) e^{iE\tau} \mathrm{d}\tau \tag{2.6}$$

one finally obtains Dyson's equation:

$$G(E) = g_0(E) + g_0(E)\Sigma(E)G(E) \tag{2.7}$$

where g_0 is the non-interacting GF, and Σ is the selfenergy, which takes into account all the interacting terms.

Green's functions out of equilibrium

Out of equilibrium the integration is performed along the C contour and, when Wick's theorem is applied, the times in each branch are mixed. However, it is possible to simplify the problem defining six GFs:

$$G^{<}(t,t') = i \left\langle \hat{\Psi}_H \left| \hat{C}_H^{\dagger}(t') \hat{C}_H(t) \right| \hat{\Psi}_H \right\rangle \tag{2.8}$$

$$G^{>}(t,t') = -i \left\langle \hat{\Psi}_H \left| \hat{C}_H(t) \hat{C}_H^{\dagger}(t') \right| \hat{\Psi}_H \right\rangle \tag{2.9}$$

$$\begin{aligned} G^{T}(t,t') &= \theta(t-t')G^{>}(t,t') + \theta(t'-t)G^{<}(t,t') = \\ &= -i \left\langle \hat{\Psi}_H \left| \hat{T}[\hat{C}_H(t)\hat{C}_H^{\dagger}(t')] \right| \hat{\Psi}_H \right\rangle \end{aligned} \tag{2.10}$$

$$\begin{aligned} G^{\bar{T}}(t,t') &= \theta(t'-t)G^{>}(t,t') + \theta(t-t')G^{<}(t,t') = \\ &= -i \left\langle \hat{\Psi}_H \left| \hat{\bar{T}}[\hat{C}_H(t)\hat{C}_H^{\dagger}(t')] \right| \hat{\Psi}_H \right\rangle \end{aligned} \tag{2.11}$$

$$G^{\mathrm{R}}(t,t') = (G^{T} - G^{<})(t,t') = (G^{>} - G^{\bar{T}})(t,t') \tag{2.12}$$

$$G^{\mathrm{A}}(t,t') = (G^{T} - G^{>})(t,t') = (G^{<} - G^{\bar{T}})(t,t') \tag{2.13}$$

These are, respectively, the lesser, greater, causal, anticausal, retarded and advanced GFs. $\hat{\bar{T}}$ is the anti-time-order operator.

Expanding $\hat{S}_C$ and following the same steps as in equilibrium it is possible to obtain another Dyson-type equation:

$$\tilde{G}(E) = \tilde{g}_0(E) + \tilde{g}_0(E)\tilde{\Sigma}(E)\tilde{G}(E) \tag{2.14}$$

where the different elements are now matrices:

$$\tilde{G} = \begin{pmatrix} G^T & G^< \\ G^> & G^{\bar{T}} \end{pmatrix} \quad \tilde{g} = \begin{pmatrix} g^T & g^< \\ g^> & g^{\bar{T}} \end{pmatrix} \tag{2.15}$$

$$\tilde{\Sigma} = \begin{pmatrix} \Sigma^T & \Sigma^< \\ \Sigma^> & \Sigma^{\bar{T}} \end{pmatrix} \tag{2.16}$$

This can be written in a more compact manner with the help of a unitary transformation:

$$\tilde{G}' = \begin{pmatrix} 0 & G^{\mathrm{A}} \\ G^{\mathrm{R}} & G^{\mathrm{K}} \end{pmatrix} \tag{2.17}$$

$$\tilde{\Sigma}' = \begin{pmatrix} \Omega & \Sigma^{\mathrm{R}} \\ \Sigma^{\mathrm{A}} & 0 \end{pmatrix} \tag{2.18}$$

where $G^{\mathrm{K}} = G^T + G^{\bar{T}} = G^< + G^> = -i \left\langle \hat{\Psi}_H \left| [\hat{C}_H(t), \hat{C}_H^\dagger(t')] \right| \hat{\Psi}_H \right\rangle$ is the Keldysh GF and $\Omega = \Sigma^T + \Sigma^{\bar{T}} = \Sigma^< + \Sigma^>$. One obtains then tree GFs, although only two of them are linearly independent (G^{K} and G^{A} or G^{R}). From this expression it is easy to demonstrate that the retarded and the advanced GFs verify two separated Dyson's equations:

$$G^{\mathrm{R/A}}(E) = g_0^{\mathrm{R/A}}(E) + g_0^{\mathrm{R/A}}(E)\Sigma^{\mathrm{R/A}}(E)G^{\mathrm{R/A}}(E) \tag{2.19}$$

Furthermore, following the same notation it is also possible to obtain another equation,

$$G^{</>} = (1 + G^{\mathrm{R}}\Sigma^{\mathrm{R}})g^{</>}(1 + \Sigma^{\mathrm{A}}G^{\mathrm{A}}) - G^{\mathrm{R}}\Sigma^{</>}G^{\mathrm{A}} = \tag{2.20}$$

$$= G^{\mathrm{R}}(g^{\mathrm{R}\,-1}g^{</>}g^{\mathrm{A}\,-1} - \Sigma^{</>})G^{\mathrm{A}} \tag{2.21}$$

This allows to express the out-of-equilibrium lesser and greater GFs in terms of the retarded and advanced GFs.

Finally, in the limit of equilibrium

$$G^<(E) = iA(E)f(E) \tag{2.22}$$

$$G^>(E) = iA(E)[f(E) - 1] \tag{2.23}$$

where $f(E) = f(E - \varepsilon_{\mathrm{F}})$ is the Fermi distribution function and $A(E) = i[G^{\mathrm{R}}(E) - G^{\mathrm{A}}(E)]$ is known as the spectral function.

2.1.2 Simple model

As a first step to understand the implementation of the Keldysh formalism I consider a very simple model which describes two semi-infinite leads and a scattering region made of only one site:

$$\begin{aligned}\hat{\mathcal{H}} = &\sum_i \epsilon_0 \hat{n}_i + \sum_{i\neq j} t_{ji}\hat{c}_i^\dagger \hat{c}_j + \\ &+ E_0\hat{n}_0 + T(\hat{c}_1^\dagger\hat{c}_0 + \hat{c}_0^\dagger\hat{c}_1) + T'(\hat{c}_0^\dagger\hat{c}_{1'} + \hat{c}_{1'}^\dagger\hat{c}_0) + \\ &+ \sum_{i'} \epsilon_0'\hat{n}_i' + \sum_{i'\neq j'} t'_{j'i'}\hat{c}_{i'}^\dagger\hat{c}_{j'}\end{aligned} \tag{2.24}$$

where $\{i,j\}/\{i',j'\}$ belong to the left/right lead, respectively. To obtain the total GF of the system (and from it the density and the current) I follow the partitioned scheme of Caroli *et al.* [71, 72, 73]:

1. Consider first the isolated leads and the scattering region. Obtain the retarded and/or advanced surface GFs of the leads, $g_{11}^{\mathrm{R/A}}$ and $g_{1'1'}^{\mathrm{R/A}}$, which in this case can be calculated analytically [74] ($g_{11}^{s,\mathrm{R/A}}(E) = \left(E \pm i\delta - \varepsilon_0 - \sqrt{(E\pm i\delta-\varepsilon_0)-4t^2}\right)/2t^2$), and the GF of the scattering region, $g_{00}^{\mathrm{R/A}}(E) = (E \pm i\delta - E_{00})^{-1}$. The plus (minus) sign is used for the retarded (advanced) GF.

2. Bring together adiabatically the leads and the scattering region. In equilibrium use Dyson's equation, $G = g + g\Sigma G$, to obtain the retarded and/or advanced GFs of the system:

$$G_{00}^{\mathrm{R/A}} = \frac{g_{00}^{\mathrm{R/A}}}{1 - g_{00}^{\mathrm{R/A}}T^* g_{11}^{\mathrm{R/A}} T - g_{00}^{\mathrm{R/A}} T' g_{1'1'}^{\mathrm{R/A}} T'^*} \tag{2.25}$$

$$G_{10}^{\mathrm{R/A}} = g_{11}^{\mathrm{R/A}} T G_{00}^{\mathrm{R/A}} \tag{2.26}$$

$$G_{01'}^{\mathrm{R/A}} = G_{00}^{\mathrm{R/A}} T' g_{1'1'}^{\mathrm{R/A}} \tag{2.27}$$

$$G_{11}^{\mathrm{R/A}} = g_{11}^{\mathrm{R/A}}(1 + TG_{01}^{\mathrm{R/A}}) \tag{2.28}$$

From this, evaluate the lesser GF as

$$G_{00}^{<}(E) = [G_{00}^{\mathrm{A}}(E) - G_{00}^{\mathrm{R}}(E)]f(E-\mu) \tag{2.29}$$

or, equivalently,

$$G^{<}_{00}(E) = -2i\mathrm{Im}\left[G^{\mathrm{R}}_{00}(E)\right]f(E-\mu) \tag{2.30}$$

where f is the Fermi distribution function and μ is the chemical potential, which in this case (zero temperature) is equal to the Fermi energy.

3. Out of equilibrium use Keldysh formalism to obtain the corresponding Dyson's equation for $G^{<}$:

$$G^{<} = (1+G^{\mathrm{R}}\Sigma^{\mathrm{R}})g^{<}(1+\Sigma^{\mathrm{A}}G^{\mathrm{A}}) - \underbrace{g^{\mathrm{R}}\Sigma^{<}g^{\mathrm{A}}}_{0} \tag{2.31}$$

The last term vanishes because it contains many-body contributions which do not exist in a single-particle Hamiltonian. From this it is trivial to obtain

$$\begin{aligned} G^{<}_{00} &= G^{\mathrm{R}}_{01}\tilde{\Sigma}_1 G^{\mathrm{A}}_{10} + G^{\mathrm{R}}_{01'}\tilde{\Sigma}_{1'}G^{\mathrm{A}}_{1'0} + G^{\mathrm{R}}_{00}\tilde{\Sigma}_0 G^{\mathrm{A}}_{00} \\ G^{<}_{10} &= G^{\mathrm{R}}_{10}\tilde{\Sigma}_0 G^{\mathrm{A}}_{00} + G^{\mathrm{R}}_{11}\tilde{\Sigma}_1 G^{\mathrm{A}}_{10} \\ G^{<}_{01'} &= G^{\mathrm{R}}_{01'}\tilde{\Sigma}_{1'}G^{\mathrm{A}}_{1'1'} + G^{\mathrm{R}}_{00}\tilde{\Sigma}_0 G^{\mathrm{A}}_{01'} \end{aligned} \tag{2.32}$$

where $\tilde{\Sigma}_{\mathrm{L(R)}} = g^{\mathrm{R}\,-1}_{\mathrm{LL(RR)}}g^{<}_{\mathrm{LL(RR)}}g^{\mathrm{A}\,-1}_{\mathrm{LL(RR)}}$ and the bias $\Delta V = V_{\mathrm{R}} - V_{\mathrm{L}}$ enters in $\tilde{\Sigma}_1(E - eV_{\mathrm{L}})$ and $\tilde{\Sigma}_{1'}(E - eV_{\mathrm{R}})$ and in the corresponding Fermi functions as $\mu_{\mathrm{L(R)}} = \varepsilon_{\mathrm{F}} + eV_{\mathrm{L(R)}}$.

4. Calculate the density matrix as

$$\rho_{ij} = \left\langle c^{\dagger}_i c_j \right\rangle = \frac{1}{2\pi i}\int_{-\infty}^{\infty} G^{<}_{ij}(E)\mathrm{d}E \tag{2.33}$$

5. Obtain the current using the continuity equation:

$$J_i - J_k + e\frac{\partial \rho_k}{\partial t} = 0 \tag{2.34}$$

where the i (k) is the immediately previous (next) site to j. Taking into account that $\dot{\rho}_k = -i/\hbar[\rho_k, \mathcal{H}]$, the current at a given site is given by:

$$\begin{aligned} J_i &= -i\frac{e}{\hbar}\left(t_{i,i-1}\left\langle c^{\dagger}_{i-i}c_i\right\rangle - t_{i-1,i}\left\langle c^{\dagger}_i c_{i-1}\right\rangle\right) = \\ &= \frac{et}{2\pi\hbar}\int_{-\infty}^{\infty}\left[G^{<}_{i-1,i}(E) - G^{<}_{i,i-1}(E)\right]\mathrm{d}E \end{aligned} \tag{2.35}$$

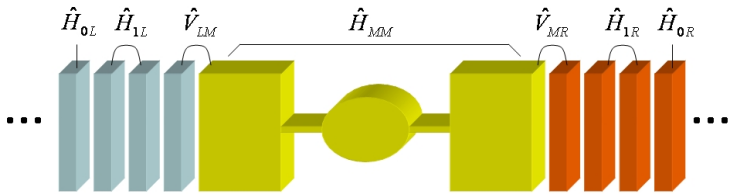

Fig. 2.2: Schematic view of the scattering region (the extended molecule) and the left and right leads.

This example can be generalized to the case of non-orthogonal basis sets, i. e. with overlap matrix elements given by $S_{ij} = \langle i|j\rangle$. With the help of bi-orthogonal basis sets , i. e. $|\underline{j}\rangle = \sum_l (S^{-1})_{lj}\,|l\rangle$ so that $\langle i|\underline{j}\rangle = \delta_i^j$, it is easy to arrive at the following equation for the GF: $(ES - \mathcal{H})\underline{G} = 1$, where $\underline{G}$ is expressed in the $\{|\underline{i}\rangle\}$ basis set, although its matrix elements are the same as those calculated in the original basis.

This simple model helps to understand the implementation of the Keldysh formalism and can be taken as a first step to study more complex systems. In fact, its formulae are very general and can be applied almost without changes to more realistic situations, as I will show in the next section.

2.1.3 General one-body problem

The above discussion can be easily generalized to more complex systems by substituting scalars with matrices. The scatterer, also called the extended molecule (M), can be a constriction, a molecule, an atomic chain, etc., and includes also those parts of the leads (L and R) whose electronic properties differ from the bulk properties, as shown in figure (2.2). Each of such regions should be larger than the screening length of the corresponding lead to make sure the Hamiltonian at the end is equal to the bulk Hamiltonian.

Surface Green's function

The surface GF, which describes the electronic structure at the end of a perfect semi-infinite lead, can be calculated from the bulk GF of an infinite system grown along the transport direction [75]. Such a system is divided in slices characterized by intraatomic $M \times M$ Hamiltonian $\hat{\mathcal{H}}_0$ and overlap matrix $\hat{S}_0$ and coupled to first nearest neighbors by $\hat{\mathcal{H}}_{\pm 1}$ and $\hat{S}_{\pm 1}$. To calculate the bulk GF [75] it is necessary to obtain M wave vectors $k_{z,l}$, for positive directions, and M wave vectors $\bar{k}_{z,l}$, for negative directions, and their corresponding eigenvectors $\Psi_{k_{z,l}}$ which for a given value of the energy E satisfy the equation

$$(\hat{\mathcal{H}}_0 + \hat{\mathcal{H}}_1 e^{ika} + \hat{\mathcal{H}}_{-1} e^{-ika} - E\hat{S})\hat{\Psi}_{k_{z,l}} = 0 \tag{2.36}$$

where z is the transport direction, a is the distance between slices and $l = 1, ..., M$ are the degrees of freedom of each slice.

Once the bulk GF has been found, the total GF of a semi-infinite lead, ranging from $z = -\infty$ to $z = z_0$, is constructed by subtracting a certain wave function (built with the previous eigenvalues and eigenvectors) which cancels out the bulk GF at the site $z_0 + 1$. The surface GF is then obtained by evaluating this GF at z_0.

Although this procedure is much better than recursive methods (see e. g. [76]), which are usually very hard to converge, it has the problem that in many situations the matrix $\hat{\mathcal{H}}_1$, which has to be inverted to find the eigenvectors, is singular. This difficulty, however, can be overcome by decimating out [77] the singularities and using an effective Hamiltonian whose connecting elements $\hat{\mathcal{H}}_{\pm 1}$ are not singular [57].

Equilibrium

If the system is not coupled the relevant retarded and advanced GFs are the surface GFs, $\hat{g}^{A/R}_{\mathrm{LL}}(Z)$ and $\hat{g}^{A/R}_{\mathrm{RR}}(Z)$ and the isolated scatterer or extended molecule GF, $\hat{g}^{A/R}_{\mathrm{MM}}(Z) = (Z^{A/R}\hat{S}_{\mathrm{MM}} - \hat{\mathcal{H}}_{\mathrm{MM}})^{-1}$, where $Z^{A/R} = E \pm i\delta$ ($+/-$ for retarded/advanced quantities). When the leads and the scatterer are brought together adiabatically, following the same steps as in the previous case, the MM and LM retarded GFs are found to be [78]:

$$\begin{aligned}
\hat{G}^{\mathrm{R}}_{\mathrm{MM}}(Z) &= \hat{g}^{\mathrm{R}}_{\mathrm{MM}}(Z)[\hat{1} - \hat{g}^{\mathrm{R}}_{\mathrm{MM}}(Z)\hat{V}^{\mathrm{R}}_{\mathrm{ML}}(Z)\hat{g}^{\mathrm{R}}_{\mathrm{LL}}(Z)\hat{V}^{\mathrm{R}}_{\mathrm{LM}}(Z) + \\
&\quad - \hat{g}^{\mathrm{R}}_{\mathrm{MM}}(Z)\hat{V}_{\mathrm{MR}}(Z)\hat{g}^{\mathrm{R}}_{\mathrm{RR}}(Z)\hat{V}_{\mathrm{RM}}(Z)]^{-1} = \\
&= [\hat{g}^{\mathrm{R}\,-1}_{\mathrm{MM}}(Z) - \hat{\Sigma}^{\mathrm{R}}_{\mathrm{L}}(Z) - \hat{\Sigma}^{\mathrm{R}}_{\mathrm{R}}(Z)]^{-1} = \\
&= [Z^R\hat{S}_{\mathrm{MM}} - \mathcal{H}_{\mathrm{MM}} - \hat{\Sigma}^{\mathrm{R}}_{\mathrm{R}}(Z) - \hat{\Sigma}^{\mathrm{R}}_{\mathrm{L}}(Z)]^{-1} \qquad (2.37) \\
\hat{G}^{\mathrm{R}}_{\mathrm{LM}}(Z) &= \hat{g}^{\mathrm{R}}_{\mathrm{LL}}(Z)\hat{V}^{\mathrm{R}}_{\mathrm{LM}}(Z)\hat{G}^{\mathrm{R}}_{\mathrm{MM}}(Z) = \hat{V}^{\mathrm{R}\,-1}_{\mathrm{ML}}(Z)\hat{\Sigma}^{\mathrm{R}}_{\mathrm{L}}(Z)\hat{G}^{\mathrm{R}}_{\mathrm{MM}}(Z) \qquad (2.38)
\end{aligned}$$

where $\hat{V}_{MR(L)/R(L)M}(Z) = Z\hat{S}_{MR(L)/R(L)M} - \hat{\mathcal{H}}_{MR(L)/R(L)M}$, and $\hat{\Sigma}^{\mathrm{R}}_{\mathrm{L(R)}} = \hat{V}^{\mathrm{R}}_{\mathrm{ML(R)}}\hat{g}^{\mathrm{R}}_{\mathrm{LL(RR)}}\hat{V}^{\mathrm{R}}_{\mathrm{L(R)M}}$ are the selfenergies, which include the coupling to the electrodes. These quantities are not Hermitian, which means that the number of electrons in the system is not conserved.

The MM GF matrix elements are given then by the following expression:

$$\hat{G}^{\mathrm{R}}_{\mathrm{MM},\mu\nu}(Z) = [Z\hat{S}_{\mathrm{MM}} - \hat{\mathcal{H}}_{\mathrm{MM}} - \hat{\Sigma}^{\mathrm{R}}_{\mathrm{L}}(Z) - \hat{\Sigma}^{\mathrm{R}}_{\mathrm{R}}(Z)]^{-1}_{\mu\nu} \tag{2.39}$$

and the density matrix elements:

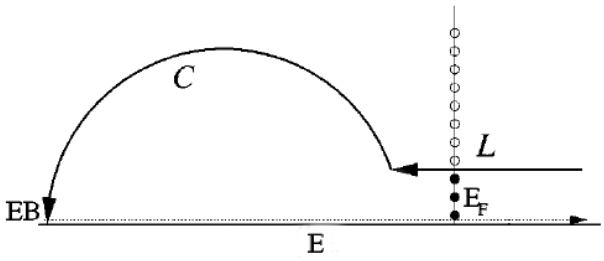

Fig. 2.3: The contour $L + C$ used to evaluated the density matrix. Figure from [56] (modified).

$$\hat{\rho}_{\mathrm{MM},\mu\nu} = \frac{-1}{\pi}\int_{-\infty}^{\infty} \lim_{\delta\to 0} \mathrm{Im}\,[\hat{G}_{\mathrm{MM},\mu\nu}(E+i\delta)] f(E-\varepsilon_{\mathrm{F}})\mathrm{d}E = \\ = \frac{1}{2\pi}\int_{-\infty}^{\infty} \hat{G}^{<}_{\mathrm{MM},\mu\nu}(E)\mathrm{d}E \tag{2.40}$$

The numerical integration on a contour close to the real axis can be very hard to evaluate due to the presence of the GF poles, which forces the inclusion of many integration points. However, such an integration can be greatly simplified if one realizes the following [56]: i) the relevant energy range goes from the lowest energy state to a bit above the Fermi energy, where the Fermi distribution function vanishes, ii) the GF is analytic on the upper half plane. Taking this into account, the previous integration contour can be then substituted by the contour shown in figure (2.3), which also includes the Fermi function poles located in a line perpendicular to the real axis at $E = \varepsilon_{\mathrm{F}}$, where $f(Z-\varepsilon_{\mathrm{F}}) \approx -k_{\mathrm{B}}T/(Z-Z_n)$ and $Z_n = i(2n+1)\pi k_{\mathrm{B}}T + \varepsilon_{\mathrm{F}}$ is one of the Fermi poles. The calculation of the density matrix reduces then to:

$$\hat{\rho}_{\mathrm{MM},\mu\nu} = -\frac{1}{\pi}\int_{C+L} \mathrm{Im}\,[\hat{G}_{\mathrm{MM},\mu\nu}(Z)] f(Z-\varepsilon_{\mathrm{F}})\mathrm{d}Z - 2\pi i k_{\mathrm{B}}T \sum_{n=1}^{N_p} \hat{G}_{\mathrm{MM},\mu\nu}(Z_n) \tag{2.41}$$

where N_p is the number of Fermi poles inside the contour. This trick reduces dramatically the number of integration points and, therefore, the computer execution time and memory.

Finally, note that in equilibrium and in an isolated system $\hat{G}^{\mathrm{R}}$ can also be obtained from the eigenvectors and eigenvalues of $\hat{\mathcal{H}}$, i. e. $\hat{G}^{\mathrm{R}}_{\mu\nu}(E) = \sum_n c_{n\mu}c^*_{n\nu}/(E+i\delta-\varepsilon_n)$, and therefore the density matrix can equally be found by directly diagonalizing the Hamiltonian (as was shown in the first chapter), i. e. $\hat{\rho}_{\mu\nu} = \sum_n c_{n\mu}c^*_{n\nu} f(\varepsilon_n - \varepsilon_{\mathrm{F}})$.

Out of equilibrium

Out of equilibrium, when a bias difference $\Delta V = V_{\mathrm{L}} - V_{\mathrm{R}}$ is applied, the expression for the lesser MM GF has the following form:

$$\hat{G}^{<}_{\mathrm{MM}} = \hat{G}^{\mathrm{R}}_{\mathrm{ML}}\hat{\tilde{\Sigma}}_{\mathrm{L}}\hat{G}^{\mathrm{A}}_{\mathrm{LM}} + \hat{G}^{\mathrm{R}}_{\mathrm{MR}}\hat{\tilde{\Sigma}}_{\mathrm{R}}\hat{G}^{\mathrm{A}}_{\mathrm{RM}} + \hat{G}^{\mathrm{R}}_{\mathrm{MM}}\hat{\tilde{\Sigma}}_{\mathrm{M}}\hat{G}^{\mathrm{A}}_{\mathrm{MM}} \tag{2.42}$$

The last term does not contribute to the density matrix when the system is coupled (when it is uncoupled it is simply equal to $\hat{g}^{<}_{\mathrm{MM}}$ and gives the density matrix) due to the fact that

$$\begin{aligned}[\hat{G}^{\mathrm{R}}_{\mathrm{MM}}\hat{\tilde{\Sigma}}_{\mathrm{M}}\hat{G}^{\mathrm{A}}_{\mathrm{MM}}](Z) = [\hat{G}^{\mathrm{R}}_{\mathrm{MM}}\hat{g}^{\mathrm{R}\,-1}_{\mathrm{MM}}\hat{g}^{<}_{\mathrm{MM}}\hat{g}^{\mathrm{A}\,-1}_{\mathrm{MM}}\hat{G}^{\mathrm{A}}_{\mathrm{MM}}](Z) \sim \\ \sim \hat{G}^{\mathrm{R}}_{\mathrm{MM}}\,(Z-\varepsilon_{\mathrm{MM}})\hat{\delta}(Z-\varepsilon_{\mathrm{MM}})(Z-\varepsilon_{\mathrm{MM}})\hat{G}^{\mathrm{A}}_{\mathrm{MM}}\end{aligned} \tag{2.43}$$

This expression vanishes when it is integrated in energies. Only two terms remain then, each of which can be written in the following way (I focus on the first one):

$$\begin{aligned}\hat{G}^{\mathrm{R}}_{\mathrm{ML}}\hat{\tilde{\Sigma}}_{\mathrm{L}}\hat{G}^{\mathrm{A}}_{\mathrm{LM}} &= \hat{G}^{\mathrm{R}}_{\mathrm{MM}}\hat{V}^{\mathrm{R}}_{\mathrm{ML}}\hat{g}^{\mathrm{R}}_{\mathrm{LL}}\hat{g}^{\mathrm{R}\,-1}_{\mathrm{LL}}\hat{g}^{<}_{\mathrm{LL}}\hat{g}^{\mathrm{A}\,-1}_{\mathrm{LL}}\hat{g}^{\mathrm{A}}_{\mathrm{LL}}\hat{V}^{\mathrm{A}}_{\mathrm{LM}}\hat{G}^{\mathrm{A}}_{\mathrm{MM}} = \\ &= \hat{G}^{\mathrm{R}}_{\mathrm{MM}}\hat{\Sigma}^{<}_{\mathrm{L}}\hat{G}^{\mathrm{A}}_{\mathrm{MM}}\end{aligned} \tag{2.44}$$

where $\hat{\Sigma}^{<}_{\mathrm{L}} \equiv \hat{\Sigma}^{<}_{\mathrm{L}}(Z - eV_{\mathrm{L}})$ is given by

$$\begin{aligned}\hat{\Sigma}^{<}_{\mathrm{L}} &= [\hat{V}^{\mathrm{R}}_{\mathrm{ML}}\hat{g}^{<}_{\mathrm{LL}}\hat{V}^{\mathrm{A}}_{\mathrm{LM}}] = i[\hat{V}^{\mathrm{R}}_{\mathrm{ML}}\hat{g}^{\mathrm{R}}_{\mathrm{LL}}\hat{V}^{\mathrm{A}}_{\mathrm{LM}} - \hat{V}^{\mathrm{R}}_{\mathrm{ML}}\hat{g}^{\mathrm{A}}_{\mathrm{LL}}\hat{V}^{\mathrm{A}}_{\mathrm{LM}}]f_{\mathrm{L}} = \\ &= i[\hat{\Sigma}^{\mathrm{R}}_{\mathrm{L}} - \hat{\Sigma}^{\mathrm{A}}_{\mathrm{L}}]f_{\mathrm{L}} = \hat{\Gamma}_{\mathrm{L}}f_{\mathrm{L}}\end{aligned} \tag{2.45}$$

with $f_{\mathrm{L}} = f(Z - \mu_{\mathrm{L}})$, $\mu_{\mathrm{L}} = \varepsilon_{\mathrm{F}} + eV_{\mathrm{L}}$ and $\hat{\Gamma} = i(\hat{\Sigma}^{\mathrm{R}} - \hat{\Sigma}^{\mathrm{A}})$ is the coupling matrix, which represents the coupling strength and the level broadening. Finally, using the left and the right terms [78]

$$\hat{G}^{<}_{\mathrm{MM}}(Z) = i\hat{G}^{\mathrm{R}}_{\mathrm{MM}}(Z)[\hat{\Gamma}_{\mathrm{L}}(Z - eV_{\mathrm{L}})f(Z - \mu_{\mathrm{L}}) + \hat{\Gamma}_{\mathrm{R}}(Z - eV_{\mathrm{R}})f(Z - \mu_{\mathrm{R}})]\hat{G}^{\mathrm{A}}_{\mathrm{MM}}(Z) \tag{2.46}$$

which reduces to the equilibrium $\hat{G}^{<}_{\mathrm{MM}}$, $\hat{G}^{<}_{\mathrm{MM,eq}}$, when $\Delta V = 0$. Out of equilibrium, however, it can be rearranged in the following way:

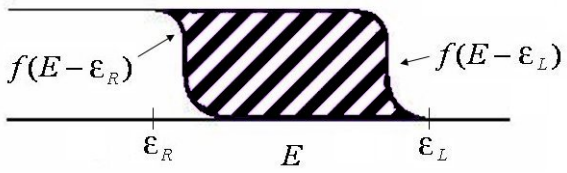

Fig. 2.4: Integration region of the out-of-equilibrium part of the density matrix.

$$\begin{aligned}\hat{G}^{<}_{\mathrm{MM}}(Z) &= \hat{G}^{<}_{\mathrm{MM,eq,L}}(Z) + i\hat{G}^{\mathrm{R}}_{\mathrm{MM}}\hat{\Gamma}_{\mathrm{R}}(Z-eV_{\mathrm{R}})\hat{G}^{\mathrm{A}}_{\mathrm{MM}}(Z)[f(Z-\mu_{\mathrm{R}})-f(Z-\mu_{\mathrm{L}})] = \\ &= \hat{G}^{<}_{\mathrm{MM,eq,L}}(Z) + \delta\hat{G}^{<}_{\mathrm{MM}}(Z) \end{aligned} \tag{2.47}$$

where $\hat{G}_{\mathrm{MM,eq,L}} = i\hat{G}^{\mathrm{R}}_{\mathrm{MM}}(\Gamma_{\mathrm{L}}+\Gamma_{\mathrm{R}})\hat{G}^{\mathrm{A}}_{\mathrm{MM}}f_{\mathrm{L}}$. A similar equation can be written using $\hat{G}_{\mathrm{MM,eq,R}}$ and $\hat{\Gamma}_{\mathrm{L}}$. The equilibrium term, which is analytic in the upper half complex plane, is integrated using the previously defined contour. The second term, however, is not in general analytic and has to be integrated directly on the real axis. However, due to the fact that the Fermi functions differ only in a region $\varepsilon_{\mathrm{L}} - \varepsilon_{\mathrm{R}} = e\Delta V + 2k_{\mathrm{B}}T$ (see figure (2.4)), this integration reduces to:

$$\delta\hat{\rho}_{\mathrm{MM}} = \frac{1}{2\pi i}\int_{\varepsilon_{\mathrm{R}}}^{\varepsilon_{\mathrm{L}}} \delta\hat{G}^{<}_{\mathrm{MM}}(E)\mathrm{d}E \tag{2.48}$$

The current that passes through the system from left to right, $I_{\mathrm{LM}} = -I_{\mathrm{ML}}$, can be calculated as follows [78]:

$$\begin{aligned} I_{\mathrm{LM}}(V) &= \frac{ie}{\hbar}\sum_{\mu,\nu}[\hat{\rho}_{\mathrm{ML},\nu\mu}(V)\hat{V}_{\mathrm{LM},\mu\nu} - \hat{V}_{\mathrm{ML},\mu\nu}\hat{\rho}_{\mathrm{LM},\nu\mu}(V)] = \\ &= \frac{e}{h}\sum_{\mu\nu}\int[\hat{G}^{<}_{\mathrm{ML},\nu\mu}(V)\hat{V}_{\mathrm{LM},\mu\nu} - \hat{V}_{\mathrm{ML},\mu\nu}\hat{G}^{<}_{\mathrm{LM},\nu\mu}(V)](Z)\mathrm{d}Z = \\ &= \frac{e}{h}\int \mathrm{Tr}[\hat{G}^{<}_{\mathrm{ML}}(V)\hat{V}_{\mathrm{LM}} - \hat{V}_{\mathrm{ML}}\hat{G}^{<}_{\mathrm{LM}}(V)](Z)\mathrm{d}Z \end{aligned} \tag{2.49}$$

The relevant matrices in this case are LM and ML due to the fact that the current is calculated between two points.

The GF is expressed as

$$\hat{G}^{<}_{\mathrm{LM}} = \hat{G}^{\mathrm{R}}_{\mathrm{LM}}\hat{\tilde{\Sigma}}_{\mathrm{M}}\hat{G}^{\mathrm{A}}_{\mathrm{MM}} + \hat{G}^{\mathrm{R}}_{\mathrm{LL}}\hat{\tilde{\Sigma}}_{\mathrm{L}}G^{\mathrm{A}}_{\mathrm{LM}} \tag{2.50}$$

where the first term does not contribute again. Therefore

$$\hat{G}^{<}_{\mathrm{LM}} = \hat{g}^{<}_{\mathrm{LL}}\hat{V}^{\mathrm{A}}_{\mathrm{LM}}\hat{g}^{\mathrm{A}}_{\mathrm{MM}} + \hat{g}^{\mathrm{R}}_{\mathrm{LL}}\hat{V}^{\mathrm{R}}_{\mathrm{LM}}\hat{G}^{\mathrm{R}}_{\mathrm{ML}}\hat{\tilde{\Sigma}}_{\mathrm{LL}}\hat{G}^{\mathrm{A}}_{\mathrm{LM}} \tag{2.51}$$

Equivalently,

$$\hat{G}^{<}_{\mathrm{ML}} = \hat{G}^{\mathrm{R}}_{\mathrm{MM}}\hat{V}^{\mathrm{R}}_{\mathrm{ML}}\hat{g}^{<}_{\mathrm{LL}} + \hat{G}^{\mathrm{R}}_{\mathrm{ML}}\hat{\tilde{\Sigma}}_{\mathrm{LL}}\hat{G}^{\mathrm{A}}_{\mathrm{LM}}\hat{V}^{\mathrm{A}}_{\mathrm{ML}}\hat{g}^{\mathrm{A}}_{\mathrm{LL}} \tag{2.52}$$

so that,

$$\begin{aligned}\hat{G}^{<}_{\mathrm{ML}}\hat{V}_{\mathrm{LM}} - \hat{V}_{\mathrm{ML}}\hat{G}^{<}_{\mathrm{LM}} = {} & \hat{G}^{\mathrm{R}}_{\mathrm{MM}}\hat{\Gamma}_{\mathrm{L}}f_{\mathrm{L}} - \hat{G}^{\mathrm{R}}_{\mathrm{MM}}\hat{\Gamma}_{\mathrm{L}}\hat{G}^{\mathrm{A}}_{\mathrm{MM}}\hat{V}^{\mathrm{A}}_{\mathrm{ML}}\hat{g}^{\mathrm{A}}_{\mathrm{LL}}\hat{V}^{\mathrm{R}}_{\mathrm{LM}}f_{\mathrm{L}} + \\ & - \hat{\Gamma}_{\mathrm{L}}\hat{G}^{\mathrm{A}}_{\mathrm{MM}}f_{\mathrm{L}} + \hat{V}^{\mathrm{R}}_{\mathrm{ML}}\hat{g}^{\mathrm{R}}_{\mathrm{LL}}\hat{V}^{\mathrm{A}}_{\mathrm{LM}}\hat{G}^{\mathrm{R}}_{\mathrm{MM}}\hat{\Gamma}_{\mathrm{L}}\hat{G}^{\mathrm{A}}_{\mathrm{MM}}f_{\mathrm{L}}\end{aligned} \tag{2.53}$$

Since the current must be the same at every point in a stationary system it is possible symmetrize the above equation using $I_{\mathrm{LM}} = -I_{\mathrm{RM}}$ [79]:

$$\begin{aligned}I(V) = \frac{1}{2}[I_{\mathrm{LM}} - I_{\mathrm{RM}}](V) = \frac{e}{2h}\int \mathrm{Tr}[(\hat{\Gamma}_{\mathrm{L}}f_{\mathrm{L}} - \hat{\Gamma}_{\mathrm{R}}f_{\mathrm{R}})(\hat{G}^{\mathrm{R}}_{\mathrm{MM}} - \hat{G}^{\mathrm{A}}_{\mathrm{MM}}) + \\ + i(\hat{\Gamma}_{\mathrm{L}} - \hat{\Gamma}_{\mathrm{R}})\hat{G}^{<}_{\mathrm{MM}}](Z,V)\mathrm{d}Z\end{aligned} \tag{2.54}$$

where the cyclic property of the trace has been used. Taking into account now Dyson's equations for $\hat{G}^{<}_{\mathrm{MM}}$ in and out equilibrium and also that the final quantity is not analytic and has to be integrated also in the real axis between ε_{R} and ε_{L}, the result is

$$I(V) = \frac{e}{h}\int_{\varepsilon_{\mathrm{R}}}^{\varepsilon_{\mathrm{L}}} \mathrm{Tr}[\hat{G}^{\mathrm{A}}_{\mathrm{MM}}\hat{\Gamma}_{\mathrm{R}}\hat{G}^{\mathrm{R}}_{\mathrm{MM}}\hat{\Gamma}_{\mathrm{L}}](E,V)[f(E-\mu_{\mathrm{L}}(V)) - f(E-\mu_{\mathrm{R}}(V))]\mathrm{d}E \tag{2.55}$$

which can be rewritten as

$$I(V) = \frac{e}{h}\int_{\varepsilon_{\mathrm{R}}}^{\varepsilon_{\mathrm{L}}} \mathrm{Tr}[\hat{t}^{\dagger}\hat{t}](E,V)[f(E-\mu_{\mathrm{L}}(V)) - f(E-\mu_{\mathrm{R}}(V))]\mathrm{d}E = \tag{2.56}$$

$$= \frac{e}{h}\int_{\varepsilon_{\mathrm{R}}}^{\varepsilon_{\mathrm{L}}} T(E,V)[f(E-\mu_{\mathrm{L}}(V)) - f(E-\mu_{\mathrm{R}}(V))]\mathrm{d}E \tag{2.57}$$

where $\hat{t}(E,V) = [\hat{\Gamma}_{\mathrm{R}}(E,V)]^{1/2}\hat{G}^{\mathrm{R}}_{\mathrm{MM}}(E,V)[\hat{\Gamma}_{\mathrm{L}}(E,V)]^{1/2}$ is the transmission amplitude matrix [80] and $T(E,V)$ the total transmission. The conductance in the linear response regime, $G = I/V$, is then given by [56]

$$G(V) = \frac{G_0}{2V} \int_{\varepsilon_R}^{\varepsilon_L} T(E,V)[f(E-\mu_L(V)) - f(E-\mu_R(V))]\mathrm{d}E \tag{2.58}$$

where $G_0 = 2e^2/h$ is the conductance quantum (note that the trace over spin components is also included here, so that for spin unpolarized cases both spin channels cancel out the 2 in the denominator of the previous equation). This expression can be simplified to

$$G = \frac{G_0}{2} T(E_F, 0) \tag{2.59}$$

when very small biases are applied.

2.2 The SMEAGOL Code

SMEAGOL [57] is composed of a series of subroutines which read the SIESTA Hamiltonian and overlap matrices and construct the GF using the non-equilibrium Green's function formalism. From the GF, SMEAGOL calculates the density matrix, which is fed back into SIESTA to build again the Hamiltonian and continue the self-consistent (SCF) procedure. When the electronic and the molecular dynamics calculations have converged, SMEAGOL obtains the transmission coefficients and the current.

Every transport simulation is partitioned according to the scheme of Caroli *et al.* [71, 72, 73], i. e. the system is divided in three parts, which are supposed to be isolated in the remote past: two semi-infinite leads and the extended molecule. Every SMEAGOL calculation is then divided in two separated simulations: one or two to obtain the bulk electronic structure of the leads and another one to calculate the transport properties of the extended molecule.

2.2.1 Bulk simulation

Previous to the transport simulation it is necessary to obtain the leads Hamiltonians $\hat{\mathcal{H}}_0$ and $\hat{\mathcal{H}}_1$, and overlap matrices, $\hat{S}_0$ and $\hat{S}_1$, which are used to calculate the surface GF and the selfenergies, in one or two separate ab initio simulations. Each lead is grown periodically along the z direction and only interactions between first nearest unit cells along z are permitted. If this condition is not fulfilled then either the cutoff radii have to be reduced or the size of the unit cell along z increased.

On the perpendicular directions, x and y, the system can also be periodic and include k points. If there is, however, large enough space and the unit cells along x and y do not

interact, the system is not periodic and the simulation describes a nanowire. Mixed cases, where periodicity is allowed along a certain vector $\vec{u} = a\vec{e}_x + b\vec{e}_y$ are also permitted.

When the bulk simulation finishes, the Hamiltonians, $\hat{\mathcal{H}}_0$ and $\hat{\mathcal{H}}_1$, and the overlap matrices, $\hat{S}_0$ and $\hat{S}_1$, are written in a separate file, which, along with the density matrix, is used in the transport calculation.

2.2.2 Transport calculations

Since SIESTA can not simulate semi-infinite leads[1], nor calculate out-of-equilibrium density matrices, the eigenvalue decomposition is substituted in the transport simulation by the non-equilibrium Green's functions subroutines which calculate the GF and the density matrix on every SCF step.

At the beginning of the transport calculation SMEAGOL reads the bulk $\hat{\mathcal{H}}_0$, $\hat{\mathcal{H}}_1$ and $\hat{S}_0$, $\hat{S}_1$ and calculates the surface GF. The problems associated with the non-invertibility of some connecting matrices are solved by identifying the singular elements with a singular value decomposition and decimating them out. Once the surface GF is obtained it is not necessary to calculate it again. The same applies to the selfenergies, $\hat{\Sigma}_{\mathrm{L(R)}} = \hat{V}_{\mathrm{ML(R)}}\hat{g}_{\mathrm{LL(RR)}}\hat{V}_{\mathrm{L(R)M}}$. However, when perpendicular k points are included, the surface GFs and, consequently, the selfenergies have to be calculated for every k point. This new variable adds a new dimension to the selfenery arrays and increases dramatically the memory requirements. In such situation it is more advantageous to compute the whole selfenergies on every SCF step rather than storage them.

Out of equilibrium the Fermi energy and the electronic states of the left and right leads are shifted by the applied bias, $\Delta V = V_{\mathrm{L}} - V_{\mathrm{R}}$, which, like in many experimental situations, is applied symmetrically, i. e. $V_{\mathrm{L}} = \Delta V/2$ and $V_{\mathrm{R}} = -\Delta V/2$. Therefore the bulk $\hat{\mathcal{H}}_0$ and $\hat{\mathcal{H}}_1$ and consequently the surface GFs and the selfenergies are rigidly shifted by $e\Delta V/2$.

The potential at the boundaries of the unit cell has a sharp discontinuity due to the fact that the values at these points have to match the bulk values as well. However, since the Hartree potential $V^{\mathrm{H}}(\vec{r})$ is calculated in SIESTA with a fast Fourier transform algorithm, which implies that it is periodic, the potential at such points has to be shifted by the corresponding $\pm\Delta V/2$ (with a linear term in between to help the self-consistent process) after the calculation of V^{H}. The total potential is then

[1] This is not completely true. As shown in Chapter 5, using slabs with a large enough number of layers it is possible to simulate surfaces, provided the electronic structure in the middle of the slab resembles the bulk electronic structure.

$$V^T = V^0 + V', \qquad V' = \begin{cases} \frac{\Delta V}{2} & z \leq z_{\mathrm{L}} \\ \frac{\Delta V}{z_{\mathrm{L}} - z_{\mathrm{R}}}(z - z_{\mathrm{R}}) - \frac{\Delta V}{2} & z_{\mathrm{L}} < z < z_{\mathrm{R}} \\ -\frac{\Delta V}{2} & z \geq z_{\mathrm{R}} \end{cases} \tag{2.60}$$

V_0 is the sum of the pseudopotential, the Hartree and the exchange-correlation potential and z_{L} and z_{R} are the positions on the left and right lead where the linear ramp starts and ends. This ramp can then be different depending on z_{L} and z_{R} but the final results are the same due to the indetermination of the Hartree potential up to a linear term. The only difference appears in the convergence of the SCF procedure, which can be improved or worsened depending on whether the potential on each SCF step resembles the final potential or not. For example, in a capacitor, made of two separated plates the best choice for z_{L} and z_{R} would be as close as possible to the vacuum region. In a continuous medium, however, the best ramp should be as flat as possible, i. e. z_{L} and z_{R} should be close to the boundaries of the unit cells, in order to make the transition from left to right smoother.

To ensure the last slices of the leads (the leftmost atoms in the left lead and the rightmost atoms in the right lead) have the bulk electronic structure and to improve the convergence of the simulation, the Hamiltonians and overlap matrices of these regions are substituted by the bulk matrices. Since this does not warranty that the density matrix in the outermost slices has the same values as the bulk density matrix, this quantity is also substituted. Furthermore, the Hartree potential at these places is also shifted rigidly to match exactly the bulk values (even at zero bias).

The main parameters of the transport calculation which are included in the input file are the following:

- Number of points in circular part, C, of the integration contour used to calculate the density matrix (see figure (2.3))
- Number of points in the linear part, L, of integration contour.
- Number of Fermi poles enclosed by the contour.
- Lowest energy value reached by the contour.
- Small imaginary part used in the GF.
- Number of energy points in the real energy axis used to calculate the out-of-equilibrium density matrix.
- Initial value of the bias potential.
- Final value of the bias potential.

- Number of points between the initial and final value of the bias potential where the current is going to be calculated.

  Apart from the SCF loop and the molecular dynamics loop, there is also a bias loop, which is the outermost one. For every point of the bias potential it is necessary then to converge the density matrix and, if necessary, relax the atoms before the current is calculated.

- Is the system periodic along the transport direction?

  If the system is periodic the electronic structure of the outermost slices can be very similar to the bulk electronic structure and the SCF convergence is better. If the system is not periodic, however, there are surfaces at the boundaries of the unit cell and it is necessary to include more bulk slices to avoid their effect.

- Initial and final energy value and number of energy points where the transmission coefficients are going to be calculated.

In summary, SMEAGOL is a very efficient combination of the Keldysh formalism with DFT and LCAO-pseudopotential methods specially designed to calculate the transport characteristics of systems with small numbers of atoms. Its main advantages are a numerically stable approximation to calculate the surface GF and the possibility of performing spin-polarized and non-collinear spin calculations. I will show two examples of magnetic calculations in the following sections.

2.2.3 Example 1: Giant magnetoresistance in organic molecules between magnetic leads

The first suggestion to use organic molecules as electronic elements had been made by Aviram and Ratner in 1974 [82] but it was not until 1997 that the first measurement of the conductance of organic molecules between non-magnetic electrodes [43] was performed. Since then, a series of theoretical calculations and computer simulations have been carried out (see e. g. [81]). More promising is, however, the case of magnetic leads, where giant magnetoresistance (GMR) effects are expected. Examples include the use of carbon nanotubes as spin valves [83], spin transfer and injection in organic molecules [84, 85, 86] and organic tunnelling junctions [87]. Such molecular systems have the advantage that the effect of the spin orbit coupling and the hyperfine interaction is very small and the spin coherence can be preserved over long distances.

One of the first calculations performed within the SMEAGOL collaboration was done by Alexandre Reily Rocha, who simulated organic molecules anchored between magnetic leads: 8-alkane-dithiolate (octane-dithiolate) and 1,4-3-phenyl-dithiolate (1,4-tricene-dithiolate) sandwiched between nickel leads, as shown in figure (2.5). The obvious

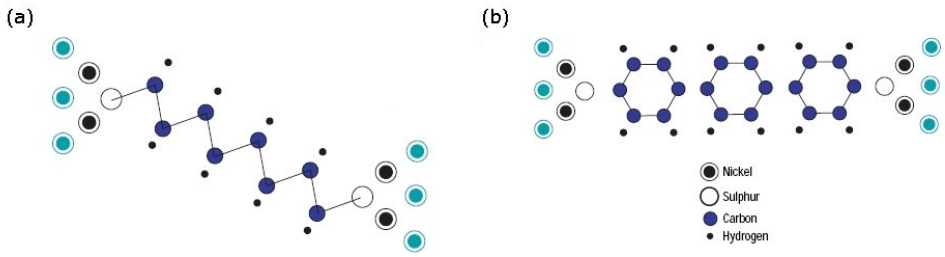

Fig. 2.5: Schematic view of the octane-dithiolate and the 1,4-tricene-dithiolate anchored between Ni leads.

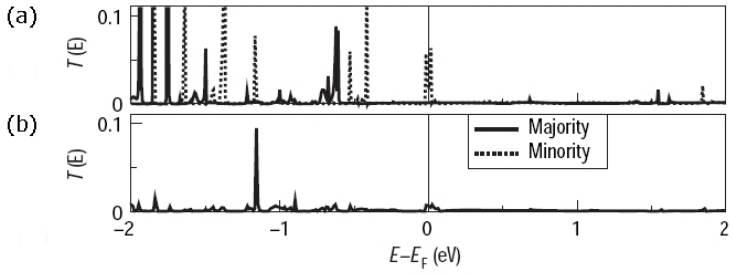

Fig. 2.6: Transmission coefficients of a Ni(001)/octane/Ni(001) spin valve in (a) the parallel and (b) antiparallel configurations. In the antiparallel case both transmission coefficients are identical.

goal was to look for possible magnetoresistive effects when the magnetic configuration of the electrodes was reversed.

In the calculations a single-ζ basis set was used for the H, C and S s orbitals, a double-ζ polarized for C and S p orbitals and a double-ζ for all Ni orbitals. Exchange and correlation was calculated with the LDA functional and the spin configuration was collinear. The leads were described by alternated planes of 4 and 5 atoms each, grown along the (001) direction of the fcc lattice and the molecule end atoms (S) were attached to the hollow site of a four atom plane.

The transmission coefficients are shown in figures (2.6) and (2.7). In the octane the transmission is dominated by a series of resonances and is in general very small, which means that the transport is in the tunnelling regime. At the Fermi energy the parallel configuration is dominated by a sharp resonance that disappears in the antiparallel case. This produces a GMR ratio $\delta G = (G_P - G_{AP})/G_{AP}$ of $\sim 40\%$. In the tricene, however, the transmission is bigger and the molecule can be considered metallic. The predicted GMR at the Fermi level in this case is $\sim 100\%$.

In conclusion, it was demonstrated with SMEAGOL the possibility of producing large

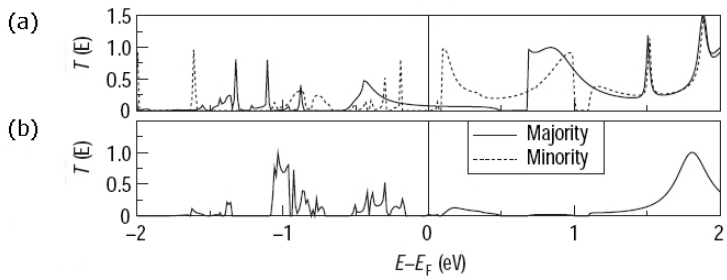

Fig. 2.7: Transmission coefficients of a Ni(001)/tricene/Ni(001) spin valve in (a) the parallel and (b) antiparallel configurations. In the antiparallel case both transmission coefficients are identical.

magnetoresistance ratios by anchoring organic molecules between magnetic leads. This study opens the door to the design of future molecular spintronics devices much faster, smaller and efficient than current magnetic-based electronic elements.

2.2.4 Example 2: Nickel nanocontacts

Magnetoresistance (MR) experiments are based on the measurement of the current change in systems composed of a non-magnetic region sandwiched between two magnetic leads when the magnetization of the leads is reversed, as in the previous example. However, MR effects have also been reported in Ni nanocontacts, [88, 89, 90, 91, 92, 93, 94, 95, 96, 97], where the chemical composition of the leads and the intermediate region is identical. Although some groups obtained high values of MR, others predicted small or even negative ratios [88, 92]. The reason of these discrepancies is that the structure of the contact, where the domain wall is constrained [98], is not exactly known and small changes in the atomic positions, due for example to the local heating or the applied magnetic field, can lead to dramatic changes in the conductance [99].

To demonstrate the capacity of SMEAGOL to deal non-collinear magnetic systems, I performed a series of calculations, based on the previous experiments, of Ni nanocontacts with different lengths of the atomic constriction. I used a double-zeta basis set and the LDA approximation. Like in the previous section, the leads were composed of alternative atomic planes with 4 and 5 atoms each, grown along the (001) direction of the fcc lattice, as shown in figure (2.8). All distances were set equal to the bulk distances.

I studied four different cases, depending on the number of atoms in the constriction (between 1 and 4). Larger chains were not considered because they are not stable [64]. In the four atom case the domain configuration can also be symmetric or non-symmetric, depending on where the domain wall is placed, as shown in figure (2.10). I also distinguished between collinear configurations, where the spin vectors are constrained to lie parallel to

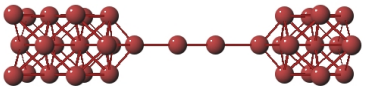

Fig. 2.8: One of the Ni nanocontacts (the four atoms case) used in the calculations.

Fig. 2.9: Example of non-collinear domain wall.

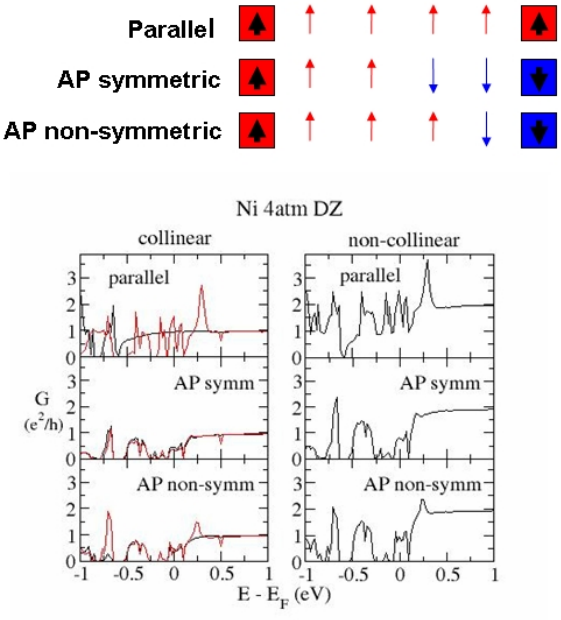

Fig. 2.10: The four-atom domain walls. The parallel, antiparallel symmetric and antiparallel non-symmetric conductances are shown for both collinear and non-collinear spins. Notice that the non-collinear conductances are just the sum of the conductances of both collinear channels.

Tab. 2.1: MR ratios for the 1-4 Ni nanocontacts.

	Magnetoresistance ratio (%)
1 atom	-2
2 atoms.	-69
3 atoms.	20
4 atoms symm.	68
4 atoms antisymm.	60

the quantization axis, and non-collinear configurations. In the latter case the Hamiltonian and, consequently, the GF are split in four components and the total transmission is given by

$$G = \frac{e^2}{h}[T_{\uparrow\uparrow} + T_{\uparrow\downarrow} + T_{\downarrow\uparrow} + T_{\downarrow\downarrow}](E_{\mathrm{F}}) \tag{2.61}$$

This configuration allows to have smoother changes of the spin vectors along the domain wall, as shown in figure (2.9), in contrast to the more abrupt variations present in the collinear configuration.

Although one would naively expect to observe a non-collinear evolution of the magnetization, i. e. to have spin vectors that rotate smoothly from atom to atom, the calculations show that this is not the case. The spin magnetization of each atom remain almost exactly collinear and the domain wall is abrupt. This is confirmed by the results for the collinear and the non-collinear calculations, which are essentially the same, as can be seen in figure (2.10). Besides, the modulus of the magnetization of the central atoms increases significantly up to a value of 1.2 μ_{B}, almost as twice as the bulk magnetization. This is somewhat expected since the abrupt reduction of the crystalline field in the constriction drives the electronic structure towards high spin configurations.

The MR results are summarized in table (2.1), where the definition $\delta G = (G_P - G_{AP})/G_P$ was used. As can be seen, for one and two atoms the MR ratio is negative and, in the first configuration, very small. This is in agreement with some experiments [88, 92]. For 3 and 4 atoms the MR ratio is positive and increases with the number of atoms in the chain. On the other hand, the 4-atoms symmetric configuration has larger MR than the non-symmetric configuration. This is also expected, since larger changes in the conductance are produced where the spin vectors are bigger, i. e. in the middle of the chains. However, in practice only the non-symmetric configuration will develop since it is 0.1 eV more stable than the symmetric configuration.

The differences between the conductances of the parallel and the antiparallel configurations can be understood in terms of the s and d levels. The s, which have no spin

polarization, are localized mainly above the Fermi level (for energies approximately bigger than 0.5 eV), with a transmission of $\sim 1\ G_0/2$ for both spin channels. However, the d orbitals, which carry the spin polarization, appear around E_F, where the differences between the parallel and the antiparallel cases are more pronounced. The fact that the magnetoresistance is not very large is due to the presence of s electrons also around E_F, which gives a non-vanishing contribution to the conductance in the antiparallel configurations.

In summary, SMEAGOL was used to show that the MR ratio in Ni nanocontacts can be either positive or negative. For long constrictions the spin vector grows in the middle of the atomic chain and increases the MR, although the non-symmetric configurations, which have smaller values of MR, are more stable. These calculations pave the way to more sophisticated studies with bulk leads and relaxed configurations in the middle of the constriction.

2.3 Single Channel Conductance of H_2 Molecules Attached to Platinum or Palladium Electrodes

The smallest possible molecule, namely the H_2 molecule, which has just one bonding and one anti-bonding state in a given energy range, is a very simple system. It should be very easy then to predict the effect of tuning a range of adjustable parameters in break junction experiments where the molecule is placed between two adjacent leads, including the position and orientation of the molecule, the distance between the electrodes and the materials which make up the electrodes. However, despite the apparent simplicity of this junction, there is currently no agreement about the position and orientation of the molecule and no explanation exist for the observed differences between some materials.

Smit and coworkers [44] found that the conductance histograms of the molecule, sandwiched between Pt leads had a sharp peak at about 0.9 G_0 and therefore argued that electronic transport was dominated by a single channel with an almost perfect transmission. In addition, from the experimental phonon spectra they concluded that the molecule bonds to the electrodes in a bridge configuration (BC), i.e. with the H_2 bond axis parallel to the transport direction (see figure (2.11)). This was also confirmed by Cuevas *et al.* [59].

A different interpretation was given by García and coworkers [60], who showed theoretically that an arrangement where the molecule bonds perpendicularly to the transport direction (perpendicular configuration, PC) has a lower energy, and therefore should be the preferred atomic configuration. Their simulations gave conductances of around 1.0 G_0 and 0.2 G_0 for PC and BC, respectively. However, Thygesen and collaborators [61, 62] challenged García's results. They performed a careful study of the vibrational spectra, providing further theoretical evidence in favor of the initial interpretation of Smit *et al* [44], and found that the current is carried by the anti-bonding state of the molecule with

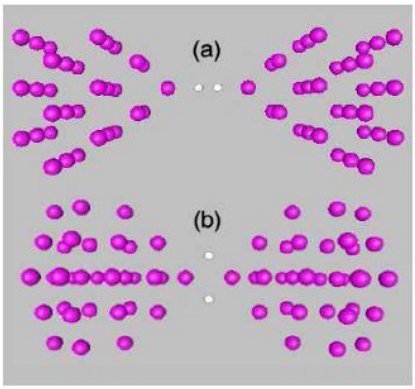

Fig. 2.11: Atomic configuration of the scattering region for the BC (a) and PC (b) arrangements. Shaded and white balls indicate Pt (or Pd) and H atoms, respectively. Figure (b) has been rotated 45 degrees around the z-axis with respect to figure (a), to achieve a better view of the orientation of the hydrogen molecule.

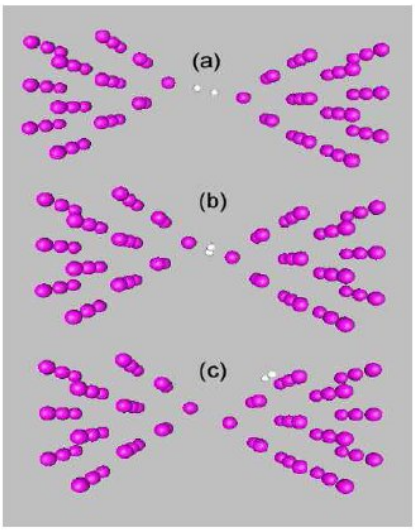

Fig. 2.12: New atomic configurations studied in this work: BC zigzag (a), PC zigzag (b) (top view of the molecule) and zigzag with the molecule chemisorbed on the surface (CZ) (c).

a conductance of the order of 1.0 G_0. But, in agreement with García, they also predicted that the PC has a lower energy than the BC when the separation between the leads is small.

Additionally, Csonka *et al.* [58] performed transport measurements on H_2 molecules sandwiched between Pd electrodes and found that the smallest peak had a conductance of $\sim 0.6G_0$. This value changed with the hydrogen gas pressure and temperature on the vacuum chamber, due to the dissolution of hydrogen into the palladium, but remained around that value. Also, due to the same reason a second peak appear sometimes around the quantum of conductance. Although the inclusion of hydrogen into the palladium could explain the origin and movement of those peaks, it is not clear why in the case where no dissolution is expected the conductance is smaller than in the valence-isoelectronic platinum.

To shed light on these contradictions and open questions I performed a detailed calculation of the stability, electronic structure and conductance of the H_2 molecule attached to either Pt or Pd electrodes. I used SIESTA [21] with a double-ζ and a double-ζ polarized basis set for H and Pt/Pd, respectively, and the LDA functional [10, 11]. These parameters gave bond distances and lattice constants very close to the experimental values (0.81 Å for the bond distance of H_2 [100] and 3.93 Å and 3.91 Å for Pt [101] and Pd [100], respectively).

The leads were simulated as a fcc crystalline structure grown along the (001) direction for both Pt and Pd, with a unit cell containing two 3×3 atomic layers, although other configurations were also used, as shown below. The scattering region, presented in figures (2.11) and (2.12), consisted of a H_2 molecule attached to the tips of two pyramids of Pt or Pd atoms. These pyramids can be viewed as a sequence of two atomic fcc (001) layers comprising 4 and 1 atoms respectively. The scattering region also included three bulk Pt (or Pd) buffer layers with the same atomic configuration of the leads, that were seamlessly attached to the pyramids. The hydrogen molecule was placed both in the BC and in the PC setup, as shown in figures (2.11) (a) and (b) respectively. Periodic boundary conditions were applied in the basal plane, and 4 irreducible k-points in the 2-dimensional Brillouin zone were used[2]. The electrical conductance was calculated using SMEAGOL [57] in the limit of small biases.

In contrast to the previously studied configurations [59, 60, 61, 62] shown in figure (2.11), I also considered BC and PC arrangements where the leads were not faced and an arrangement where the Pt or Pd leads were bonded directly and the molecule was located on one of the surfaces (zigzag configuration, CZ)[3], as can be seen in figure (2.12). Every simulation was labelled according to the distance d between the innermost buffer layers of

[2] Tests performed with 12 k-points provided essentially the same results. 4 k-points are enough to avoid spurious peaks or gaps in the transmission coefficients.

[3] I call this cases "zigzag" because in longer chains the most stable arrangement corresponds to a zigzag configuration.

the scattering region. For a given distance d the pyramids and the hydrogen atoms were always relaxed and the total energy and transport were calculated at zero applied bias.

2.3.1 Influence of the leads

As a first step I used finite leads along the x and y directions, made of alternating slices of 4 and 5 atoms. The results are shown in figure (2.13), where the conductances of the parallel and the perpendicular configurations are plotted for a series of distances. Around the Fermi energy the conductances are very irregular and have many peaks and gaps. When the 9-12 leads are used (figure (2.14)) there is no improvement and many sharp variations still remain.

I note first that $T(E)$ of gold, where the d-levels lie below E_{F}, is smooth regardless of the size of the section of the leads employed in the simulation. On the contrary, I find for platinum that the presence of d-states at the Fermi energy opens minibands and minigaps that translate into strong oscillations in $T(E \sim E_{\mathrm{F}})$. These minibands and minigaps arise from interference effects of the d-states along the transverse directions. Consequently, oscillations in $T(E)$ should disappear when bulk electrodes are used. Indeed, this is what I find when slabs made of 3×3 atomic planes with PBC are employed, as shown in figures (2.15). I moreover show how $T(E)$ converges when the number of transverse k points is increased from 4 to 12. Although some small variations and peaks still remain when 4 k points are used, the transmission at the Fermi level is essentially converged. These results demonstrate the importance of using bulk electrodes in systems with open d shells.

2.3.2 Platinum electrodes

I consider first the case of Pt electrodes. As stated above, I find that the isolated molecule has an equilibrium distance of 0.81 Å and a bonding-antibonding energy gap of about 11.5 eV. This bond is weakened when the molecule is attached to the electrodes, since the relaxed distances are 0.99 Å for BC and 2.46 Å for PC (this last configuration is close to a dissociated state).

The densities of states projected onto either hydrogen or the Pt atom at the apex are shown in figure (2.16) for both BC and PC configurations. Figure (2.16) (a) demonstrates that the bonding state in BC arrangement remains a localized state of the junction. On the other hand, the DOS projected onto the hydrogen atom shows that this state is essentially unaffected by the proximity of the electrodes. It indeed remains as a sharp peak located at almost the same energy as for the isolated molecule, somewhat below the lower Pt valence band edge. These results are confirmed by also plotting the DOS projected onto the neighboring Pt atoms, where the weight of such bonding state has decreased by a factor of four. In contrast, the anti-bonding state is completely spread,

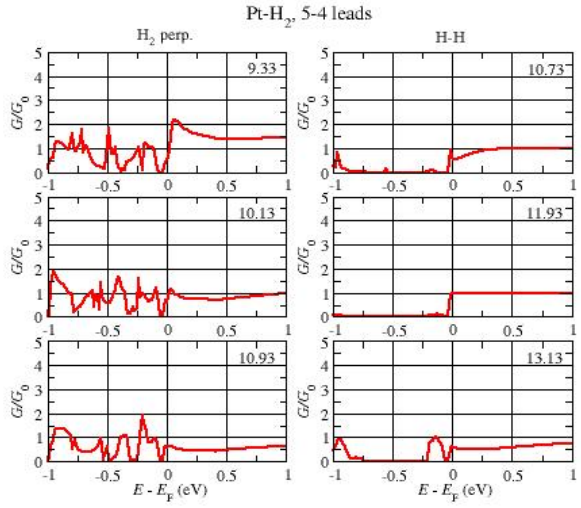

Fig. 2.13: Conductance of H_2 molecules sandwiched between platinum leads made of alternating slices of 4 and 5 atoms, in the perpendicular (left column) and parallel (right column) configurations, for different separations between the outer slices of the electrodes: 9.33, 10.13 and 10.93 Å in the perpendicular case and 10.73, 11.93 and 13.13 Å in the parallel case.

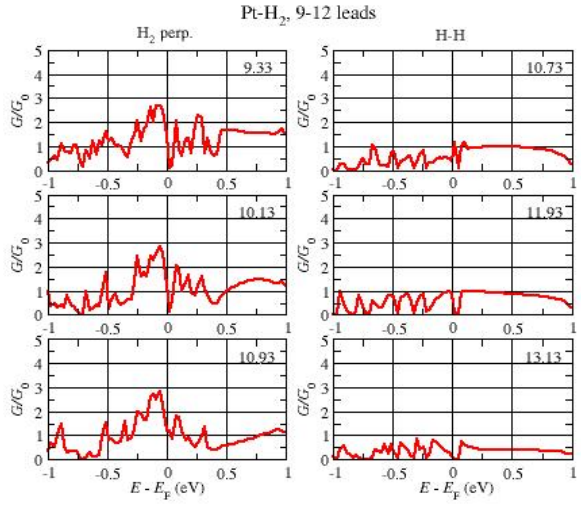

Fig. 2.14: The same as figure (2.13) but using platinum leads made of alternating slices of 9 and 12 atoms.

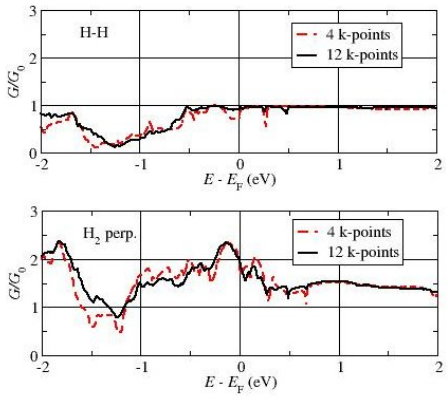

Fig. 2.15: Conductance of H_2 molecules sandwiched between bulk platinum leads in the parallel (top) and perpendicular (bottom) configurations, for 4 and 12 k points, calculated at the equilibrium distances ($\sim$ 9.5 and 11 Å, respectively).

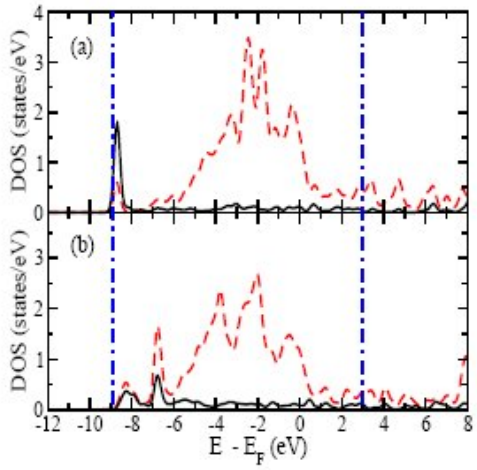

Fig. 2.16: Pt electrodes: DOS projected on one of the hydrogen atoms and the Pt atom at one of the two apexes (solid and dashed lines, respectively) in (a) BC and (b) PC configurations. Dashed-dotted vertical lines: position of the bonding and anti-bonding energy levels of an isolated H2 molecule. Energies have been referred to the Fermi energy of the Pt leads.

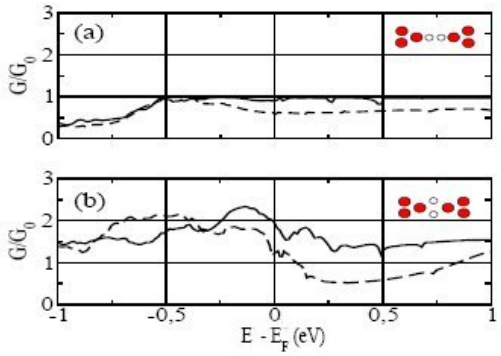

Fig. 2.17: Transmission coefficients in (a) BC, and (b) PC settings at their equilibrium distances. Solid and dashed lines indicate platinum and palladium, respectively.

coupling strongly to the leads. I can therefore conclude that the bonding channel of conduction is completely closed down, having zero transmission, while the antibonding state is clearly open. Moreover, a closer examination of the density of states (DOS) projected onto single orbitals and also of the Hamiltonian shows that such antibonding state hybridizes only with the s and d_{z^2} orbitals of the leads, as expected by symmetry. Indeed, I find that each hydrogen atom gains 0.27 electrons, that populate the antibonding state DOS below the Fermi energy.

The situation of the PC arrangement is somehow different. In this case the H_2 molecule hybridizes again with both the s and d_{z^2} orbitals of the tips. However, figure (2.16) (b) shows that the bonding state of the molecule participates also in the chemical bond to the leads since the corresponding peak in the DOS has slightly moved up in energies and splitted, to place itself at the band edge of the d-band of the Pt electrodes. Moreover, the amplitude of the peak does not decrease when moving from the hydrogen to the Pt atom at the apex. These facts demonstrate that the bonding state becomes delocalized and therefore opens up as a conduction channel.

Turning now the attention to the electron transmission through these states in the BC configuration I find that the conductance is almost flat, and approximately equal to 0.9 G_0, for a wide range of energies around E_F within the Pt bandwidth, as seen in figure (2.17). Moreover, I also found that T(E) remains essentially the same for the whole range of distances where BC is stable until the contact breaks. This almost perfect and constant transmission of the anti-bonding channel, added to the fact that the bonding channel is completely closed down, leads to the prediction of a narrow peak in conductance histograms with low conductance fluctuations.

In contrast, for the PC arrangement I obtain a conductance of about 2.0 G_0. In this case T (E) shows strong variations around E_F and achieves values even higher than 2

for distances around $d_{\mathrm{eq}} \sim 9.5$ Å, which implies the existence of more than two channels available for conduction. These arise from direct transport through Pt atoms at the apices of the pyramids, which at such a short distance have a small but finite overlap. Therefore if the PC were realized experimentally, one would expect the conductance histograms to display a peak centered at 2.0 G_0, with rather strong fluctuations around that value. This result is in contradiction with that of García [60].

I discuss now the stability of the structural configurations of the junction. The simulations confirm that the PC has a lower energy than the BC as shown in figure 5, in agreement with other authors [60, 61]. At first sight, this seems to be in contradiction with the experimental data, since the PC configuration has a conductance of about 2.0 G_0 instead on 1.0 G_0. However, a closer look into the energetics of the problem reveals two important features.

First, the last Pt atoms of the tips may prefer to bond in a zigzag configuration, thereby continuing the fcc alignment. I performed further simulations using such zigzag arrangements and found that their energy is substantially lower than the energy of the aligned counterparts whenever the two Pt atoms at the tip bond directly. In contrast, the energy-cohesion curves are insensitive to the alignment of the pyramids if a hydrogen molecule sits between the two Pt atoms, independently of the BC or PC configurations.

Secondly, if the distance between electrodes is too short, the hydrogen molecule may prefer to gain energy by bonding elsewhere on the Pt surface. I simulated then zigzag configurations (CZ) where the hydrogen molecule is initially on the surface of one of the leads, as shown in figure (2.12) (c), and, after relaxing the coordinates, found that both atoms achieve their equilibrium position on top of the triangular sites between the pyramid and the lead. Figure (2.18) shows that the CZ arrangement is indeed lowest in energy for short distances, as expected, while there is a window of about 1 Å where the PC is stable and competes in energy with all the different possible realizations of CZ. This last configuration snaps for distances larger than 11 Å, giving zero conductance. For these distances the BC becomes then the most stable configuration.

Based on the above results, I propose the following evolution of a Pt break junction in presence of hydrogen as a function of the Pt-Pt lead separation. For short distances (up to about 10 Å) the junction arranges itself as a zigzag Pt point contact. The H_2 molecules attach to the Pt surface at the triangular sites, away from the atomic constriction. The electrons travel then between the leads through several Pt channels and the conductance can vary between values much larger than G_0 and $\sim 1.5\ G_0$. As the separation between the contacts increases from 10 to 11 Å, the PC configuration may take over in a few of the pulling cycles of the break junction. For distances larger than about 11 Å, all configurations other than BC snap. The junction therefore arranges in a BC configuration before eventually also snapping at a distance $\sim$12.5 Å. This latter arrangement provides a single channel conductance of about 0.9 G_0, that results in the sharp peak found in the experimental conductance histograms [44].

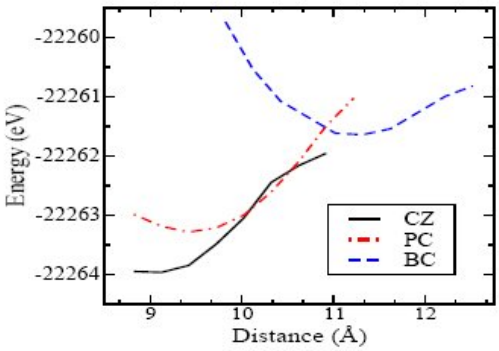

Fig. 2.18: Energy-cohesion curves E(d): energy E of different atomic configurations of the junction as a function of distance d. Solid, dashed and dash-dotted lines indicate CZ, BC and PC arrangements.

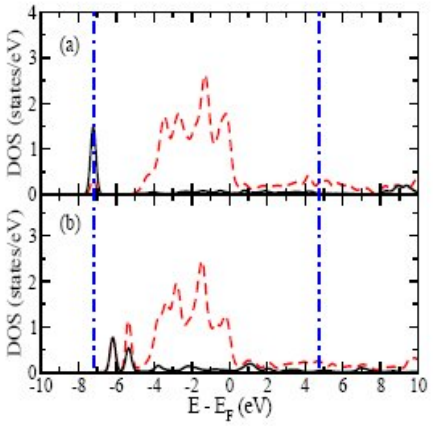

Fig. 2.19: Pd electrodes: DOS projected on one of the Hydrogen atoms and the Pd atom at one of the two apexes (solid and dashed lines, respectively) in (a) BC and (b) PC configurations. Dashed-dotted vertical lines: position of the bonding and anti-bonding energy levels of an isolated H_2 molecule. Energies have been referred to the Fermi energy of the Pd leads.

2.3.3 Palladium electrodes

Finally I consider the case of Pd [58], whose bonding properties are similar to those of Pt. For the BC, I find again that the bonding state of the H_2 molecule does not participate in the chemical bond. Figure (2.19) (a) shows that the bonding state remains a sharp peak that is clearly detached from the lower edge of the d-band of Pd. The amplitude of the peak in the DOS decays very fast as one moves away from the Hydrogen atom. As in the platinum case I also find that the anti-bonding state strongly hybridizes with the s and d_{z^2} orbitals of neighboring Pd atoms, so that electronic conduction is carried again by the anti-bonding channel. For the PC configuration, the bonding state also hybridizes, leading to the opening of a second conduction channel. Figure (2.19) (b) shows that the peak of the bonding state moves up in energies by 2 eV when the molecule hybridizes with the Pd electrodes in the PC configuration, placing itself at the band edge of the d-band. Moreover, the amplitude of the peak is almost the same on the hydrogen and the Pd atom at the apex of the electrode.

The transmission coefficients for the BC and PC are shown as dashed lines in figure (2.17). In complete agreement with the experimental data [58], I find a conductance of 0.6 G_0 for the BC arrangement at distances around $d_{\mathrm{eq}} \sim 11$ Å. This means that the transmission through the anti-bonding channel is not so perfect as in the case of Pt electrodes. I also find that the conductance of the PC is somewhat larger than 1.0 G_0 for distances around $d_{\mathrm{eq}} \sim 9.2$ Å. Interestingly I find in the BC configuration that Pd atoms in the tip acquire a net magnetic moment for distances larger than about 12 Å. This produces a spin polarized current, which is different for spin up and spin down electrons. Experimental evidence for spin-polarized transport in Pd point contacts has also been reported [102].

The different transmissions found for Pt and Pd may be understood in terms of the alignment of the centers of the s-d band of the atoms in the tip and the hybridized anti-bonding state. Analyzing the Hamiltonian matrix elements one finds that in Pd the misalignment is much bigger than in Pt. Indeed, a simple one-dimensional tight-binding model [72] (shown in the next subsection) consisting of two leads connected to a two-level system shows that the transmission coefficient $T(E)$ plateau, which has a value close to 1 if the on-site energies of the level and the atoms at the leads differ only slightly, is rounded and the transmission decreases as the difference between both energies is made larger. This behavior is evident in figure (2.17), which demonstrates the validity of the model in this special case and helps to understand the different transport behavior of the isostructural and valence-isoelectronic Pt and Pd.

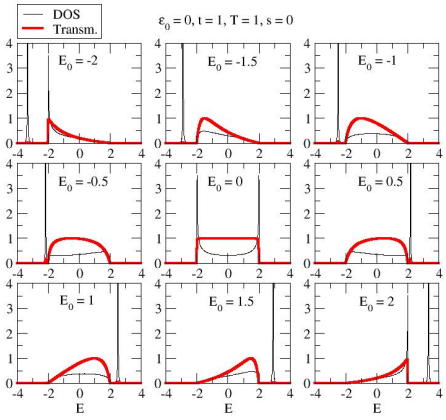

Fig. 2.20: DOS and transmission of the one-dimensional model with two sites in the scattering region as a function of the on-site energy E_0 (in arbitrary units) for an orthogonal basis set ($S = 0$).

2.3.4 Simple model with overlaps

To study the effect of the misalignment between the energy levels of the hydrogen molecule and the tip atoms it is useful to use a simple one-dimensional model which describes a one- or two-level system coupled to semi-infinite leads. If a non-orthogonal basis is used the retarded surface GF acquires the following form:

$$g^s_{11}(E) = \frac{E - \varepsilon_0 - \sqrt{(E-\varepsilon_0)^2 - 4t_S^2}}{2t_S^2} = \frac{E - \varepsilon_0 - R}{2t_S^2} \tag{2.62}$$

where $t_S = t - ES$ and $E \equiv E + i\delta$.

Using expressions previously obtained (Equations (2.25-2.28)) it is straightforward to find the retarded G_{00} and G_{01} for a one-level system:

$$G_{00} = \frac{g_{00}}{1 - 2g_{00}T_S^* g^s_{11} T_S} = \frac{1}{E - E_0 - \frac{T_S}{t_S}(E - \varepsilon_0 - R)} \tag{2.63}$$

$$G_{01} = G_{00} T_S^* g^s_{11} \tag{2.64}$$

where $T_S = T - ES$.

The total DOS (Λ) and the conductance (G) are given, respectively, by $\Lambda = -(1/\pi)\mathrm{Im}[\mathrm{Tr}(\hat{G}\hat{S})] = -(1/\pi)\mathrm{Im}[G_{00} + 2SG_{01}]$ and $G = G_0\mathrm{Tr}[\mathbf{t}^2]$, where

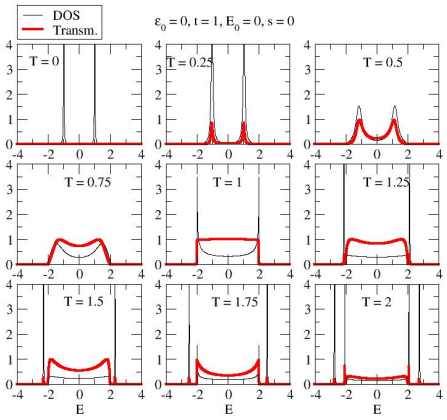

Fig. 2.21: DOS and transmission of the one-dimensional model with two sites in the scattering region as a function of the coupling T (in arbitrary units) for an orthogonal basis set ($S = 0$).

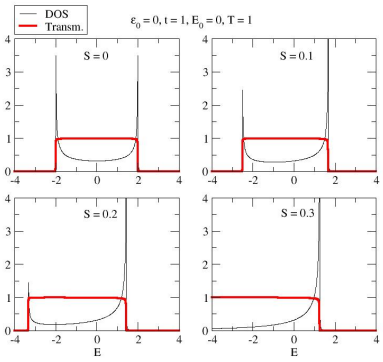

Fig. 2.22: DOS and transmission of the one-dimensional model with two sites in the scattering region as a function of the overlap S (in arbitrary units).

$$\mathbf{t} = 2\pi(\rho^s_{11})^{1/2} T_S G_{00} T_S (\rho^s_{11})^{1/2} = 2\pi \rho^s_{11} T_S^2 G_{00} \tag{2.65}$$

is the transmission amplitude and $\rho^s_{11} = -(1/\pi)\mathrm{Im}[g^s_{11}]$.

The generalization to a two-level system is direct: the couplings are $\hat{T}_S^{01} = (T_S, 0)$ and $\hat{T}_S^{10\,\dagger} = (0, T_S)$ and $\hat{G}_{00}$ is a 2×2 matrix, with intra-coupling T_0 and intra-overlap S_0. The DOS and the transmission are given respectively by $\Lambda = -(1/\pi)\mathrm{Im}[2G^{11}_{00}(1 + 2ST_S g^s_{11}) + 2S_0 G^{12}_{00}]$ and $\mathbf{t} = 2\pi\rho^s_{11} T_S^2 G^{12}_{00}$.

The results are summarized in figures (2.20), (2.21) and (2.22). In the first one it is shown the DOS and the transmission as a function of the on-site energy of the central region, E_0 (for simplicity I consider here all the overlaps equal to zero). From the evolution of the transmission it is evident that the conductance becomes asymmetric and decreases when the mismatch between the on-site energies increases. Also, for very big mismatches the DOS shows that the states of the central region decouple from the band and become localized states. These facts are in complete agreement with the behavior observed in the ab initio simulations, despite the simplicity of the model.

It is also interesting to observe the evolution of the DOS and the transmission as a function of the couplings and the overlaps. In the first case (figure (2.21)) the system evolves from a isolated site ($T = 0$), characterized by two single eigenvalues and zero transmission, to a perfect one-dimensional system ($T = t$), characterized by a dispersion relation $E(k) = \varepsilon_0 + 2t\cos k$ and one single channel with perfect transmission within the band. Note that for very small couplings the transmission is given by resonances of height equal to one located at the molecular levels (this is the resonant transport regime, which can be described by the Breit-Wigner formula [103]). On the other hand, if the coupling becomes stronger than the couplings in the leads, the transmission decreases again and the DOS tends to a configuration with four states (two states of the molecule and another two corresponding to the end atoms of the leads).

When the overlaps are included (2.22) the definition of the band is modified, i. e. $E(k) = (\varepsilon_0 + 2t\cos k)/(1 + 2S\cos k)$. Such overlaps have to be smaller than 0.5, otherwise this expression has singularities when $\cos k = -1/(2S)$. Their net effect is to drive the ban towards smaller energies, making it asymmetric, and increase its width.

2.3.5 Conclusions

In summary, I found that H_2 molecules bind to Pt or Pd leads in the PC or the BC configurations but only the BC corresponds to the sharp peak observed in the conductance histograms. The bonding state of the H_2 molecule does not participate in the chemical bond, and does not contribute to the low bias conductance. The conductance is close to 1.0 G_0 for Pt leads, since the energy of the hybridized antibonding orbital is close to

the center of the s-d band. Such alignment is not realized for Pd electrodes, leading to a smaller conductance, in agreement with a very simple model.

2.4 Conductance Oscillations in Zigzag Platinum Chains.

The existence of single atom chains was demonstrate using the scanning tunnelling microscope (STM) and mechanically-controllable break junctions (MCBJ) [41, 42] where a quantized conductance close to G_0 for gold was measured, in agreement with previous theoretical predictions [52]. Since then, a number of experiments [104, 63] and theoretical calculations [64] have proved that the 5d elements Ir, Pt and Au can be used to produce monoatomic chains. The chain length is usually obtained from MCBJs [42] by measuring the distribution of lengths of the last conductance plateau over a large number of contact-breaking cycles. These length histograms typically show three or four equally-spaced peaks indicating the lengths at which the chains break [104, 63]. For gold chains [41, 42], the average distance between conductance peaks was found to be 2.5 Å, with the conductance G of the last plateau being very close to G_0. The ensemble-averaged conductance also shows small oscillations around G_0 as the length of the chain increases [63]. Although the actual structure of these chains (zigzag vs straight chains) is still a matter of debate [65, 66], both the integer conductance and the small dispersion in the conductance distribution were attributed to the monovalency of this metal.

For platinum, the average distance between peaks in the length-histograms is about 1.9-2.3 Å [104, 63] and it is not known whether the structural configuration is linear or zigzag. In contrast with gold, the conductance is no longer an integer multiple of G_0, but instead decreases from 1.6 G_0 to 1.2 G_0 as the length of the chain increases [63]. Significant conductance oscillations are also superimposed on top of this decreasing trend, which have been attributed to a universal, even-odd parity effect associated with chains of fixed atomic spacing, but varying numbers of atoms [63, 105, 106]. The rich behavior of platinum [106], compared with gold arises from the larger number of conduction channels at the Fermi energy due to the presence of d bands.

2.4.1 Infinite chains

To understand the structural, electronic and transport properties of platinum chains attached to platinum fcc leads, I performed a complete series of first principles simulations using SIESTA [21] and SMEAGOL [57] with double-ζ polarized basis set and the LDA functional [10, 11]. I start, however, by discussing the case of infinite platinum chains, which is useful to understand the basic physics of the constriction when a long chain is formed. I used a two atom cubic cell with the chain grown along the z direction and large enough distances along x and y to avoid spurious intra-chain interactions. I simulated

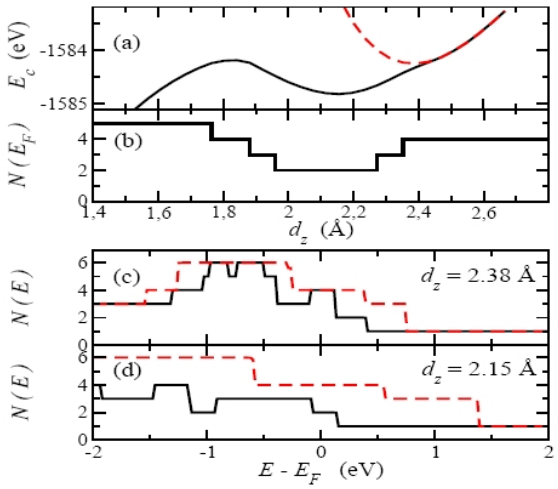

Fig. 2.23: (a) Cohesive energy E_c and (b) number of open scattering channels at the Fermi energy $N(E_{\rm F})$ of infinite platinum chains as a function of d_z. Number of open scattering channels $N(E)$ as a function of energy E calculated at (c) $d_z = 2.38$ and (d) $d_z = 2.15$ Å. Solid and dashed lines stand for zigzag and linear chains, respectively.

two kinds of chains: linear chains, where the atoms are constrained to lie on the z axis, and zigzag chains, where forces are allowed to relax along the three spatial coordinates. In agreement with previous theoretical simulations of gold [65] I find that zigzag chains are more stable than linear chains, as it can be seen in figure (2.23) (a). The equilibrium distances along z are $d_{z,\rm eq} = 2.15$ and 2.38 Å for the zigzag and linear chains, respectively. In the zigzag arrangement the Pt-Pt bonds are located in the xz plane and make a 24.8 degrees angle with the z axis. This means that the interatomic distance for the zigzag configuration is $d = 2.37$ Å, which is very similar to the distance of the linear case. The angle decreases almost linearly as the chains are stretched, and becomes approximately zero for d_z larger than 2.5 Å. Interestingly, if the distance is reduced below the zigzag minimum the system falls into another stable configuration with a ladder arrangement, similar to that predicted by Sen *et al.* [107]

The number of open scattering channels $N(E_{\rm F})$ at the Fermi energy of an infinite zigzag chain is equal to 5 for small d_z, but decreases to 2 as the chain is stretched beyond 1.95 Å and maintains that value for quite a large range of distances, as can be seen in figure (2.23) (b). For d_z somewhat larger than 2.25 Å, $N(E_{\rm F})$ increases in two steps to 4, and stays constant thereafter until the chain breaks. To understand which channels are opening and closing, I analyzed the projected density of states (PDOS) for chains at different stretching. As limiting cases I compared a linear chain at $d_z = 2.38$ with a zigzag chain at $d_z = 2.15$ Å. For the linear chain I find that the d_{xy} and $d_{x^2-y^2}$ orbitals are

completely filled, while the hybridized s, d_{xz}, d_{yz} and d_{z^2} orbitals have all finite weight at E_F, leading to four open channels, as shown in figure (2.23) (c). Atoms in zigzag chains make small angles with the z axis at this distance and, therefore, the d_z-dependence of the PDOS and $N(E_F)$ look both fairly similar to those of the linear chain.

In contrast, the number of open channels $N(E)$ as a function of energy E, shown in figure (2.23)(d), and the PDOS of zigzag chains at dz = 2.15 Å look rather different from those of the linear chains. The zigzag chain has only two, and not four, open channels at the Fermi energy, corresponding to a mixture of all d orbitals, since now the s orbital is completely filled, while the d_{xy} and $d_{x^2-y^2}$ have moved up in energy. This analysis of infinite chains can explain why in some experiments the conductance increases when the electrodes separate: there is a gradual transition from a zigzag to a linear configuration upon the stretching of the chain, with the linear chain presenting larger number of open scattering channels.

2.4.2 Chains between fcc electrodes

The simplified picture of an infinite chain cannot however explain all the features that are present in a real experiment, since the contact to the electrodes and the rearrangement of the leads near the surface can decrease the transmission of some channels or even close them. To investigate this possibility, I simulated finite chains of various lengths (between 1 and 5 atoms), attached to fcc platinum leads oriented along the (001) direction (see figure (2.24)). The leads were composed of repeated slices of 3×3 atoms and connected to the chain through a square of 4 atoms, i.e. through the fcc (001) hollow site. In order to get rid of undesirable oscillations in the transmission coefficients, I used periodic boundary conditions along the xy plane and summed over 12 k points. Finally, to treat the contact region self-consistently, I included number of atomic planes of bulk platinum (between 3 and 5) in the scattering region until the results were converged.

I calculated the most stable configuration for each chain keeping fixed the bulk Pt leads and relaxing the central region, i. e. the two 2×2 planes forming the hollow site and the chain. The ground state energy was therefore calculated as a function of the distance d_z between the innermost 3×3 planes, as indicated in figure (2.24). In figure (2.25) I plot the cohesion curves for zigzag atomic chains with a number of atoms ranging between 2 and 5.

The cohesion curve of the single atom contact (not shown) is a parabola whose minimum is located at the equilibrium distance $d_{z,\mathrm{eq}} = 6.3$ Å. A parabolic dependence is also found when two atoms are placed facing each other, with $d_{z,\mathrm{eq}} = 9.1$ Å. However, if the outer planes are allowed to move along the x and y directions, these two atoms achieve a zigzag configuration that has a lower energy, as shown in figure (2.25), although this arrangement is actually a local minimum, since for shorter distances the atoms gain energy by forming further chemical bonds to other atoms at the electrodes. The same kind of

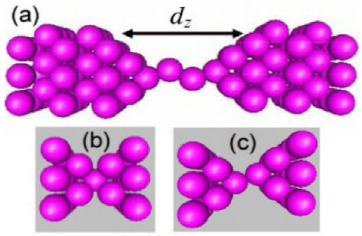

Fig. 2.24: The different atomic chains connecting (001) oriented fcc leads studied in this paper: (a) Four-atoms chain, (b) single atom contact and (c) 2-atom chain. d_z is the distance between leads

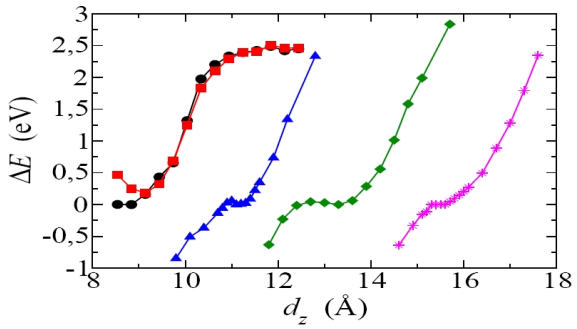

Fig. 2.25: Cohesion curves of the chain plus leads systems, for zigzag and linear chains of two atoms (circles and squares, respectively), and zigzag chains containing 3, 4 and 5 atoms (triangles, diamonds and stars, respectively). All curves have been shifted in energy in order to make the local minimum coinciding with the zero value and allow a better comparison. d_z is the distance between leads. Lines have been added to guide the eye.

curves are observed for 3, 4 and 5 atoms, with $d_{z,\mathrm{eq}} = 11.4$, 13.3 and 15.4 Å, respectively. The distance between chains of n and $n+1$ atoms lies in the range $1.9 - 2.1$ Å, in very good agreement with experiments [63]. The only configuration which does not fit into this pattern is the single atom contact, whose equilibrium distance is 2.8 Å away from the two-atom chain. Indeed, the single atom contact does not constitute a chain by itself, since a large number of bonds link the central atom to its neighbors, which must be broken simultaneously in order to snap the chain. In contrast, atomic chains can be topologically characterized as broken by cutting just one single bond. Consequently, the peaks found in length histograms [63] can be ascribed to chains 2-, 3-, 4- and 5-atoms long. Figure (2.25) also indicates that the region of stability of the $(n+1)$ atom chain begins at a distance where the n-atom chain is very stretched and therefore close to being broken. This helps to understand why the first two peaks found in length-histograms, which correspond to chains with two or three atoms, are much higher than those attributed to chains of four or five atoms [104, 63]. At a more detailed level, the angles between the atomic bonds and the chain axis are small for short chains (9.1 degrees for the 3-atom chain), but increase with the chain length (21.6 degrees for 4-atom chain). The case of the 5-atom chain is more complicated: the two atoms joining the leads make angles of 36.3 degrees, while those in the middle have angles equal to 16.1 degrees.

Moving to transport, the calculations show that the single atom contact behaves very differently from any other, with a conductance of about 5.9 G_0 at the equilibrium distance, which decreases almost linearly to $G = 3.5\ G_0$ until the contact breaks. These values are very different from those obtained by Nielsen *et al.* [105], where the pyramid-like structure of the contact was not included, leading probably to an overestimation of the interatomic distance. For the 2-atom chain I find a conductance of 1.5 G_0 at the equilibrium distance in the zigzag arrangement and a conductance ranging between 1.8 and 2.0 G_0 in the linear case, as shown in figure (2.26) (a). The second value can be associated with the return conductance measured when a contact is made after the system breaks [105]. I therefore propose that the first configuration established between two atoms when both tips are brought together is linear.

For larger chains there is a clear non-monotonic behavior of the conductance as a function of d_z. When the separation between the leads increases, the conductance initially decreases and then exhibits a plateau at around the equilibrium distance. Under further expansion it grows again (for stretching of about 1 Å beyond the equilibrium separation) and finally decreases exponentially, as can be seen in figure (2.26) (b). This behavior can be understood as follows. For small distances the number of open channels is large, since atoms in the chain are very close to each other. As the distance increases, the transmission through many of these channels is reduced and the conductance decreases until a value between 1.0 and 1.5 G_0, corresponding to the zigzag configuration. If the chain is stretched further, the conductance increases again, following the evolution from a zigzag to a linear chain, until a value of 2.0 G_0, where a small plateau is formed. Finally, the chain enters the exponential tunnelling regime, as shown in the inset to figure (2.26)

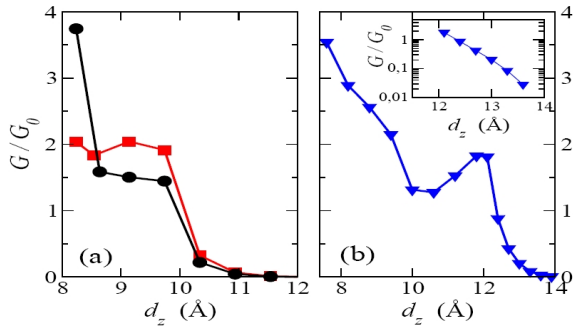

Fig. 2.26: Conductance of platinum monoatomic chains. (a) 2 atoms in a zigzag or linear arrangement (circles or squares, respectively). (b) 3 atoms; in the inset is plotted the tail of the curve in a logarithmic scale, that clearly shows the tunnelling behavior when the chain breaks.

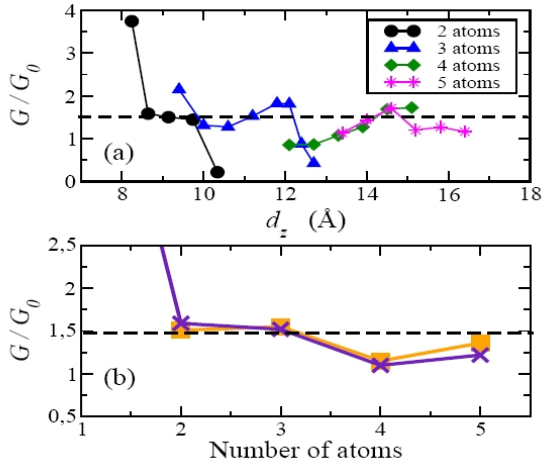

Fig. 2.27: (a) Evolution of the conductance of 2-, 3-, 4- and 5-atoms chains as a function of d_z (circles, triangles, diamonds and stars, respectively). (b) Conductance vs. the number of atoms in the chain measured at the equilibrium distance (crosses) and averaged over a range of two Angstrom about such equilibrium distance (squares).

(b), whose onset signals the point where the chain would break or a new atom would enter into it.

To make contact with the experiments of Smit *et al.* [63], the conductances of all chains are shown together in figure (2.27) (a). I find clear oscillations with a periodicity equal to the interatomic distance, which have a structural origin. These oscillations are due to the gradual closing and opening of channels, which occur as the angles between the atomic bonds and the z-axis increase and decrease. For a stretched chain, the angles increase if a new atom enters the chain, and subsequently decrease as the chain is further stretched. The size of the conductance is linked to the biggest angle subtended by atoms in the middle of the chain. Larger chains tend to have bigger angles and lower conductances. One exception is the 5-atom chain, whose conductance, 1.2 G_0 , is slightly bigger than that of the four-atom chain (1.0 G_0). This is also easily explained by the calculations, since atoms in the middle of the 5-atoms chains have a smaller angle than those of four atoms chains (16.1^0 versus 21.6^0).

The large geometry oscillations shown in figure (2.27) (a) may mask those due to the parity effect, which have a larger periodicity but a smaller amplitude. Since the experimental conductance curves are obtained by averaging individual conductance traces over thousands of pulling cycles, the short-distance fluctuations, such as the large geometry oscillations discussed above, should be smoothed out and only the parity oscillations, that have a longer wavelength, should remain. To explore such a possibility, I plot in figure (2.27) (b) the conductance of each chain, taken at its equilibrium distance. As can be seen, the large geometry oscillations have been completely washed out, leaving only a small oscillation that has a periodicity equal to twice the interatomic distance. To further check the stability of these results, I plot in figure (2.27) (b) the conductance of each chain, but now averaged over a range of lengths of about two Angstroms around each equilibrium distance. Such a procedure may reproduce the most important features of the experimental averaging of conductance curves. Interestingly, both curves almost overlap. The remaining curve actually shows two peaks, corresponding to chains with three and five atoms. The position of the conductance peaks, the overall shape of the curve and the magnitude of the conductance are in excellent quantitative agreement with the results of Smit *et al.* [63]. In view of the above results, I propose that the geometry oscillations found in the simulations are averaged over in the experiments, leaving only the smaller-amplitude but robust parity oscillations.

2.4.3 Conclusions

To summarize, I have found that zigzag platinum chains are more stable than linear chains, both in the case of perfect infinite chains, whose conductance is halved compared to that of the linear configuration, and the case of chains between two fcc (001) electrodes. The smallest chains are composed of at least two atoms, while the single atom contact shows

significantly different structural and transport features. The negative slope observed in the experiments is easily explained by the increasingly large angles subtended by atoms in the middle of long chains. Superimposed to the negative slope there are conductance oscillations which can have a structural or electronic origin. The first are related to the evolution from a zigzag to a linear structure and are washed out in the experimental averages. The second are due to the parity or even-odd effect and do not disappear in the experiments.

2.5 Electrical Nanowires

Since the demonstration of the possibility of filling carbon nanotubes with differnet compounds [67], a large number of nanowire devices with new and interesting electronic properties have been produced [45, 46, 47, 48, 49, 50, 51]. These experiments demonstrate, on one hand, that it is feasible to fabricate long and stable chains of single molecules or atomic clusters by placing them in the interior of CNTs and, on the other hand, that electronic and structural properties of CNT can be conveniently tailored by the encapsulation of different compounds. A special case corresponds to the filling of single-walled CNTs with metallocenes [108], a process that strongly depends on the diameter of the nanotube and involves chemical bonding between the metallocene and the CNT. Based on this experiment I performed a series of ab initio simulations of metallocene chains inside metallic and semiconducting CNTs. I studied the stability, the electronic and magnetic configurations and the transport characteristics, and I found that some metallocenes can give rise to magnetoresistive effects, among other interesting properties.

2.5.1 Isolated metallocenes and metallocene chains

Bis-cyclopentadienyl TM ($TMCp_2$) is a kind of metallocene composed of a transition metal atom, TM, sandwiched between two aromatic rings made of five carbon and five hydrogen atoms each. It may be formed with the six elements in the middle of the 3d-row, V, Cr, Mn, Fe, Co, and Ni, as well as with those in the column of iron, Ru and Os. All $TMCp_2$ therefore share a similar shape, which is depicted in figure (2.31). Their electronic structure, which I calculated using SIESTA [21] with a double-ζ basis set for hydrogen and carbon atoms, a double-ζ polarized basis set for the 3d metal atom, and the GGA functional [13], is also very similar, with differences that can be traced to the diverse electronic filling of the d-shell of the TM atom.

The crystal field associated with the benzene rings lifts the degeneracy of the d-shell into a triplet that lies lower in energy ($d_{x^2-y^2}$, d_{xy} and d_{z^2}) and a doublet (d_{xz} and d_{yz}). The levels in the doublet are split into two peaks due to their bonding with the carbon atoms. In addition, there is an exchange field that breaks the spin degeneracy to

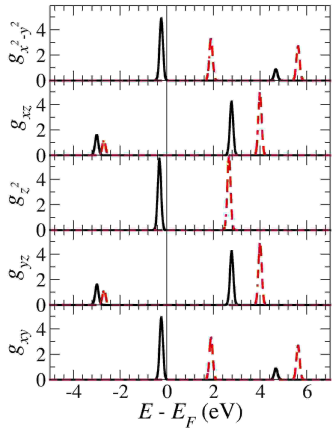

Fig. 2.28: Densities of states g_i of VCp_2, projected onto the d-shell orbitals of the vanadium atom, for spin up and down electrons (black solid and red dashed lines, respectively).The index i denotes the orbital flavor, $i = d_{x^2-y^2}, d_{xz}, d_{z^2}, d_{yz}, d_{xy}$.

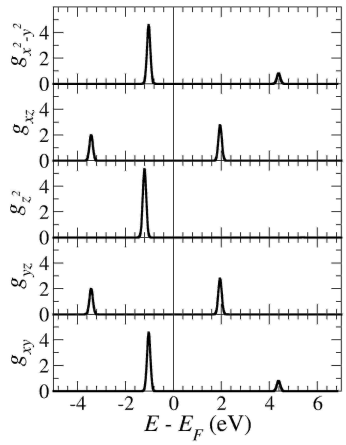

Fig. 2.29: Densities of states g_i of $FeCp_2$, projected onto the d-shell orbitals of the cobalt atom, for both spin up and down electrons. The notation is the same as in figure (2.28).

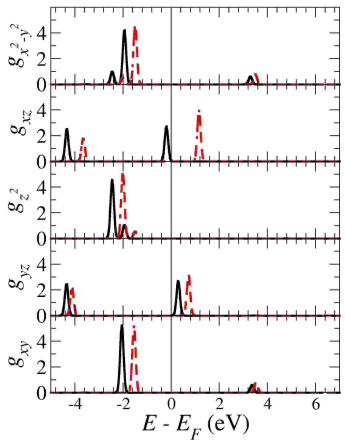

Fig. 2.30: Densities of states g_i of $CoCp_2$, projected onto the d-shell orbitals of the cobalt atom, for spin up and down electrons (black solid and red dashed lines, respectively). The notation is the same as in figure (2.28).

accommodate the magnetism predicted by Hund's first rule. Accordingly, VCp_2, $CrCp_2$, $MnCp_2$, $FeCp_2$, $CoCp_2$ and $NiCp_2$ have magnetic moments equal to 3, 2, 1, 0, 1 and 2 μ_B, respectively. $FeCp_2$ is paramagnetic since its core atom has a closed-shell electronic structure. The other metallocenes display a sort of mirror symmetry about $FeCp_2$. In figures (2.28), (2.29) and (2.30) I plot the density of states projected onto the d-shell of VCp_2, $FeCp_2$ and $CoCp_2$, respectively.

The high magnetic moment present in some metallocenes could give rise to magnetoresistive effects in chains made with these compounds. However, metallocene chains (grown along the C_5 axis) are insulating due to the small charge transfer between them (as expected in stable molecules) and, although they are energetically more favorable than the isolated molecule, the difference in energy is so small (< 0.02 eV) that in practice they are not formed. It is necessary then to look for alternative methods to stabilize them and increase the charge transfer.

2.5.2 Metallocenes inside armchair nanotubes

The obvious candidates to stabilize metallocene chains are carbon nanotbutes. The different behavior of the metallocenes is highly advantageous, since by placing these molecules in the interior of CNTs it is possible to fabricate molecular chains whose electrical and magnetic properties can be tailored at will. The CNT is the external coating, whose conducting properties can also be modified by changing its chirality from armchair to zigzag. Such a coating isolates mechanically and, to a point, electrically the metallocene chain.

Tab. 2.2: Lattice constants of carbon nanotubes, whose chirality is expressed in parentheses, and $TMCp_2$ chains, all given in Angstrom.

(n,n)	$(n,0)$	(12,4)	(15,5)	V	Cr	Mn	Fe	Co	Ni
2.50	4.32	15.59	15.59	7.88	7.99	7.63	7.55	7.93	8.20

In the simulations the periodicity along the axis of the nanotube or the chain was modeled using a number of k points ranging between 20 and 100 and all atomic coordinates of all atoms in the unit cell were relaxed. The resulting lattice constants are shown in Table (2.2). According to such results, metallocene chains can be accommodated rather well inside armchair (n,n) CNTs, with one molecule every three unit cells of the nanotube. They can also be placed inside zigzag $(n,0)$ CNTs, with one molecule every two unit cells, but in this case the chains are somewhat stretched. Other chiralities may also be chosen for the CNT. For instance, (15,5) and (12,4) CNTs can also host metallocene chains, with two molecules per unit cell.

To test the stability of the encapsulated chains, I simulated $CoCp_2$ chains inside metallic (n,n) CNTs, with n ranging from 6 to 10, i. e. with radii between 3.39 Å and 6.78 Å, respectively. The structural periodic unit of the simulations, denoted as $TMCp_2@N(n,n)$, comprised $N = 2$, 3 or 4 unit cells of the nanotube and a single metallocene. In addition, the C_5 axis of the metallocene was oriented either parallel or perpendicular to the axis of the nanotube, as shown in figures (2.31) (a) and (b). I obtained the binding energy E_B per structural unit cell,

$$E_B = E_{\mathrm{TMCp_2@}N(n,n)} - NE_{(n,n)} - E_{\mathrm{TMCp_2}} \tag{2.66}$$

as well as the charge transferred from the metallocene to the CNT, ΔQ, and its magnetic moment, m, as a function of the radii of the armchair CNTs. Figure (2.32) shows the results for parallel and perpendicular $CoCp_2@N(n,n)$ wires, with $N = 3$ and 4. The small energy differences between $N = 3$ and $N = 4$ are due to the formation energy of the chain. The configuration $N = 2$ is always energetically unfavorable because the metallocenes are too compressed.

Figure (2.32) (a) shows that parallel $CoCp_2@N(n,n)$ nanowires become energetically favorable for n equal or larger than 7. The most stable configuration, with a binding energy as large as 0.85 eV, is parallel $CoCp_2@N(7,7)$, which has a radius equal to 4.75 Å. This result is in excellent agreement with the experiment of Li *et al.* [108], where the preferred radius was found to be 4.67 Å.

By examining also the motion of single cobaltocenes along the nanotube axis it is possible to obtain information about the chain formation, since large energy barriers

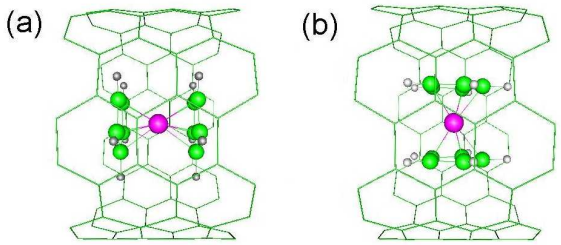

Fig. 2.31: Schematic view of a $TMCp_2$@3(7,7) unit cell, where the axes of the metallocene and the nanotube are parallel (a) or perpendicular (b) to each other. The atoms in the metallocene have been highlighted in red, green and grey colours (TM, C and H atoms, respectively).

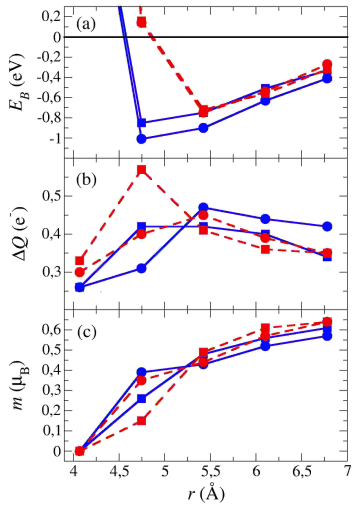

Fig. 2.32: (a) Binding energy E_B, (b) charge transferred to the nanotube ΔQ, and (c) total magnetic moment m, for $CoCp_2$@$N(n,n)$ wires, where n varies from 6 to 10. Blue solid and red dashed lines correspond to parallel and perpendicular $CoCp_2$@$N(n,n)$, respectively. Circles represent $N = 3$ and squares $N = 4$.

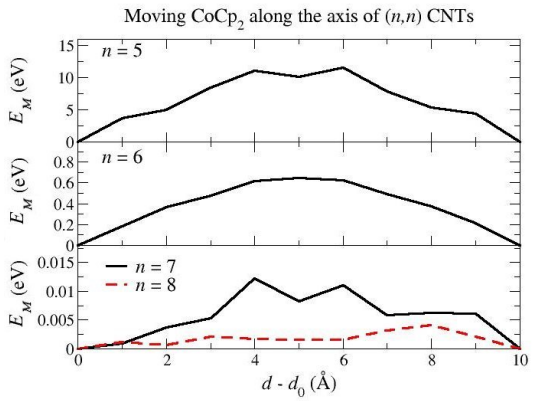

Fig. 2.33: Energetic barriers E_M that cobaltocenes have to overcome when they move along a (n, n) nanotube axis. The energies are referred to the most stable configuration.

will hinder the fabrication of chains with no faults, while if the barriers are too small, metallocenes will move almost freely, rendering nanowires useless for operation at room temperature. I therefore simulated parallel $CoCp_2$@4(n, n) with the cobaltocene placed at different positions along the nanotube axis without relaxing the coordinates again. I estimated the energy barrier E_M as the difference between the energy at each position and the energy of the relaxed configuration. The results are shown in figure (2.33). Thin nanowires have energy barriers of the order of several eV. On the contrary, $CoCp_2$@4(7,7) has an energy barrier of only 12 meV, which along with its large binding energy, makes this nanotube a promising candidate for encapsulating cobaltocenes. For larger radii, E_M decreases to values smaller than 3 meV, which allows the molecules to move almost freely.

Operation at room temperature also requires perfect alignment of the metallocenes. I therefore studied now how easy was to rotate a cobaltocene from a parallel to a perpendicular configuration. Taking into account that perpendicular cobaltocenes only fit inside CNTs with n equal or larger than 8, only for this radius or bigger radii can the chains be broken. I found that the energy cost to rotate a cobaltocene in $CoCp_2$@3(8,8) nanowires is as large as 0.15 eV. On the contrary, metallocenes can be missaligned at room temperature in $CoCp_2$@4(8,8) nanowires, due to the negligible overlap of metallocene wave functions that leads to a energy difference between both orientations of only 30 meV.

A Mulliken-population analysis of the total amount of charge transferred from the cobaltocene to the nanotube reveals that the nanotube is always n-doped and does not acquire any spin polarization [48]. The total charge transferred is of about 0.3 to 0.4 e^-, depending on the configuration, as shown in figure (2.32) (b). The effect of such transference is a reduction of the total magnetic moment, which is considerably smaller

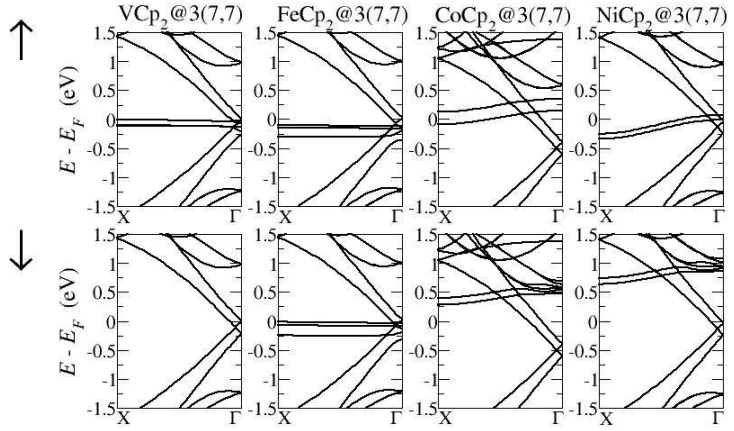

Fig. 2.34: Band structure of parallel $TMCp_2@3(7,7)$, for spin up and down electrons, where TM = V, Fe, Co and Ni. The perpendicular case is similar but the cobaltocene bands are flat due to the negligible overlap between the wave functions of the molecules.

than in the isolated molecule ($1.0\,\mu_B$).

The charge transfer is also evident in the band structures, shown in figure (2.34), where I plot the spin up and down electronic bands of parallel $TMCp_2@3(7,7)$, with TM = V, Fe, Co and Ni. The relative position of the CNT and the transition metal 3d bands signals the charge transferred and therefore the strength of the chemical bond. As a consequence, some metallocene bands appear at the Fermi level, as opposed to the isolated chains which were found to be always insulating.

The ferrocene in the $FeCp_2@3(7,7)$ has three 3d bands at the Fermi energy that are essentially unsplit and dispersionless. The CNT bands show on the contrary a large dispersion. This implies that the conducting properties of this nanowire must be carried by the external coating. Something similar happens in the vanadium wire, where the bands are exchange-split, but still dispersionless and therefore not conducting. In contrast, the 3d bands of cobaltocene and nickelocen nanowires are both exchange-split and dispersive and therefore can carry a spin polarized current.

According to the above discussion, parallel $CoCp_2@3(7,7)$ and $CoCp_2@3(8,8)$ are the best candidates for spintronics devices and can give rise to magnetoresistive phenomena. To test this possibility I simulated with SMEAGOL devices comprised of two leads, each made of $CoCp_2@3(7,7)$ with spin up, that sandwich a scattering region which contains one unit cell of $CoCp_2@3(7,7)$ with spin up or down or a CNT without the metallocene (a fault), and computed their conducting properties in the limit of small biases. This made

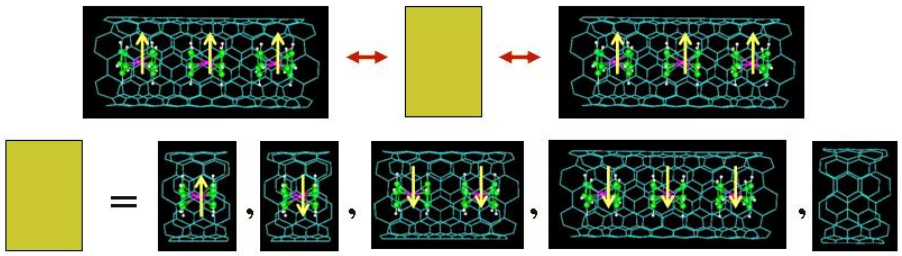

Fig. 2.35: Different configurations simulated with SMEAGOL to obtain the conductance of $CoCp_2$@3(7,7) chains.

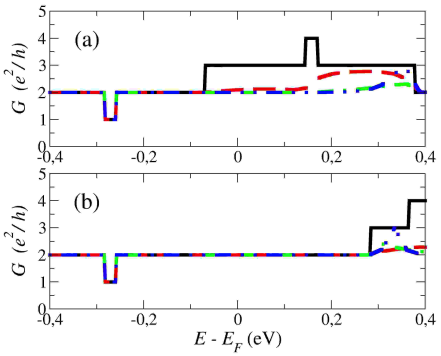

Fig. 2.36: Conductance of the $CoCp_2$@3(7,7) magnetorresistive devices u, d, dd and ddd (black solid, red dashed, green dash-dotted and blue dash-double-dotted lines, respectively), for (a) spin up and (b) spin down electrons.

a total of 9 nanotube unit cells and 315 atoms in the heaviest simulations. I denote each device by the spin (u or d) of the metallocene in the scattering region. Flipping such spin from up to down costs an energy of 0.05 eV, which means that the ferromagnetic configuration can be stabilized at room temperature but that a relatively small magnetic field may switch it.

The u configuration, where the spin of all cobaltocenes points upwards, corresponds to a perfect ferromagnetic chain with no scattering. The transmission coefficients are determined then from the band structure and are equal to the number of open scattering channels. Figure (2.36) shows three channels for spin up in a region around the Fermi energy that extends from -0.1 eV up to 0.4 eV. Two of them correspond to the nanotube and one to the cobaltocene. This excludes a tiny segment, where both cobaltocene bands contribute. For spin down, however, there are only two channels at the Fermi energy, associated to the nanotube, while the cobaltocene channels appear 0.3 eV above E_{F}.

In the d configuration the spin up channel associated with the cobaltocene is severely

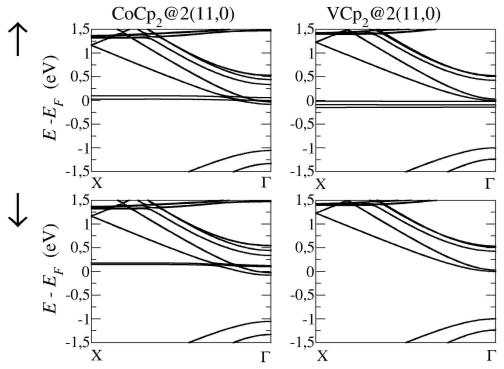

Fig. 2.37: Band structure of parallel $CoCp_2@2(11,0)$ and $VCp_2@2(11,0)$, for spin up (top panels) and down (bottom panels).

reduced, whereas the transmission for spin down is unaffected. As a consequence, the difference in conductance between u and the d configurations is $0.9\,e^2/h$. Defining the magnetoresistance (MR) ratio as $\delta G = (G_u - G_d)/G_d$, the predicted ratio is $\delta G = 22\%$.

Since the spin flipping of only one cobaltocene may be difficult to achieve in practice, I also simulated two other configurations with two and three $CoCp_2@3(7,7)$ unit cells in the scattering region and all the metallocene spins pointing downwards (see (2.35)). These configurations, which had a total of 420 and 525 atoms, are denoted by *dd* and *ddd*, respectively. As shown in figure (2.36), the resulting transmission for spin up channels around the Fermi energy decreases slightly, yielding a modest additional increase in the magnetoresistance ratio to 25%.

I also studied configurations with no cobaltocene in the scattering region, i. e. with a fault, and found that the cobaltocene channels completely disappear, remaining only those associated with the CNT. This implies that the chains should be as perfect as possible to reproduce the previous magnetoresistive behavior.

2.5.3 Metallocenes inside semiconducting or insulating nanotubes

Finally I also examined the effect of the CNT coating. With a view to improving the MR ratio, it is desirable to increase the fraction of the current passing through the metallocene chain and so, instead of using armchair CNTs, which are always metallic, I choose now non-conducting zigzag CNTs, which make an insulating coating. However, the charge transferred from the metallocene to the CNT moves the CNT valence bands downwards in energy, as illustrated in figure (2.37), and the CNT coating becomes conducting for $CoCp_2@2(11,0)$ and semimetallic for $VCp_2@2(11,0)$. For chiral nanotubes, such as (12,4) and (15,5) CNTs, the coating also becomes semimetallic, as shown in figure (2.38) for

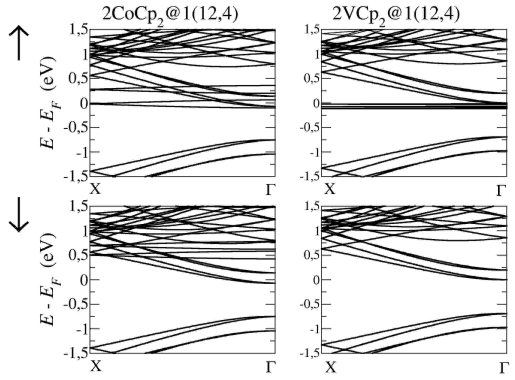

Fig. 2.38: Band structure of parallel $2CoCp_2@1(12,4)$ and $2VCp_2@1(12,4)$, for spin up (top panels) and down (bottom panels).

$2CoCp_2@1(12,4)$ and $2VCp_2@1(12,4)$. Consequently, the magnetoresistive ratio at low voltages does not improve when the character of the coating is changed.

2.5.4 Conclusions

In summary, I demonstrated that electrical nanowires consisting of a core made of a metallocene chain and a CNT coating may be fabricated. Their magnetic and electrical properties can be tailored at will by the appropriate choice of metallocene molecule and chirality of the CNT. The numerical simulations agree very well with the experiments and show that engineering of molecular spintronics properties is possible.

3

Non-Collinear Magnetism and Spin Spirals

In this chapter I describe the implementation in SIESTA of the generalized Bloch's theorem [109], which is necessary to simulate spin-spiral arrangements of spins, and an approximation to calculate the GGA exchange-correlation potential in non-collinear spin systems. The resulting code will be used to obtain the structural and magnetic properties of the iron phases.

3.1 Introduction

Many magnetic systems have collinear magnetic configurations, i. e. all their magnetic moments are parallel to a spin quantization axis (ferromagnets) or alternating antiparallel/antiparallel (antiferromagnets). The collinear or spin-polarized Hamiltonian is split then into two components, spin up and spin down, with different exchange-correlation potentials [110], and the size of the resulting ab initio calculation is twice the size of the corresponding non-magnetic calculation since the Schrödinger equation has to be solved separately for each component. On the other hand, in non-collinear systems [111, 112, 113, 114] the spin magnetization is described by a vector which can point to any direction and vary from site to site. The components of the vector are given by the inner product of the density matrix and the x, y and z components of the Pauli matrices. The non-collinear Hamiltonian and density matrix terms are therefore transformed into 2×2 matrices and the size of the calculation increases by a factor of 4.

Examples of non-collinear configurations include systems of low dimensionality (clus-

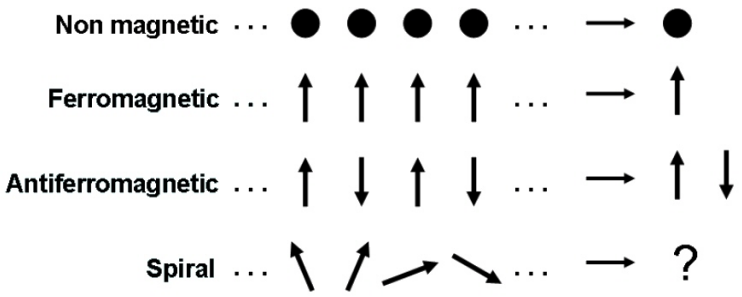

Fig. 3.1: Example of unit cells which can be used to simulate (a) paramagnetic, (b) ferromagnetic, (c) antiferromagnetic and (d) helical or spiral structures.

ters [113, 114] and molecular magnets [115], whose magnetic properties can be explained in many cases with only the Pauli exclusion principle and Hund's rules [121]), systems with low symmetry or in a disordered state [116, 117], and periodic systems with spin-spiral arrangements [118, 119]. Non-collinear magnetism is also important to describe spin waves, as I will show in chapter 3, and temperature effects [120]. In many of such systems the non-collinearity is usually understood in terms of a combination of spin-orbit and superexchange [122, 123]. However, in metals the spin-orbit interaction is much smaller than the spin-spin interaction and does not give a significant contribution to the energy. Only the exchange interaction remains as the main source of magnetic order and, consequently, has to be accurately calculated. This means that the exchange-correlation functional plays a crucial role in the characterization of the magnetic properties.

3.1.1 Spiral arrangements of spins

In infinite and periodic systems (wires, surfaces and crystalline solids) the wave function has the following form:

$$\hat{\Psi}_{\vec{k}}(\vec{r}) = e^{i\vec{k}\cdot\vec{r}}\hat{u}_{\vec{k}}(\vec{r}) \tag{3.1}$$

with $\hat{u}_{\vec{k}}(\vec{r}+\vec{R}) = \hat{u}_{\vec{k}}(\vec{r})$. It verifies then Bloch's theorem:

$$\hat{\vec{R}}\hat{\Psi}_{\vec{k}}(\vec{r}) = e^{i\vec{k}\cdot\vec{R}}\hat{\Psi}_{\vec{k}}(\vec{r}) \tag{3.2}$$

where $\hat{\vec{R}}$ is the translation operator and $\hat{\Psi}_k$ are eigenfunctions of the Hamiltonian $\hat{\mathcal{H}}$. Since $\hat{\vec{R}}$ and $\hat{\mathcal{H}}$ commute, the Hamiltonian eigenstates have translational symmetry and

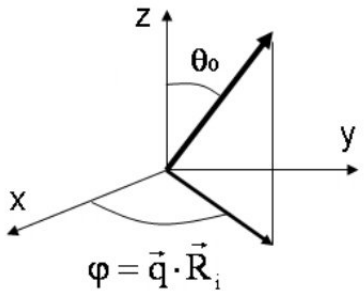

Fig. 3.2: The direction of the magnetization at a certain lattice site can be described in terms of the polar (θ) and azimutal (φ) angles.

therefore only one unit cell is needed to simulate the whole system. However, when some physical observable vary from cell to cell, like for example the magnetization in antiferromagnetic or helicoidal systems, it is necessary to use more than one unit cell, i. e. a supercell, to completely characterize the system, as shown in figure (3.1). Such a supercel can increase dramatically the size of the calculation.

However, using Herring's theory [109] it is possible to generalize Bloch's theorem to cases with translational symmetry of the lattice and rotational symmetry of the magnetization. This later quantity, which can vary smoothly from site to site, is described in a certain unit cell I by the vector

$$\vec{M}_I = M\vec{u}_I = M(\cos(\vec{q}\cdot\vec{R}_I)\sin\theta_0, \sin(\vec{q}\cdot\vec{R}_I)\sin\theta_0, \cos\theta_0) \tag{3.3}$$

where M and $\vec{u}_I$ are the magnitude and direction of the magnetization, respectively, θ_0 is the polar angle, which is fixed, and φ is the azimutal angle, which is calculated as the product of the vector of the unit cell, $\vec{R}_I$, and the spiral pitch vector, $\vec{q}$, which is used to describe the spiral structure (see figure (3.2)). The new wave function is defined in such a way that it verifies the generalized Bloch's theorem [124]:

$$\{\vec{R}|\vec{q}\cdot\vec{R}\}\hat{\Psi}_{\vec{k}}(\vec{r}) = \Psi_{\vec{k}}(\vec{r}+\vec{R})\hat{U}_{z,\vec{q}}(\vec{R})\hat{\chi} = e^{i\vec{k}\cdot\vec{R}}\hat{\Psi}_{\vec{k}}(\vec{r}) \tag{3.4}$$

The operator $\{\vec{R}|\vec{q}\cdot\vec{R}\}$ translates the spatial part of the wave function by a unit cell vector $\vec{R}$ and rotates the spinor an angle $\vec{q}\cdot\vec{R}$. The rotational matrix is defined as

$$\hat{U}_{z,\vec{q}}(\vec{r}) = e^{i\frac{\hat{\tau}_z}{2}\vec{q}\cdot\vec{r}} \tag{3.5}$$

where $\hat{\tau}_z$ is the third Pauli matrix. The wave function is then an eigenfunction of the Hamiltonian and takes into account all the translational and rotational symmetries. Therefore, only one unit cell is then needed to describe the system and the simulation becomes feasible.

3.2 Implementation in a DFT-LCAO Scheme

To be able to simulate spiral arrangements of spins, the Hamiltonian, the overlap matrix and the density matrix have to be redefined, since the rotation matrices, which act on the spinors, modify the general structure of the wave function. Such matrices implement the generalized Bloch's theorem with an azimutal angle $\varphi = \vec{q} \cdot \vec{r}$, which defines the spiral arrangement.

3.2.1 Wave function

The wave function, which can be described as an electronic part multiplied by a two component spinor, has the following form:

$$\hat{\Psi}_{n\vec{k}\vec{q}}(\vec{r}) = \frac{1}{\sqrt{N_u}} \sum_{\vec{R},\mu} e^{i\vec{k}\cdot\vec{R}_\mu} \hat{U}^\dagger_{z,\vec{q}}(\vec{R}_\mu) \hat{c}_{n\vec{k}\mu} \phi_{\vec{R}_\mu}(\vec{r} - \vec{R}_\mu) \tag{3.6}$$

where

$$\hat{U}_{z,\vec{q}}(\vec{r}) = e^{i\frac{\hat{\tau}_z}{2}\vec{q}\cdot\vec{r}} = \begin{pmatrix} e^{i\frac{\vec{q}\cdot\vec{r}}{2}} & 0 \\ 0 & e^{-i\frac{\vec{q}\cdot\vec{r}}{2}} \end{pmatrix} \tag{3.7}$$

is the azimutal rotation matrix and τ_z is the z component of the Pauli matrices. The initial state of the spinor is produced by rotating an angle θ_0 a collinear state:

$$\hat{c}^\sigma_{n\vec{k}\mu} = \begin{pmatrix} c^\uparrow_{n\vec{k}\mu} \\ c^\downarrow_{n\vec{k}\mu} \end{pmatrix} = \hat{U}^\dagger_y(\theta_0) \begin{pmatrix} c^0_{n\vec{k}\mu} \\ 0 \end{pmatrix} \tag{3.8}$$

where

$$\hat{U}_y(\theta_0) = e^{i\frac{\hat{\tau}_y}{2}\theta_0} = \begin{pmatrix} \cos\frac{\theta_0}{2} & \sin\frac{\theta_0}{2} \\ -\sin\frac{\theta_0}{2} & \cos\frac{\theta_0}{2} \end{pmatrix} \tag{3.9}$$

is the matrix which performs the polar rotation.

3.2.2 Bloch's theorem

When the translation and rotation operator acts on the previous wave function the result is the following:

$$\{\vec{q}\cdot\vec{R}|\vec{R}\}\hat{\Psi}_{n\vec{k}}(\vec{r}) = \frac{1}{\sqrt{N_u}}\sum_{\vec{R}',\mu} e^{i\vec{k}\cdot\vec{R}'_\mu}\hat{U}^\dagger_{z,\vec{q}}(\vec{R}'_\mu-\vec{R})\hat{c}_{n\vec{k}\mu}\phi_{\vec{R}'\mu-\vec{R}}(\vec{r}-\vec{R}'_\mu+\vec{R}) \tag{3.10}$$

where the property $\hat{U}_{z,\vec{q}}(\vec{R})\hat{U}^\dagger_{z,\vec{q}}(\vec{R}'_\mu) = \hat{U}^\dagger_{z,\vec{q}}(\vec{R}'_\mu-\vec{R})$ has been used. Applying the change $\vec{R}'' = \vec{R}'_\mu - \vec{R}$, the outcome is

$$\frac{1}{\sqrt{N_u}}\sum_{\vec{R}'',\mu} e^{i\vec{k}\cdot(\vec{R}''_\mu+\vec{R})}\hat{U}^\dagger_{z,\vec{q}}(\vec{R}''_\mu)\hat{c}_{n\vec{k}\mu}\phi_{\vec{R}''_\mu}(\vec{r}-\vec{R}''_\mu) = e^{i\vec{k}\cdot\vec{R}}\hat{\Psi}_{n\vec{k}}(\vec{r}) \tag{3.11}$$

The wave function verifies then Bloch's theorem. Such a wave function can be expressed as the product of a phase, a rotation matrix and a function which has the periodicity of the basic unit cell:

$$\begin{aligned}\hat{\Psi}_{n\vec{k}\vec{q}}(\vec{r}) &= e^{i\vec{k}\cdot\vec{r}}\hat{U}^\dagger_{z,\vec{q}}(\vec{r})\left[e^{-i\vec{k}\cdot\vec{r}}\hat{U}_{z,\vec{q}}(\vec{r})\frac{1}{\sqrt{N}}\sum_{\vec{R},\mu} e^{i\vec{k}\cdot\vec{R}_\mu}\hat{U}^\dagger_{z,\vec{q}}(\vec{R}_\mu)\hat{c}_{n\vec{k}\mu}\phi_{\vec{R}_\mu}(\vec{r}-\vec{R}_\mu)\right] = \\ &= e^{i\vec{k}\cdot\vec{r}}\hat{U}^\dagger_{z,\vec{q}}(\vec{r})\hat{u}_{n\vec{k}}(\vec{r})\end{aligned} \tag{3.12}$$

The generalized Bloch's theorem ensures the conservation of the azimutal angle $\vec{q}\cdot\vec{r}$ in the ab initio calculation. However, it does not work when the $\hat{U}_y$ matrices are included, since in such situation the Hamiltonian and the total rotation operator do not commute and, consequently, the polar angle θ_0 is not conserved. There are, however, some cases like $\theta = 0\,^\circ$ and $\theta = 90\,^\circ$, where the total rotation operator and the Hamiltonian commute. Spirals are simulated with $\theta = 90\,^\circ$, since for $0\,^\circ$ the azimutal rotations have no effect.

3.2.3 Schrödinger equation

As was shown in the first chapter, the Schrödinger equation has two terms which are calculated separately. When the rotation matrices are included the first term, which involves the Hamiltonian, can be written as follows:

$$\left\langle \hat{\Psi}_{n\vec{k}} \left| \hat{\mathcal{H}} \right| \hat{\Psi}_{n\vec{k}} \right\rangle = \sum_{\mu,\vec{R},\nu} e^{-i\vec{k}\cdot(\vec{d}_\mu - \vec{R}_\nu)} \hat{c}^\dagger_{n\vec{k}\mu} \hat{U}_{z,\vec{q}}(\vec{d}_\mu) \hat{\mathcal{H}}_{\mu\vec{R}_\nu} \hat{U}^\dagger_{z,\vec{q}}(\vec{R}_\nu) \hat{c}_{n\vec{k}\nu} =$$

$$= \sum_{\mu,\nu} \sum_{\sigma,\sigma'} c^{\sigma\,*}_{n\vec{k}\mu} \left\{ \sum_{\vec{R}} e^{-i\vec{k}\cdot(\vec{d}_\mu - \vec{R}_\nu)} \sum_{\sigma'',\sigma'''} \hat{U}^{\sigma\sigma''}_{z,\vec{q}}(\vec{d}_\mu) \mathcal{H}^{\sigma''\sigma'''}_{\mu\vec{R}_\nu} \hat{U}^{\dagger\,\sigma'''\sigma'}_{z,\vec{q}}(\vec{R}_\nu) \right\} c^{\sigma'}_{n\vec{k}\nu} \tag{3.13}$$

The second term, which is the overlap matrix, is calculated in the same way:

$$\left\langle \hat{\Psi}_{n\vec{k}} \left| \hat{\Psi}_{n\vec{k}} \right\rangle = \sum_{\mu,\vec{R},\nu} e^{-i\vec{k}\cdot(\vec{d}_\mu - \vec{R}_\nu)} \hat{c}^\dagger_{n\vec{k}\mu} \hat{U}_{z,\vec{q}}(\vec{d}_\mu) \hat{S}_{\mu\vec{R}_\nu} \hat{U}^\dagger_{z,\vec{q}}(\vec{R}_\nu) \hat{c}_{n\vec{k}\nu} =$$

$$= \sum_{\mu,\nu} \sum_{\sigma,\sigma'} c^{\sigma\,*}_{n\vec{k}\mu} \left\{ \sum_{\vec{R}} e^{-i\vec{k}\cdot(\vec{d}_\mu - \vec{R}_\nu)} S_{\mu\vec{R}_\nu} \sum_{\sigma''} \hat{U}^{\sigma\sigma''}_{z,\vec{q}}(\vec{d}_\mu) \hat{U}^{\dagger\,\sigma''\sigma'}_{z,\vec{q}}(\vec{R}_\nu) \right\} c^{\sigma'}_{n\vec{k}\nu} \tag{3.14}$$

All matrices are then defined in terms of the orbitals of the unit cell and the resulting Schrödinger equation is the same as the Schrödinger equation of the first chapter, but the terms between braces are different.

3.2.4 Electron density

The electron density in a non-collinear system was expressed as a two by two matrix. When the spiral is included it acquires the following form:

$$\hat{n}_{\vec{q}}(\vec{r}) = \frac{1}{N_k} \sum_{\mu,\vec{R},\nu} \sum_{n,\vec{k}} f_{n\vec{k}} e^{i\vec{k}\cdot(\vec{d}_\mu - \vec{R}_\nu)} \hat{U}^\dagger_{z,\vec{q}}(\vec{d}_\mu) \hat{c}_{n\vec{k}\mu} \otimes \hat{c}^\dagger_{n\vec{k}\nu} \hat{U}_{z,\vec{q}}(\vec{R}_\nu) \times$$

$$\times\, \phi_\mu(\vec{r} - \vec{d}_\mu) \phi_{\vec{R}_\nu}(\vec{r} - \vec{R}_\nu) = \sum_{\mu,\vec{R},\nu} \hat{\rho}_{\mu\vec{R}_\nu} \phi_\mu(\vec{r} - \vec{d}_\mu) \phi_{\vec{R}_\nu}(\vec{r} - \vec{R}_\nu) \tag{3.15}$$

so that

$$\hat{n}(\vec{r}) = \frac{1}{2} \left[n(\vec{r}) \hat{I} + \vec{m}(\vec{r}) \cdot \hat{\vec{\tau}} \right] = \begin{pmatrix} \tilde{n}^{\uparrow\uparrow}(\vec{r}) & \tilde{n}^{\uparrow\downarrow}(\vec{r}) \\ \tilde{n}^{\downarrow\uparrow}(\vec{r}) & \tilde{n}^{\downarrow\downarrow}(\vec{r}) \end{pmatrix} =$$

$$= \hat{U}^\dagger_{z,\vec{q}}(\vec{r}) \hat{U}^\dagger_y(\theta) \begin{pmatrix} n^\uparrow(\vec{r}) & 0 \\ 0 & n^\downarrow(\vec{r}) \end{pmatrix} \hat{U}_y(\theta) \hat{U}_{z,\vec{q}}(\vec{r}) \tag{3.16}$$

Equivalently,

$$\begin{aligned}\hat{\rho}_{\mu\vec{R}_\nu} &= \frac{1}{N_k}\sum_{n,\vec{k}} f_{n\vec{k}} e^{i\vec{k}\cdot(\vec{d}_\mu-\vec{R}_\nu)} \hat{U}^\dagger_{z,\vec{q}}(\vec{d}_\mu)\hat{c}_{n\vec{k}\mu}\otimes\hat{c}^\dagger_{n\vec{k}\nu}\hat{U}_{z,\vec{q}}(\vec{R}_\nu) = \\ &= \begin{pmatrix} \tilde{\rho}^{\uparrow\uparrow}_{\mu\vec{R}_\nu} & \tilde{\rho}^{\uparrow\downarrow}_{\mu\vec{R}_\nu} \\ \tilde{\rho}^{\downarrow\uparrow}_{\mu\vec{R}_\nu} & \tilde{\rho}^{\downarrow\downarrow}_{\mu\vec{R}_\nu} \end{pmatrix} = \\ &= \hat{U}^\dagger_{z,\vec{q}}(\vec{d}_\mu)\begin{pmatrix} \rho^{\uparrow\uparrow}_{\mu\vec{R}_\nu} & \rho^{\uparrow\downarrow}_{\mu\vec{R}_\nu} \\ \rho^{\downarrow\uparrow}_{\mu\vec{R}_\nu} & \rho^{\downarrow\downarrow}_{\mu\vec{R}_\nu} \end{pmatrix}\hat{U}_{z,\vec{q}}(\vec{R}_\nu) = \\ &= \hat{U}^\dagger_{z,\vec{q}}(\vec{d}_\mu)\hat{U}^\dagger_y(\theta)\hat{\rho}^d_{\mu\vec{R}_\nu}\hat{U}_y(\theta)\hat{U}_{z,\vec{q}}(\vec{R}_\nu) \end{aligned} \tag{3.17}$$

where

$$\tilde{\rho}^{\sigma\sigma'}_{\mu\vec{R}_\nu} = f(\rho^{\uparrow\uparrow}_{\mu\vec{R}_\nu}, \rho^{\uparrow\downarrow}_{\mu\vec{R}_\nu}, \rho^{\downarrow\uparrow}_{\mu\vec{R}_\nu}, \rho^{\downarrow\downarrow}_{\mu\vec{R}_\nu}, \vec{q}\cdot\vec{d}_\mu, \vec{q}\cdot\vec{R}_\nu), \tag{3.18}$$

and

$$\hat{\rho}^d_{\mu\vec{R}_\nu} = \begin{pmatrix} \rho^{\uparrow}_{\mu\vec{R}_\nu} & 0 \\ 0 & \rho^{\downarrow}_{\mu\vec{R}_\nu} \end{pmatrix} \tag{3.19}$$

is the diagonal density matrix.

3.2.5 Magnetization

The non-collinear magnetization operator is defined in the following way:

$$\hat{M}(\vec{r}) \simeq -\hat{m}(\vec{r}) = -\hat{U}^\dagger_{z,\vec{q}}(\vec{r})\hat{U}^\dagger_y(\theta)\hat{\tau}_z\hat{U}_y(\theta_0)\hat{U}_{z,\vec{q}}(\vec{r}) \tag{3.20}$$

This operator does not commute in general with the Hamiltonian and therefore the wave functions $\Psi_{n\vec{k}}(\vec{r})$ are not eigenstatates of it. This means that the initial magnetization is not conserved in the self-consistent procedure.

3.2.6 Exchange and correlation potential

The current LDA and GGA functionals are only valid in a collinear reference frame. This implies that the density has to be diagonalized at every point. In case of LDA, which

only needs local information to calculate exchange and correlation, the collinear potential at every point $\vec{r}$ is calculated as follows:

$$\begin{aligned}\hat{V}^{xc}(\vec{r}) &= \frac{\delta E[\hat{n}]}{\delta \hat{n}(\vec{r})} = \hat{U}_y(\theta)\hat{U}_{z,\vec{q}}(\vec{r})\hat{V}^{xc\,d}(\vec{r})\hat{U}^{\dagger}_{z,\vec{q}}(\vec{r})\hat{U}^{\dagger}_y(\theta) = \\ &= \begin{pmatrix} V^{xc\uparrow\uparrow}(\vec{r}) & V^{xc\uparrow\downarrow}(\vec{r}) \\ V^{xc\downarrow\uparrow}(\vec{r}) & V^{xc\downarrow\downarrow}(\vec{r}) \end{pmatrix} = \frac{1}{2}\left[V_0^{xc}(\vec{r})\hat{I} + \vec{V}_v^{xc}(\vec{r})\hat{\vec{\tau}}\right] \end{aligned} \tag{3.21}$$

where

$$V_0^{xc}(\vec{r}) = \mathrm{Tr}\{\hat{I}\hat{V}^{xc}(\vec{r})\} = V^{xc\uparrow\uparrow}(\vec{r}) + V^{xc\downarrow\downarrow}(\vec{r}) \tag{3.22}$$

and

$$\vec{V}_v^{xc}(\vec{r}) = V_v^{xc}(\vec{r})\vec{u}_v = \mathrm{Tr}\{\hat{\vec{\tau}}\hat{V}^{xc}(\vec{r})\} \tag{3.23}$$

Since the functional dependence in the LDA is $f^{xc}(n, m, \vec{u}_m)$, where the vector $\vec{u}_m$ defines the spin direction, $\vec{u}_v$ coincides with $\vec{u}_m$ and the rotation angles which transform the density and the potential turn out to be the same (with opposite sign). The procedure to follow is then

$$\hat{n}(\vec{r}) \overset{\theta,\phi}{\rightarrow} \hat{n}^d(\vec{r}) \rightarrow \hat{V}^{xc\,d}[n^{\uparrow}(\vec{r}), n^{\downarrow}(\vec{r})] \overset{-\theta,-\phi}{\rightarrow} \hat{V}^{xc}(\vec{r}) \tag{3.24}$$

Consequently, with LDA no approximation is needed to rotate back the potential and the scheme is exact within the limits of the functional.

With GGA the procedure is not so simple because the functional dependence, $f^{xc}(n, m, \vec{u}_m, \nabla n, \nabla m, \nabla^2 \vec{u}_m)$, also includes a gradient term which changes the direction of the potential:

$$\begin{aligned}\hat{V}^{xc}(\vec{r}) &= \frac{\delta E[\hat{n}, \nabla\hat{n}]}{\delta \hat{n}(\vec{r})} + \sum_{i=1}^{3} \frac{\delta E[\hat{n}, \nabla\hat{n}]}{\delta(\nabla\hat{n})_i(\vec{r})} \frac{\delta(\nabla\hat{n})_i(\vec{r})}{\delta\hat{n}(\vec{r})} = \\ &= \frac{1}{2}\left[V_0^{xc}(\vec{r})\hat{I} + \left\{V_m^{xc}\vec{u}_m + V_{\nabla\parallel}^{xc}\nabla^2\vec{u}_m + V_{\nabla\perp}^{xc}\vec{u}_m \times \nabla^2\vec{u}_m\right\}(\vec{r})\hat{\vec{\tau}}\right] \end{aligned} \tag{3.25}$$

The last three elements correspond to vectors parallel to $\vec{u}_m$ and $\nabla^2\vec{u}_m$ and perpendicular to both of them, respectively. The GGA discrepancies come from the fact that the

rotation matrices which are used to diagonalize the density can not be applied in general to diagonalize the components of the gradient of the density. The exchange and correlation potential is then approximated following two possible ways: (i) the density is rotated to the collinear reference frame where the gradient is also calculated,

$$\hat{n}(\vec{r}) \rightarrow \hat{n}^d(\vec{r}), \nabla\hat{n}^d(\vec{r}) \rightarrow \hat{V}^{xc\,d}[\hat{n}^d(\vec{r}), \nabla\hat{n}^d(\vec{r})] \tag{3.26}$$

or (ii) the gradient of the non-collinear density is also rotated and the small non-collinear terms are drop [125]:

$$\begin{aligned} \hat{n}(\vec{r}), \nabla\hat{n}(\vec{r}) \rightarrow \hat{n}^d(\vec{r}), \begin{pmatrix} [\nabla n(\vec{r})]^{\uparrow'} & \vec{\delta} \\ \vec{\delta}' & [\nabla n(\vec{r})]^{\downarrow'} \end{pmatrix} \rightarrow \\ \rightarrow \hat{n}^d(\vec{r}), \begin{pmatrix} [\nabla n(\vec{r})]^{\uparrow'} & \vec{0} \\ \vec{0} & [\nabla n(\vec{r})]^{\downarrow'} \end{pmatrix} \rightarrow \hat{V}^{xc\,d}[\hat{n}^d(\vec{r}), \nabla\hat{n}^{d'}(\vec{r})] \end{aligned} \tag{3.27}$$

Although these approaches seem to be rather different I have implemented both of them and verified that in practice the results are very similar. This means that, in many cases, the rotation matrices which diagonalize the density and the gradient of the density are very similar. Such a property suggests that rotations of the magnetic vector from point to point of the grid are very small, i. e. in a intraatomic scale the magnetization changes only smoothly and tends to be largely collinear [126].

3.3 Structural and Magnetic Properties of Iron

The most common state of iron in the earth crust is the bcc phase (α-iron), which is firmly established to be ferrromagnetic and remains stable for a wide range of pressures and temperatures. When it is highly compressed ($\approx$ 13 GPa) it undergoes a transition to a hcp phase (ϵ-iron) [127] which looses the ferromagnetic long range order [128] and can even develop superconductivity [129]. At 1183 K there is another transition, this time to a fcc phase (γ-iron), which can also be stabilized at room temperature and below in the form of alloys [130], thin films grown on an appropriate substrate [132, 133] and pellets in noble metal matrices [119, 134]. This phase exhibits very interesting phenomena like the invar effect (the suppression of the thermal expansion in a wide range of temperatures [131], which was explained by the existence of high- and low-spin configurations [135]) and a magnetic configuration which stands at a crossing point between high spin ferromagnetic and antiferromagnetic states and whose actual realization depends sensitively on the atomic volume and, possibly, strains [133]. Tsunoda discovered a decade ago using neutron scattering experiments that γ-iron could be easily stabilized as pellets of radii up

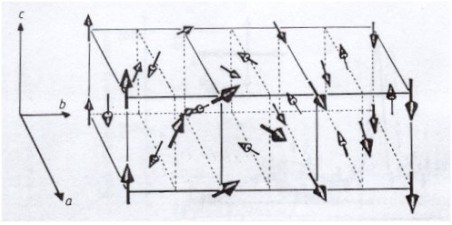

Fig. 3.3: Spiral configuration in the γ phase of iron. Figure from [119]

to 100 nm, with a lattice constant of 3.577 Å[119, 134]. He also found that the magnetic structure of the pellets was helicoidal, with pitch vector $\vec{q}_{\text{exp}} = (2\pi/a)(0.12, 0, 1)$, as shown in figure (3.3).

A number of authors have subsequently looked for theoretical low-energy collinear and non-collinear states appearing in such γ-phase. [125, 126, 136, 137, 138, 139, 140, 141]. In almost all cases the predicted spiral minimum at the theoretical lattice constant was found to be $\vec{q} = (2\pi/a)(0, 0, 0.6)$, both with LDA and GGA, whereas the experimental minimum developed for much smaller lattice constants. Bylander and Kleinman included a spin stiffness correction to LDA which improved considerably the results [141], but they calculated the spiral curve at the Cu lattice constant (3.61 Å) and, besides, the absolute minimum appeared at the antiferromagnetic configuration, $\vec{q} = (2\pi/a)(0, 0, 1)$. Knöpfle and co-workers [125] found that the GGA ground state was indeed a spiral with the correct pitch vector, but, since the augmented spherical waves method which they used tends to overestimate the atomic volume, it is difficult to extract what their equilibrium lattice constant a_0 might be. Finally, Marsman and Hafner simulated γ-iron under tetrahedric, orthorombic and monoclinic distortions [126]. They obtained for the undistorted case the correct spiral state but at an equilibrium lattice constant $a = 3.49$ Å, like in previous studies. They also found an equilibrium lattice constant $a = 3.51$ Å for $\vec{q} = (2\pi/a)(0, 0, 0.6)$, which was also very far from the experimental value.

In order to verify the accuracy of the previous simulations and study the influence of different parameters and approximations, I carried out with SIESTA a complete study of the iron phases. Since the degree of precision needed in some cases was very high (of the order of 1 meV) it was very important to converge the system very well before doing any serious simulation. For that reason the influence of the pseudopotential, the integration grids and the basis set, among other parameters, had to be carefully analyzed.

3.3.1 Choice of pseudopotential and integration grids

Izquierdo and coworkers [142] proposed to generate the norm conserving pseudopotential (NCPS) for iron from the atomic configuration $[\text{Ar}]3\text{d}^7 4\text{s}^1$, with core radii for 4s, 4p, 3d

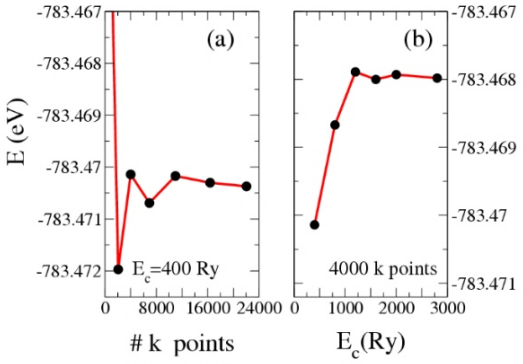

Fig. 3.4: Total free energy as a function of (a) number of k points in half the Brillouin zone (with a Grid Cutoff of 400 Ry) and (b) grid cutoff (with 4.000 k points in half the Brillouin zone). An optimized double$-\zeta$ (DZ) basis and the GGA functional were used.

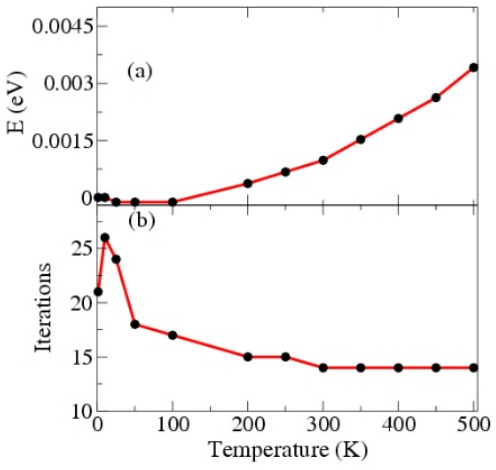

Fig. 3.5: Energy difference (a) and number of iterations (b) as a function of the electronic temperature. The calculation was performed with 4.000 k points, a grid cutoff of 400 Ry (27.000 real space points), an optimized DZ basis and the GGA functional.

and 4f orbitals set equal to 2.00 a.u. They found that the optimal radius for partial-core corrections was 0.7 a.u. Instead, I looked carefully for a pseudopotential which could produce a better fit to bulk bcc iron. The first criterium was to determine the cutoff radii comparing the eigenvalues of the valence shells of atomic iron obtained from the NCPS and the all-electrons Hamiltonians and try to minimize their differences. The resulting radii obtained using such procedure were very different from each other and the pseudopotential produced fits to the bulk bcc phase of poor quality as compared with the proposal of Izquierdo *et al.* Inclusion of the partial-core 3p levels into the valence did not help, mostly due to the fact that 3s electrons are still taken as part of the core and therefore there remains a strong overlap between valence and pseudocore charge. The chosen pseudopotential was then the one proposed by Izquierdo and coworkers.

Since the energy of the different states does not shift rigidly when increasing accuracy and moreover competing ground states for (fcc) iron have energy differences as tiny as 5 meV, the number of k points[1], the electronic temperature and the grid cutoff[2] were set to match an accuracy of about 1 meV. Figure (3.4) shows typical results for the convergence of the energy of bcc ferromagnetic iron as a function of those parameters. 4.000 k points and up to 700 Ry (which corresponds to 50.000 points in the real space grid) were then needed to meet the desired accuracy. Figure (3.5) shows that increasing the temperature to an optimal value of about 200 or 300 K speeds the convergence of the self-consistent process significantly while not damaging the accuracy required for the energy.

3.3.2 Optimization of the atomic basis and phase diagram for bulk iron

The minimum basis required to accommodate the eight valence electrons of iron is SZ for both s and d orbitals, which provides a total of 6 wave functions per spin. SIESTA is set up to the default maximum basis set TZTP, which corresponds to 72 wave functions (WF) per spin. Using more wave functions is equivalent to filling up the Hilbert space and provides a better variational estimate of the ground state. Junquera and coworkers [31] pointed out that the confinement radius of each orbital are also variational parameters. Very fast calculations or simulations of a large number of atoms may therefore be performed using SZ basis of rather confined orbitals. Such calculations usually provide much of the features of a material or device but they tend to be very inaccurate, and DZ bases with polarized s orbitals are rather used.

I minimized basis sets ranging from SZ-SZ (6 WF) to TZTP-TZTP-TZTP (72 WF). Figure (3.6) shows the evolution of the cohesion curves for different basis sets in the

[1] SIESTA performs Brillouin zone integrations on a grid of Monkhorst-Pack [143] special points typically extended to cover half of it [21, 144] due to time reversal symmetry.

[2] Hamiltonian matrix elements are partly computed on a real space grid, whose fineness Δx is controlled by a grid cutoff, $E_c \approx (\pi/\Delta x)^2/2$.

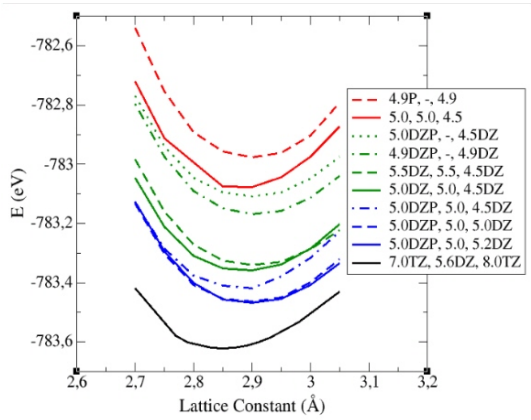

Fig. 3.6: Cohesion curves of the bcc ferromagnetic phase of iron calculated with different basis sets.

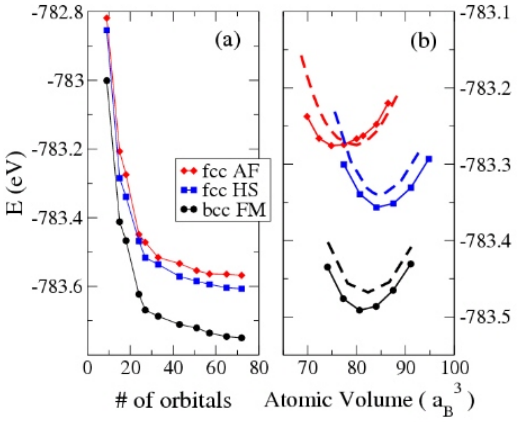

Fig. 3.7: (a) Evolution of the free energy of some of the most stable states of iron as a function of the size of the basis set. AF = antiferromagnetic (fcc), HS = high-spin ferromagnetic (fcc), FM = ferromagnetic (bcc). (b) Cohesive energy curves of those same three states as a function of the atomic volume ($V_{\mathrm{bcc}} = a^3/2$, $V_{\mathrm{fcc}} = a^3/4$), calculated with a double-ζ basis set. The discontinuous curves correspond to radii of 6 a. u. and the continuous to 10 a. u. The calculations were performed with the GGA functional.

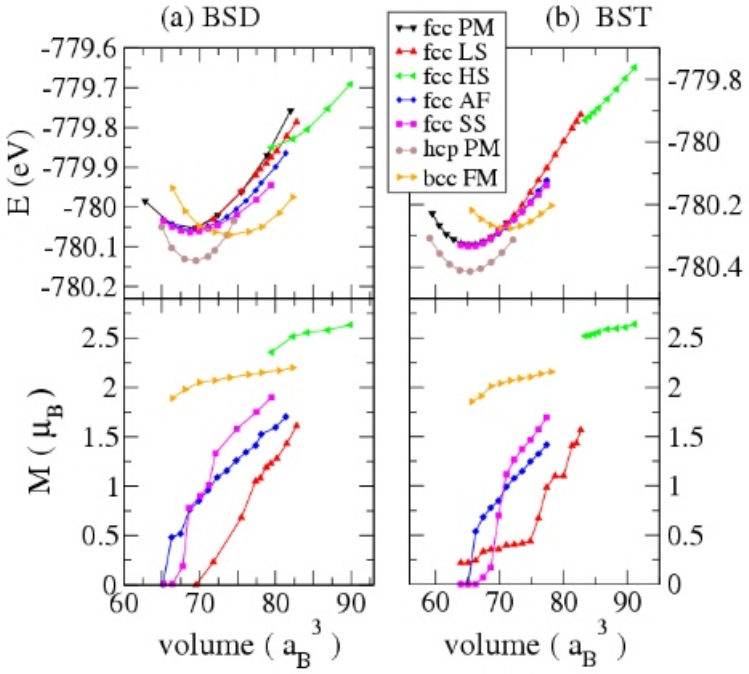

Fig. 3.8: Free energy and magnetic moment of the ground and lowest excited states of bulk iron as predicted by LDA, using (a) BSD and (b) BST, as a function of the atomic volume. PM = paramagnetic, FM = ferromagnetic, LS = low spin ferromagnetic, HS = high spin ferromagnetic, AF = antiferromagnetic, SS = spin spiral.

bcc ferromagnetic phase of bulk iron while figure (3.7) (a) shows the convergence of the energy for bcc ferromagnetic, fcc ferromagnetic high spin and fcc antiferromagnetic as a function of the number of orbitals used in each basis set. A TZ-TZ-TZ basis set (27 WF) is essentially converged for p, d and f orbitals, since the free energy of the three states changes only a little when more basis functions (polarized orbitals) are added. While I have not checked explicitly that a fourth ζ for the s orbital may still change somewhat the energy, a inspection of the curve shows that the results are completely converged.

Special attention was paid to the minimization of the basis set DZP-SZ-DZ (BSD, double-ζ polarized) and TZ-TZ-TZ (BST, triple-ζ polarized), where a grid software program was used to look for local minima of the energy as a function of the radii of the first ζ of s, p and d orbitals. There is a first local minimum for somewhat confined radii of about 6 a.u. and a deeper one for radii of about 10 a.u. The energy still decreased upon looking further away, tending to the ideal case of infinite radii. Figure (3.7) (b) shows

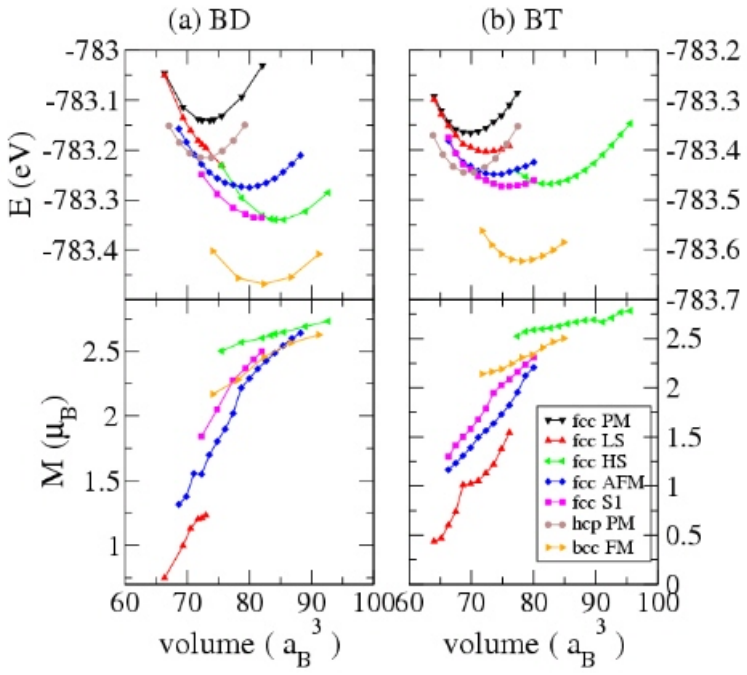

Fig. 3.9: Free energy and magnetic moment of the ground and lowest excited states of bulk iron as predicted by GGA functional, using (a) BSD and (b) BST, as a function of the atomic volume. The notation is the same as in figure (3.8).

Tab. 3.1: Bond length a (Å), binding energy per atom E_b (eV/atom) and total magnetic moment M (μ_B) for iron clusters with up to 5 atoms, calculated with a TZ basis and GGA.

	a (Å)	B (eV/Å)	M (μ_B)
Fe_2	2.02	1.51	6.00
Fe_3 $D_{\infty h}$	2.28	1.72	5.62
Fe_3 C_{3v}	2.27	1.88	10.00
Fe_4 C_{4v}	2.30	2.21	14.00
Fe_4 T_d	1,2↔3,4 2.27	2.31	14.00
	1↔2, 3↔4 2.65		
Fe_5 D_{3h}	1↔2,3 2↔3 2.43	2.58	17.07
	1,2,3↔4,5 2.37		

that extended radii improve both the energy and the lattice constant substantially. For instance, the lattice constant of the bcc ferromagnetic state obtained using BSD with the GGA functional as predicted by the first minimum is 2.90 Å, while the second one gives $a_0 = 2.88$ Å.

BSD predicts erroneous orderings of the ground and first excited states. Such effect is particularly evident in LDA. Figure (3.8) (a) shows that BSD erroneously gives lower energies for the LDA ferromagnetic bcc state than for the paramagnetic fcc one. Figure (3.8) (b) shows that usage of more complete basis sets correct such a mistake. Under such proviso, SIESTA provides pretty accurate results for the LDA predictions of the different physical magnitudes. For instance, the lattice constant, magnetic moment and bulk modulus of ferromagnetic bcc iron are found to be 2.76 Å, 2.08μ_{B} and 2.68 Mbar, which compare extremely well with the best all-electrons Plane-wave calculations [145]. Moreover, the lattice constant for paramagnetic fcc, 3.38 Å, is also very similar to all-electrons estimate of 3.375 Å, while the energy difference between both states is somewhat underestimated (55 versus about 70-80 meV). [145].

BSD also provides awkward results with the GGA functional, even though the relative stability of the lowest energy states is correct (see figure (3.9)). Nevertheless, the shape of the energy curves of the fcc states change significantly when the size of the basis is increased from BSD to BST. Increasing further the size of the basis set, including more polarization orbitals of p, d and f symmetry, does not change significantly the energy of these curves, which means that they are essentially converged (see figure (3.7)). The spiral state was computed for lattice constants well below 3.54 Å, which produced a binding energy curve with clear parabolic shape and a minimum at $a = 3.56$ Å, very close to the experimental value (3.577 Å). In the bcc phase the equilibrium lattice constant, magnetic moment and bulk modulus are 2.85 Å, 2.31 μ_{B} and 1.83 Mbar, which compare reasonably well with former all-electrons or ultrasoft-pseudopotentials-based plane waves calculations

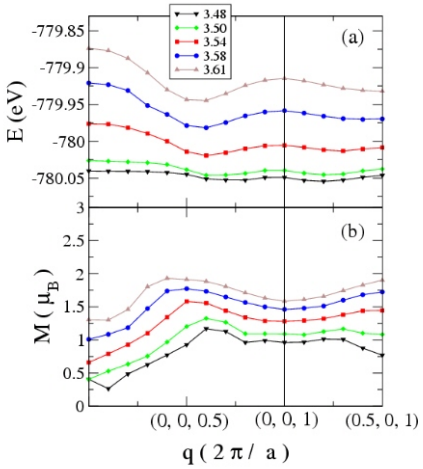

Fig. 3.10: Free energy (a) and magnetic moment (b) as a function of pitch vector $\vec{q}$ of the spiral state for lattice constants ranging from 3.48 Åto 3.61 Å, calculated with LDA and a double-ζ basis.

[146, 125] and with the experimental values 2.87 Å, 2.22 μ_B and 1.68 Mbar.

I also simulated clusters with a number of atoms ranging from 2 to 5, using a BST and the non-collinear GGA, as shown in table (3.1). These calculations compare again very well with previous theoretical simulations [113, 147, 142, 148, 115] and even improve them when comparisons are made with the experimental values of the Fe_2 cluster [149].

3.3.3 Spiral states in the γ phase

I turn now to the predictions for the spiral state in LDA. The energy was scanned as function of pitch vector along the ΓX and XW directions, where it has two minima, $\vec{q}_1 = (2\pi/a)(0, 0, 0.6)$ and $\vec{q}_2 = (2\pi/a)(0.2, 0, 1)$. On closer inspection of figure (3.10), it can be seen that the energy curves for lattice constants equal or larger than 3.58 Å only develop the $\vec{q}_1$ minimum. The second minimum appears when the lattice constant a is decreased below 3.54 Å, becoming lowest in energy at $a \approx 3.50$ Å. The curves corresponding to smallest lattice constants are very shallow. Their two minima have almost the same energy up to 1 meV, and are separated by energy barriers as small as 4 meV. If LDA were accurate enough for iron, one would expect both phases not only to coexist but also to change dynamically from one to the other.

On the other hand, the results obtained with GGA show that the $\vec{q}_2$ state has already clearly developed when $a = 3.52$ Å, but the ground state is $\vec{q}_1$ down to lattice constants of 3.47 Å (see figure (2.26)). The energy curves change rather much when the size of the

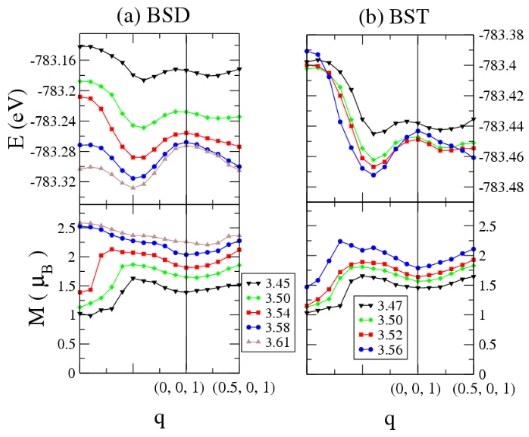

Fig. 3.11: Free energy (top) and magnetic moment (bottom) as a function of pitch vector $\vec{q}$ of the spiral state for lattice constants ranging from 3.45 Åto 3.61 Å, calculated with GGA and double (a) or triple (b) ζ bases.

basis is increased, but for BST the ferromagnetic state has always considerably higher energy and there is a clearer asymmetric double-well structure with activation barriers of about 5-7 meV. The equilibrium lattice constant for the $\vec{q}_1$ state is $a = 3.56$ Å, which is much closer to experiments than the result of Marsman and Hafner [126], and the resulting spiral curve, which interpolates between the antiferro and the ferro high-spin, has a clear minimum, in contrast to the case of Knöplfe and coworkers [125].

3.3.4 Conclusions

In summary, I can say that this results reproduce or even improve previous calculations. I found lattice constants and magnetic moments which compare very well with the experiments. Using my implementation of the generalized Bloch's theorem in SIESTA I found a spiral cohesion curve with a well defined minimum and a lattice parameter almost identical to the experimental value. However, I also failed to reproduce the correct pitch vector. The discrepancies are probably due to some inherent failure of the GGA functional, since it was originally developed for collinear configurations. I would expect then that a more accurate functional, which would also include the off-diagonal elements of the density matrix, would produce better results.

4

Ab Inito Calculations of Spin Wave Spectra

I describe in this chapter the implementation and optimization of a theoretical approach to calculate spin waves and other spin configurations. I apply the resulting code to the study of the magnon dispersion relation in Fe and Ni and I obtain results which nicely agree with previous theoretical simulations. This work paves the way to future studies of spin wave spectra in a wide range of materials.

4.1 Introduction

The finite temperature behavior of magnetic materials can be understood in terms of spin fluctuations which rotate or reorient locally the local magnetic moments. These low-energy excitations, characterized by energy scales of tens of meV, can explain the Curie-Weiss law and the observed Curie temperatures [120] and take active part or influence many properties that lie in the same energy range: electrical and heat transport, specific heat and superconductivity. Accessibility to the knowledge of such fluctuations is obtained experimentally by measuring the neutron scattering cross section, which is directly related to the imaginary part of the magnetic susceptibility [150]. Such a knowledge opens the way to understand many intriguing phenomena related to spin dynamics. For example, some people believe that the high-temperature superconductivity could be mediated by a spin fluctuation mechanism [150].

The wave vector and frequency dependent spin susceptibility, which gives the response of the medium to an external perturbation, is, according to the fluctuation-dissipation

theorem, directly related to the fluctuation spectrum [151]. Theoretical calculations of this quantity based on first principles simulations can give then accurate information about the spin configurations and spin dynamics of many materials [152, 153, 154], and can be taken as as first step to reproduce and understand other properties. Typical dynamical responses studied by ab initio methods are spin waves, also called magnons, which can be generated applying a transverse oscillatory magnetic field to a magnetic material [155, 156, 157, 158]. Additional information about magnetic configurations is also given by the zero frequency susceptibility, which provides an alternative method to calculate spin spiral arrangements.

4.1.1 The magnetic susceptibility

When a magnetic field $\vec{H}$ is applied to a magnetic material it induces changes in the magnetization $\delta\vec{M} = \vec{M} - \vec{M}_0$ which can be highly nontrivial. In the limit of small $\vec{H}$, however, it is possible to get rid of non-linear components and express the dependence of the induced magnetization as follows [151]:

$$\delta\vec{M}(\vec{r},t) = \int \mathrm{d}\vec{r}' \int_{-\infty}^{t} \mathrm{d}t' \hat{\chi}(\vec{r},\vec{r}';t,t')\vec{H}(\vec{r}',t') \tag{4.1}$$

or, in reciprocal space,

$$\delta\vec{M}(\vec{k},\Omega) = \sum_{\vec{q}} \int \mathrm{d}\omega \hat{\chi}(\vec{k},\vec{q};\Omega,\omega)\vec{H}(\vec{q},\omega) \tag{4.2}$$

where $\hat{\chi}(\vec{q},\omega)$ is the dynamic susceptibility,

$$\chi_{\mu\nu} = \frac{\partial M_\mu}{\partial H_\nu} = \frac{\partial^2 E}{\partial H_\nu \partial H_\mu} \tag{4.3}$$

which is a functional of the magnetic field. In stationary and/or spatially uniform mediums the susceptibility depends only on the difference of times $t - t'$ and/or the relative spatial coordinates $\vec{r} - \vec{r}'$ [151]. It can also be complex when the magnetization and the field have different phases. Experimentally it is measured using neutron scattering [155, 156, 157].

In ferromagnets and other collinear systems it is possible to distinguish between transverse and longitudinal susceptibilities. Longitudinal responses are produced by fields that change the moduli of the magnetic vectors. The longitudinal component of such fields generates spin-spin, spin-charge, charge-spin and charge-charge susceptibilities [160, 159] which increases dramatically the complexity of the calculation. However, pure transverse responses, which are created by transverse magnetic fields that change only the direction

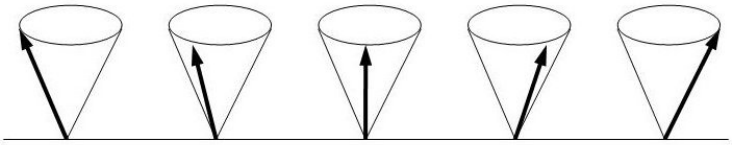

Fig. 4.1: A schematic example of the magnetization in a transverse magnetic wave propagating perpendicular to the magnetic field.

of the magnetization [158, 159], are much easier to compute since only the spin response is necessary to describe them.

Modern investigations of the transverse dynamical susceptibility were initiated by Izuyama and coworkers [161], who, using the Hubbard model [162], obtained the result

$$\chi(\vec{q},\omega) = \frac{\chi^0(\vec{q},\omega)}{1 - U\chi^0(\vec{q},\omega)} \tag{4.4}$$

where U is the intraatomic repulsion and χ^0 is the susceptibility of the noninteracting reference system. In general any transverse magnetic susceptibility calculated using perturbation theory can be reduced to the above expression [158, 159].

4.2 Spin Waves

Transverse spin fluctuations are generated when an oscillatory transverse magnetic field is applied to a ferromagnetic material. Such fluctuations can give rise to collective excitations known as spin waves or magnons (see figure (4.1)) when the applied magnetic field is circularly polarized,

$$\begin{aligned}\vec{H}(\vec{r},t) &= H[\cos(\vec{q}\cdot\vec{r}-\omega t)\vec{e}_x + \sin(\vec{q}\cdot\vec{r}-\omega t)\vec{e}_y] = \\ &= \frac{H}{\sqrt{2}}[e^{-i(\vec{q}\cdot\vec{r}-\omega t)}\vec{e}_+ + e^{i(\vec{q}\cdot\vec{r}-\omega t)}\vec{e}_-] = \\ &= \frac{1}{\sqrt{2}}[H_-\vec{e}_+ + H_+\vec{e}_-]\end{aligned} \tag{4.5}$$

where $\vec{e}_\pm = (\vec{e}_x \pm i\vec{e}_y)/\sqrt{2}$ and $H_\pm = H_x \pm iH_y$. The wave vectors and frequencies at which spin waves are generated are given by the poles of the imaginary part of dynamic suscep-

tibility, which can be calculated using perturbation theory [158] within the formalism of time-dependent density functional theory [163]. This section shows how to do it.

4.2.1 Magnetization

The circularly polarized magnetic field induces a new spin vector, $\vec{m} = \vec{m}^0 + \vec{m}^1$ (see figure (4.2)), which drives the initial collinear and stationary density matrix into a non-collinear and non-stationary state [158]:

$$\begin{aligned}\hat{n}(\vec{r},t) &= \begin{pmatrix} n^{\uparrow\uparrow}(\vec{r},t) & n^{\uparrow\downarrow}(\vec{r},t) \\ n^{\downarrow\uparrow}(\vec{r},t) & n^{\downarrow\downarrow}(\vec{r},t) \end{pmatrix} = \hat{n}^0(\vec{r},t) + \hat{n}^1(\vec{r},t) = \\ &= \begin{pmatrix} n^0(\vec{r},t) + \frac{1}{2}m^0(\vec{r},t) & 0 \\ 0 & n^0(\vec{r},t) - \frac{1}{2}m^0(\vec{r},t) \end{pmatrix} + \\ &+ \begin{pmatrix} n^1(\vec{r},t) + \frac{1}{2}m^1(\vec{r},t)\cos\theta & \frac{1}{2}m^1_-(\vec{r},t) \\ \frac{1}{2}m^1_+(\vec{r},t) & n^1(\vec{r},t) - \frac{1}{2}m^1(\vec{r},t)\cos\theta \end{pmatrix}\end{aligned} \tag{4.6}$$

where θ is the polar angle (see figure (3.2)) of the $\vec{m}^1$ vector and the transverse components are given by

$$m^1_\pm = -\mathrm{Tr}\{\hat{\tau}_\pm \hat{n}^1\} = -m^1 \sin\theta e^{\pm i\varphi} \tag{4.7}$$

where $\tau_\pm = \tau_x \pm i\tau_y$ and φ is the azimutal angle. When the induced part of the density and the modulus of the induced spin vector, n^1 and m^1, are much smaller than n^0 and m^0, respectively, it is possible to get rid of the longitudinal terms:

$$\hat{n}^1(\vec{r},t) \simeq \frac{1}{2}\begin{pmatrix} 0 & m^1_-(\vec{r},t) \\ m^1_+(\vec{r},t) & 0 \end{pmatrix} \tag{4.8}$$

Finally, the components of the magnetization are $M^1_\pm \simeq -m^1_\pm$.

4.2.2 Susceptibility

Next step is to link the spin components $m^1_\pm$ to the magnetic field components $H_\pm$ using the susceptibility. According to the fluctuation-dissipation theorem [151], which relates the susceptibility to the spin fluctuations, it is possible express χ in terms of the correlation function:

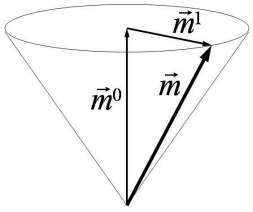

Fig. 4.2: Change induced in the spin vector by an external magnetic field. The magnetization has the opposite sign.

$$\chi_{ij} \sim < S_i^\dagger S_j > \tag{4.9}$$

where $i, j = \{x, y, z, +, -\}$. For pure transverse responses one has

$$\hat{\chi} = \begin{pmatrix} \chi_{xx} & \chi_{xy} & 0 \\ \chi_{yx} & \chi_{yy} & 0 \\ 0 & 0 & 0 \end{pmatrix} \tag{4.10}$$

Taking into account that $S_\pm = S_x \pm iS_y$, $H_\pm = H_x \pm iH_y$, $< S_+^\dagger S_- >=< S_- S_- >= 0$ and $< S_-^\dagger S_+ >=< S_+ S_+ >= 0$, it is easy to demonstrate that

$$M_+ = \frac{1}{2}\chi_{++} H_+ \tag{4.11}$$

$$M_- = \frac{1}{2}\chi_{--} H_- \tag{4.12}$$

where $\chi_{++} =< S_+^\dagger S_+ >=< S_- S_+ >$ and $\chi_{--} =< S_-^\dagger S_- >=< S_+ S_- >$, which verify

$$\mathrm{Re}\left[\chi_{++}(\vec{q}, \omega)\right] = \mathrm{Re}\left[\chi_{--}(\vec{q}, -\omega)\right] \tag{4.13}$$

$$\mathrm{Im}\left[\chi_{++}(\vec{q}, \omega)\right] = -\mathrm{Im}\left[\chi_{--}(\vec{q}, -\omega)\right] \tag{4.14}$$

For an oscillatory field acting on a stationary medium one has

$$\begin{aligned} M_+(\vec{r}, t) &= \frac{1}{2}\int\int \chi_{++}(\vec{r}, \vec{r}\,'; t - t') H_+(\vec{r}\,', t')\mathrm{d}t'\mathrm{d}\vec{r}\,' = \\ &= \frac{H}{2}\int\int \chi_{++}(\vec{r}, \vec{r}\,'; t - t') e^{i(\vec{q}\cdot\vec{r}\,' - \omega t')}\mathrm{d}t'\mathrm{d}\vec{r}\,' \end{aligned} \tag{4.15}$$

By the causality principle, $\chi(\vec{r},\vec{r}';t-t')=0$ for $t<t'$, and then

$$M_+(\vec{r},t)=\frac{H}{2}\chi_{++}(\vec{r},\vec{q},-\omega)e^{-i\omega t} \tag{4.16}$$

In periodic systems the susceptibility verifies Bloch's theorem and can be decomposed as the product of a phase and a periodic function

$$\chi(\vec{r},\vec{q},\omega)=e^{i\vec{q}\cdot\vec{r}}\bar{\chi}(\vec{r},\vec{q},\omega) \tag{4.17}$$

with $\bar{\chi}(\vec{r}+\vec{R},\vec{q},\omega)=\bar{\chi}(\vec{r},\vec{q},\omega)$. This periodic part can be expanded in Fourier series, as I will show later. The first term of the Fourier expansion gives the value of χ integrated to the whole unit cell, which is what is needed to determine the poles.

4.2.3 Hamiltonian

The initial stationary and collinear Hamiltonian is the usual DFT Hamiltonian:

$$\hat{\mathcal{H}}^0(\vec{r})=\left[T(\vec{r})+\int \mathrm{d}\vec{r}'\frac{n^0(\vec{r}')}{|\vec{r}-\vec{r}'|}\right]\hat{I}+\begin{pmatrix}V^{xc\uparrow}[\hat{n}^0(\vec{r})] & 0\\ 0 & V^{xc\downarrow}[\hat{n}^0(\vec{r})]\end{pmatrix} \tag{4.18}$$

On the other hand, the external oscillatory magnetic field introduces an external potential given by

$$\hat{V}^{\mathrm{ext}}(\vec{r},t)=g\vec{H}(\vec{r},t)\cdot\hat{\vec{S}}=\frac{1}{2}g\vec{H}(\vec{r},t)\cdot\hat{\vec{\tau}}\simeq\vec{H}(\vec{r},t)\cdot\hat{\vec{\tau}}=\begin{pmatrix}0 & H_-(\vec{r},t)\\ H_+(\vec{r},t) & 0\end{pmatrix} \tag{4.19}$$

Such a potential produces a change in the density matrix which induces a first order component

$$\hat{\mathcal{H}}^1(\vec{r},t)=\underbrace{\int \mathrm{d}\vec{r}'\frac{n^{1\,l}(\vec{r}',t)}{|\vec{r}-\vec{r}'|}}_{\sim 0}+\left.\frac{\delta V^{xc}[\hat{n}(\vec{r})]}{\delta\hat{n}(\vec{r})}\right|_{\hat{n}^0}\hat{n}^1(\vec{r},t) \tag{4.20}$$

where $n^{1\,l}$ is the longitudinal change in the density matrix, which is negligible. The second term can be approximated in LDA by

$$\left.\frac{\delta V^{xc}[\hat{n}(\vec{r})]}{\delta\hat{n}(\vec{r})}\right|_{\hat{n}^0}\hat{n}^1(\vec{r},t)\simeq\frac{V^{xc\uparrow}[n^0(\vec{r})]-V^{xc\downarrow}[n^0(\vec{r})]}{|n^{0\uparrow}(\vec{r})-n^{0\downarrow}(\vec{r})|}\frac{1}{2}\begin{pmatrix}0 & m^1_-(\vec{r},t)\\ m^1_+(\vec{r},t) & 0\end{pmatrix} \tag{4.21}$$

The spin vector is related to the component of the magnetization and, subsequently, to the magnetic field. The sum of the external potential and the induced Hamiltonian is a matrix whose diagonal elements are zero and whose off-diagonal elements are given by

$$\begin{aligned}\hat{\mathcal{H}}^{1\uparrow\downarrow}(\vec{r},t)+\hat{V}^{\text{ext}\uparrow\downarrow}(\vec{r},t)&=V_{--}(\vec{r},\vec{q},-\omega)=\\&=H\left(-\frac{V^{xc\uparrow}(\vec{r})-V^{xc\downarrow}(\vec{r})}{4m^0(\vec{r})}\chi_{--}(\vec{r},-\vec{q},\omega)+e^{-i\vec{q}\cdot\vec{r}}\right)e^{i\omega t} \qquad (4.22)\\ \hat{\mathcal{H}}^{1\downarrow\uparrow}(\vec{r},t)+\hat{V}^{\text{ext}\downarrow\uparrow}(\vec{r},t)&=V_{++}(\vec{r},\vec{q},-\omega)=\\&=H\left(-\frac{V^{xc\uparrow}(\vec{r})-V^{xc\downarrow}(\vec{r})}{4m^0(\vec{r})}\chi_{++}(\vec{r},\vec{q},-\omega)+e^{i\vec{q}\cdot\vec{r}}\right)e^{-i\omega t} \qquad (4.23)\end{aligned}$$

The final time-dependent Hamiltonian[1] is then written as the sum of the initial Hamiltonian and an additional term which is supposed small enough to perform a perturbative expansion.

4.2.4 Perturbation theory

Using first order time-dependent perturbation theory[2] it is easy to arrive at the following expression:

$$\left(i\frac{\partial}{\partial t}-\hat{\mathcal{H}}^0(\vec{r})\right)\hat{\Psi}^1_{n\vec{k}}(\vec{r},t)=\left(\hat{\mathcal{H}}^1(\vec{r},t)+\hat{\mathcal{H}}^{\text{ext}}(\vec{r},t)\right)\hat{\Psi}^0_{n\vec{k}}(\vec{r},t) \tag{4.24}$$

where the unperturbed and collinear wave functions $\Psi^{0\,\sigma}_{n\vec{k}}(\vec{r},t)=\Psi^{0\,\sigma}_{n\vec{k}}(\vec{r})e^{-i\varepsilon^{0\,\sigma}_{n\vec{k}}t}$ are eigenstates of $\hat{\mathcal{H}}^0$. The perturbed wave functions $\hat{\Psi}^1$ are expanded in terms of such eigenstates:

$$\Psi^{1\,\sigma}_i(\vec{r},t)=\sum_j c^{-\sigma}_{ij}(t)\Psi^{0\,-\sigma}_j(\vec{r},t) \tag{4.25}$$

[1] The time-dependent version of the Hohenberg-Kohn theorems are the Runge-Gross theorems, which relate the time-dependent density and the time-dependent potential [163].

[2] Since the susceptibility is calculated as the second derivative of the energy with respect to the magnetic field, it is necessary to obtain the energy up to second order. This implies, according to the $2n+1$ theorem [164], that the wave function has to be determined to first order.

where $\sigma = \{\uparrow, \downarrow\}$ and i and j stand for $\{n, \vec{k}\}$. The expansion terms have opposite spin because the magnetic field flips it. Using equation (4.24) is is possible to obtain the following relation (I focus on the ++ component):

$$c_{ij}^{\uparrow}(t) = \int \frac{V_{++}(\vec{r}, \vec{q}, -\omega)}{\omega + \varepsilon_i^{0\downarrow} - \varepsilon_j^{0\uparrow} - i\delta} \Psi_j^{0\uparrow *}(\vec{r}) \Psi_i^{0\downarrow}(\vec{r}) e^{-i(\omega - \varepsilon_i^{0\downarrow} - \varepsilon_j^{0\uparrow})t} \mathrm{d}\vec{r} \tag{4.26}$$

where δ is a small imaginary part which is added to fulfill the causality principle.

4.2.5 Selfconsistent equation

The induced density matrix is calculated in this way:

$$\hat{n}^1(\vec{r}, t) = \frac{1}{2} \begin{pmatrix} 0 & m_-^1(\vec{r}, t) \\ m_+^1(\vec{r}, t) & 0 \end{pmatrix} = \sum_{i,\sigma} f_i^{\sigma} \left(\hat{\Psi}_i^{0\,\sigma\,\dagger}(\vec{r}, t) \hat{\Psi}_i^{1\,\sigma}(\vec{r}, t) + \hat{\Psi}_i^{1\,\sigma\,\dagger}(\vec{r}, t) \hat{\Psi}_i^{0\,\sigma}(\vec{r}, t) \right) \tag{4.27}$$

where $f_i^{\sigma} = f(\varepsilon_i^{0\,\sigma} - \varepsilon_{\mathrm{F}})$ is the Fermi distribution function. Working out this equation and taking into account equation (4.26), it is possible to derive the following expression:

$$\begin{aligned} \frac{1}{2} m_+^1(\vec{r}, t) = \sum_{i,j} & \frac{f_i^{\downarrow} - f_j^{\uparrow}}{\omega + \varepsilon_i^{0\downarrow} - \varepsilon_j^{0\uparrow} - i\delta} \Psi_i^{0\downarrow *}(\vec{r}) \Psi_j^{0\uparrow}(\vec{r}) e^{-i\omega t} \times \\ & \times \int V_{++}(\vec{r}\,', \vec{q}, -\omega) \Psi_i^{0\downarrow}(\vec{r}\,') \Psi_j^{0\uparrow *}(\vec{r}\,') \mathrm{d}\vec{r}\,' \end{aligned} \tag{4.28}$$

Using now equations (4.7) and (4.11) which relate the spin vector, the magnetization m_+^1 and the susceptibility, the following self-consistent equation is found [158]:

$$\begin{aligned} \chi_{++}(\vec{r}, \vec{q}, -\omega) = 4 \sum_{i,j} & \frac{f_j^{\uparrow} - f_i^{\downarrow}}{\omega + \varepsilon_i^{0\downarrow} - \varepsilon_j^{0\uparrow} - i\delta} \Psi_i^{0\downarrow *}(\vec{r}) \Psi_j^{0\uparrow}(\vec{r}) \times \\ & \times \int \left(- \frac{V^{xc\uparrow}(\vec{r}\,') - V^{xc\downarrow}(\vec{r}\,')}{4m^0(\vec{r}\,')} \chi_{++}(\vec{r}\,', \vec{q}, -\omega) e^{-i\vec{q}\cdot\vec{r}\,'} + 1 \right) \times \\ & \times e^{i\vec{q}\cdot\vec{r}\,'} \Psi_i^{0\downarrow}(\vec{r}\,') \Psi_j^{0\uparrow *}(\vec{r}\,') \mathrm{d}\vec{r}\,' \end{aligned} \tag{4.29}$$

Decomposing also the susceptibility as a product of a phase and a periodic function (equation (4.17)) and defining it as

$$\chi_{++}(\vec{r},\vec{q},-\omega) = 4e^{i\vec{q}\cdot\vec{r}}\bar{\chi}_{++}(\vec{r},\vec{q},-\omega) \tag{4.30}$$

one finally obtains

$$\begin{aligned}\bar{\chi}_{++}(\vec{r},\vec{q},-\omega) = \sum_{i,j}\frac{f_j^{\uparrow}-f_i^{\downarrow}}{\omega+\varepsilon_i^{0\downarrow}-\varepsilon_j^{0\uparrow}-i\delta}e^{-i\vec{q}\cdot\vec{r}}\Psi_i^{0\downarrow *}(\vec{r})\Psi_j^{0\uparrow}(\vec{r})\times\\ \times\int\left(-\frac{V^{xc\uparrow}(\vec{r}\,')-V^{xc\downarrow}(\vec{r}\,')}{m^0(\vec{r}\,')}\bar{\chi}_{++}(\vec{r}\,',\vec{q},-\omega)+1\right)\\ \times e^{i\vec{q}\cdot\vec{r}\,'}\Psi_i^{0\downarrow}(\vec{r}\,')\Psi_j^{0\uparrow *}(\vec{r}\,')\mathrm{d}\vec{r}\,'\end{aligned} \tag{4.31}$$

Taking into account that $\bar{\chi}_{++}(\vec{r},\vec{q},\omega)$ is periodic, $e^{-i\vec{q}\cdot\vec{r}}\sum_{n,n',\vec{k},\vec{k}'}\Psi_{n'\vec{k}'}^{0\downarrow *}(\vec{r})\Psi_{n\vec{k}}^{0\uparrow}(\vec{r})$ must also be periodic[3]. On the other hand, using the fact that each wave function $\hat{\Psi}_{n\vec{k}}$ can be decomposed as a product of a phase and a periodic function, it is easy to demonstrate that $\vec{k}'=\vec{k}+\vec{q}$. Finally, expressing the wave functions as linear combinations of atomic orbitals (see equation (1.39)) the previous terms can be written as follows:

$$\sum_{n,n',\vec{k},\vec{k}'}\Psi_{n'\vec{k}'}^{0\downarrow *}(\vec{r})\Psi_{n\vec{k}}^{0\uparrow}(\vec{r}) = \sum_{n,n',\vec{k}}\sum_{\mu,\vec{R},\nu}e^{-i\vec{k}\cdot(\vec{d}_\mu-\vec{R}_\nu)}c_{n'\vec{k}+\vec{q}\mu}^{\downarrow *}c_{n\vec{k}\nu}^{\uparrow}\phi_\mu(\vec{r}-d_\mu)\phi_{\vec{R}_\nu}(\vec{r}-\vec{R}_\nu) \tag{4.32}$$

Equation (4.29) acquires then the following form:

$$\begin{aligned}\bar{\chi}_{++}(\vec{r},\vec{q},-\omega) = \sum_{n,n',\vec{k}}\frac{f_{n\vec{k}}^{\uparrow}-f_{n'\vec{k}+\vec{q}}^{\downarrow}}{\omega+\varepsilon_{n'\vec{k}+\vec{q}}^{\downarrow}-\varepsilon_{n\vec{k}}^{\uparrow}-i\delta}\times\\ \times e^{-i\vec{q}\cdot\vec{r}}\sum_{\mu,\vec{R},\nu}e^{i\vec{q}\cdot d_\mu}e^{-i\vec{k}\cdot(\vec{d}_\mu-\vec{R}_\nu)}c_{n'\vec{k}+\vec{q}\mu}^{\downarrow *}c_{n\vec{k}\nu}^{\uparrow}\phi_\mu(\vec{r}-\vec{d}_\mu)\phi_{\vec{R}_\nu}(\vec{r}-\vec{R}_\nu)\times\\ \times\int\left(-\frac{V^{xc\uparrow}(\vec{r}\,')-V^{xc\downarrow}(\vec{r}\,')}{m_0(\vec{r}\,')}\bar{\chi}_{++}(\vec{r}\,',\vec{q},-\omega)+1\right)\times\\ \times e^{i\vec{q}\cdot\vec{r}\,'}\sum_{\mu',\vec{R}',\nu'}e^{-i\vec{q}\cdot\vec{d}_{\mu'}}e^{i\vec{k}(\vec{d}_{\mu'}-\vec{R}'_{\nu'})}c_{n'\vec{k}+\vec{q}\mu'}^{\downarrow}c_{n\vec{k}\nu'}^{\uparrow *}\times\\ \times\phi_{\mu'}(\vec{r}\,'-\vec{d}_{\mu'})\phi_{\vec{R}'_{\nu'}}(\vec{r}\,'-\vec{R}'_{\nu'})\mathrm{d}\vec{r}\,'\end{aligned} \tag{4.33}$$

This is a self-consistent or Dyson-type equation [158] which is used to calculate the magnetic susceptibility from the electronic structure provided by the DFT calculation.

[3] From now on the indexes i and j are substituted by $(n,\vec{k})$ and $(n',\vec{k}')$ respectively.

Equation (4.33) can be solved using a recursive method, i. e. starting from a guessed χ_{++} and iterating the equation until the difference between the input and the output susceptibilities is small enough. However, it is more convenient to work in reciprocal space, expanding the susceptibility in terms of the reciprocal lattice vectors $\vec{G}$:

$$\bar{\chi}_{++}(\vec{r},\vec{q},-\omega) = \frac{1}{V}\sum_{\vec{G}} \tilde{\chi}_{++}(\vec{G},\vec{q},-\omega)e^{i\vec{G}\cdot\vec{r}} \tag{4.34}$$

$$\tilde{\chi}_{++}(\vec{G},\vec{q},-\omega) = \int \bar{\chi}(\vec{r},\vec{q},-\omega)e^{-i\vec{G}\cdot\vec{r}}\mathrm{d}\vec{r} \tag{4.35}$$

where V is the unit cell volume. The self-consistent equation is then transformed into a matrix equation:

$$\begin{aligned}
\tilde{\chi}_{++}(\vec{G},\vec{q},-\omega) = & \sum_{n,n',\vec{k}} \frac{f^{\uparrow}_{n\vec{k}} - f^{\downarrow}_{n'\vec{k}+\vec{q}}}{\omega + \varepsilon^{\downarrow}_{n'\vec{k}+\vec{q}} - \varepsilon^{\uparrow}_{n\vec{k}} - i\delta} \times \\
& \times \int e^{-i(\vec{G}+\vec{q})\cdot\vec{r}} \sum_{\mu,\vec{R},\nu} e^{i\vec{q}\cdot d_\mu} e^{-i\vec{k}\cdot(\vec{d}_\mu - \vec{R}_\nu)} c^{\downarrow\,*}_{n'\vec{k}+\vec{q}\mu} c^{\uparrow}_{n\vec{k}\nu} \times \\
& \times \phi_\mu(\vec{r}-\vec{d}_\mu)\phi_{\vec{R}_\nu}(\vec{r}-\vec{R}_\nu)\mathrm{d}\vec{r} \times \\
& \times \int \left(-\frac{V^{xc\,\uparrow}(\vec{r}\,') - V^{xc\,\downarrow}(\vec{r}\,')}{m_0(\vec{r}\,')} \sum_{\vec{G}'} \tilde{\chi}_{++}(\vec{G}',\vec{q},-\omega) e^{i(\vec{G}'+\vec{q})\cdot\vec{r}\,'} + e^{i\vec{q}\cdot\vec{r}\,'} \right) \times \\
& \times e^{i\vec{q}\cdot\vec{r}\,'} \sum_{\mu',\vec{R}',\nu'} e^{-i\vec{q}\cdot\vec{d}_{\mu'}} e^{i\vec{k}(\vec{d}_{\mu'} - \vec{R}'_{\nu'})} c^{\downarrow}_{n'\vec{k}+\vec{q}\mu'} c^{\uparrow\,*}_{n\vec{k}\nu'} \times \\
& \times \phi_{\mu'}(\vec{r}\,' - \vec{d}_{\mu'})\phi_{\vec{R}'_{\nu'}}(\vec{r}\,' - \vec{R}'_{\nu'})\mathrm{d}\vec{r}\,'
\end{aligned} \tag{4.36}$$

The final equation can then be written as follows:

$$\tilde{\chi}_{++}(\vec{G},\vec{q},-\omega) = \tilde{\chi}^0_{++}(\vec{G},\vec{q},-\omega) + \sum_{\vec{G}} \Pi(\vec{G},\vec{G}',\vec{q},-\omega)\tilde{\chi}_{++}(\vec{G}',\vec{q},-\omega) \tag{4.37}$$

where

$$\tilde{\chi}^0_{++}(\vec{G},\vec{q},-\omega) = \sum_{n,n',\vec{k}} \frac{f^{\downarrow}_{n\vec{k}} - f^{\uparrow}_{n'\vec{k}+\vec{q}}}{\omega + \varepsilon^{\downarrow}_{n'\vec{k}+\vec{q}} - \varepsilon^{\uparrow}_{n\vec{k}} - i\delta} B^{\uparrow\downarrow}_{n\vec{k}n'\vec{k}+\vec{q}}(\vec{G},\vec{q}) B^{\uparrow\downarrow\,*}_{n\vec{k}n'\vec{k}+\vec{q}}(\vec{0},\vec{q}) \tag{4.38}$$

$$\Pi(\vec{G},\vec{G}',\vec{q},-\omega) = \sum_{n,n',\vec{k}} \frac{f^{\downarrow}_{n\vec{k}} - f^{\uparrow}_{n'\vec{k}+\vec{q}}}{\omega + \varepsilon^{\downarrow}_{n'\vec{k}+\vec{q}} - \varepsilon^{\uparrow}_{n\vec{k}} - i\delta} B^{\uparrow\downarrow}_{n\vec{k}n'\vec{k}+\vec{q}}(\vec{G},\vec{q}) C^{\uparrow\downarrow\,*}_{n\vec{k}n'\vec{k}+\vec{q}}(\vec{G}',\vec{q}) \tag{4.39}$$

and

$$B^{\uparrow\downarrow}_{n\vec{k}n'\vec{k}+\vec{q}}(\vec{G},\vec{q}) = \sum_{\mu,\vec{R},\nu} e^{i\vec{q}\cdot\vec{d}_\mu} e^{-i\vec{k}\cdot(\vec{d}_\mu-\vec{R}_\nu)} c^{\downarrow\,*}_{n'\vec{k}+\vec{q}\mu} c^{\uparrow}_{n\vec{k}\nu} S_{\mu\vec{R}_\nu}(\vec{G},\vec{q}) \tag{4.40}$$

$$C^{\uparrow\downarrow}_{n\vec{k}n'\vec{k}+\vec{q}}(\vec{G},\vec{q}) = \sum_{\mu,\vec{R},\nu} e^{i\vec{q}\cdot\vec{d}_\mu} e^{-i\vec{k}\cdot(\vec{d}_\mu-\vec{R}_\nu)} c^{\downarrow\,*}_{n'\vec{k}+\vec{q}\mu} c^{\uparrow}_{n\vec{k}\nu} \mathcal{H}_{\mu\vec{R}_\nu}(\vec{G},\vec{q}) \tag{4.41}$$

with

$$S_{\mu\vec{R}_\nu}(\vec{G},\vec{q}) = \int e^{i(\vec{G}+\vec{q})\cdot\vec{r}} \phi_\mu(\vec{r}-\vec{d}_\mu)\phi_{\vec{R}_\nu}(\vec{r}-\vec{R}_\nu)\mathrm{d}\vec{r} \tag{4.42}$$

$$\mathcal{H}_{\mu\vec{R}_\nu}(\vec{G},\vec{q}) = -\int e^{i(\vec{G}+\vec{q})\cdot\vec{r}} \frac{V^{xc\,\uparrow}(\vec{r}) - V^{xc\,\downarrow}(\vec{r})}{V m_0(\vec{r})} \phi_\mu(\vec{r}-\vec{d}_\mu)\phi_{\vec{R}_\nu}(\vec{r}-\vec{R}_\nu)\mathrm{d}\vec{r} \tag{4.43}$$

Finally,

$$\tilde{\chi}_{++}(\vec{G},\vec{q},-\omega) = \sum_{\vec{G}'} \left[1-\Pi\right]^{-1}(\vec{G},\vec{G}',\vec{q},-\omega)\tilde{\chi}^0_{++}(\vec{G}',\vec{q},-\omega) \tag{4.44}$$

The solution is calculated for every vector $\vec{G}$, although only the $\vec{G}=\vec{0}$ term, which gives the integral of the susceptibility in the unit cell, is needed. These expressions, which are implemented numerically as an appendix to the SIESTA code (the 'magnon code') are used at the end of the self-consistent procedure of SIESTA to evaluate the magnon dispersion relation.

4.2.6 Paramagnetic systems

In systems with no spin polarization both density matrix components, $n^{0\,\uparrow}$ and $n^{0\,\downarrow}$, and both exchange-correlation potential components, $V^{xc\uparrow}[\hat{n}^0(\vec{r})]$ and $V^{xc\downarrow}[\hat{n}^0(\vec{r})]$, are equal. The first part of the term V_{++} is then calculated using L'Hôpital rule, i. e. taking the functional derivative of the numerator and the denominator. With the LDA functional the result is the following:

$$\lim_{m\to 0} \frac{V^{xc\,\uparrow}[n,m] - V^{xc\,\downarrow}[n,m]}{m} = \frac{\delta\left(V^{xc\,\uparrow}[n,m] - V^{xc\,\downarrow}[n,m]\right)}{\delta m} = \\ = \frac{1}{2}\sum_{\sigma=\uparrow,\downarrow} \mathrm{sgn}(\sigma)\left(\frac{\delta V^{xc\,\uparrow}[n^\uparrow,n^\downarrow]}{\delta n^\sigma} - \frac{\delta V^{xc\,\downarrow}[n^\uparrow,n^\downarrow]}{\delta n^\sigma}\right) \tag{4.45}$$

where $\mathrm{sgn}(\uparrow) = 1$ and $\mathrm{sgn}(\downarrow) = -1$.

With GGA the derivation is a bit more complicated because gradients have to be taken into account:

$$\lim_{m\to 0} \frac{V^{xc\uparrow}[n,m,\nabla n,\nabla m] - V^{xc\downarrow}[n,m,\nabla n,\nabla m]}{m} =$$
$$= \frac{1}{2}\sum_{\sigma=\uparrow,\downarrow} \mathrm{sgn}(\sigma)\left\{\frac{\delta V^{xc\uparrow}[n^\uparrow,n^\downarrow,\nabla n^\uparrow,\nabla n^\downarrow]}{\delta n^\sigma} - \frac{\delta V^{xc\downarrow}[n^\uparrow,n^\downarrow,\nabla n^\uparrow,\nabla n^\downarrow]}{\delta n^\sigma} + \right.$$
$$\left. + \sum_{i=1}^{3}\left(\frac{\delta V^{xc\uparrow}[n^\uparrow,n^\downarrow,\nabla n^\uparrow,\nabla n^\downarrow]}{\delta(\nabla n^\sigma)_i} - \frac{\delta V^{xc\downarrow}[n^\uparrow,n^\downarrow,\nabla n^\uparrow,\nabla n^\downarrow]}{\delta(\nabla n^\sigma)_i}\right)\frac{\delta(\nabla n^\sigma)_i}{\delta n^\sigma}\right\} \quad (4.46)$$

The zero-frequency $\vec{q}$-space structure of the paramagnetic susceptibility can be used to study non-collinear or spiral magnetic configurations that may be stabilized in these systems at low temperature [165, 166, 167]. This method, apart from giving information about spin fluctuations, provides an alternative technique to reproduce spin spiral arrangements.

4.3 Approximations

The numerical execution of the previous method is extremely demanding due to the large amount of computer memory and processor time that it needs. The first problem is produced by the matrix $\Pi(\vec{G},\vec{G}',\vec{q},-\omega)$, which depends on four components and generates an array with $N_{\vec{G}}^2 N_{\vec{q}} N_\omega$ elements. Another problem comes from the huge amount of sums that enter the calculation of $\hat{\Pi}$ and $\bar{\chi}_0$. These sums, which involve many different terms (bands, atomic and orbital indexes, k points, ω-points, and G-points), originate multiple loops that increase the execution time dramatically. In order to make the calculation feasible it is then necessary to reduce its size with some approximations.

4.3.1 Leading matrix term

The number of loops can be considerably reduced by using perturbation theory to approximate the product of the $\hat{\Pi}$ matrix and the $\hat{\bar{\chi}}$ vector,

$$\sum_{\vec{G}'} \Pi(\vec{G},\vec{G}')\bar{\chi}(\vec{G}') \simeq \Pi(\vec{G},\vec{0})\bar{\chi}(\vec{0}) + \Pi(\vec{G},\vec{G})\bar{\chi}(\vec{G}) \quad (4.47)$$

and extracting the term $\bar{\chi}(\vec{0})$:

$$\bar{\chi}(\vec{0}) \simeq \frac{\bar{\chi}_0(\vec{0}) + \sum_{\vec{G}} \frac{\Pi(\vec{0},\vec{G})\bar{\chi}_0(\vec{G})}{1-\Pi(\vec{G},\vec{G})}}{1 - \sum_{\vec{G}} \frac{\Pi(\vec{0},\vec{G})\Pi(\vec{G},\vec{0})}{1-\Pi(\vec{G},\vec{G})}} \tag{4.48}$$

This simple trick, which assumes the leading terms in the $\hat{\Pi}$ matrix for a certain column/row are the first and the diagonal element, simplifies the calculation dramatically but produces results which differ significantly from the exact solution. Anyhow, it can be used in some cases to obtain information about the simulation (for example, to study the dependence on the basis set, the number of k points, etc.).

4.3.2 Padé approximant

The evaluation of $\chi_0(\omega)$ and $\Pi(\omega)$ near the real frequency axis can be numerically very expensive due to the large number of points which are needed to reproduce the lorentzian peaks. To decrease such a number and further simplify the problem it is better to calculate these functions, which I will call $F(\omega)$, on a set of N points on the imaginary axis (Matsubara frequencies) $\{z_n = i\omega_n, n = 1, ..., N\}$ an then make the analytic continuation to the real axis using a N-point Padé approximant [168]:

$$P_N(z = \omega - i\delta) = \frac{A_N(z)}{B_N(z)} \tag{4.49}$$

where A_N and B_N are polynomials of order $(N-2)/2$ and $N/2$ for even N and $(N-1)/2$ for odd N. Such polynomials are calculated with Thiele's reciprocal method:

$$A_{n+1}(z) = A_n(z) + (z - z_n)a_{n+1}A_{n-1}(z) \tag{4.50}$$
$$B_{n+1}(z) = B_n(z) + (z - z_n)a_{n+1}B_{n-1}(z) \tag{4.51}$$

where $A_0 = 0$, $A_1 = a_1$ and $B_0 = B_1 = 1$ and

$$a_n = g_n(z_n), \quad g_1(z_n) = F(z_n), \quad n = 1, ..., N \tag{4.52}$$
$$g_n(z) = \frac{g_{n-1}(z_{n-1}) - g_{n-1}(z)}{(z - z_{n-1})g_{n-1}(z)}, \quad n \geq 2 \tag{4.53}$$

are the coefficients of the expansion.

This approximation reduces dramatically the execution time and the required amount of memory since it decreases significantly the number of ω-points which are used in the most demanding part of the simulation. According to Lee and Chang [168], it can also reduce the number of k points if the functions are smooth enough. However, to obtain results similar to the exact solution I had to use as many k points as in the case without Padé approximant. This means that the approximated functions $\chi_0(\omega)$ and $\Pi(\omega)$ are not smooth and have to be calculated very carefully.

4.3.3 Numerical cutoffs

In the calculation of $\hat{\Pi}$ and $\hat{\chi}_0$ there are many elements which are very small and do not influence the final result. To optimize the code it is necessary to get rid of them:

- Only the bands close to the Fermi energy whose Fermi weight differences are not vanishing (see equation (4.29)) and whose energy difference is smaller than the maximum value of ω need to be taken into account.
- Many matrix elements of $S_{\mu\vec{R}_\nu}(\vec{G},\vec{q})$ and $\mathcal{H}_{\mu\vec{R}_\nu}(\vec{G},\vec{q})$ are negligible. Such elements can be identified and eliminated before the summations are performed.
- Many of the products $B^{\uparrow\downarrow}_{n\vec{k}n'\vec{k}+\vec{q}}(\vec{G},\vec{q})C^{\uparrow\downarrow\,*}_{n\vec{k}n'\vec{k}+\vec{q}}(\vec{G},\vec{q})$ are also negligible since their size progressively decreases as $|\vec{G}|$ or $|\vec{G}'|$ increase. It is possible then to use a G- and G'-dependent cutoff, $c = a(1 + (\vec{G}| + |\vec{G}'|)/b$ where a is an the biggest cutoff value and b is a constant which is optimized for every system, to reduce the execution time and the size of the arrays that depend on $\vec{G}$ and $\vec{G}'$.

With an intelligent selection of the cutoffs the calculation can be dramatically speeded up. However, care must be taken to ensure the final results are good enough, since large cutoffs can significantly decrease the accuracy of the calculation.

4.4 Spin Wave Spectra of Iron and Nickel

I applied the magnon code to study the spin wave dispersion relation in the bcc phase of iron and the fcc phase of nickel. The dynamic susceptibility of bcc iron, which has been largely studied, is characterized by a parabolic dispersion relation for $\vec{q}$ along the (001) direction (in units of $2\pi/a$) [155, 157, 169, 170, 152, 171, 153, 154, 172] before it is damped by the presence of Stoner excitations [151]. The dispersion relation in fcc nickel along the same direction is also parabolic at the beginning [156, 159, 170] but has an acoustic and an optical branch which split at $\omega \sim 100$ meV. This behavior is not accurately described by LDA due to its overestimation of the exchange splitting [173, 169, 174, 175, 152, 154, 172].

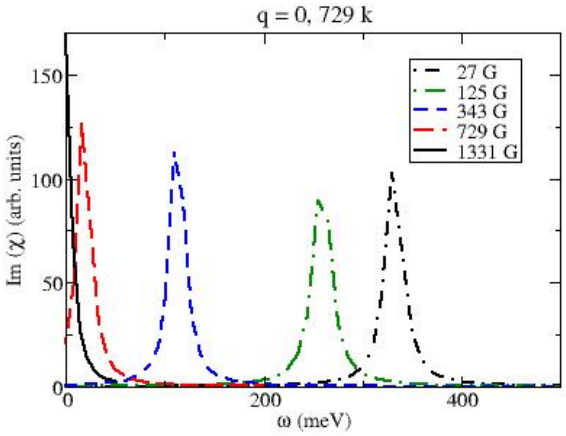

Fig. 4.3: Dependence of the position of the $q = 0$ peak on the number of G's. A single$-\zeta$ basis set and 729 k points were used. The Padé approximant was not included.

I use iron and nickel as test cases to check the validity of the general theory, the numerical implementation in a DFT scheme and the precision of the approximations. The aim of this section is, therefore, to verify that the code works and determine the minimum number of k, G and Padé points and the size of the numerical cutoffs needed to perform accurate and fast calculations. I used the LDA functional, whose expression for the derivative of the exchange-correlation potential can be explicitly derived, and single$-\zeta$ or double$-\zeta$ basis sets. Most of the simulations were performed in the bcc phase of iron at the theoretical lattice constant (2.78 Å). The following examples refer to this material.

4.4.1 Optimization of the code

First I check Goldstone's Theorem [176], which predicts an excitation at $q = 0$ and $\omega = 0$ for ferromagnetic systems. This implies that the imaginary part of $\chi(\vec{0}, \vec{0}, \omega)$ must have a peak at $\omega = 0$. In practice, however, such a peak only appears at the correct position for very high accuracies, i. e. for very large numbers of k, G and Padé-points, as I will show in the following paragraphs.

The dependence on the number of G's is shown in figure (4.3). For few G's the peak[4] appears at very high energies, but progressively moves towards the origin as the number of G's is increased[5]. For $q \neq 0$ the dependence is very similar to the case $q = 0$ and,

[4] The units of the vertical axis are arbitrary because the height of the peaks depend on the value of δ (see equation (4.26)). I take δ equal to the separation between ω points in the real energy axis, but sometines I multiply it by a certain factor to smooth the curve.

[5] Each $\vec{G}$ is calculated as a combination of integer multiples of the reciprocal lattice vectors and its

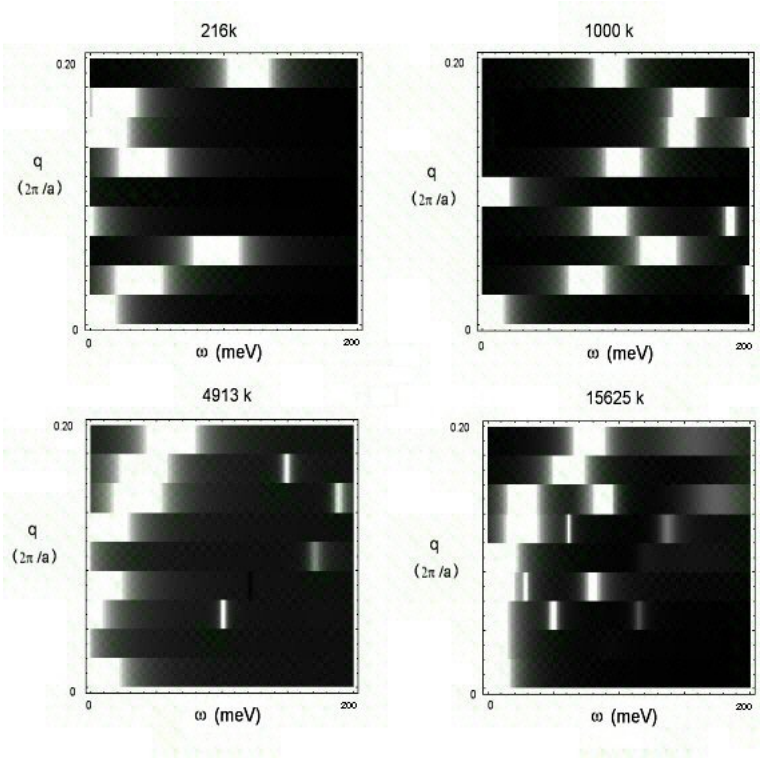

Fig. 4.4: Dependence of the dispersion relation curve on the number of k points. A single$-\zeta$ basis set and 1331 G points were used. The Padé approximant was not included.

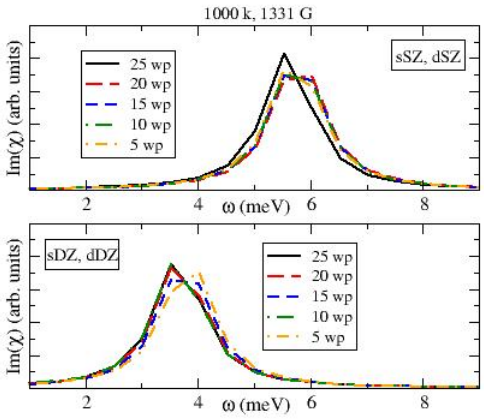

Fig. 4.5: Dependence of the $q = 0$ peak on the number of Padé-points and the basis set (single$-\zeta$ and double$-\zeta$). 1000 k points and 1331 G points were used.

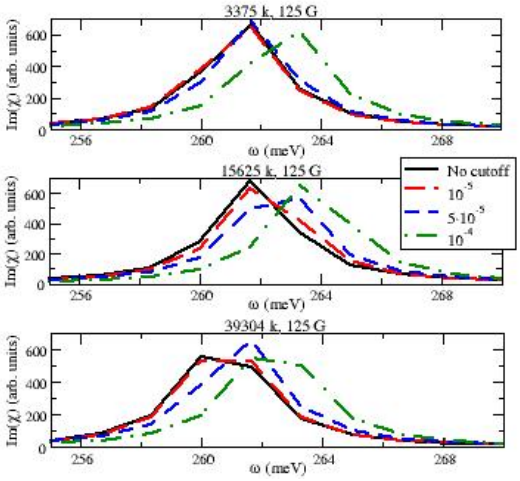

Fig. 4.6: Dependence of the $q = 0$ peak on the number of k points and the numerical cutoff used for the products $B^{\uparrow\downarrow}_{n\vec{k}n'\vec{k}+\vec{q}}(\vec{G},\vec{q})C^{\uparrow\downarrow\,*}_{n\vec{k}n'\vec{k}+\vec{q}}(\vec{G},\vec{q})$, calculated with a single-ζ basis set. The observed behavior does not depend on the number of G's and therefore a relatively small number (125) was used.

therefore, the curve moves almost rigidly when this parameter is changed. However, the overall shape of the curve for $q \neq 0$ depends dramatically on the number of k points, as can be seen in figure (4.4). The minimum number of k points needed for bcc iron is 15625, although some noise still remains. To obtain very smooth curves, like the one shown in figure (4.11), it is necessary to employ even more k's.

Another important parameter is the number of Padé-points, whose dependence is shown in figure (4.5). In general a number of 25 Padé-points is enough to accurately describe all features of the dispersion relation, both with single$-\zeta$ and double$-\zeta$ basis sets. Without such approximation, the number of ω points needed to generate accurate curves increases to 100 or even more. Therefore, the Padé approximant really decreases the execution time, although, as stated above, the minimum number of k points remains almost unchanged due to the fact that the functions $\chi_0(\omega)$ and $\Pi(\omega)$ are not smooth.

The effect of using a numerical cutoff in the products $B^{\uparrow\downarrow}_{n\vec{k}n'\vec{k}+\vec{q}}(\vec{G},\vec{q})C^{\uparrow\downarrow\,*}_{n\vec{k}n'\vec{k}+\vec{q}}(\vec{G},\vec{q})$ is shown in figures (4.6) and (4.7). To obtain reliable results for $q = 0$ the numerical cutoff has to be equal or smaller than 10^{-5}. Such a cutoff produces a reduction in the execution time of a 30%. For $q \neq 0$ the dependence is very similar to the case $q = 0$ (see Fig (4.7)) and, therefore, this parameter does not change the shape of the curve.

The cutoff introduced in the overlap and Hamiltonian matrix elements, $S_{\mu\vec{R}_\nu}(\vec{G},\vec{q})$

modulus has to be smaller than a certain $G_{\max}$. Therefore, the number of G points can not have arbitrary values but it is given by $(2n+1)^3$, where n is a positive integer which depends on $G_{\max}$.

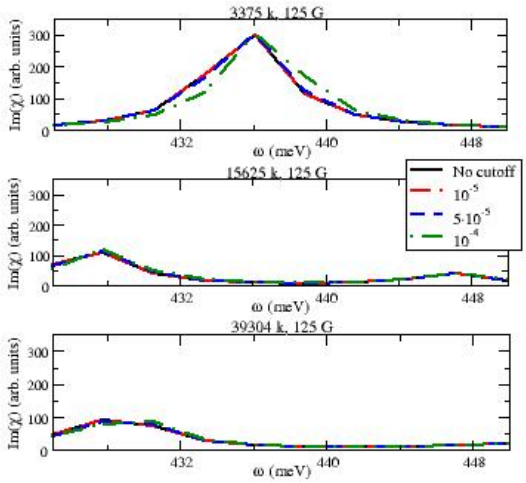

Fig. 4.7: The same as figure (4.6) calculated at $q = 0.40 \times 2\pi/a$.

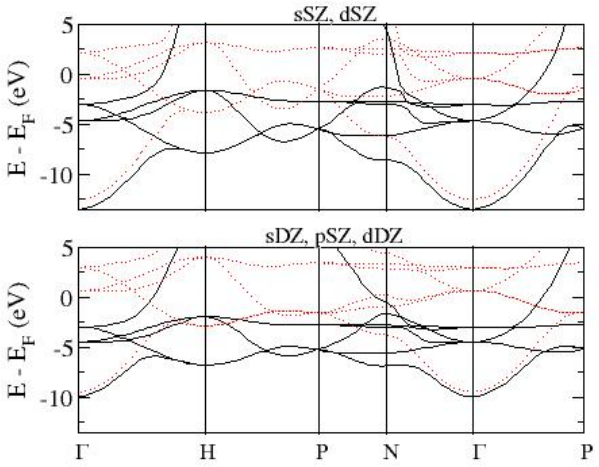

Fig. 4.8: Band structure of bcc iron calculated with a single$-\zeta$ and a double$-\zeta$ polarized basis set. Continuous and dotted lines represent majority and minority spins, respectively.

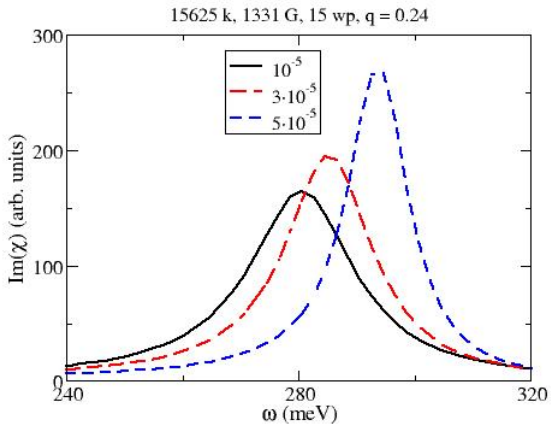

Fig. 4.9: Dependence of the $q = 0.24 \times 2\pi/a$ peak on the cutoff used in the elements $S_{\mu\vec{R}_\nu}(\vec{G},\vec{q})$ and $\mathcal{H}_{\mu\vec{R}_\nu}(\vec{G},\vec{q})$, calculated with a double-ζ basis set. The case without cutoff is indistinguishable from the black curve (10^{-5}).

and $\mathcal{H}_{\mu\vec{R}_\nu}(\vec{G},\vec{q})$ respectively, reduces also substantially the execution time. Such a cutoff becomes very important when double$-\zeta$ or higher bases are included, since the number of matrix elements increases sharply when new orbitals are used. The use of more complete basis sets is essential to converge the band structure and obtain reliable results (see the comparison between the band structure provided by single$-\zeta$ and a double$-\zeta$ polarized basis sets in figure (4.8) an the positions of the peaks calculated with a single$-\zeta$ and a double$-\zeta$ basis sets in figure (4.5)). The results obtained with a double-ζ basis set are shown in figure (4.9). The maximum numerical cutoff, which is of the order of 10^{-5}, reduces the execution time a 40%.

4.4.2 Results

Once the minimum number of k, G and Padé points and the best cutoffs have been determined it is possible to carry out an accurate calculation in a reasonable period of time (smaller than one week). I used the code to obtain the spin wave dispersion relation along (001) in bcc ferromagnetic iron and fcc ferromagnetic nickel. The experimental and theoretical curves are shown in figure (4.10) and my results, obtained with double-ζ basis set and the LDA functional, in figure (4.11).

In iron the resulting dispersion relation, calculated at the theoretical lattice constant (2.78 Å), is parabolic and agrees qualitatively with other theoretical calculations [152]. However, for $q \neq 0$ the curve moves to much higher frequencies and maintains always the same shape (compare it with figure (4.10) (a)). Such behavior is probably due to the basis

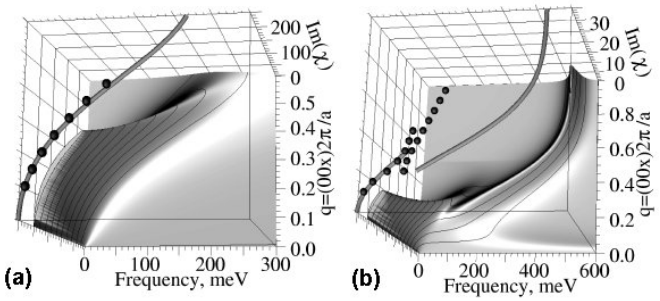

Fig. 4.10: Theoretical (continuous line and background) and experimental (dots) magnon dispersion relations for bcc ferromagnetic iron (a) and fcc ferromagnetic nickel (b) calculated along the (001) direction. Figure from [152].

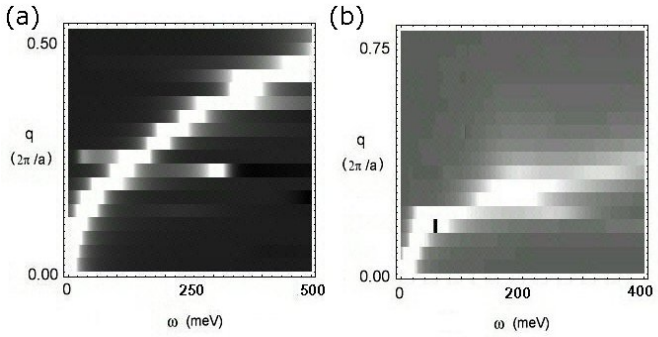

Fig. 4.11: (a) Magnon dispersion relation for bcc ferromagnetic iron calculated along (001) at the theoretical lattice constant (2.78 Å) with the LDA functional and a double$-\zeta$ basis set. (b) Magnon dispersion relation for fcc ferromagnetic nickel calculated along (001) at the theoretical lattice constant (3.40 Å) with the LDA functional and a double$-\zeta$ basis set. 39304 k points, 1331 G points, 25 Padé points and numerical cutoffs of the order of 10^{-5} were used in both cases. The scale goes from dark ($\chi = 0$) to white (highest values of χ).

set, a double-ζ without polarization, since, as shown in the previous chapter, at least a triple-ζ polarized basis set is needed to accurately describe iron. Another reason could be the number of G points, which was probably too small. However, without further simulations it is difficult to say. More work is needed to clarify this point.

The case of nickel, which was also calculated at the theoretical lattice constant (3.40 Å), agrees relatively well with the theoretical result [152, 154], although due to the small number of q and ω points used in the calculation (as as consequence of a lack of time and computer memory) it is not possible to clearly distinguish the central region where the acoustic and the optical branches split. Anyhow, this example demonstrates that the code works and can produce good results.

4.4.3 Conclusions

In conclusion, I have shown that it is possible to perform fast calculations of spin wave spectra starting from the ab initio electronic structure provided by SIESTA. I used bcc iron and fcc nickel as test cases to check the accuracy of the method and I found that, although the dispersion relation in iron moves to high frequencies due to a lack of precision, the agreement with previous studies is good. This study opens the door to future simulations of magnons and magnetic configurations in many different materials.

5

Tailoring Surface States via Strain

I present in this chapter a series of ab initio simulations of Cu/Ru(0001) layers and surfaces which help to understand the main processes that influence the superficial reactivity, i. e. strain, proximity of the last layer to the substrate, crystal structure, etc. Such effects modify the surface state and populate/depopulate it, altering dramatically many surface properties. By knowing how this state moves and behaves it is possible then to design surfaces with the desired reactivity.

5.1 Introduction

Real materials are not infinite solids but have surfaces surrounding and limiting them which interact with the atoms and molecules around. Each surface has characteristic physical and chemical properties which depend mainly on the material. Among these properties, the surface reactivity and catalytic behavior have a prominent role [177] and great effort has been devoted to understand and modify them at will. Only with the development of new experimental techniques (the scanning tunnelling microscope [190]) and theoretical methods (density functional theory [1, 2]) it has been possible to shed light on many of their mechanisms and achieve the desired goal of tailoring their behavior. Such an understanding will have deep consequences in the processes related to the adsorption and modification of molecules and will allow the fabrication of materials with very specific properties.

The reactivity is directly linked to the electronic structure of the surface, which can

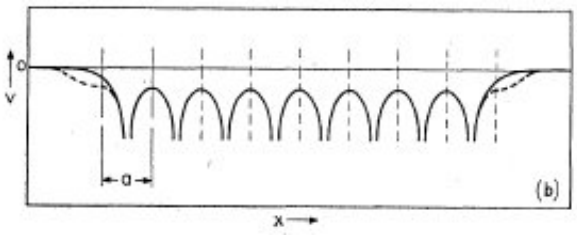

Fig. 5.1: Periodic potential (dotted lines) and corrected potential (continuous line) which produces surface states. Figure from [181].

differ strongly from the bulk electronic structure as a consequence of the deep changes in the potential and the boundary conditions. Such changes give rise to important rearrangements of charge and atomic positions and produce what is called the dipole, depletion or double layers [178]. The shape and extension of this region depend on whether the material is metallic or semiconducting/insulating. In the former the charge can be easily distributed near the surface and the effect of the electric fields goes sharply to zero away from it [179]. In the later, however, due to the lack of screening the depletion region is much larger and spreads deep into the bulk [180].

The charge redistribution, which depends on the material and the surface orientation, produces an increase in the work function, on one hand, and induces a relaxation of the atomic coordinates closer to the surface, on the other hand. Depending then on the type of system and the growth direction it is possible to obtain different electronic states and structural configurations which dramatically influence the reactivity and other properties of the surface.

5.1.1 Surface states

Every surface has electronic states that contribute to the local charge density localized between the material and the vacuum. These states, which play a very important role in many physical properties (adsorption of molecules, catalysis, surface reconstruction, surface magnetism, etc.) can be classified in two types: *surface resonances* and *surface states*. The former are bulk states with a enhanced weight on the surface. They can be considered as modified bulk states or surface states which overlap with bulk states. Surface states, however, are confined to the surface and decay exponentially into the vacuum and the solid. It is very easy to find them by using the bulk projected band structure, since they are localized in forbidden regions, i. e. within bulk band gaps, whereas the surface resonances appear inside bulk regions. The wave vector dependence of a perfect surface state can be then decomposed as follows:

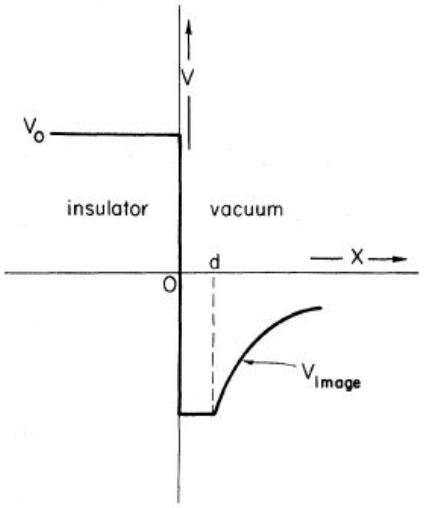

Fig. 5.2: Image potential felt by an electron in a surface state localized inside a bulk band gap that contains the vacuum. d is of the order of the interatomic distance, where the simple electrostatic model does not apply. Figure from [182].

$$\Psi_{\vec{k}}(\vec{r}) = \begin{cases} e^{\kappa r_\perp} e^{-i\vec{k}_\parallel \cdot \vec{r}_\parallel} u_{\vec{k}_\parallel}(\vec{r}) & r_\perp < 0 \\ e^{-\kappa' r_\perp} e^{-i\vec{k}_\parallel \cdot \vec{r}_\parallel} u_{\vec{k}_\parallel}(\vec{r}) & r_\perp > 0 \end{cases} \tag{5.1}$$

where $\parallel$ and $\perp$ denote the parallel and perpendicular components to the surface, respectively. The surface state has then an extended character on the plane parallel to the surface and an inverse exponential behavior in the perpendicular directions, where it can not penetrate due to the absence of bulk states.

The origin of these states can be understood by observing how the energy of a set of atoms varies when they are brought together to make a solid with the corresponding surfaces [181]. As the distance decreases the wave functions begin to overlap and the degenerated states split. If the potential is kept symmetric, as in the bulk (see figure (5.1)), there appear forbidden zones or gaps between bands, jus like in the case of an infinite crystal. However, if a more realistic potential is used, i. e. one that is a bit higher at the outer positions due to the absence of other atoms in the vacuum region, some states move into the bulk forbidden region. Such states correspond to typical surface states, with an imaginary component of k perpendicular to the surface.

An special case, which explains some situations where charge can appear far away from the surface, arises when the band gap contains the vacuum level. In such a configuration an electron outside the surface feels two forces: an repulsive force coming from the material and an attractive force coming from the image potential created by the image charge

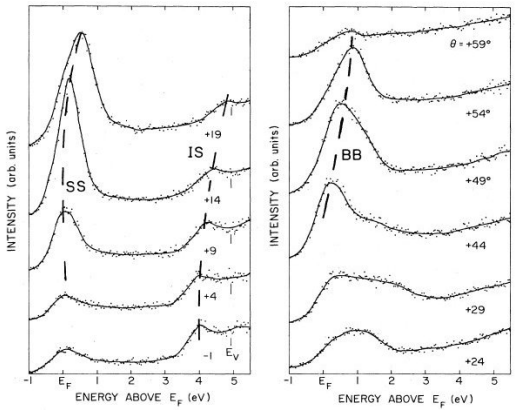

Fig. 5.3: KRIPES measurements taken on the Cu(111) surface as a function of the incident angle in the $\bar{\Gamma}\bar{K}$ azimuth at the phonon energy $\hbar\omega = 10.2$ eV. SS corresponds to a crystal-induced surface state, IS to a image-potential state and BB to a bulk band feature. Figure from [183] (modified).

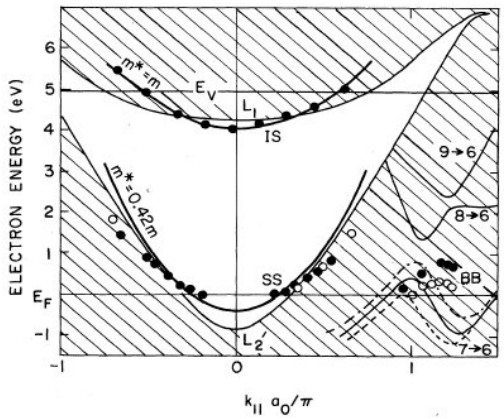

Fig. 5.4: Dispersion relation in the Cu(111) surface corresponding to figure (5.3) (full circles). Crosshatched area is the projection of the bulk band structure. Open circles and dashed lines correspond to measurements at other photon energies and numbers refer to the bulk bands. SS follows a parabolic dispersion ($m^* = 0.42m$) whereas IS has a free electron dispersion ($m^* = m$). Figure from [183].

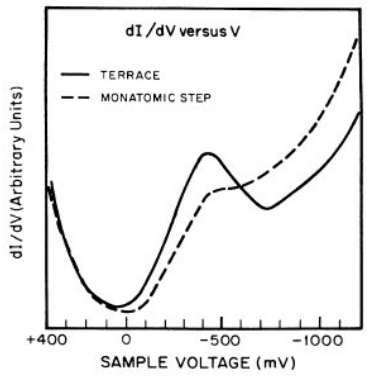

Fig. 5.5: STS spectra measured on top of a Au(001) surface on a terrace and a monoatomic step. Figure from [189].

[182, 184, 185, 183]. Electrons in such situation are less localized and can be as far as 200 Å away from the surface, giving rise to what are called image-potential states (see figure (5.2)).

Experimental characterization

Experimentally, surface states can be measured by using k resolved inverse photoemission spectroscopy (KRIPES) [186, 184]. This technique is based on bombarding the sample with electrons with a defined energy and a certain angle θ (which defines the incident $\vec{k}$ vector) and measuring the intensity of photons produced at a given energy by the decaying of the excited electrons within the solid. Such technique is sensitive to the surface due to the short path length of low energy electrons. The surface state is observed as a peak in the photoelectron spectrum within the energy bulk band gap, which is sensitive to adsorbates and other changes in the surface. Surface resonances are found similarly but they appear inside bulk bands. A typical example is shown in figure (5.3) for the Cu(111) surface. From the information provided by such measurements it is possible to construct dispersion relations like the one shown in figure (5.4). KRIPES, together with other methods such as Auger electron spectroscopy (AES) [187] and low-energy electron diffraction (LEED) [188], can then be used to completely characterize the electronic and structural properties of surfaces.

In the last decades, however, the most popular technique has been the scanning tunnelling microscope (STM) [190], which allows, on one hand, to measure surface structures in real space by mapping the variation of the tip height for a given tunnelling current, and, on the other hand, to determine the local density of states (LDOS) at a given point above the surface (scanning tunnelling spectroscopy, STS [191]). The LDOS is related to the differential conductance measured at a fixed height [192]:

$$\frac{\mathrm{d}I}{\mathrm{d}V} \propto \sum_{\text{sample}} |\Psi_{\text{sample}}(\vec{r}_{\text{tip}})|^2 \, \delta(E_{\text{sample}} - E_{\text{F}}) \tag{5.2}$$

Surface states are observed as peaks in the differential conductance curves, as shown in figure (5.5). The STM also allows to measure other interesting properties like the formation of standing waves of quantum interference [193], the shape of the Fermi contour [194], surface state dispersions [193] and surface state lifetimes [195].

Strain and finite size effects

Surface states are very sensitive to structural and electronic changes, which can dramatically alter their shape and occupation [196]. For example, by adding atoms below the surface which modify the electronic properties of the dipole layers [196] or by covering the surface with different adsorbates [197], the work function can be substantially affected and, therefore, the energy barrier at the surface can be lowered or increased, something which substantially modifies the energy position and dispersion of the surface state. Other changes include reducing the number of layers until the depth is smaller than the decay length of the surface state (this allows it to interact with the substrate), modifying the terrace width [198] (which has dramatic consequences on the mass transport and the growth behavior), or straining the material by using different substrates [196] or changing the temperature [199]. All these possibilities allow a precise tuning of the electronic and chemical properties of many surfaces.

5.1.2 Surface reactivity

Surfaces can be used to adsorb atoms and molecules or catalyze chemical reactions. In both situations a detailed knowledge of the electronic structure is essential to understand the elementary processes involved, but their complexity makes this a difficult task. In some cases, however, just by taking into account the number of dangling bonds and their shape it is easy to estimate the differences in reactivity between different sites on the surface [200]. Something similar can be applied to surfaces of transition or noble metals, whose chemistry is dominated by s, p and d states. In such surfaces it is possible to identify some rules that greatly influence the chemical interactions, due to the fact that the sp states are essentially the same for all these elements (although they make the biggest contribution to the adsorption energy) and the trends in reactivity are dictated by the d states. Such rules, which are based on the correlation between the surface core level shift and the molecular adsorption [201], are i) the position of the centroid of the d band[1], ii) the degree of filling of the *d* band and iii) the coupling matrix elements between

[1] In a very crude approximation the whole d band is substituted by its center of mass (the centroid).

the d band and the adsorbate states [202, 203].

However, there is another contribution that has not been properly taken into account. It comes from the surface state, since it was predicted that its depopulation can dramatically enhance the reactivity [204]. A populated surface state increases the charge in the surface and consequently increases the electronic repulsion between the surface electrons and the electrons of the incoming molecule. This repulsive interaction produces a high physisorption barrier which forbids the molecule to bind to the surface. However, if the surface state is depopulated, the repulsion becomes much smaller and the molecule can easily reach the surface.

The physisorption/chemisorption process can be understood easily by analyzing the energetic curve of a simple molecule that approaches a surface, as shown in figure (5.6). When the molecule is far away from the surface the relevant forces have an electrostatic origin (dipole-dipole interactions and/or van der Waals (dispersion) forces). Such forces attract the molecule to the physisorption minimum, where it is weakly bound. If the distance is decreased more, two effects coming from the sp states start gaining influence. One is the hybridization of the molecular levels with the sp continuum, which splits and broadens them. The second effect is a pure electrostatic repulsion. Schematically this process can be understood in terms of bonding and an antibonding orbitals: first both of them are occupied, but when the antibonding orbital crosses the Fermi energy (which defines the top of the activation barrier) its electrons pass to the surface and the process becomes energetically favorable. After that, the molecular levels start hybridizing with the d band until the Pauli repulsion becomes important. Therefore, the sp states are responsible of the physisorption barrier whereas the d states define the chemisorption minimum.

The energy of the d states and the sp surface states can be conveniently modified by straining or compressing the surface. This can be done for example by including bubbles of noble gases below the surface during the fabrication process, which expand locally the surface and compress the regions in between [205]. However, the most efficient way of producing a lateral expansion is by growing a material on top of a substrate with a larger lattice constant [206, 196, 207, 208]. Such an expansion produces an increasing in the reactivity which has been attributed to the up-shift in energy of the d states [209]. However, the influence of the sp states, which also change dramatically during the deformation process, was clearly underestimated.

5.1.3 The system Cu/Ru(0001)

The interest in this system comes from the fact that the Ru(0001) surface works reasonably well as catalyst to convert hydrocarbons. However, this catalytic activity can be enhanced as much as a factor of 40 when a monolayer of Cu is added on top of it [210], something that has deep consequences on the chemical reactions that involve these molecules.

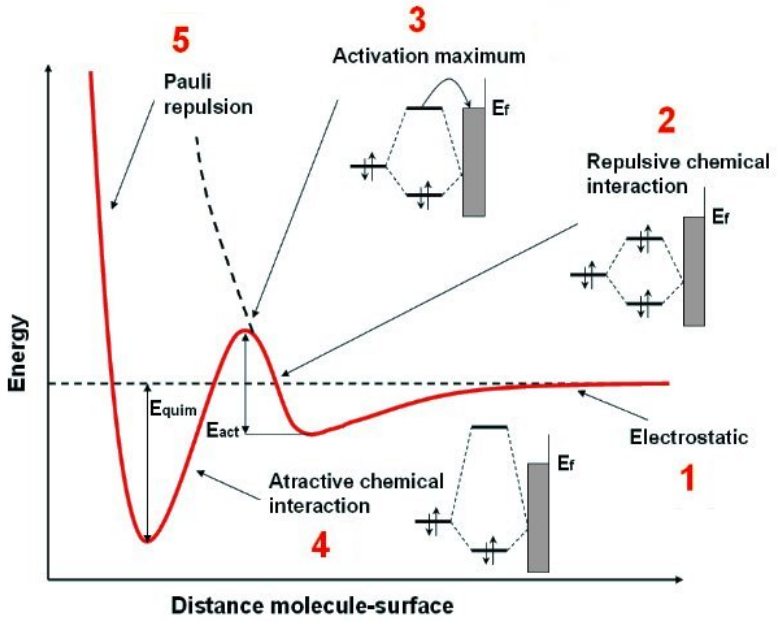

Fig. 5.6: Energetic curve which describes the adsorption process of a simple molecule that approaches the surface. The first step (1) corresponds to an attractive electrostatic potential which brings the molecule to the physisorption minimum. When the distance is decreased the interaction with the sp surface state starts being repulsive (2) until the antibonding state crosses the Fermi energy and its electrons pass to the surface (3). The process becomes then energetically favorable (4) until the Pauli repulsion increases the energy again (5). The interplay of the last two processes defines the chemisorption minimum.

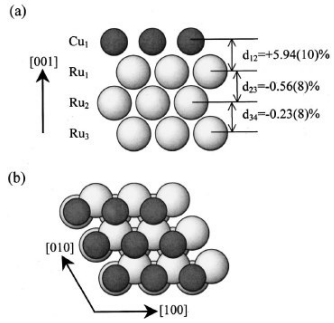

Fig. 5.7: Side (a) and top (b) view of the hcp Cu/Ru(0001)-(1×1) structure. Distances are given in terms of the hard sphere model, where Cu atoms are supposed to be a 5.8% smaller than Ru atoms. Figure from [208].

The structure of monolayers (ML) of Cu on top of hcp Ru grown along (0001) has been extensively characterized using LEED and x-ray photoelectron diffraction [211, 212, 207, 208]. The first Cu monolayer is pseudomorphic wit the Ru substrate [206] and is separated from it 2.10-2.15 Å. An schematic representation can be seen in figure (5.7), where distances are calculated in terms of a hard spheres model. When more Cu layers are added, the vertical distances tend progressively to the bulk Cu distance (2.08 Å). The same happens with the lateral distances but the uniaxial relaxation of the strain produces a stripe-phase reconstruction, with three possible directions along which the atomic positions of the second Cu layer can relax (see figures (5.8) and (5.9)). When more ML are added the reconstruction becomes more complex due to the fact that the atoms can relax along more directions, as can be seen in figure (5.10). For more than ten layers the surface is indistinguishable from a Cu(111) surface.

Experiment

The experiment was performed by the group of R. Miranda at Universidad Autonoma de Madrid. It was carried out in a ultrahigh vacuum chamber equipped with a variable temperature scanning tunnelling microscope, LEED, AES, and facilities for ion sputtering, metal evaporation and control of the gas exposure. The Ru(0001) crystal was Ar^+ sputtered and heated until no traces of contaminants were observed. The resulting morphology consisted of 600 Å wide terraces separated by monoatomic steps and some bunching areas in between. In some cases it is also detected a small density of smooth circular protrusions due to the presence under the surface of Ar bubbles originated during the sputtering, which produce a upwards bending of the surface layer. Cu was deposited from a W basket filled with Cu pellets. To obtain well ordered Cu films with thicknesses below 2 ML the sample was kept at 500 K during deposition. The I-V curves were taken at 65-300 K and numerically differentiated to obtain the $\mathrm{d}I/\mathrm{d}V$ tunnelling conductance

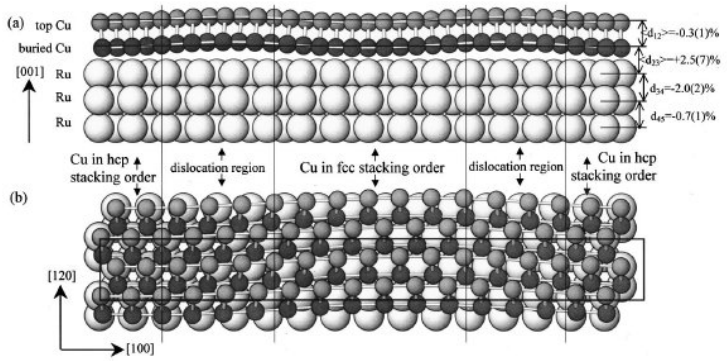

Fig. 5.8: Top (a) and side (b) view of the surface reconstruction in the second Cu layer. Distances as in figure (5.7). Figure from [208].

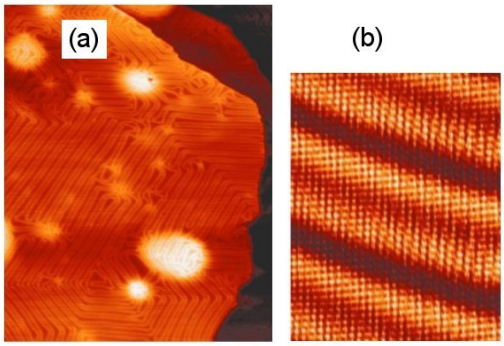

Fig. 5.9: (a) 160 nm×127 nm STM image of 2 ML of Cu grown on Ru(0001). The brighter parts of the image correspond to subsurface Ar bubbles. (b) 10 nm×8 nm STM image of 2 ML of Cu grown on Ru(0001) which shows the atomic details of the reconstruction (see figure (5.8)).

spectra. Finally, oxygen was dosed by backfilling the vacuum chamber with molecular oxygen.

The STS spectra recorded on a clean Ru(0001) surface shows the presence of a sharp peak located slightly above the Fermi level, as can be seen in figure (5.11). This peak disappears if the measurement is performed on a step, which clearly shows the surface character of the state. A similar peak is also found in the Cu(111) surface (see figure (5.12)) but it is completely filled since it is located below the Fermi level. However, in a pseudomorphic ML of Cu on top of Ru the peak shifts upwards in energy and crosses the Fermi energy. This is accompanied by a sudden change in the reactivity of the surface, seen as a sharp increase in the adsorption of oxygen[2]. When a second layer is added and

[2] The surface chemical reactivity can be quantified by measuring the initial average sticking probability,

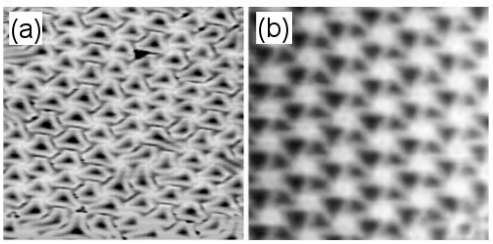

Fig. 5.10: 3 ML (a) and 4 ML (b) of Cu on top of Ru(0001). The average lattice constants are 2.610 Å and 2.557 Å, respectively.

Tab. 5.1: Sticking coefficients for different Cu thicknesses on top of Ru(0001) and a clean Cu(111) surface.

Cu coverage (ML)	Initial sticking coefficient
1	0.6 ± 0.1
2	0.10 ± 0.05
3	0.002 ± 0.001
Cu(111)	0.0005 ± 0.0002

the strain is partially relaxed the peak moves down and the adsorption rate decreases, starting thus a trend in the peak shift and the surface reactivity that can be clearly seen in figure (5.12) and table (5.1). In view of these results it is possible to conclude that those effects are correlated, i. e. the strain induces the depopulation of the surface state and decreases the activation barrier needed to adsorb oxygen. This is also verified by measuring STS spectra on top of locally strained zones produced by the presence of Ar bubbles. Such zones are very reactive and produce another upward shift of the surface state (see figure (5.13)).

5.2 Ab Initio Study of Cu/Ru(0001)

To understand the basic physics involved in this system and unveil the influence of strain, proximity to the substrate, crystal structure, and other properties, I performed a series of ab initio simulations of surfaces of Ru, Cu and layers of Cu on top of Ru(0001) (1-4 ML) with the ab initio package SIESTA. The special characteristics of this code (density functional theory, localized basis sets and pseudopotentials) allowed me to simulate a relatively large amount of atoms with a reasonable degree of accuracy and obtain results

which is defined as the ratio of the rate of adsorption (determined using AES) and the rate of impingement of molecules on the surface.

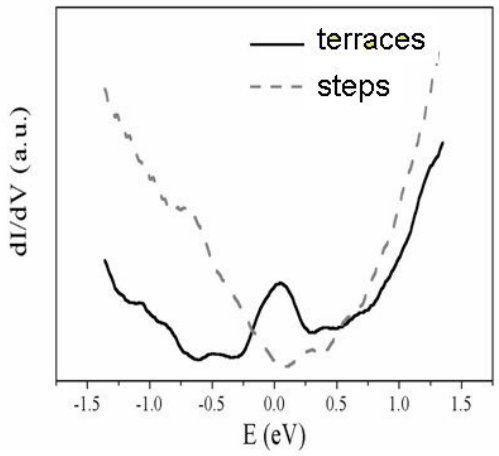

Fig. 5.11: STS spectra recorded on on a clean Ru(0001) surface, on top of a terrace (continuous line) and a step (dashed line). The disappearance of the peak recorded on the step demonstrates the surface character of the state.

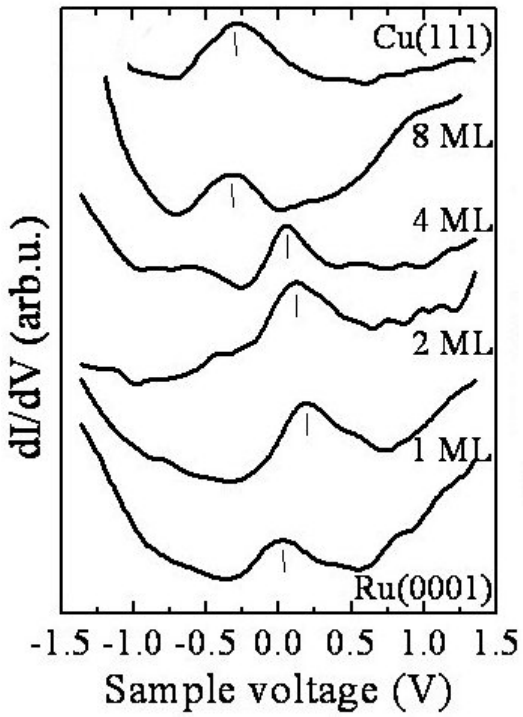

Fig. 5.12: Tunnelling conductance vs. sample voltage measurements taken on Ru(0001), 1, 2, 4 and 8 ML thick Cu films and Cu(111). All curves have been shifted along the vertical direction for clarity.

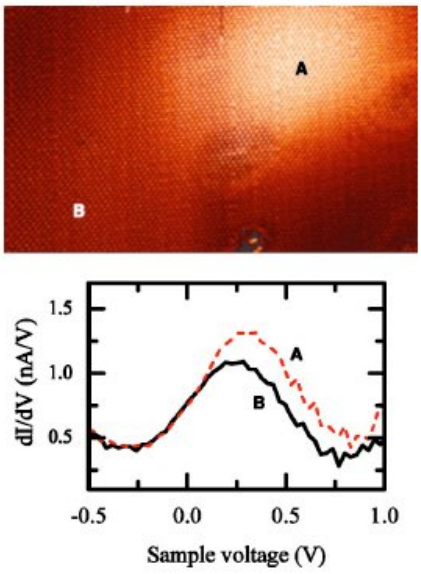

Fig. 5.13: Upper panel: 23.2 nm × 14 nm STM image of 1 ML of Cu on Ru(0001). Lower panel: STS spectra recorded above the Ar bubbles (A) and on the flat terrace (B).

that nicely agree with the experiments.

5.2.1 Parameters of the calculation

Since LDA works reasonably well for non-magnetic materials, I used this functional instead of GGA, which tends to overestimate the lattice constant, although I also performed some tests with GGA and I obtained very similar results. Other important parameters that I had to consider were the real space grid cutoff and the k grid cutoff. For the first one I used 400 Ry, which gave, like in the case of iron, an accuracy of about 0.02 eV. To determine the minimum number of k points (along x and y) I used two criteria: the convergence of the energy (with an accuracy of at least 0.02 eV) and the spurious oscillations that appear in the DOS if few k points are used. The minimum number of k points necessary to achieve the desired accuracy and get rid of the oscillations was $70 \times 70 = 4900$ (defined according to Monkhorst and Pack [143]), which was reduced to 2520 thanks to time reversal symmetry.

Other 'parameters' that had to be taken into account were the number of basis orbitals and the cutoff radii. An accurate determination of these quantities is very important since the precision of the calculation and the computer execution time and memory depend dramatically on them. In principle the number of basis orbitals should be as big as

possible, but a clever determination of the most important shells allows to reduce it. The initial number of basis orbitals was not very big (SZ for both Ru and Cu) but in order to reproduce the correct behavior of the d-band centroid and the surface state (see below) upon expansion of the lattice I had to use TZ in the d of Cu and DZP in the d of Ru[3]. To determine the radii cutoffs I used a mixed procedure where some of the radii were found variationally and other were adjusted to give equilibrium lattice constants closer to the experimental values. Such a procedure was justified by the fact that a careful determination of the structural parameters was very important for this study. Finally I used Ru(6.0DZ, 6.0DZ, 6.0DZDP) and Cu(5.2, 5.2, 5.2(4.0)TZ) for s, p and d orbitals, respectively. The second ζ, the polarization orbital, and the third ζ were calculated automatically by SIESTA using the split norm parameter (see chapter 1). Such basis sets gave theoretical lattice constants of 3.60 Å for bulk Cu and 2.71 Å for bulk Ru and reproduced accurately the d bands and the surface states.

5.2.2 Determination of the minimum number of slices on each surface

To simulate a surface I used a slab made of a large enough number of atomic planes grown along z (the direction perpendicular to the surface), large unit cell vectors along the same direction to avoid interactions between the first and last layers of different unit cells, and periodic boundary conditions along x and y. In this case it was only necessary to include one atom per plane and, consequently, the number of atoms in the unit cell was equal to the number of slices. The last number should be as big as possible to ensure that the physical properties of the atoms in the middle of the slab do not differ significantly from the bulk properties. However, as the number of slices increases, the computer execution time and memory increase dramatically. It is necessary then to look for a compromise, as I show below. Finally, is important to stress that the surface layer was not relaxed along the z direction because the experimental distances were found to very similar to the bulk distances in both Cu and Ru [207, 208].

The electronic properties of the atoms in the middle of the slab were compared with the electronic properties of bulk atoms using the projected density of states (PDOS). In the case of Cu, the minimum number of layers necessary to converge the calculation was 15. In figure (5.14) I plot the total density of states obtained in a bulk calculation and the PDOS on central atoms in slabs of 6 and 15 monolayers. In the 6 ML case the central PDOS differs significantly from the bulk PDOS at many points, whereas the 15 ML PDOS is almost converged. Clearly the DOS is dominated by the d states, which have a very large contribution below the Fermi level. However, at this level the s and p states have also a large DOS. In figure (5.15) I plot the central PDOS on these orbitals. As can be

[3] A double-ζ polarized basis set for both Cu and Ru is enough to describe accurately the surface state but not the d band complex.

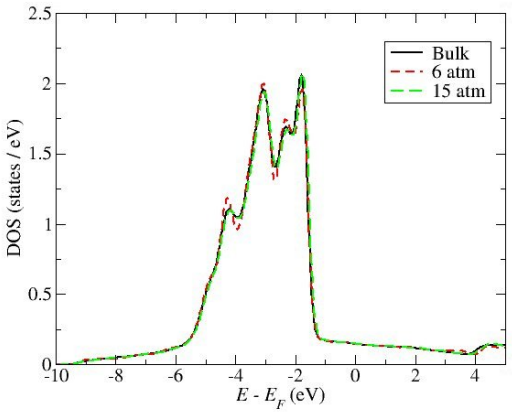

Fig. 5.14: Total density of states of bulk Cu and projected density of states on central atoms of Cu(111) slabs constructed with 6 and 15 leads.

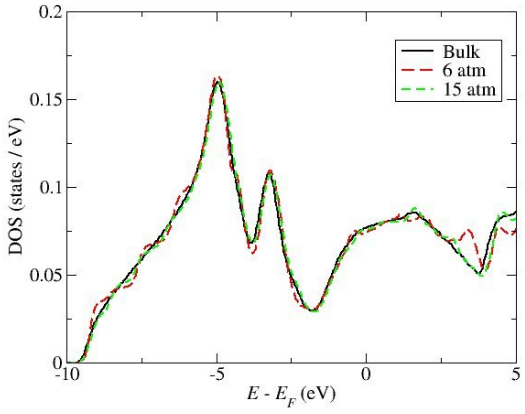

Fig. 5.15: s + p PDOS of bulk Cu and projected on central atoms of Cu(111) slabs constructed with 6 and 15 leads.

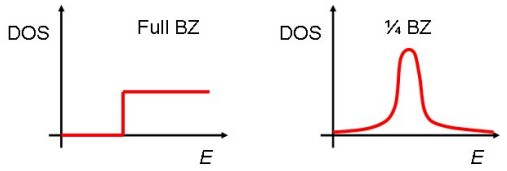

Fig. 5.16: Schematic representation of the density of states of a 2-dimensional surface state, calculated integrating to the whole BZ (left) and to 1/4 of the BZ (right).

seen, the degree of convergence needed to have a good agreement at the Fermi energy was only achieved with 15 ML. For Ru the central and surface PDOS evolutions were very similar to those observed in Cu, but the minimum number of slices needed to converge the results was 13.

5.2.3 Brillouin zone integration and character of the surface states

The PDOS on atoms of the surface shows dramatic disagreements between slabs with small number of slices and converged slabs, as can be seen in figure (5.17) (a). The reason for such big discrepancies is due to the penetration of the wave function of the surface state into the substrate, which can 'see' the other surface when few slabs are used. This again demonstrates that calculations performed with a relatively small number of slices are not precise and can produce significant errors. However, this was not taken into account in previous works [202, 203, 213], where a small number of slices was used and only the change in the d states was studied.

The most important contribution to the surface state comes from electrons with momenta close to the center of the 2D Brillouin zone, which have the largest component perpendicular to the surface, decay slowly into the vacuum and, therefore, give the largest contribution to the tunnelling current. For those reasons the PDOS has to be integrated to 1/4 of the 2D Brillouin zone (BZ) in order to clearly distinguish the surface state and obtain results similar to the experimental curves. As a consequence of such integration, the density of states of the 2-dimensional surface state, which ideally has a step-like shape (see figure (5.16)), transforms into a sharp peak which resembles a single state. Such behavior was also found in the ab initio result, plotted in figure (5.17) (b). In addition, the integration increased further the difference between non-converged and converged surfaces. This demonstrates again the importance of using a big enough number of slices.

Once the minimum number of slices has been determined next step is to find the biggest contribution to the surface state. One would naively expect that those orbitals which have the smallest decay into the vacuum, i. e. the s and the p_z orbitals, which point outside the surface, would have the largest weight. Indeed this is what I found in

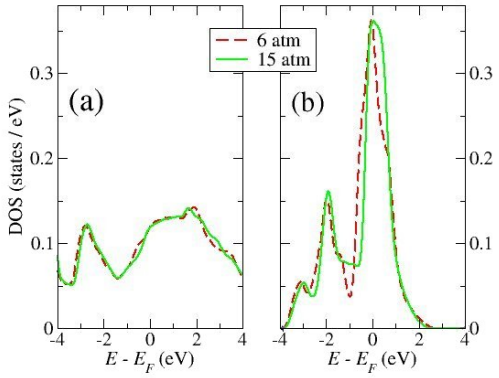

Fig. 5.17: s + p surface PDOS calculated with 6 and 15 ML of Cu(111). (a) Total s + p surface PDOS. (b) s + p surface PDOS integrated to 1/4 of the BZ.

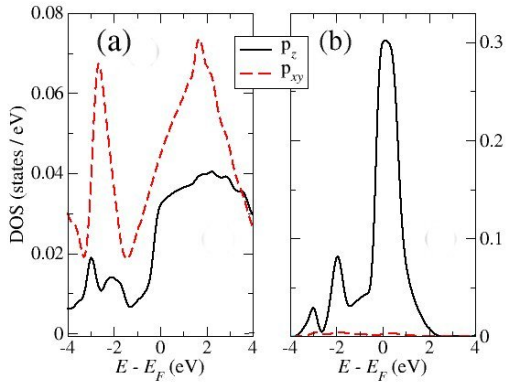

Fig. 5.18: Orbital resolved surface PDOS of s + p_z and p_x + p_y character integrated to the whole BZ (a) and to 1/4 of the BZ (b) calculated with 15 ML of Cu(111).

the orbital-resolved PDOS, plotted in figure (5.18), where a slab of Cu(111) with 15 ML was used (I found also something very similar with 13 ML of Ru). While the whole PDOS did not allow to distinguish the presence of the surface state, when it was integrated to 1/4 of the BZ the state clearly appeared as a sharp peak with s + p_z character. I can conclude then that the central states of the BZ with s and p_z character produce the main signal in the STS spectrum and are responsible of many properties associated with these surfaces.

It is also important to point out that the PDOS was obtained by integrating in real space and projecting on the surface atoms, instead of calculating the local density of states (LDOS) at some point a bit above the surface, where the STM measurements are performed. However, due to the localized character of the surface state (as opposed to a image-potential state) I expect not to find much deviation between both cases. This is confirmed by the fact that results agree very well with experiments, as I will show.

5.2.4 Effect of lattice expansion, crystalline structure and interlayer separation

When films of Cu are grown on top of Ru there are various possible influences which can affect the surface state, namely the strain, the proximity to the substrate and the structure of the growing films. In order to separate these influences from each other I simulated first slabs of fcc Cu(111) and hcp Cu(0001) under different conditions of strain. In figure (5.19) I show results obtained with 15 ML of Cu(111). In the non-expanded case all distances were equal to the bulk distances of Cu ($a_x y = 2.55$ Å and $a_z = 2.08$ Å). The d PDOS of the surface atoms shows the characteristic two peaked shape of Cu and the s + p_z PDOS has a clear peak whose onset (defined as the midpoint of the rise, which corresponds to the bottom of the surface state) starts below the Fermi energy. When the lattice was uniformly expanded, the corresponding PDOS maintained their shape but both the d band centroid (defined as the center of mass of the band), shown in table (5.2), and the surface state were shifted upwards in energy, as detected in previous simulations [213, 214]. The shift of the surface state is partly in contradiction with simple arguments based on a single band model, where expansion of the lattice parameter leads to smaller overlaps among atomic orbitals which in turn narrow the bands. In such a model, all features above (below) the Fermi level are then shifted downwards (upwards) in energy. The centroid of the d band, which is completely occupied, shifts 210 meV towards the Fermi level and supports the established idea that expanding the lattice moves these states upwards in energy [213, 214]. Other calculations for hcp Cu(0001) indicate that the the shifts of the centroid and the surface state detected upon expansion of the lattice are obtained independently of crystalline structure.

An additional parameter that could possibly be tuned in some experiments was the distance a_z between the last two layers. To clearly see the effect of varying it, I simulated

Tab. 5.2: Calculated centroid of the surface d bands for fcc Cu(111) slabs under different strain conditions. a_{xy} is the lateral nearest neighbor distance, a_z the interlayer distance and a_{surf} the interlayer separation of the surface layer. All distances are given in Å.

a_{xy}	a_z	a_{surf}	Centroid (eV)
2.55	2.08	2.88	-2.64
2.70	2.20	2.20	-2.43
2.70	2.20	1.94	-2.47

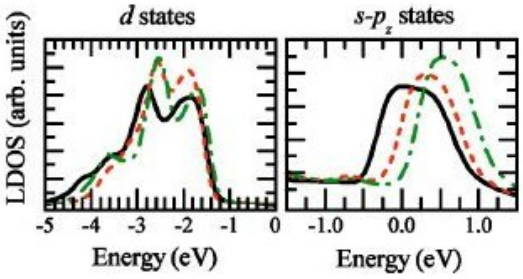

Fig. 5.19: d (left panels) and s + p_z (right panels) surface PDOS calculated with 15 ML of Cu(111). The continuous line corresponds to bulk distances $a_{xy} = 2.55$ Å and $a_z = 2.08$ Å, where a_{xy} is the nearest neighbor distance in the surface plane and a_z is the distance between layers. The broken line corresponds to a uniformly expanded lattice, $a_{xy} = 2.70$ Å and $a_z = 2.20$ Å, while the dashed-dotted line shows the results for an expanded lattice with the surface layer contracted to $a_z = 1.94$ Å.

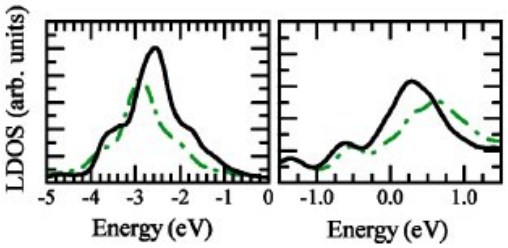

Fig. 5.20: 1 ML of Cu on top of 13 ML of Ru(0001), calculated at the bulk Ru distances $a_{xy} = 2.70$ Å and $a_z = 2.14$ Å. Continuous and dashed-dotted lines represent Cu-Ru distances of 2.10 Å and 1.94 Å, respectively.

Tab. 5.3: Calculated centroids of the surface d bands in Cu films 1-4 ML thick on Ru(0001) under different strain conditions. a_{xy} is the lateral nearest neighbor distance, a_z the interlayer distance, $a_{\mathrm{Cu-Ru}}$ the interlayer separation between the first Cu layer and the Ru substrate and $a_{\mathrm{Cu-Cu}}$ the interlayer distances in the Cu film. All distances are given in Å.

	a_{xy}	a_z	$a_{\mathrm{Cu-Ru}}$	$a_{\mathrm{Cu-Cu}}$	Centroid (eV)
1ML	2.70	2.14	2.10		-2.53
2ML	2.61	2.14	2.10	2.08	-2.60
4ML	2.55	2.14	2.10	2.08	-2.63
2ML	2.70	2.14	2.10	2.08	-2.45
4ML	2.70	2.14	2.10	2.08	-2.46

uniformly expanded Cu with the last layer compressed from 2.20 to 1.94 Å ($\sim 12\%$). The net result, which can be seen in figure (5.19) and table (5.2), was another upward shift of the surface state, whereas the d band centroid followed timidly the opposite trend. This demonstrates on the one hand that only big changes in a_z produce reasonable effects and, on the other hand, it suggests a possible method to separate the effects of the d band and the s + p_z states.

5.2.5 Simulations of 1, 2 and 4 ML of Cu on top of Ru(0001)

In 1 ML of Cu/Ru(0001) simulated at the experimental distances (a_{xy} = 2.70 Å, a_z = 2.14 Å, a_{surf} = 2.10 Å) the calculated shape of the d band complex showed only one peak, in excellent agreement with ultraviolet photoelectron spectroscopy (UPS) spectra [215]. Such a peak moves 250 meV towards the Fermi level compared with the main peak of pure Cu(111) at the equilibrium distances and is even higher in energy than the peak of pure Ru(0001). This agrees well with experiments which show that both the $2p_{3/2}$ [216] and the d states [215] are shifted upwards by 0.3 eV when going from thick Cu films to the first ML of Cu on Ru(0001). However, the calculated centroid was found to move only 110 ev upwards, as shown in table (5.3), which suggest that this quantity is not a good parameter to quantify surface properties. The corresponding surface state PDOS also changed, becoming more pronounced, and was completely depopulated due to the upward shift in energy. Simulations performed contracting the interlayer distance at the surface (figure (5.20)) showed that the surface state was also shifted upwards in energy.

Results for Ru(0001) covered with 1, 2 and 4 ML of Cu are shown in figure (5.21), with the DOS projected on d and s + p_z orbitals (left and right panels, respectively). The lateral lattice constant of the slabs, a_{xy}, was taken for each thicknesses as the average experimental distance among Cu atoms at the surface. The theoretical model did not

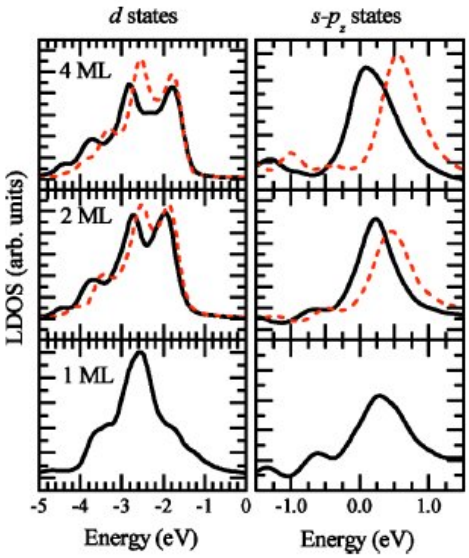

Fig. 5.21: Calculated evolution of the surface DOS projected on the d orbitals (left panels) and the s + p_z orbitals (right panels) for increasing Cu thicknesses in Cu/Ru(0001). Solid lines represent results obtained at the experimental lateral distances for each coverage (2.70, 2.61 and 2.55 Å for 1, 2 and 4 ML, respectively) and broken lines correspond to results calculated at the lateral distance of Ru(0001).

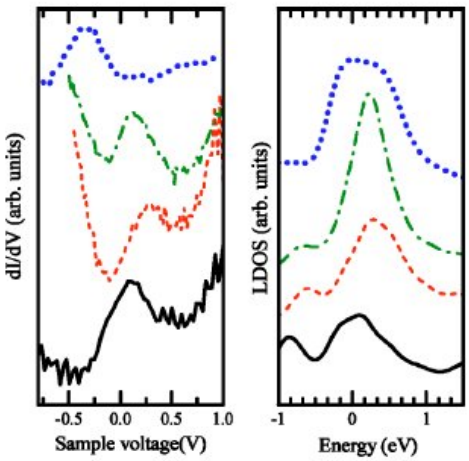

Fig. 5.22: The left panel shows the tunnelling conductance vs. sample voltage measurements on clean Ru(0001) (continuous line) and (from bottom to top) 1 and 2 ML-thick Cu films grown on Ru(0001) and Cu(111). The right panel shows the calculated PDOS of s + p_z character at the surface atoms. All curves have been shifted in the vertical direction for clarity.

consider then the observed reconstruction of the Cu layers, due to the extremely large unit cell needed to simulate such a system. The perpendicular interlayer distances $a_{\mathrm{Cu-Ru}}$ and the distances among Cu layers $a_{\mathrm{Cu-Cu}}$ for films of thickness 2 and 4 ML were set according to x-ray diffraction [208] and x-ray photoelectron diffraction data [207]. In addition, to separate unambiguously the effect of strain and proximity to the substrate the same system was simulated at the lateral distances of bulk Ru.

In agreement with the experimental trends, I found that both the d band complex and the surface state shifted downwards in energy with increasing thickness of Cu, as the lattice was compressed due to strain relaxation. For a 4 ML thick Cu film the position of the centroid was almost identical to that of a thick fcc slab and the overall shape of the d band was indistinguishable from that of Cu(111). Furthermore, the characteristic two-peak structure was already recovered for a Cu coverage of 2 ML independently of the applied strain, which means that the presence of only one peak for 1 ML of Cu is entirely due to the influence of the Ru layer.

Assuming that the Cu film keep on growing pseudomorphic with the Ru substrate shifts the centroid and the surface state upwards in energy as the film thickens (see table (5.3) and the broken lines of figure (5.21)). For 4 ML of Cu/Ru(0001) the surface state was calculated to be 500 meV above the Fermi level, i. e., almost at the same energy position that the state for a thick slab of fcc Cu(111) expanded to the lattice parameter of Ru (see figure (5.19)). This indicates that, if the geometry of the film is kept constant, the Cu(111) surface state is lower in energy closer to the substrate. This prediction is in excellent agreement with STM and UPS data for Ag films on Cu(111) [217], where the Ag layers keep their own lattice parameter from the first monolayer on due to the large mismatch between Ag and Cu, and the surface state is 120 meV lower in energy for 1 ML of Ag/Cu(111) than for bulk Ag(111).

5.2.6 Conclusions

In summary, the energetic evolution of surface states and d band complexes was studied in Cu, Ru and 1-4 ML of Cu on top of Ru(0001). In general the surface state and the d band shift upwards in energy when the surface is strained and then progressively move to the bulk values as the strain is reduced when the number of layers increases. The energy of the surface state for increasing thicknesses was determined by the competing effects of increasing distance to the Ru substrate, which moves the state to higher energies, and the partial relaxation of the strain, which pushes it downwards in energy. Since the experimental an the theoretical results show a continuous trend to lower energies, as shown in figure (5.22), the conclusion is that strain is the main responsible of the shift in the surface state.

6

General Conclusions

Ab initio calculations are a fundamental tool to understand many experiments and make new predictions. One of the most important approaches used by the ab initio community is density functional theory (DFT), which allows to simulate systems with relatively large numbers of atoms and high degrees of accuracy. Based on DFT, SIESTA uses also linear combinations of atomic orbitals and pseudopotentials which reduce even more the execution time and memory consumption. In this thesis it was indeed shown that very big systems can be simulated with high precision and the results compare nicely with experiments. However, in some cases, like SnO_2 with cobalt impurities, the results differ from the measured values due to inherent failures of the exchange and correlation functional. Anyhow, such results can be improved with the use of more sophisticated approximations.

Another important code is SMEAGOL, which uses non-equilibrium Green's function techniques to calculate the transport characteristics of nanoscale materials from the electronic structure provided by SIESTA. This code, which was used to study atomic constrictions and nanotube-based devices, incorporates the possibility of doing spin-polarized and non-collinear spin calculations, as shown in the studies of giant magnetoresistance in organic molecules between nickel leads and nickel nanocontacts. It was also used to examine the structural stability and transport characteristics of (i) H_2 molecules sandwiched between platinum and palladium leads and (ii) platinum atomic chains. In the first case it was demonstrated that the most stable configuration of the H_2 molecule in the constriction corresponds to an arrangement where it bridges both leads. Such configuration gives conductances of 0.9 and 0.6 G_0 for platinum and palladium electrodes, respectively. The differences between both materials are due to the different alignment of the on-site energies of the contact atoms and the molecule. In platinum chains it was

predicted that the ground state configuration corresponds to a zigzag arrangement. This structure generates the non-monotonic behavior of the conductance which, apart from the typical even-odd effect, is found when the electrodes are separated, and can explain why in some experiments the conductance increases upon stretching. Finally, SMEAGOL was also used to study the stability, electronic structure and transport characteristics of metallocenes encapsulated inside carbon nanotubes. These new and interesting systems can produce high magnetoresistance ratios and can be used to fabricate electrical nanowires with the desired properties.

SIESTA was also used to study the structural and magnetic properties of iron and try to reproduce the correct magnetic ordering in the γ phase. In order to do that it was necessary to implement in SIESTA the generalized Bloch's theorem and an approximation to calculate the non-collinear GGA. The results showed that (i) at least a triple-ζ basis set is necessary to obtain the correct theoretical energetic ordering found with LDA, (ii) the GGA works much better than the LDA since it correctly predicts that the bcc phase is the most stable and gives equilibrium lattice constants much closer to experiments, and (iii) both approximations give an incorrect spiral ground state. The LDA gives the correct magnetic order but predicts a very small equilibrium lattice constant. With GGA happens just the opposite: the equilibrium lattice constant is similar to the experimental lattice constant but the predicted magnetic order is incorrect. The disagreement is due to deficiencies of the exchange and correlation functionals.

A code to calculate spin waves (magnons) was also implemented as an appendix to SIESTA. Once the self-consistency is finished, the magnon dispersion relation is calculated from the Hamiltonian eigenvalues and eigenvectors by using first order perturbation theory. The code works and gives proper results, but the amount of memory and execution time needed to perform accurate calculations were very high. It was necessary to use different numerical cutoffs and the Padé approximation to reduce the size of the numerical loops and decrease the effective number of energy points that enter in the calculation. Thanks to such approximations it was possible to obtain the magnon dispersion relation in fcc nickel and bcc iron. The results for iron agree qualitatively with the experiments, although the curve moves to higher frecuencies. In the case of nickel the magnon curve does not fit the experimental data due to the wrong exchange splitting given by LDA but it agrees with previous theoretical calculations.

Finally, SIESTA was also used to investigate the change in the surface states of clean ruthenium, clean copper and one to four monolayers of copper on top of ruthenium under different expansions of the lattice, in a first step to understand the influence of these states on the surface reactivity and separate their effect from the centroid of the d bands. When the lattice is laterally expanded the surface state moves upwards in energies and is depopulated. The same effect is also found when the last monolayer is contracted, although the d band follows the opposite trend. When the number of copper layers increases there is a competition between the contraction of the lattice, which drives the state to lower energies, and the loss of influence of the substrate, which produces the

opposite trend. The total effect is a movement of the state downwards in energy, which is therefore populated. This can be linked to the surface reactivity, since it decreases with the number of copper layers.

In summary, the work done in this thesis clearly demonstrates that ab initio methods based on density functional theory are an essential tool to characterize and understand many systems with small numbers of atoms and bulk solids. In general the theoretical predictions given by SIESTA and SMEAGOL agree very well with the experiments and can be used as a starting point to new studies.

Conclusiones Generales

Los cálculos ab initio son una herramienta fundamental para comprender muchos experimentos y a hacer a su vez nuevas predicciones. En particular, los códigos basados en la teoría del funcional de la densidad son realmente eficientes y permiten simular sistemas formados por cantidades relativamente grandes de átomos. Uno de los más importantes es SIESTA, que usa combinaciones lineales de orbitales atómicos y pseudopotenciales para reducir aún más el tiempo de ejecución y la cantidad de memoria. En esta tesis se demostró que se pueden simular sistemas muy grandes con mucha precisión. Un ejemplo fueron las matrices de SnO_2 con impurezas de cobalto, aunque en este caso particular, debido a fallos inherentes a la aproximación que calcula el canje y la correlación, los resultados finales difirieron de los experimentales.

Otro código importante es SMEAGOL, que utiliza el formalismo de funciones de Green de no equilibrio para calcular propiedades de transporte en sistemas de tamaño nanométrico a partir de la estructura electrónica producida por SIESTA. Este código, que fue utilizado para estudiar contricciones atómicas y dispositivos basados en nanotubos, incorpora la posibilidad de realizar cálculos de espín polarizado y espín no colineal, como se mostró en los estudios de magnetorresistencia gigante en moléculas orgánicas entre electrodos de níquel y en nanocontactos de níquel. Además también fue empleado para examinar la estabilidad estructural y las características de transporte de (i) moléculas H_2 situadas entre electrodos de platino y paladio y (ii) cadenas atómicas de platino. En el primer caso se demostró que la configuración más estable de la molécula en la constricción es aquella en la que la molécula se sitúa paralela al flujo de la corriente, con conductancias de 0.9 y 0.6 G_0 para electrodos de platino y paladio, respectivamente. También se mostró que las diferencias entre los dos materiales son debidas al distinto alineamiento de las energías de la molécula y los átomos de contacto. En el caso de cadenas de platino se predijo que el estado fundamental corresponde a una configuración zigzag. Esta estructura es responsable del comportamiento no monótono de la conductancia que, a parte

del típico efecto de paridad, aparece cuando los electrodos se separan, y puede explicar por qué en en algunos experimentos la conductancia aumenta al estirar. Finalmente, SMEAGOL también se usó para estudiar la estabilidad, estructura electrónica y características de transporte de metalocenos encapsulados dentro de nanotubos de carbono. Estos nuevos e interesantes sistemas pueden presentar altos porcentajes de magnetorresistencia dependiendo del tipo de molécula y pueden ser utilizados para producir nanohilos con determinadas propiedades.

SIESTA fue empleado para estudiar las propiedades estructurales y magnéticas de hierro e intentar reproducir el ordenamiento magnético correcto en la fase γ. Para ello fue necesario implementar en SIESTA el teorema de Bloch generalizado y una aproximación para calcular la GGA no colineal. Los resultados mostraron que (i) al menos una base triple-ζ es necesaria para obtener el orden energético teórico correcto con la LDA, (ii) la GGA funciona mucho mejor que la LDA puesto que predice correctamente que la fase bcc es la más estable y da constantes de equilibrio mucho más cercanas a los experimentos, y (iii) las dos aproximaciones producen un estado fundamental de la espiral incorrecto. La LDA da el estado magnético correcto pero la constate de red es muy pequeña. Con la GGA ocurre justo lo contrario: la constante de red es similar a la experimental pero el orden magnético es incorrecto. Sin embargo, los resultados obtenidos con SIESTA son mejores que los producidos por otros códigos, donde las diferencias entre las constantes de red teóricas y las experimentales eran mucho mayores. El desacuerdo en la configuración magnética de la fase γ se debe básicamente a deficiencias inherentes a las aproximaciones de canje y correlación.

También se desarrolló un código para calcular la relación de dispersión de ondas de espín (magnones) utilizando los autovalores y autovectores del Hamiltoniano producido por SIESTA y aplicando teoría de perturbaciones de segundo orden. Sin embargo, aunque el código funciona y da resultados razonables, la cantidad de memoria y tiempo de ejecución necesarios para llevar a cabo cálculos precisos son muy elevados. Para resolver este problema fue necesario utilizar diferentes cortes numéricos y la aproximación de Padé para reducir el tamaño de los ciclos numéricos y disminuir el número efectivo de puntos de energía que entran en el cálculo. Gracias a ello fue posible obtener la relación de dispersion de magnones en el hierro y el níquel. Los resultados del hierro están de acuerdo cualitativamente con los experimentos, aunque la gráfica se curva hacia energías mayores debido al uso de una base de orbitales no convergida. Sin embargo, en el caso del níquel la curva no casa con los datos experimentales debido a la incorrecta separación de canje producida por la LDA pero verifica los cálculos teóricos.

Finalmente, también se utilizó SIESTA para investigar el cambio en los estados de superficie de cobre, rutenio y monocapas de cobre sobre rutenio sometidos a varios tipos de expansión, como un primer paso para entender la influencia de estos estados en la reactividad de las superficies y separar su efecto del centroide de las bandas d. Se mostró que cuando la red es expandida lateralmente el estado de superficie se mueve hacia arriba en energías y se despuebla. El mismo efecto se encuentra cuando la última monocapa se

contrae, aunque la banda d sigue la tendencia opuesta. Cuando el número de capas de cobre aumenta hay una competición entre la contracción de la red, que mueve el estado a menores energías, y la pérdida de influencia del substrato, que produce la tendencia contraria. El efecto total es un movimiento del estado hacia energías menores, el cual acaba ganando carga.

En resumen, el trabajo hecho en esta tesis demuestra claramente que usando métodos ab initio es posible caracterizar y entender muchas propiedades físicas asociadas con sistemas con pequeños números de átomos o sistemas infinitos (cristales). En general las predicciones teóricas de SIESTA y SMEAGOL verifican muy bien los datos experimentales y pueden utilizarse como puntos de partida para nuevos estudios.

BIBLIOGRAPHY

[1] P. Hohenberg and W. Kohn, Phys. Rev. **136**, B864 (1964).

[2] W. Kohn and L. J. Sham, Phys. Rev. **140**, A1133 (1965).

[3] S. Redner, Physics Today **58**, 49 (June 2005).

[4] W. Kohn, Rev. Mod. Phys. **71**, 1253 (1999).

[5] V. Fock, Z. Phys. **61**, 126 (1930); **62**, 795 (1930).

[6] J. A. Pople, Rev. Mod. Phys. **71**, 1267 (1999).

[7] O. Gunnarsson, and B. I. Lundqvist, Phys. Rev. B **13**, 4276 (1976).

[8] O. Gunnarsson, M. Jonson, and B. I. Lundqvist, Phys. Rev. B **20**, 3136 (1979).

[9] K. Burke and Friends, The ABC of DFT. http://dft.rutgers.edu/kieron/beta (2003).

[10] D. M. Ceperley and B. J. Alder, Phys. Rev. Lett. **45**, 566 (1980).

[11] J. P. Perdew and A. Zunger, Phys. Rev. B **23**, 5048 (1981).

[12] S.-K. Ma and K. A. Brueckner, Phys. Rev. **165**, 18 (1968).

[13] J. P. Perdew, K. Burke, and M. Ernzerhof, Phys. Rev. Lett. **77**, 3865 (1996); **78** 1396(E) (1997).

[14] A. E. Mattsson, Science **298**, 759 (2002).

[15] A. D. Becke, J. Chem. Phys. **98**, 1372 (1993).

[16] J. P. Perdew and K. Schmidt, in *Density Functional Theory and Its Applications to Materials*, edited by V. Vand Doren *et al.* (AIP Press, Melville, New York, 2001).

[17] M. Ernzerhof and G. E. Scuseria, J. Chem. Phys. **110**, 5029 (1999).

[18] A. D. Becke, J. Chem. Phys. **109**, 2092 (1998).

[19] J. Tao, J. P. Perdew, V. N. Staroverov, and G. E. Scuseria, Phys. Rev. Lett. **91**, 146401 (2003).

[20] E. Artacho, J. Gale, A. García, J. Junquera, R. M. Martin, P. Ordejón, D. Sánchez-Portal, and J. Soler, SIESTA (Spanish Initiative for Electronic Simulations with Thousands of Atoms. www.uam.es/departamentos/ciencias/fismateriac/siesta/)

[21] J. M. Soler, E. Artacho, J. D. Gale, A. Garcia, J. Junquera, P. Ordejón, D. Sánchez-Portal, J. Phys.: Condens. Matter **14**, 2745 (2002).

[22] N. Troullier and J. L. Martins, Phys. Rev. B **43**, 1993 (1991).

[23] L. Kleinman and D. M. Bylander, Phys. Rev. Lett. **48**, 1425 (1982).

[24] D. R. Hamann, M. Schlüter, and C. Chiang, Phys. Rev. Lett. **43**, 1494 (1979).

[25] D. Vanderbilt, Phys. Rev. B **41**, R7892 (1990).

[26] L. Kleinman, Phys. Rev. B **21**, 2630 (1980).

[27] G. B. Bachelet and M. Schlüter, Phys. Rev. B **25**, 2103 (1982).

[28] E. Engel, A. Höck, and S. Varga, Phys. Rev. B **63**, 125121 (2001).

[29] S. G. Louie, S. Froyen, and M. L. Cohen, Phys. Rev. B **26**, 1738 (1982).

[30] O. F. Sankey and D. J. Niklewski, Phys. Rev. B **40**, 3979 (1989).

[31] J. Junquera, O. Paz, D. Sánchez-Portal, and E. Artacho, Phys. Rev. B **64**, 235111 (2001).

[32] E. Anglada, J. M. Soler, J. Junquera, and E. Artacho, Phys. Rev. B **66**, 205101 (2002).

[33] D. Sánchez-Portal, J. M. Soler, and E. Artacho, J. Phys.: Condens. Matter **8**, 3859 (1996).

[34] S. Huzinaga *et al.*, *Gaussian Basis Sets for Molecular Calculations*, Elsevier (Berlin, 1984).

[35] E. Artacho, D. Sánchez-Portal, P. Ordejón, A. García, and J. M. Soler, Phys. Status Solidi B **215**, 809 (1999).

[36] D. Khomskii, in *Spin Electronics*, edited by M.J. Thornton, M. Ziese, Lecture Notes in Physics **569**, 89 (2001).

[37] J. B. Goodenough, in *Magnetism and Chemical Bond*, Interscience Publ. (New York-London 1963).

[38] S. B. Ogale, R. J. Choudhary, J. P. Buban, S. E. Lofland, S. R. Shinde, S. N. Kale, V. N. Kulkarni, J. Higgins, C. Lanci, J. R. Simpson, N. D. Browning, S. Das Sarma, H. D. Drew, R. L. Greene, and T. Venkatesan, Phys. Rev. Lett. **91**, 077205 (2003).

[39] J. M. D. Coey and S. Sanvito, J. Phys. D: Appl. Phys **37**, 988 (2004).

[40] V. I. Anisimov, J. Zaanen, and O. K. Andersen, Phys. Rev. B **44**, 943 (1991).

[41] H. Ohnishi, Y. Kondo, and K. Takayanagi, Nature (London) **395**, 780 (1998).

[42] A. I. Yanson, G. Rubio Bollinger, H. E. van der Brom, N. Agrait, and J. M. van Ruitenbeek, Nature (London) **395**, 783 (1998).

[43] M. A. Reed, C. Zhou, C. J. Muller, T. P. Burgin, and J. M. Tour, Science **278**, 252 (1997).

[44] R. H.M. Smit, Y. Noat, C. Untiedt, N. D. Lang, M. C. van Hemert, and J. M. van Ruitenbeek, Nature (London) **419**, 906 (2002).

[45] C. Guerret-Piécourt, Y. Le Bouar, A. Loiseau, and H. Pascard, Nature (London) **372**, 761 (1994).

[46] D. J. Hornbaker, S.-J. Kahng, S. Misra, B. W. Smith, A. T. Johnson, E. J. Mele, D. E. Luzzi, and A. Yazdani, Science **295**, 828 (2002).

[47] J. Lee, H. Kim, S.-J. Kahng, G. Kim, Y.-W. Son, J. Ihm, H. Kato, Z. W. Wang, T. Okazaki, H. Shinohara, and Y. Kuk, Nature (London) **415**, 1005 (2002).

[48] J. Lu, S. Nagase, D. Yu, H. Ye, R. Han, Z. Gao, S. Zhang, and L. Peng, Phys. Rev. Lett. **93**, 116804 (2004).

[49] T. Takenobu, T. Takano, M. Shiraishi, Y. Murakami, M. Ata, H. Kataura, Y. Achiba, and Y. Iwasa, Nature Materials **2**, 683 (2003).

[50] T. Mühl, D. Elefant, A. Graff, R. Kozhuharova, A. Leonhardt, I. Mönch, M. Ritschel, P. Simon, S. Groudeva-Zotova, and C. M. Schneider, Journal of Applied Physics **93**, 7894 (2003).

[51] J. W. Jang, K. W. Lee, C. E. Lee, T. J. Lee, C. J. Lee, and S. C. Lyu, Phys. Stat. Sol. (b) **241**, 1605 (2004).

[52] J. Ferrer, A. Martín-Rodero, and F. Flores, Phys. Rev. B **38**, R10113 (1988).

[53] R. Landauer, Philos. Mag. **21**, 863 (1970).

[54] M. Büttiker, Y. Imry, R. Landauer, and S. Pinhas, Phys. Rev. B **31**, 6207 (1985).

[55] L. V. Keldysh, JETP **20**, 1018 (1965).

[56] M. Brandbyge, J.-L. Mozos, P. Ordejón, J. Taylor, and K. Stokbro, Phys. Rev. B **65**, 165401 (2002).

[57] A. R. Rocha, V. M. García-Suárez, S. W. Bailey, C. J. Labmbert, J. Ferrer and S. Sanvito, SMEAGOL (Spin and Molecular Electronics in an Atomically-Generated Orbital Landscape. www.smeagol.tcd.ie).

[58] Sz. Csonka, A. Halbritter, G. Mihály, O. I. Shklyarevskii, S. Speller, and H. van Kempen, Phys. Rev. Lett. **93**, 016802 (2004).

[59] J. C. Cuevas, J. Heurich, F. Pauly, W.Wenzel, and G. Schön, Nanotechnology **14**, R29 (2003).

[60] Y. García, J. J. Palacios, E. SanFabián, J. A. Vergés, A. J. Pérez-Jiménez, and E. Louis, Phys. Rev. B **69**, 041402(R) (2004).

[61] D. Djukic, K. S. Thygesen, C. Untiedt, R. H. M. Smit, K. W. Jacobsen, and J. M. van Ruitenbeek, Phys. Rev. B **71**, 161402(R) (2005)

[62] K. S. Thygesen and K. W. Jacobsen Phys. Rev. Lett. **94**, 036807 (2005).

[63] R. H. M. Smit, C. Untiedt, G. Rubio-Bollinger, R. C. Segers, and J. M. van Ruitenbeek, Phys. Rev. Lett. **91**, 076805 (2003).

[64] S. R. Bahn and K. W. Jacobsen, Phys. Rev. Lett. **87**, 266101 (2001).

[65] D. Sánchez-Portal, E. Artacho, J. Junquera, P. Ordejón, A. García, and J. M. Soler, Phys. Rev. Lett. **83**, 3884 (1999).

[66] F. D. Novaes, A. J. R. da Silva, E. Z. da Silva, and A. Fazzio, Phys. Rev. Lett. **90**, 036101 (2003).

[67] S. C. Tsang, Y. K. Chen, P. J. F. Harris, and M. L. H. Green, Nature (London) **372**, 159 (1994).

[68] J. Schwinger, J. Math. Phys. **2**, 407 (1961).

[69] M. Wagner, Phys. Rev. B **44**, 6104 (1991).

[70] G. D. Mahan, in *Many-Particle Physics*, edited by Plenum Press (New York, 1990).

[71] C. Caroli, R. Combescot, P. Nozieres, and D. Saint-James, J. Phys. C: Solid St. Phys. **4**, 916 (1971).

[72] C. Caroli, R. Combescot, D. Lederer, P. Nozieres and D. Saint-James, J. Phys. C: Solid St. Phys. **4**, 2598 (1971).

[73] C. Caroli, R. Combescot, P. Nozieres and D. Saint-James, J. Phys. C: Solid St. Phys. **5**, 21 (1972).

[74] E. N. Economou, in *Green's Functions in Quantum Physics*, edited by Springer-Verlag (Berlin, Heidelberg, New York, 1983).

[75] S. Sanvito, C. J. Lambert, J. H. Jefferson, and A. M. Bratkovsky, Phys. Rev. B **59**, 11936 (1999).

[76] K. S. Dy, S.-Y. Wu, and T. Spratlin, Phys. Rev. B **20**, 237 (1979).

[77] F. Guinea, C. Tejedor, F. Flores, and E. Louis, Phys. Rev. B **28**, 4397 (1983).

[78] Y. Xue, S. Datta, and M. A. Ratner, Chem. Phys. **281**, 151 (2002).

[79] Y. Meir and N. S. Wingreen, Phys. Rev. Lett. **68**, 2512 (1992).

[80] J. C. Cuevas, A. Levy-Yeyati, and A. Martín-Rodero, Phys. Rev. Lett. **80**, 1066 (1998).

[81] M. Di Ventra, S. T. Pantelides, and N. D. Lang, Phys. Rev. Lett. **84**, 979 (2000).

[82] A. Aviram and M. A. Ratner, Chem. Phys. Lett. **29**, 277 (1974).

[83] K. Tsukagoshi, B. W. Alphenaar, and H. Ago, Nature (London) **401**, 572 (1999).

[84] V. Dediu, M. Murgia, F. C. Matacotta, C. Taliani, and S. Barbanera, Solid State Commun. **122**, 181 (2002).

[85] M. Ouyang and D. D. Awschalom, Science **301**, 1074 (2003).

[86] Z. H. Xiong, D. Wu, Z. Valy Vardeny, and J. Shi, Nature (London) **427**, 821 (2004).

[87] J. R. Petta, S. K. Slater, and D. C. Ralph, Phys. Rev. Lett. **93**, 136601 (2004).

[88] H. Oshima and K. Miyano, Appl. Phys. Lett. **73**, 2203 (1998).

[89] N. García, M. Muñoz, and Y.-W. Zhao, Phys. Rev. Lett. **61**, 2472 (1999).

[90] T. Ono, Y. Ooka, H. Miyahima, and Y. Otani, Appl. Phys. Lett **75**, 1622 (1999).

[91] S. H. Chung, M. Muñoz, N. García, W. F. Egelhoff, and R. D. Gomez, Phys. Rev. Lett. **89**, 287203 (2002).

[92] M. Viret, S. Berger, M. Gabureac, F. Ott, D. Olliqs, I. Petej, J. F. Greqq, C. Fermon, G. Francinet, and G. Le Goff, Phys. Rev. B **66**, 220401(R) (2002).

[93] H. D. Chopra and S. Z. Hua, Phys. Rev. B **66**, 020403(R) (2002).

[94] S. Z. Hua and H. D. Chopra, Phys. Rev. B **67**, 060401(R) (2003).

[95] M. Gabureac, M. Viret, F. Ott, and C. Fermon, Phys. Rev. B **69**, 100401(R) (2004).

[96] W. F. Egelhoff, Jr., L. Gan, H. Ettedgui, Y. Kadmon, C. J. Powell, P. J. Chen, A. J. Shapiro, R. D. McMichael, J. J. Mallett, T. P. Moffat, M. D. Stiles, and E. B. Svedberg, J. Appl. Phys. **95**, 7554 (2004).

[97] M. Sullivan, D. A. Boehm, D. A. Ateya, S. Z. Hua, and H. D. Chopra, Phys. Rev. B **71**, 024412 (2005).

[98] P. Bruno, Phys. Rev. Lett. **83**, 2425 (1999).

[99] D. Jacob, J. Fernández-Rossier, and J. J. Palacios, Phys. Rev. B **71**, 220403(R) (2005).

[100] D. Tománek, Z. Sun, and S. G. Louie, Phys. Rev. **43**, 4699 (1991).

[101] A. Khein, D. J. Singh, and C. J. Umrigar, Phys. Rev. B **51**, 4105 (1995).

[102] V. Rodrigues, J. Bettini, P. C. Silva and D. Ugarte, Phys. Rev. Lett. **91**, 096801 (2003).

[103] N. R. Claughton, M. Leadbeater, and C. J. Lambert, J. Phys.: Condens. Matter **7** 8757 (1995).

[104] R. H. M. Smit, C. Untiedt, A. I. Yanson, and J. M. van Ruitenbeek, Phys. Rev. Lett. **87**, 266102 (2001).

[105] S. K. Nielsen, Y. Noat, M. Brandbyge, R. H. M. Smit, K. Hansen, L. Y. Chen, A. I. Yanson, F. Besenbacher, and J. M. van Ruitenbeek, Phys. Rev. B **67**, 245411 (2003).

[106] L. de la Vega, A. Martín-Rodero, A. L. Yeyati, and A. Saúl, Phys. Rev. B **70**, 113107 (2004).

[107] P. Sen, S. Ciraci, A. Buldum, and I. P. Batra, Phys. Rev. B **64**, 195420 (2001).

[108] L.-J. Li, A. N. Khlobystov, J. G. Wiltshire, G. A. D. Briggs, and R. J. Nicholas, Nature Materials **4**, 481 (2005).

[109] C. Herring, in *Magnetism IV*, edited by G. T. Rado and H. Suhl (Academic Press, New York, London, 1966).

[110] U. von Barth and L. Hedin, J. Phys. C: Solid State Phys. **5**, 1629 (1972).

[111] L. M. Sandratskii and P. G. Guletskii, J. Phys. F: Met. Phys. **16**, L43 (1986).

[112] J. Kübler, K. H. Höck, J. Sticht, and A. R. Williams, J. Appl. Phys. **63**, 3482 (1988).

[113] T. Oda, A. Pasquarello, and R. Car, Phys. Rev. Lett. **80** 3622 (1998).

[114] A. V. Postnikov, P. Entel, and J. M. Soler, Eur. Phys. J. D **25**, 261 (2003).

[115] A. V. Postnikov, J. Kortus and M. Pederson, Scientific Highlight of the month, Newsletter 61 of the Psi-k Network (February 2004).

[116] R. Lorenz, J. Hafner, S. S. Jaswal, and D. J. Sellmyer, Phys. Rev. Lett. **74**, 3688 (1995).

[117] M. Liebs, K. Hummler, and M. Fähnle, Phys. Rev. B **51**, 8664 (1995).

[118] J. Sticht, K.-H. Höck, and J. Kübler, J. Phys.: Condens. Matter **1** 8155 (1989).

[119] Y. Tsunoda, J. Phys.: Condens. Matter **1**, 10427 (1989).

[120] M. Uhl and J. Kübler, Phys. Rev. Lett. **77**, 334 (1996).

[121] W. Geertsma and D. Khomskii, Phys. Rev. B **54**, 3011 (1996).

[122] I. Dzyaloshinsky, J. Phys. Chem. Solids **4**, 241 (1958).

[123] T. Moriya, Phys. Rev. **117**, 635 (1960).

[124] L. M. Sandratskii, Adv. Phys. **47**, 91 (1998).

[125] K. Knöpfle, L. M. Sandratskii, and J. Kübler, Phys. Rev. B **62**, 5564 (2000).

[126] M. Marsman and J. Hafner, Phys. Rev. B **66**, 224409 (2002).

[127] D. Bancroft, E. L. Peterson, and S. Minshall, J. Appl. Phys. **27**, 291 (1956).

[128] M. Nicol and G. Jura, Science **141**, 1035 (1963).

[129] K. Shimizu, T. Kimura, S. Furomoto, K. Takeda, K. Kontani, Y. Onuki, and K. Amaya, Nature (London) **412**, 316 (2001).

[130] V. L. Moruzzi, Phys. Rev. B **41**, 6939 (1990).

[131] R. Hayn and V. Drchal, Phys. Rev. B **58**, 4341 (1998).

[132] P. Krüger, Phys. Rev. B **64**, 094404 (2001).

[133] D. Spišak and J. Hafner, Phys. Rev. Lett. **88**, 056101 (2002).

[134] Y. Tsunoda, Y. Nishioka, and R. M. Nicklow, J. Magn. Magn. Matter **128**, 133 (1993).

[135] L. Kaufman, E. V. Clougherty, and R. J. Weiss, Acta Metall. **11**, 323 (1963).

[136] M. Uhl, L. M. Sandratskii, and J. Kübler, J. Magn. Magn. Materials **103**, 314 (1992).

[137] M. Uhl, L. M. Sandratskii, and J. Kübler, Phys. Rev. B **50**, 291 (1994).

[138] M. Korling and J. Ergon, Phys. Rev. B **54**, R8293 (1996).

[139] D. M. Bylander, L. Kleinman, Phys. Rev. B **58**, 9207 (1998).

[140] D. M. Bylander and L. Kleinman, Phys. Rev. B **59**, 6278 (1999).

[141] D. M. Bylander and L. Kleinman, Phys. Rev. B **60**, R9916 (1999).

[142] J. Izquierdo, A. Vega, L. C. Balbás, D. Sánchez-Portal, J. Junquera, E. Artacho, J. M. Soler, and P. Ordejon, Phys. Rev. B **61**, 13639 (2000).

[143] H. J. Monkhorst and J. D. Pack, Phys. Rev. B **13**, 5188 (1976).

[144] J. Moreno and J. Soler, Phys. Rev. B **45**, 13891 (1992).

[145] C. S. Wang, B. M. Klein, and H. Krakauer, Phys. Rev. Lett. **54**, 1852 (1985).

[146] E. G. Moroni, G. Kresse, J. Hafner, J. Furtmuller, Phys. Rev. B **56**, 15629 (1997).

[147] D. Hobbs, G. Kresse, and J. Hafner, Phys. Rev. B **62**, 11556 (2000).

[148] O. D. Diéguez, M. M. Alemany, C. Rey, P. Ordejón, and L. J. Gallego, Phys. Rev. B **63**, 205407 (2001).

[149] H. Purdum, P. A. Montano, G. K. Shenoy, and T. Morrison, Phys. Rev. B **25**, 4412 (1982).

[150] D. J. Scalapino, Phys. Rep. **250**, 329 (1995).

[151] R. W. White, in *Quantum Theory of Magnetism*, edited by Springer-Verlag (Berlin, Heidelberg, 1983).

[152] S. Y. Savrasov, Phys. Rev. Lett. **81**, 2750 (1998).

[153] M. I. Katsnelson and A. I. Litchtenstein, Phys. Rev. B **61**, 8906 (2000).

[154] K. Karlsson and F. Aryasetiawan, Phys. Rev. B **62**, 3006 (2000).

[155] H. A. Mook and R. M. Nicklow, Phys. Rev. B **7**, 336 (1973).

[156] H. A. Mook, J. W. Lynn, and R. M. Nicklow, Phys. Rev. Lett **30**, 556 (1973).

[157] J. W. Lynn, Phys. Rev. B **11**, 2624 (1975).

[158] J. Callaway and C. S. Wang, J. Phys. F: Metal Phys. **5**, 2119 (1975).

[159] J. Callaway, A. K. Chatterjee, S. P. Singhal, and A. Ziegler, Phys. Rev. B **28**, 3818 (1983).

[160] J. Callaway and A. K. Chatterjee, J. Phys. F: Metal Phys. **8**, 2569 (1978).

[161] I. Izuyama, D. J. Kim, and R. Kubo, J. Phys. Soc. Jpn. **18**, 1025 (1963).

[162] J. Hubbard, Proc. R. Soc. London **276A**, 238 (1963).

[163] E. Runge and E. K. U. Gross, Phys. Rev. Lett. **52**, 997 (1984).

[164] X. Gonze, Phys. Rev. A **52**, 1086 (1995).

[165] J. B. Staunton, J. Poulter, B. Ginatempo, E. Bruno, and D. D. Johnson, Phys. Rev. Lett. **82**, 3340 (1999).

[166] J. B. Staunton, J. Poulter, B. Ginatempo, E. Bruno and D. D. Johnson, Phys. Rev. B **62**, 1075 (2000).

[167] V. Thakor, J. B. Staunton, J. Poulter, S. Ostanin, B. Ginatempo, and E. Bruno, Phys. Rev. B **67**, 180405 (2003).

[168] K.-H. Lee and K. J. Chang, Phys. Rev. B **54**, R8285 (1996).

[169] J. F. Cooke, J. W. Lynn, and H. L. Davis, Phys. Rev. B **21**, 4118 (1980).

[170] S. V. Halilov, A. Y. Perlov, P. M. Oppeneer, and H. Eschrig, Europhys. Lett. **39**, 91 (1997).

[171] R. Gebauer and S. Baroni, Phys. Rev. B **61**, R6459 (2000).

[172] O. Grotheer, C. Ederer, and M. Fähnle, Phys. Rev. B **63**, 100401 (2001).

[173] H. A. Mook and D. Tocchetti, Phys. Rev. Lett. **43**, 2029 (1979).

[174] H. A. Mook and D. McK. Paul, Phys. Rev. Lett. **54**, 227 (1985).

[175] J. F. Cooke, J. A. Blackman, and T. Morgan, Phys. Rev. Lett. **54**, 718 (1985).

[176] J. Goldstone, Nuovo Cimento **19**, 154 (1961).

[177] J. H. Sinfeld, Surf. Sci. **500**, 923 (2002).

[178] N. W. Ashcroft, N. D. Mermin, in *Solid State Physics*, edited by Holt, Rinehart and Winston (New York 1976).

[179] V. E. Kenner, R. E. Allen, and W. M. Saslow, Phys. Rev. B **8**, 576 (1973).

[180] T. Rakshit, G.-C. Liang, A. W. Ghosh, and S. Datta, Nano Lett. **4**, 183 (2004).

[181] W. Shockley, Phys. Rev. **56**, 317 (1939).

[182] M. W. Cole and M. H. Cohen, Phys. Rev. Lett. **23**, 1238 (1969).

[183] S. L. Hulbert and P. D. Johnson, Phys. Rev. B **31**, 6815 (1985).

[184] P. D. Johnson, P. V. Smith, Phys. Rev. B **27**, 2527 (1983).

[185] D. Straub, F. J. Himpsel, Phys. Rev. Lett. **52**, 1922 (1984).

[186] D. F. Woodruff, N. M. Smith, P. D. Johnson, and W. A. Royer, Phys. Rev. B. **26**, 2943 (1982).

[187] P. Auger, Compt. Rend. **182**, 973 (1926).

[188] J. J. Lander, Progr. Solid State Chem. **2**, 26 (1965).

[189] L. C. Davis, M. P. Everson, and R. C. Jaklevic, Phys. Rev. B **43**, 3821 (1991).

[190] G. Binning, H. Rohrer, Ch. Gerber, and E. Weibel, Phys. Rev. Lett. **50**, 120 (1983).

[191] R. S. Becker, J. A. Golovchenco, D. R. Hamann, and B. S. Swartzentruber, Phys. Rev. Lett. **55**, 2032 (1985).

[192] J. Tersoff and D. R. Hamann, Phys. Rev. B **31**, 805 (1985).

[193] M. F. Crommie, C. P. Lutz, and D. M. Eigler, Nature (London) **363**, 524 (1993).

[194] Ph. Hofmann, B. G. Briner, M. Doering, H.-P. Rust, E. W. Plummer, and A. M. Bradshaw, Phys. Rev. Lett. **79**, 265 (1997).

[195] J. Li, W. Schneider, R. Berndt, O. R. Bryant, and S. Crampin, Phys. Rev. Lett. **81**, 4464 (1998).

[196] G. Neuhold and K. Horn, Phys. Rev. Lett. **78**, 1327 (1997).

[197] J.-Y. Park, U. D. Ham, S.-J. Kahng, Y. Kuk, K. Miyake, K. Hata, and H. Shigekawa, Phys. Rev. B **62**, R16341 (2000).

[198] M. Giesen, G. Schulze Icking-Konert, and H. Ibach, Phys. Rev. Lett. **82**, 3101 (1999).

[199] R. Paniago, R. Matzdorf, G. Meister, and A. Goldmann, Surf. Sci. **336**, 113 (1995).

[200] Ph. Avouris, R. Wolkow, Phys. Rev. B **39**, 5091 (1989).

[201] J. A. Rodriguez and D. W. Goodman, Science **257**, 897 (1992).

[202] B. Hammer, Y. Morikawa, J. K. Nørskov, Phys. Rev. Lett. **76**, 2141 (1996).

[203] A. Ruban, B. Hammer, P. Stoltze, H. L. Skriver, J. K. Nørskov, J. Mol. Catal. A **115**, 421 (1997).

[204] E. Bertel, M. Memmel, Appl. Phys. A **63**, 523 (1996).

[205] M. Gsell, P. Jakob, D. Menzel, Science **280**, 717 (1998).

[206] J. E. Houston, C. H. F. Peden, D. S. Blair, and D. W. Goodman, Surf. Sci. **167**, 427 (1986).

[207] S. D. Ruebush, R. E. Couch, S. Thevuthasan, and C. S. Fadley, Surf. Sci. **421**, 205 (1999)

[208] H. Zajonj, A. P. Baddorf, D. Gibbs, and D. M. Zehner, Phys. Rev. B **62**, 10436 (2000).

[209] M. Mavrikakis, B. Hammer, and J. K. Nørskov, Phys. Rev. Lett. **81**, 2819 (1998).

[210] C. H. F. Peden and D. W. Goodman, J. Catal. **104**, 347 (1987).

[211] P. J. Feibelman, J. E. Houston, H. L. Davis, D. G. O'Neill, Surf. Sci. **302**, 81 (1994).

[212] Y. G. Shen, D. J. O'Connor, J. Yao, H. van Zee, R. H. Roberts, R. J. MacDonnald, and K. Wandelt, J. Vac. Sci. Technol. A **13**, 1478 (1995).

[213] Y. Xu, M. Mavrikakis, Surf. Sci. **494**, 131 (2001).

[214] S. Sakong and A. Groß, Surf. Sci. **525**, 107 (2003).

[215] H. Koschel, U. Birkenheuer, G. Held, and H. P. Steinrück, Surf. Sci. **477**, 113 (2001).

[216] J. A. Rodríguez, R. A. Campbell, and D. W. Goodman, J. Phys. Chem. **95**, 2477 (1991).

[217] A. Bendounam, Y. Fagot Revurat, B. Kierren, F. Bertran, V. Yu Yurov, and D. Malterre, Suf. Sci. **496**, L43 (2002).

List of Publications

- *Tailoring surface electronic states via strain to control adsorption: O/Cu/Cu(0001).* R. Otero, F. Calleja, V. M. García-Suárez, J. J. Hinarejos, J. de la Figuera, J. Ferrer, A. L. V. de Parga, and R. Miranda, Surface Science **550**, 65 (2004).

- *Optimized basis sets for the collinear and non-collinear phases of iron.* V. M. García-Suárez, C. M. Newman, C. J. Lambert, J. M. Pruneda, and J. Ferrer, Journal of Physics-Condensed Matter **16**, 5453 (2004).

- *First principles simulations of the magnetic and structural properties of Iron.* V. García-Suárez, C. Newman, C. Lambert, J. Pruneda, and J. Ferrer, European Physical Journal B **40**, 371 (2004).

- *Towards molecular spintronics.* A. R. Rocha, V. M. García-Suárez, S. W. Bailey, C. J. Lambert, J. Ferrer, and S. Sanvito, Nature Materials **4**, 335 (2005).

- *Relationship between strain and the surface electronic structure of Cu(111) films on Ru(0001): Theory and experiment.* F. Calleja, V.M. García-Suárez, J. J. Hinarejos, J. Ferrer, A. L. V. de Parga, and R. Miranda, Physical Review B **71**, 125412 (2005).

- *Single-channel conductance of H_2 molecules attached to platinum or palladium electrodes.* V. M. García-Suárez, A. R. Rocha, S. W. Bailey, C. J. Lambert, S. Sanvito, and J. Ferrer, Physical Review B **72**, 045437 (2005).

- *Conductance Oscillations in zigzag platinum chains.* V. M. García-Suárez, A. R. Rocha, S. W. Bailey, C. J. Lambert, S. Sanvito, and J. Ferrer. Accepted in Physical Review Letters.

Submitted Articles

- *Tuning the electrical conductivity of nanotube-encapsulated metallocene wires.* V. M. García-Suárez, J. Ferrer, and C. J. Lambert. Submitted to Physical Review Letters.

- *Giant magnetoresistance of nickel-contacted carbon nanotubes.* S. Athanasopoulos, S. W. Bailey, J. Ferrer, V. M. García-Suárez, C. J. Lambert, A. R. Rocha, and S. Sanvito. Submitted to Physical Review Letters.

- *Engineering the band structure of decachlorofullerene[50] carbon nanotube peapods.* S. W. Bailey, V. M. García-Suárez, J. Ferrer, and C. J. Lambert. Submitted to Physical Review B.

- *Non-universal behavior of the parity effect in monovalent atomic wires.* P. Mayor, V. M. García-Suárez, S. Sirichantaropass, J. Cserti, C. J. Lambert, J. Ferrer, and G. Tichy. Submitted to Physical Review B.

- *Smeagol: a computational tool for molecular- and spin-electronics.* A. R. Rocha, V. M. García-Suárez, S. W. Bailey, C. J. Lambert, J. Ferrer, and S. Sanvito. Submitted to Physical Review B.